

Dissertation
submitted to the
Combined Faculties for the Natural Sciences and for
Mathematics
of the Ruperto-Carola University of Heidelberg, Germany
for the degree of
Doctor of Natural Sciences

put forward by
Dipl.-Phys. Andreas Bauer
born in Villingen-Schwenningen
Date of oral exam: 14.10.2015

Reionization in the Illustris Universe and Novel Numerical Methods

Referees:

Prof. Dr. Volker Springel

Prof. Dr. Cornelis Dullemond

Abstract

Numerical simulation methods provide powerful tools to study astrophysical processes in cosmic structure formation. Further advancing their utility requires to improve their accuracy and to account for more of the relevant physics. In this thesis, we pursue this goal by developing novel numerical approaches for studying the epoch of cosmic reionization and for simulating hydrodynamical flows with accurate higher-order methods. We introduce a novel GPU-based radiative transfer code designed to study cosmic reionization. Our implementation of radiative transfer uses either a cone-based or a moment-based advection method and is able to accurately follow the epoch of cosmic reionization in postprocessing. To validate our methods, we consider a number of standard reionization test problems. We then apply our implementation to the state-of-the-art Illustris simulation of galaxy formation. We find that the stellar populations of the galaxies forming in Illustris are able to reionize the universe at an epoch consistent with observations. In particular, our results reproduce Lyman- α constraints for the reionization history and yield an optical depth towards the surface of last scattering of $\tau = 0.065$, which is in reassuring agreement with recent Planck observations. In our simulations, reionization proceeds ‘inside-out’ and predicts an evolving size distribution of ionized bubbles that is characterized by ever larger maximum sizes of the bubbles with time, whereas the abundance of small bubbles stays relatively constant over an extended period until reionization is completed. The results obtained with both of our radiative transfer schemes are rather similar, suggesting that the details of these methods are not a major source of uncertainty.

We also present the implementation of a novel hydrodynamics solver based on a discontinuous Galerkin method. To this end we design and add an adaptive mesh refinement module to the hydrodynamical moving-mesh code AREPO. As a first application of this new tool, we discuss simulations of driven subsonic turbulence. There, we find an enlarged inertial range for our discontinuous Galerkin simulations compared with finite volume methods for an equal number of degrees of freedom. Furthermore, the overall compute time to solution at a prescribed accuracy is shorter as well for the new discontinuous Galerkin code, demonstrating the potential of this technique for future astrophysical applications.

Zusammenfassung

Numerische Simulationsmethoden sind ein mächtiges Werkzeug bei der Erforschung astrophysikalischer Prozesse in der kosmischen Strukturentstehung. Ihre Anwendung wird hauptsächlich limitiert durch die Genauigkeit der Simulation, deren Verbesserung sowie die Berücksichtigung weiterer physikalischer Prozesse der Schwerpunkt dieser Arbeit ist. Unser Ziel ist es, neue numerische Verfahren zu entwickeln, die es erlauben die Reionisationsepoche zu studieren und hydrodynamische Flüsse mit Methoden höherer Ordnung zu simulieren. Wir stellen eine neue GPU basierte Strahlungstransportanwendung vor, die entwickelt wurde, um die kosmische Reionisation zu studieren. Unsere Implementierung ist in der Lage die Reionisationsepoche in der Nachbearbeitung zu simulieren und verwendet dabei entweder eine Kegel-basierte oder eine Moment-basierte Advektionsmethode. Um unsere Implementierung zu validieren, zeigen wir standardisierte Testprobleme. Anschließend wenden wir unsere Implementierung auf die moderne Illustris Simulation der Galaxienentstehung an. Unsere Ergebnisse zeigen, dass die Sterne der in Illustris entstandenen Galaxien in der Lage sind, das Universum zu einem Zeitpunkt zu reionisieren, der mit Beobachtungen verträglich ist. Wir sind in der Lage Lyman α Messungen des Reionisationsverlaufs zu reproduzieren und erhalten eine optische Tiefe zum kosmischen Mikrowellenhintergrund von $\tau = 0.065$, was in sehr gutem Einklang mit aktuellen Planck Messungen ist. In unserem Modell findet Reionisation von innen nach außen statt. Es wird eine über die Zeit wachsende Häufigkeitsverteilung von ionisierten Blasen vorausgesagt, die durch eine ansteigende maximale Größe über die Zeit charakterisiert ist, während die Anzahl kleiner Blasen dabei über einen langen Zeitraum konstant bleibt bis die Reionisation vollendet ist. Die Ergebnisse, die wir mit unseren beiden Strahlungstransport Methoden erhalten sind sehr ähnlich, was den Schluss nahelegt, dass die Details dieser Methoden keine bedeutende Quelle von Unsicherheiten sind.

Weiterhin führen wir eine neue Methode hydrodynamischer Berechnungen ein, die auf diskontinuierlichen Galerkin Methoden beruht. Dafür haben wir für den hydrodynamischen moving mesh code AREPO ein adaptive mesh refinement Modul entworfen und implementiert. Als eine erste Anwendung dieses neuen Werkzeuges diskutieren wir Simulationen der getriebenen subsonischen Turbulenz. Hier sehen wir, dass Simulationen mit unserer diskontinuierlichen Galerkin Methode einen größeren inertialen Bereich haben als finiten Volumen Methoden bei gleicher Anzahl von Freiheitsgrade. Darüber hinaus verkürzt unsere neue diskontinuierliche Galerkin Methode die Laufzeit bis zur Lösung bei gegebener Genauigkeit. Dies veranschaulicht die Möglichkeiten dieser neuen Technik für zukünftige astrophysikalische Anwendungen.

Contents

List of Abbreviations	ix
List of Symbols	xi
I Introduction	1
1 Introduction	3
1.1 Cosmological foundations	3
1.2 Reionization	5
1.2.1 Sources of ionizing photons	6
1.2.2 Simulating reionization	7
1.2.3 Observing the Epoch of Reionization	8
1.3 Numerical methods for radiative transfer	11
1.4 GPU computing	12
1.5 Discontinuous Galerkin methods	13
1.6 Outline of this thesis	14
2 Physical Processes and Equations	15
2.1 Basic cosmological equations	15
2.2 Gravity	16
2.3 Equations of hydrodynamics	16
2.3.1 Euler equations	17
2.4 Radiative transfer	18
2.4.1 Absorption and emission mechanisms	18
2.4.2 The radiative transfer equation	19
2.4.3 Thermodynamic equilibrium	20
2.4.4 Moments of the transfer equation	21
2.5 Atomic processes	21
2.5.1 Photoionization and recombination	22
2.5.2 Collisional ionization	23
2.5.3 Collisional excitation	24
2.5.4 Bremsstrahlung	24
2.5.5 Compton scattering	24

II	Radiative Transfer and Cosmic Reionization	25
3	A GPU Based Radiative Transfer Solver for Simulating the Epoch of Reionization	27
3.1	Introduction	27
3.2	Radiative transfer	28
3.2.1	Cone-based advection method	28
3.2.2	A moment-based method with an M1 closure	29
3.2.3	Ionization network	30
3.3	Numerical discretization	32
3.3.1	Photon advection for the cone-based method	32
3.3.2	Photon advection for the M1 method	33
3.3.3	Solving the stiff thermochemical network	33
3.3.4	Time integration	35
3.4	Implementational details	35
3.4.1	Domain decomposition and parallelization	36
3.4.2	GPU parallelization	36
3.5	Test problems	37
3.5.1	Isothermal Strömgren sphere	38
3.5.2	Non-isothermal Strömgren sphere	40
3.5.3	Trapping of an ionization front by a cold dense clump	43
3.5.4	Cosmological box	47
3.6	Discussion	49
3.6.1	Performance characteristics	50
3.6.2	On the fly radiative transfer in a large cosmological simulations	53
4	Hydrogen Reionization in the Illustris Universe	55
4.1	Introduction	55
4.2	Methods	59
4.2.1	The Illustris simulation	59
4.2.2	Reionization in post processing	60
4.2.3	Escape fraction	60
4.2.4	Source modelling	62
4.3	Simulation results	64
4.3.1	Reionization history	65
4.3.2	UV background	69
4.3.3	Optical depth τ	71
4.3.4	Bubble size statistics	73
4.3.5	Distribution function of neutral volume fraction	75
4.4	Caveats and discussion	77
4.4.1	Reionization feedback	77
4.4.2	Moment-based vs cone-based RT method	78
4.4.3	How accurate is the reduced speed of light approximation?	80
4.4.4	Clumping factors	81

4.4.5	Spatial resolution and convergence	84
4.4.6	Comparison with a global reionization model	85
4.5	Conclusions	87
5	Flux Limited Diffusion in AREPO	91
5.1	Flux limited diffusion	91
5.2	Numerical implementation and implicit formulation	93
5.2.1	Discretization of the diffusion operator	94
5.2.2	Matrix solver	95
5.3	Marshak test	95
5.3.1	Marshak boundary condition	96
5.3.2	Results	96
5.4	Levitation test	97
5.4.1	Setup	99
5.4.2	Results	100
5.5	Discussion	108
III	Towards Novel Numerical Methods	111
6	An AMR Module for Arepo	113
6.1	Introduction	113
6.2	AMR mesh generation	114
6.3	Refinement and derefinement	116
6.4	Gradient estimation	117
6.5	Finite volume method	118
6.5.1	Slope limiting	118
6.6	Test problems	120
6.6.1	Shock tube	120
6.6.2	Kelvin-Helmholtz instability	121
6.6.3	Sedov-Taylor blast wave	124
6.6.4	Rayleigh-Taylor instability	126
6.7	Summary	128
7	Discontinuous Galerkin Hydrodynamics	129
7.1	Introduction	129
7.2	Field representation using basis functions	130
7.2.1	Basis functions	130
7.3	Initial conditions	132
7.4	Time evolution equations	132
7.4.1	Time integration	134
7.4.2	Time-step calculation	134
7.4.3	External force fields	135

Contents

7.5	DG with adaptive mesh refinement	135
7.5.1	Refinement	135
7.5.2	Derefinement	136
7.5.3	Refinement criterion	137
7.6	Slope limiting	137
7.6.1	Component-wise limiter	137
7.6.2	Positivity limiter	138
7.7	Discussion	140
8	Subsonic Turbulence Simulations using Discontinuous Galerkin Hydrodynamics	141
8.1	Introduction	141
8.2	Simulational setup	142
8.2.1	Turbulent driving	142
8.2.2	Dissipation measurement	144
8.2.3	Power spectrum measurement	145
8.3	Results	146
8.3.1	Mach number evolution	147
8.3.2	Injected and dissipated energy	148
8.3.3	Velocity power spectra	149
8.3.4	Density PDFs	150
8.4	Discussion	151
IV	Conclusion	155
9	Conclusion and Outlook	157
9.1	Conclusion	157
9.1.1	Radiative transfer and reionization	157
9.1.2	Discontinuous Galerkin hydrodynamics	158
9.2	Outlook	159
	Appendix	163
	Bibliography	179
	Acknowledgments	181

List of Abbreviations

AGN	active galactic nuclei
AMR	adaptive mesh refinement
CGM	circumgalactic medium
CIC	clouds-in-cells
CMB	cosmic microwave background
DG	discontinuous Galerkin
EoR	epoch of reionization
FLD	flux limited diffusion
GLF	global Lax Friedrich
GLL	Gauss-Lobatto-Legendre
GPGPU	general-purpose computing on graphics processing units
GPU	graphics processing unit
IGM	intergalactic medium
ISM	interstellar medium
JWST	James Webb Space Telescope
kSZ	kinetic Sunyaev-Sel'dovich effect
LTE	local thermodynamic equilibrium
Ly α	Lyman α
NGP	nearest-grid-point
OTSA	on the spot approximation
OTVET	optically thin variable Eddington tensor approximation
OU	Ornstein-Uhlenbeck process
OV	Ostriker-Vishniac effect
PDF	probability density function
QCD	quantum chromodynamics
QED	quantum electrodynamics
RHD	radiation hydrodynamics
SDSS	Sloan Digital Sky Survey
SKA	Square Kilometre Array
SPH	smooth particle hydrodynamics
SSP	strong stability preserving
TV	total variation
TVB	total variation bounded
TVD	total variation diminishing
UV	ultraviolet
VET	variable Eddington tensor

List of Symbols

<i>Used notation</i>	
$\mathbf{a}\mathbf{b}$	scalar product
$\mathbf{a} \otimes \mathbf{b}$	dyadic product, $(\mathbf{a} \otimes \mathbf{b})_{ij} = a_i b_j$
f	scalar quantity
\mathbf{f}	vector quantity, with entries f_i
\mathbf{F}	rank two tensor, with columns \mathbf{F}_i
$\nabla \cdot \mathbf{F}$	divergence of a tensor, $\sum_i \partial \mathbf{F}_i / \partial x_i$

<i>General</i>	
A	surface area
c	speed of light
e	specific energy
ϵ	specific internal energy
f	distribution function
\mathbf{F}	force vector
\mathbf{F}	flux tensor (with columns \mathbf{F}_i)
\mathcal{F}	numerical flux
ϕ	gravitational potential
ϕ	gravitational potential
g_i	statistical weight
G	gravitational constant
γ	adiabatic index
k_B	Boltzmann constant
l	AMR level
m	particle mass
μ	mean molecular weight
\mathbf{n}	surface normal vector
P	pressure
\mathbf{q}	state vector
ρ	density
σ	cross section
σ_{th}	Thomson cross section
t	time
T	temperature
\mathbf{u}	microscopic velocity

List of Symbols

ψ	slope limiter
\mathbf{v}	macroscopic velocity / mean velocity
V	volume (element)
Ω	angular direction / element
\mathbf{x}	coordinate vector

Cosmology

a	cosmological scale factor
h	Hubble parameter
$H(a)$	Hubble function
Λ	cosmological constant
ρ_{crit}	critical density
Ω_{b}	baryon fraction
Ω_{dm}	dark matter fraction
Ω_{r}	fraction of relativistic particles
Ω_{Λ}	dark energy fraction / cosmological constant
z	cosmological redshift

Radiative transfer

a_{R}	radiation constant
A_{ij}	Einstein coefficient of spontaneous emission
α	opacity
α_{E}	energy mean opacity
α_{F}	flux mean opacity
α_{P}	Planck mean opacity
α_{R}	Rosseland mean opacity
B	Planck function
B_{ij}	Einstein coefficient of simulated emission / absorption
E	radiation energy density
η	emissivity
\mathbf{F}	radiation flux (vector)
h	Planck constant
I	radiation intensity / photon distribution function
κ	specific opacity
λ	flux limiter
ν	frequency
\mathbf{P}	radiation pressure tensor
S	source function
τ	optical depth

Reionization

α	recombination rate
β	collisional ionization rate

C	clumping factor
\mathcal{C}	cooling rate
f_{esc}	escape fraction
Γ	reaction rate
\mathcal{H}	heating rate
n_e	free electron number density
n_{H}	hydrogen number density
r_{S}	Strömgren radius
t_{rec}	recombination time scale
Q	ionized volume fraction
x_{HI}	neutral fraction
x_{HII}	ionization fraction
x_{M}	mass weighted neutral fraction
x_{V}	volume weighted neutral fraction

Discontinuous Galerkin

k	degree of the DG scheme
ξ	coordinate vector in cell coordinate system $([-1, 1])$
P	Legendre polynomial
\tilde{P}	scaled Legendre polynomial
\mathbf{P}	projection matrix
ψ	basis function
ω	quadrature weight
\mathbf{w}	DG weight vector (one entry per hydro quantity)
$\hat{\mathbf{w}}$	DG weights of a single quantity

Turbulence

\mathbf{a}	acceleration field
$\hat{\mathbf{a}}$	acceleration field in Fourier space
C	correlation function
E	power spectrum
\mathbf{k}	Fourier space coordinate
\mathcal{M}	Mach number

Part I

Introduction

1

Introduction

1.1 Cosmological foundations

Ever since its existence, human mankind has been looking for a cosmological model, describing the world and the Universe. Guided by many astronomical observations, a lot of progress has been made over the last centuries in developing such a model that is based on physical assumptions. Nowadays, the most widely favoured model is the Λ cold dark matter (Λ CDM) universe, filled with an unknown kind of matter, called ‘cold dark matter’, and an even more mysterious form of ‘dark energy’, which in the simplest case takes the form of a cosmological constant Λ .

The most favoured model for the very early Universe is the hot big bang scenario. Due to a lack of observations at the earliest times, it is not known what caused the big bang in first place, so this remains a highly speculative area in cosmology. It is clear, however, that the Universe was initially in an extremely hot and dense state. Right after the big bang, the Universe presumably went through an epoch of inflation, during which the Universe expanded exponentially. Eventually, the field driving the inflation decayed and left a quark-gluon plasma behind. The normally expected equal abundance of matter and antimatter particles got violated in this phase by a process called baryogenesis. This effectively produced an extremely tiny imbalance between baryons and anti-baryons, leading to the matter content of today’s Universe after all antimatter annihilated but some normal matter was still left over.

It is customary to parametrize the expansion of the Universe since the big bang by the cosmological scale factor a , which relates the scale of the Universe in the past to its present day size. This scale factor a is directly related to the cosmological redshift z in the observed spectra of distant sources, through $z = 1/a - 1$. Both, redshift and scale factor are interchangeably used as a measure of time, effectively labelling

certain epochs (i.e. time) with the corresponding size of the Universe. The present day epoch is $z = 0$ and higher redshifts refer to earlier times.

During the rapid expansion of the early universe, the energy density decreases further and further. This means that creation and annihilation reactions which had been in thermodynamical equilibrium start to eventually freeze out. At a temperature of around 160 MeV, the quantum chromodynamics (QCD) phase transition took place. As a result, quarks were no longer free, but started to form baryons. These baryons could still react with other particles and were not stable. At around 2.7 MeV, the neutrino background froze out, followed shortly afterwards by electrons and positrons at 1 MeV. Protons and neutrons only freeze out at far lower temperatures of 800 keV. Finally, at around 78 keV deuterium can form. Afterwards all light elements up to Lithium are created.

Considerably later, the epoch of recombination happened, where neutral hydrogen atoms are formed¹. This occurs once the photons were not energetic enough anymore to split neutral hydrogen into a proton and an electron. For this phase transition, the temperature had to fall down to 0.3 eV, which happened at a redshift of about $z = 1100$. Note that this is considerably lower than 13.6 eV, the ionization potential of hydrogen. This is due to the high photon-to-baryon ratio and the large number of photons in the tail of the Planck distribution, which is delaying recombination.

After recombination had been completed, photons started to travel (almost) freely. This relic radiation is now observable as the cosmic microwave background (CMB) radiation. Due to cosmic expansion, the initially hot CMB cooled down to only 2.7 K today. The tiny temperature fluctuations of about 10^{-5} observed in the CMB contain a wealth of information about our universe. Pioneering work in mapping the CMB has been done by the COBE and WMAP satellite missions. The most precise measurement of the CMB up till now was recently obtained by the PLANCK satellite. Combined also with other cosmological data, this has led to quite tightly constrained parameters of the Λ CDM cosmology. The latest set of cosmological constraints inferred from the Planck mission can be found in Planck Collaboration et al. [2015b].

The initial density perturbations seen in the CDM are believed to originate in quantum fluctuations which are stretched and enlarged during the inflationary phase. Due to gravitational instability, the fluctuations act as seeds for cosmic structure formation. Until about $z_{\text{eq}} = 3371 \pm 23$, the energy content of the Universe is dominated by the radiative component. During this time, fluctuations on scales larger than light could travel since the Big Bang – the so-called Hubble horizon – were not causally connected and could grow as $\propto a^2$. Once they entered the Hubble horizon, their growth was stifled by the fast expansion of the Universe during the radiation dominated era. This therefore suppresses modes which enter the Hubble horizon during the radiation dominated era relative to those entering it only later in the matter dominated era.

¹The term ‘recombination’ is arguably a bit of a misnomer here as the atoms had never existed earlier and hence cannot ‘reform’.

After recombination, the so called “dark ages” began [Rees, 2000] to ensue in the universe. During this epoch, small dark matter perturbations collapsed into halos for the first time. The formation of larger dark matter halos then happened in a hierarchical way, with small perturbations collapsing first into small halos and then forming ever larger objects through mergers. In sufficiently massive dark matter halos, gas could then fall in, radiatively cool, and form the first stars and galaxies. The dark ages ended as the first stars form inside these galaxies and start to reionize the neutral gas, eventually making the Universe transparent. In fact, we know that this must have happened at some point because today’s Universe is highly ionized.

1.2 Reionization

With the emergence of the first luminous ultraviolet (UV) sources in the Universe, a phase transition from a neutral to an ionized intergalactic medium (IGM) began. This transition occurred most likely in a highly inhomogeneous manner, starting around the first bright UV photon sources. At the same time, reionization left its imprint in many quantities observable today, as we will discuss further below [for reviews see Barkana and Loeb, 2001; Fan et al., 2006a; Loeb and Barkana, 2001; Morales and Wyithe, 2010].

A so called Strömgren sphere of ionized material forms around each UV source. The progression of this first phase of reionization is mostly determined by how many ionizing photons become available per baryon. This can be parametrized as

$$N_{\text{ion}} = N_{\gamma} f_{\text{star}} f_{\text{esc}}, \quad (1.1)$$

with N_{γ} being the number of photons per stellar baryon, f_{star} denoting the star formation efficiency and f_{esc} the escape fraction. Typical required values are 10000 to 50000 ionizing photons per stellar baryon, a star formation efficiency of about $f_{\text{star}} = 0.2 - 0.4$ and an escape fraction of only a few percent up to $f_{\text{esc}} = 0.2$ [Aubert and Teyssier, 2010; Iliev et al., 2006a]. This ratio depends on the assumed IMF and metallicity of the gas as well as how many photons can escape from the dense host galaxies of the source.

This first phase of reionization is followed by a phase of percolation. During this stage, individual HII spheres began to overlap. Once an overlap between two Strömgren spheres happened, baryons in the overlapping region are receiving ionizing photons from multiple sources and the UV background turns to be much more homogeneous. This enables the reionization of denser parts in the overlap region. In this last phase of reionization, the residual neutral fraction is reduced down to $x_{\text{HI}} \sim 10^{-5}$ in the IGM and reionization is completed.

A critical star formation rate required to reionize the universe is estimated in Madau et al. [1999]:

$$\dot{\rho}_{\odot} \approx 0.013 f_{\text{esc}}^{-1} \left(\frac{1+z}{6} \right)^3 \text{M}_{\odot} \text{yr}^{-1} \text{Mpc}^{-3}, \quad (1.2)$$

assuming a Salpeter IMF at solar metallicity. However, cosmological simulations of galaxy formation require a declining star formation history towards high redshift [see e.g. Hernquist and Springel, 2003; Stinson et al., 2013], and this is also inferred from observations [see e.g. Ellis et al., 2013].

A much debated issue in the literature has been whether reionization proceeds first in dense regions and propagates then to lower densities (inside-out) [Chardin et al., 2014; Ciardi et al., 2003; Iliev et al., 2006a, 2014; So et al., 2013; Zahn et al., 2007], or the opposite is the case (outside - in) [Gnedin, 2000; Miralda-Escudé et al., 2000]. Another possible scenario suggests a late reionization of filaments (inside - out - middle), which may especially be the case if high degrees of ionization are considered [Finlator et al., 2009; So et al., 2013].

The two most abundant elements after primordial nucleosynthesis are hydrogen and helium. Neutral hydrogen has an ionization edge of $E_\nu = 13.6 \text{ eV}$. Neutral helium is singly ionized roughly at a similar time as hydrogen due to its similar ionization potential of $E_\nu = 24.6 \text{ eV}$ and comparable recombination cross section. However, full helium reionization is believed to happen only as late as $z \sim 3$. This is due to the much higher ionization potential of $E_\nu = 54.4 \text{ eV}$ of HeII, and its higher recombination cross section. The soft UV spectrum of stellar sources is not able to provide the required energetic UV photons, and thus full helium reionization is delayed until hard enough UV photons from active galactic nuclei (AGN) become available. The lateness of the reionization of helium makes this process potentially easier to observe, but thus far its observational detection is still tentative. Note that while hydrogen reionization heats the IGM to about 10^4 K , helium reionization is able to heat the universe to higher temperatures of about 210^4 K .

Reionization is expected to act as a negative feedback mechanism on its sources. The photoionization heating associated with reionization can evaporate small halos and hence recycle previously collapsed gas back into the intergalactic medium. Additionally, the Jeans mass is increased after reionization, preventing small scale halos from accreting baryons. This suppresses star formation in small halos and might in turn react back on the progress of reionization, diminishing the number of UV photons that become available from young stars.

1.2.1 Sources of ionizing photons

A lower limit for the ionizing UV luminosity of all sources can be derived from the requirement to keep the universe ionized since $z \sim 6$ and the need to balance losses from recombinations given the hydrogen density distribution. Miralda-Escudé et al. [2000] finds a minimum UV luminosity per comoving volume of

$$\dot{N}_{\text{ion}}(z) = 10^{51.2} \text{ s}^{-1} \text{ Mpc}^{-3} \left(\frac{C}{30} \right) \left(\frac{1+z}{6} \right)^3 \left(\frac{\Omega_b h^2}{0.02} \right)^2, \quad (1.3)$$

where the IGM clumping factor $C = \langle n_{\text{H}}^2 \rangle / \langle n_{\text{H}} \rangle^2$ is typically derived from simulations.

A promising class of sources for ionization are in principle AGN, which are particularly bright UV photon emitters. However, their low cumulative luminosity and low

abundance at high redshift [Faucher-Giguère et al., 2009; Hopkins et al., 2007] make it unlikely that quasars are the driving source of hydrogen reionization. Nevertheless, their hard UV spectrum is believed to be essential for doubly ionizing helium at around $z \sim 3$, which coincides also with the peak of quasar activity.

The most likely candidates for being the responsible UV sources for reionization are small star-forming galaxies. The host halos of these stellar populations can be subdivided into mini-halos and atomic cooling halos [Ahn et al., 2012; Paardekooper et al., 2013]. Mini-halos have masses below $\sim 10^8 M_\odot$ and a virial temperature below $\sim 10^4$ K. They can only cool and form stars through molecular hydrogen cooling. However, molecular hydrogen is easily destroyed by reionization heating. Thus, reionization provides a strong negative feedback on these small halos.

Atomic cooling halos on the other hand are dense enough for atomic hydrogen cooling to become effective, making them less affected by reionization heating. The low mass galaxies associated with these halos might not be able to complete reionization alone, but they may significantly contribute to an early onset of reionization [Ahn et al., 2012]. These small mass galaxies also have a high escape fraction [Wise et al., 2014], which further increases their contribution to reionization. The very first stars, the so-called population III stars, could have provided substantial amounts of ionizing photons at even higher redshift, but their overall contribution to reionization is found to be negligible in recent works [Paardekooper et al., 2013; Wise et al., 2014].

1.2.2 Simulating reionization

There is a tremendous interest in making predictions for future observations of the epoch of reionization using computer simulations [for a review see Trac and Gnedin, 2011]. Most of these simulations focus on studying reionization in post processing [e.g. Ahn et al., 2012; Aubert and Teyssier, 2010; Ciardi et al., 2003; Croft and Altay, 2008; Iliev et al., 2006b; McQuinn et al., 2007a; Sokasian et al., 2001; Trac et al., 2008; Zahn et al., 2007]. Lately, a lot of progress has also been made on dynamically coupling a radiative transfer solver with a cosmological hydrodynamic simulation of galaxy formation [e.g. Gnedin, 2000, 2014; Gnedin and Kaurov, 2014; Norman et al., 2013; Paardekooper et al., 2013; Pawlik et al., 2015; Petkova and Springel, 2011b; So et al., 2014]. This allows in principle for a self-consistent inclusion of reionization feedback processes on star formation and hydrodynamics. However, if a large volume at a high spatial resolution is needed, dynamically coupled methods are still not feasible due to their high computational cost.

Indeed, a volume of at least $100h^{-1}$ Mpc is needed to obtain converged results [Iliev et al., 2014] for cosmic reionization. Such large box sizes are needed for reasons of cosmic variance and because the mean free path of photons can be tens of Mpc at around $z = 6 - 10$ [Trac and Gnedin, 2011]. Ideally, a much larger box size of around 1000 Mpc would be desirable in order to also contain a representative sample of rare high mass objects. At the same time the resolution should be sufficient to resolve halos of $10^8 M_\odot$, which are very abundant and able to form at least some stars. Also their gas clumping can be significant, making them important photon sinks.

Aubert and Teyssier [2010]; Kohler et al. [2007] used a sub-resolution model to include the recombination in unresolved clumps. These effective clumping factors can be inferred from small-scale simulations that directly resolve the sinks but which contain only one or a few galaxies. Large-scale simulations on the other hand typically use dark matter only models, and add stellar sources in postprocessing into the formed halos. Another important aspect is the adoption of an escape fraction, which models the escape of photons from their host galaxies or halos. Most previous simulations have assumed a globally constant escape fraction. However, in Kuhlen and Faucher-Giguère [2012] a variable escape fraction based on a measured high redshift UV luminosity function was suggested, which we shall also use in our study.

1.2.3 Observing the Epoch of Reionization

CMB optical depth measurements

The CMB provides constraints on the Epoch of Reionization and the reionization history through the temperature and polarization anisotropy power spectrum [see e.g. Kaplinghat et al., 2003; Keating et al., 1998; Zaldarriaga, 1997]. After decoupling, CMB photons can scatter off from free electrons released during reionization. The CMB temperature anisotropy power spectrum is then damped as $C_l^{T'} = e^{-2\tau} C_l^T$, where τ is the Thomson optical depth towards the surface of last scattering. This damping is degenerate with the primordial power spectrum amplitude for scales smaller than the horizon scale at last scattering. However, the polarization power spectrum allows a breaking of this degeneracy. In the E-mode power spectrum a new peak at large scales develops through reionization if the CMB radiation has a quadrupole component. The measurement of the position of this peak, which is on scales of $> 10^\circ$, allows a determination of the reionization redshift when one assumes an instantaneous transition from a neutral to an ionized medium.

The optical depth to the last scattering surface provides only an integral constraint on the reionization history. Two secondary anisotropic effects could allow more insights on the homogeneity of reionization and how it proceeded: The kinetic Sunyaev-Sel'dovich effect (kSZ) and the Ostriker-Vishniac (OV) effect. Unfortunately, their impact on the CMB spectrum might be very hard to detect [Hu, 2000; Seshadri and Subramanian, 1998].

For a long time, CMB observations by WMAP favoured a high value for the optical depth of $\tau = 0.088 \pm 0.013$, corresponding to $z_{\text{reion}} = 10.5 \pm 1.1$ [Hinshaw et al., 2013]. This indication of an early epoch of reionization resulted in some tension with reionization redshifts inferred from quasar absorption spectra observations. However, the latest PLANCK results [Planck Collaboration et al., 2015a] have revised the constraints to a lower optical depth of $\tau = 0.066 \pm 0.016$ and now predict a later reionization transition at $z_{\text{reion}} = 8.8_{-1.4}^{+1.7}$ which reduces this tension a lot.

Quasar absorption spectra

Spectra of quasars with $z_{\text{source}} > z_{\text{reion}}$ provide another important observable to constrain the redshift z_{reion} of reionization. Lyman α ($\text{Ly}\alpha$) photons from the source are absorbed by neutral hydrogen in the IGM along the line of sight. The Gunn-Peterson optical depth is

$$\tau_{\text{GP}} = \frac{\pi e^2}{m_e c} f_{\alpha} \lambda_{\alpha} H^{-1}(z) n_{\text{HI}}, \quad (1.4)$$

with the oscillator strength f_{α} , the $\text{Ly}\alpha$ transition frequency $\lambda_{\alpha} = 1216 \text{ \AA}$ and Hubble constant $H(z)$ [Gunn and Peterson, 1965]. The photons become redshifted as they travel towards the observer and thus photons are shifted out of resonance with the $\text{Ly}\alpha$ transition. Afterwards, these photons can travel freely towards the observer. Using this mechanism, the spectra of a distant quasar can be converted into a neutral hydrogen density map along the line of sight, which is also referred to as the $\text{Ly}\alpha$ forest. This measurement is very sensitive to neutral hydrogen and even a tiny residual fraction of $x_{\text{HI}} \sim 10^{-4}$ is enough to lead to complete absorption in the $\text{Ly}\alpha$ forest. The absorbed $\text{Ly}\alpha$ photons are reemitted, leading to a $\text{Ly}\alpha$ halo around the host galaxy [Loeb and Rybicki, 1999; Rybicki and Loeb, 1999], which may provide further constraints.

A similar measurement is possible using the $\text{Ly}\beta$ and $\text{Ly}\gamma$ transitions. Due to the smaller optical depth of these transitions, they can still be used to infer the ionization state in case the $\text{Ly}\alpha$ transition is already saturated. The bright quasars drive a Strömgen sphere around themselves. Using the difference of the redshift of the quasar and the edge of the Gunn-Peterson trough, the size of the Strömgen sphere can be inferred, and typical sizes of about $\sim 5 \text{ Mpc}$ at $z > 6$ have been found [Fan et al., 2006c; Walter et al., 2003; White et al., 2003; Wyithe and Loeb, 2004, 2005].

In Djorgovski et al. [2001] a dark gap in the spectrum of SDSS J1044 - 0125 with $\tau_{\text{GP}} > 4.6$ at $z = 5.2 - 5.6$ was discovered, but the first clear case of a Gunn-Peterson trough was found in Becker et al. [2001]; Fan et al. [2001] at $5.95 < z < 6.15$. In Fan et al. [2006c], nineteen Sloan Digital Sky Survey (SDSS) quasars with redshifts $z > 5.7$ were studied. They found a rapid increase in the optical depth at around $z > 5.5$, indicating that reionization must be complete at around the same time. Using $\text{Ly}\alpha$ forest observations, the ionization state of the IGM and the UV background can be estimated [Faucher-Giguère et al., 2009; Haardt and Madau, 2012; McDonald and Miralda-Escudé, 2001; McDonald et al., 2000; Weinberg et al., 1997]. These authors report a substantial drop in the UV background from $z \sim 5$ to $z > 6$. At $z > 6$ the volume averaged neutral fraction is $> 10^{-3.5}$, perhaps even as high as 0.1, but drops to $\leq 10^{-4}$ at $z < 5.5$ [Cen, 2002; Fan et al., 2002, 2006c; Lidz et al., 2002].

21 cm observations

A very promising upcoming method to observe the Epoch of Reionization is given by 21 cm radio observations [see Furlanetto et al., 2006; Zaroubi, 2013, for a review].

The energy difference of the hyperfine structure splitting of the 1s ground state of the neutral hydrogen atom is about $5.87 \mu\text{eV}$ which corresponds to a wave length of 21 cm in the atom's rest frame. The two states differ in the orientation of the electron spin relative to the proton spin. The 21 cm line can be seen either in absorption or in emission against the CMB. The differential brightness temperature of the signal is

$$\delta T \approx \frac{T_S - T_{\text{CMB}}}{1+z} \tau \approx 7(1+\delta)x_{\text{HI}} \left(1 - \frac{T_{\text{CMB}}}{T_S}\right) (1+z)^{1/2} \text{mK}, \quad (1.5)$$

with optical depth τ , overdensity δ and ionization state x_{HI} .

The signal depends on the ratio between spin temperature and CMB temperature. This leads to the following four regimes [Ali et al., 2005; Barkana and Loeb, 2004; Carilli et al., 2004]: Initially at $z > 200$ the spin and CMB temperature are in equilibrium through Thomson scattering which results in no 21 cm signal. Due to adiabatic expansion, the gas cools faster than the CMB, such that the 21 cm signal is seen in absorption ($30 \sim z < 200$). Later, due to the low density the gas temperature can no longer stay coupled to the spin temperature, allowing the spin temperature approach the CMB temperature again ($20 < z < 30$). However, locally the spin and gas temperature may still be coupled through Ly- α photons. Also, X-rays could locally warm the IGM. This leads to a mix of regions without a signal, regions seen in absorption and regions seen in emission, leading to a rich 21 cm signal.

Afterwards, additional physical processes leave their imprints on the 21 cm signal. Quasars and stars start to ionize and heat the IGM. Shocks and X-ray radiation lead to additional heating of the universe. Interestingly, a HII bubble itself would show no significant signal, as the neutral region around the bubble would show an emission signal due to the heated medium which is compensated by a cooler expanding shell seen in absorption [Tozzi et al., 2000].

A great advantage of 21 cm measurements is the fact that regions with high neutral densities can be directly imaged, including those which would be saturated in Ly- α forrest observations. By observing the redshifted 21 cm signal in multiple frequency bins, tomography is possible, yielding full 3D information instead of only integral quantities like the optical depth inferred from CMB observations. This would hence allow for a direct mapping of the HI density in redshift space and straightforward comparisons to simulation predictions [Ciardi et al., 2003; Furlanetto et al., 2004; Gnedin and Shaver, 2004; Mellema et al., 2006b; Mondal et al., 2015; Zahn et al., 2007]. Furthermore, power spectra of the globally averaged differential brightness temperature δT can be computed as well. So far, this is still all an observational frontier of the future, but several 21 cm observational programs are already on the way or in an advanced planning stage. In particular, the signatures of reionization may be observable with the LOFAR telescope array, which is already operating. The future SKA should definitely be sensitive enough to provide detailed 3D maps of the Epoch of Reionization [see Iliev et al., 2015; Semelin and Iliev, 2015]. Reliably interpreting these upcoming observations and extracting their full cosmological information content relies on the availability of accurate theoretical

models for detailed comparisons. Providing such models through new numerical methods is therefore the primary goal of this thesis.

1.3 Numerical methods for radiative transfer

Solving the radiative transfer equation numerically still poses a great challenge. An accurate solution requires usually a high temporal resolution, due to the – compared to other cosmologically relevant processes – fast speed of light. The collisionless behaviour of light in a rarefied medium further complicates radiative transfer, as the transfer method has to somehow track the angular dependency in the distribution function of photons, which is a six dimensional distribution composed of three spatial, two angular, and one frequency dimension (ignoring polarization). The need to create sharp shadows around dense absorbers provides a further challenge for radiative transfer methods. This demanding problem led to the development of many approximate methods for radiative transfer which greatly differ in the adopted tradeoff between accuracy and computational cost. Thus, whether a certain radiative transfer method is suitable or not depends strongly on the specific problem. Existing radiative transfer algorithms can be categorized broadly into three classes of methods, which we will briefly describe in the following.

Monte Carlo Methods

A large class of methods are the so-called Monte Carlo based techniques [e.g. Altay et al., 2008; Baek et al., 2009; Ciardi et al., 2001; Dullemond, 2011, 2012; Maselli et al., 2003; Nayakshin et al., 2009; Pawlik and Schaye, 2008; Semelin et al., 2007]. These methods discretize the radiation field into independent photon packets and follow them through the simulation until they are either absorbed or escape from the simulation domain. Sources of photons replenish the photon packets. If in addition to absorption by ionization photon scattering should be included, additional modifications to the method are required to prevent a high computational cost that would otherwise be caused by photons trapped in dense clouds. In the limit of a very high number of photon packets, Monte Carlo methods produce very accurate results. Unfortunately, they typically show a slow convergence rate of only \sqrt{N} , where N is the number of photon packets used, negatively impacting their computational efficiency.

Long and short characteristics methods

Another major class of methods are the long and short characteristics methods [e.g. Abel and Wandelt, 2002; Abel et al., 1999; Ahn and Shapiro, 2007; Altay et al., 2008; Alvarez et al., 2006; Baek et al., 2009; Cantalupo and Porciani, 2011; Cen, 2002; Davis et al., 2012; Greif, 2014; Gritschneider et al., 2009; Hasegawa and Umemura, 2010; Kunasz and Auer, 1988; Maselli et al., 2003; McQuinn et al., 2007c; Mellema et al., 1998, 2006a; Mihalas and Mihalas, 1984; Nakamoto et al., 2001; Razoumov

and Cardall, 2005; Shapiro et al., 2004; Sokasian et al., 2001; Susa, 2006; Trac and Cen, 2007; Whalen and Norman, 2006]. These methods cast many rays through the simulation domain and discretize the radiative transfer equation along these rays. The rays start at the sources and are coupled to other rays in regions where they interact, ending up with a large coupled system of (linear) equations. If enough rays are used and every photon source is well connected with the surrounding absorption sites, the results can become very accurate. In such a ‘long characteristic methods’, each ray spans the entire simulation domain. The down-side of the this type of method is the fact that the number of rays needed scales with the number of sources. If only a few dominant radiation sources are within the domain, this is not a critical limitation and these methods are able to accurately track the radiation field around the sources with high angular resolution. The efficiency of the method can be greatly improved in so-called ‘short characteristics methods’, where only rays of limited length that only couple cells in the neighbourhood of each other are used. The use of short rays instead of long ones allows one to track many sources and still keep the computational cost manageable.

Moment-based methods

The third large class of methods are the so-called moment-based methods [Aubert and Teyssier, 2008; Davis et al., 2012; Finlator et al., 2009; Gnedin and Abel, 2001; Petkova and Springel, 2009; Rosdahl et al., 2013]. In these approaches moments of the radiative transfer equations are taken by integrating over the angular dependency of the Boltzmann equation. The resulting hierarchy of equations is closed by making additional assumptions, for example by conjecturing a relation between the local radiation pressure tensor and the angle averaged intensity. The resulting time evolution equations for the moments are then discretized and solved on a grid, yielding a photon intensity field. The big advantage of these methods is their independence on the number of sources. Every cell can be a photon source or sink without significantly impacting the performance of the method. The methods of this class differ primarily in whether only the zeroth, or the zeroth and first moments of the Boltzmann equation are taken into account, and which closure relation is adopted. The simplest version of a moment-based method is flux-limited diffusion.

1.4 GPU computing

General-purpose computing on graphics processing units (GPGPU) is a modern trend in high performance computing. Instead of using a traditional CPU only, all or some computations are offloaded to a Graphics Processing Unit (GPU). These GPUs can provide significant computational power, however, efficiently making use of it requires a massive amount of highly parallel workload. The execution path taken in each parallel thread has to be as similar as possible to the execution paths of neighbouring threads. Otherwise, the diverging parts of the code will not be executed in parallel anymore. This special kind of massive parallelism can only be achieved

with specially tailored algorithms and numerical implementations. Additionally, the amount of memory directly available on a GPU is rather small compared with what is available nowadays as main memory to conventional CPUs.

If an algorithm can be formulated in a highly parallel way, a significant speed up compared to a traditional CPU-only implementation can be achieved when using GPUs. This makes GPGPU computing interesting for compute-intensive applications like radiative transfer. A particularly interesting idea is to solve the radiative transfer equation on the GPU, while the remaining parts of the simulation are solved on the CPU. However, it is clear that developing such methods only pays off if sufficiently large and demanding problems have to be solved. The scientific topic of the epoch of reionization clearly falls into this category. We also note that more and more of the largest supercomputers in the world obtain their huge compute power from accelerator cards like GPUs. GPUs are leading in terms of energy efficiency as well, which makes them an interesting key component for the exa-scale machines (which can carry out 10^{18} floating point operations) anticipated at the end of this decade. Thus, if these machines shall be used efficiently in the future for cosmological simulations, GPGPU-aware applications will be a requirement.

1.5 Discontinuous Galerkin methods

In astrophysics, the two main methods traditionally in use for solving the Euler equations are smoothed particle hydrodynamics (SPH) [Gingold and Monaghan, 1977; Lucy, 1977] and mesh-based methods using a finite volume discretization. With the arrival of massively parallel exa-scale machines, there is however plenty of motivation to search for more accurate and more efficient methods for handling hydrodynamics. If such a faster scheme can be found, additional computational performance becomes available which can be used to obtain a more accurate solution.

Discontinuous Galerkin (DG) methods represent such a promising class of methods. They are mesh-based and allow a straightforward extension to schemes with arbitrary high order. Especially for applications involving comparatively smooth problems, such as subsonic turbulence, these higher-order methods are very interesting and promise to be very efficient. Instead of representing the state within a cell by its mean value and constructing local reconstructions for higher order, polynomials of up to a certain degree are used to describe the state within a cell. The coefficients of these polynomials are evolved forward in time and retained after the end of a timestep instead of being reconstructed from neighbouring values at every step. The used stencils remain short independent of the order, and involve only the direct neighbours, such that the compute to data-access ratio is more favourable. Thus, they proved a viable and promising alternative for solving the hyperbolic Euler equations in astrophysics, something that we demonstrate in detail in this thesis.

1.6 Outline of this thesis

This thesis is structured as follows:

- In Chapter 2 we summarize the main physical processes and equations used in this thesis. A very brief review of hydrodynamics, radiative transfer and the relevant atomic processes is given.
- Chapter 3 presents the implementation of our radiative transfer solver. We implement two approaches, a cone-based method and a moment-based method with an M1 closure. To speed up the computations, we make use of GPUs.
- In Chapter 4 we present an application of our radiative transfer code by studying reionization in the Illustris simulation. The results are based on radiative transfer simulations in post processing. This Chapter has been previously published in Bauer et al. [2015]
- In Chapter 5 we present the implementation of a flux limited diffusion (FLD) solver in AREPO. We show two test problems, assessing the correctness of our implementation.
- In Chapter 6 we turn to the implementation of an adaptive mesh refinement (AMR) method in the cosmological simulation code AREPO. This AMR module allows detailed comparisons of the moving mesh-based hydro solver with more traditional mesh-based methods. Furthermore it provides a test bed to implement novel numerical methods without the need to find a discretization on an irregular Voronoi mesh.
- The AMR module is used to implement a Discontinuous Galerkin (DG) hydro solver in Chapter 7. The underlying ideas and equations of DG methods are presented. Implementational details are given and advantages and disadvantages of DG methods are briefly discussed.
- The DG implementation is applied to subsonic turbulence simulations in Chapter 8. Here, we can show some of the numerical and computational advantages of DG methods over traditional finite volume approaches.
- Finally, we conclude and summarize our main findings in Chapter 9. A brief outlook of future work is given as well.

2

Physical Processes and Equations

2.1 Basic cosmological equations

On the largest scales, the universe can be assumed to be isotropic and homogeneous. The most general metric in such a universe is given by the Robertson Walker metric:

$$ds^2 = c^2 dt^2 - a^2 (dr^2 + r^2 (d\theta^2 + \sin^2 \theta d\phi^2)), \quad (2.1)$$

where c is the speed of light and the cosmological scale factor a describes the expansion of the universe.

The Universe is assumed to be filled with ordinary matter, dark matter, and a so called dark energy or cosmological constant. Initially, during the radiation dominated epoch, the dominant component were photons. The total present day matter density is $\rho_{m,0} = \rho_{dm,0} + \rho_{b,0}$, with dark matter density $\rho_{dm,0}$ and baryon density $\rho_{b,0}$. Other components are the present day radiation density $\rho_{r,0}$ and the cosmological constant or dark energy density $\rho_{\Lambda,0}$. Further components such as the neutrino density are ignored in the following. The densities ρ_i can be expressed in terms of the critical density $\rho_0 = 3H_0^2/8\pi G$ as $\Omega_{i,0} = \rho_{i,0}/\rho_{crit,0}$ and $\sum_i \Omega_{i,0} = 1$. The most recent constraints for those cosmological parameters are reported in Planck Collaboration et al. [2015b].

The time evolution of the scale factor is given by the Friedmann equation:

$$\left(\frac{\dot{a}}{a}\right)^2 = H^2(a)H_0 \left(\Omega_{m,0} (1+z)^3 + \Omega_{r,0} (1+z)^4 + \Omega_{\Lambda,0}\right)^2, \quad (2.2)$$

with the present day Hubble constant $H_0 = H(0)$. The redshift z is related to the scale factor a through

$$a = \frac{1}{z+1}. \quad (2.3)$$

2.2 Gravity

The most important driver behind cosmological structure formation is gravity. The state and evolution the dark matter particles can be described by specifying the position \mathbf{x}_i and velocity \mathbf{u}_i of each particle. If, in addition, the forces \mathbf{F}_{ij} between all pairs of particles are given, the equations of motion fully describe the evolution of the entire system. However, the sheer number of particles involved makes this approach not applicable to most practical problems. Especially simulations would be only possible for tiny systems. Fortunately, the system can alternatively be described in terms of a phase space distribution function $f(\mathbf{x}, \mathbf{u}, t)$, describing the number of particles in an infinitesimal phase space volume $d\mathbf{x}d\mathbf{u}$ at position and velocity (\mathbf{x}, \mathbf{u}) . Because dark matter interacts only gravitationally, its time evolution can be described as a phase-space fluid, where f is governed by the collisionless Boltzmann equation:

$$\frac{\partial f(\mathbf{x}, \mathbf{u}, t)}{\partial t} + \mathbf{u} \frac{\partial f(\mathbf{x}, \mathbf{u}, t)}{\partial \mathbf{x}} - \frac{\partial \varphi}{\partial \mathbf{x}} \frac{\partial f(\mathbf{x}, \mathbf{u}, t)}{\partial \mathbf{u}} = 0, \quad (2.4)$$

where the phase space density $f(\mathbf{x}, \mathbf{u}, t)$ describes a velocity distribution over \mathbf{u} at every point \mathbf{x} in space, at time t .

The gravitational field φ is obtained from the density distribution using the Poisson equation

$$\Delta \varphi = 4\pi G \rho(\mathbf{x}, t) \quad (2.5)$$

with gravitational constant G and total matter density $\rho(\mathbf{x}, t)$. The density in turn is given by the distribution function f after integrating out the velocity distribution. Together, these equations form a system of integro-partial differential equations and are called the Poisson-Vlasov system. To solve it numerically, the distribution function f can be sampled using N particles (which are just fiducial numerical entities and not identical to the real particles/atoms of the physical system), which allows for a numerical integration of the system using so-called N -body methods.

2.3 Equations of hydrodynamics

Similar as the dark matter system, the baryonic component can in principle be modelled using a distribution function f . On cosmologically relevant time and length scales, the fluid is however highly collisional and thus can be treated in a fluid approximation. One can formally derive this by considering the time evolution equation for f with the collisional Boltzmann equation:

$$\frac{\partial f}{\partial t} + \mathbf{u} \frac{\partial f}{\partial \mathbf{x}} + \mathbf{F} \frac{\partial f}{\partial \mathbf{u}} = \frac{\partial f}{\partial t} \Big|_{\text{coll}}, \quad (2.6)$$

with an (external) force per unit mass \mathbf{F} and $\frac{\partial f}{\partial t} \Big|_{\text{coll}}$ describing collisions between particles.

2.3.1 Euler equations

By taking moments of Equation (2.6), conservation laws can be obtained. To do this, we first define the density field ρ for a fluid with particle mass m :

$$\rho(\mathbf{x}, t) = \int_V m f(\mathbf{x}, \mathbf{u}, t) d\mathbf{u}, \quad (2.7)$$

the mean velocity field \mathbf{v}

$$\mathbf{v}(\mathbf{x}, t) = \frac{1}{\rho} \int \mathbf{u} m f(\mathbf{x}, \mathbf{u}, t) d\mathbf{u}, \quad (2.8)$$

and the specific internal energy field ϵ

$$\epsilon(\mathbf{x}, t) = \frac{1}{2\rho} \int (\mathbf{u} - \mathbf{v})^2 m f(\mathbf{x}, \mathbf{u}, t) d\mathbf{u}. \quad (2.9)$$

The specific internal energy is then related to the temperature T for a monoatomic gas by

$$\epsilon = \frac{3}{2} \frac{k_B}{m} T \quad (2.10)$$

For an ideal gas, the pressure is given by

$$P = (\gamma - 1)\rho\epsilon = \frac{1}{3} \text{tr} \int (\mathbf{u} - \mathbf{v})_i (\mathbf{u} - \mathbf{v})_j m f d\mathbf{u}, \quad (2.11)$$

with an adiabatic index of $\gamma = 5/3$.

By multiplying Equation (2.6) with 1, \mathbf{u} , or \mathbf{u}^2 and integrating over $d\mathbf{u}$, the conservation laws of mass, momentum and total energy can then be derived. Here, no analytic expression for the collision term is needed, except for the assumption that collisions are isotropic and do not create or destroy particles, and individually conserve mass, momentum and energy.

These conservation laws for ideal hydrodynamics are called the Euler equations and can be written as a set of hyperbolic conservation laws. In differential form, they are given by:

$$\frac{\partial \mathbf{q}}{\partial t} + \nabla \cdot \mathbf{F}(\mathbf{q}) = 0, \quad (2.12)$$

with a vector of conserved quantities

$$\mathbf{q} = \begin{pmatrix} \rho \\ \rho \mathbf{v} \\ \rho e \end{pmatrix}, \quad (2.13)$$

and total specific energy $e = \epsilon + \frac{1}{2}\mathbf{v}^2$. The flux tensor is given by

$$\mathbf{F}(\mathbf{q}) = \begin{pmatrix} \rho\mathbf{v} \\ \rho\mathbf{v} \otimes \mathbf{v} + P \\ (\rho e + P)\mathbf{v} \end{pmatrix}, \quad \mathbf{F}(\mathbf{q}) = (\mathbf{F}_1(\mathbf{q}), \mathbf{F}_2(\mathbf{q}), \mathbf{F}_3(\mathbf{q})) \quad (2.14)$$

Note, that the equations in the differential form only allow for continuously differentiable solutions. However, many astrophysical problems involve discontinuous solutions, as they contain shocks and contact discontinuities. In this case, the integral form of the Euler equations is more appropriate, which allows for weak solutions:

$$\frac{d}{dt} \int_{V_i} \mathbf{q}(x, t) dV + \int_{\partial V_i} \mathbf{F}(\mathbf{q}(x, t)) \mathbf{n} dA = 0, \quad (2.15)$$

with normal vector \mathbf{n} . The differential form of the Euler equations can be easily derived from the integral form.

2.4 Radiative transfer

Even though radiation energy contributes only a tiny fraction of the total energy density in the Universe today, radiative processes play an important role in many aspects of theoretical astrophysics. The equations of radiative transfer describe how the radiation field evolves over time. Similarly to the hydrodynamic fields, the radiation field can be described by a phase space distribution function $I_\nu(\mathbf{x}, \mathbf{n}, t)$, the so-called radiation intensity with units of $\text{erg s}^{-1} \text{cm}^{-2} \text{Hz}^{-1} \text{ster}^{-1}$. Here, the unit direction vector \mathbf{n} and scalar frequency ν play the role of the fluid velocity \mathbf{v} , as photons are massless and always travel with the speed of light c . The bolometric intensity is obtained by integration over the frequency dependence:

$$I = \int_\nu I_\nu d\nu. \quad (2.16)$$

A related quantity is the radiative flux

$$F = I\Delta\Omega, \quad (2.17)$$

with opening angle $\Delta\Omega$ and units $\text{erg s}^{-1} \text{cm}^{-2}$. If absorption around a source can be ignored, the radiation intensity I is constant at any distance away from the source. The radiation flux F however shows a $\sim r^{-2}$ scaling with distance r .

2.4.1 Absorption and emission mechanisms

Radiation passing through a medium is usually subject to absorption, emission and scattering processes. The amount of radiation intensity lost due to absorption or gained by emission depends on the opacity of the medium. The loss of energy can be modelled as

$$dE = \alpha_\nu(\mathbf{x}, \mathbf{n}, t) I_\nu(\mathbf{x}, \mathbf{n}, t) dl dA d\Omega d\nu dt, \quad (2.18)$$

along an infinitesimal volume of length dl and area dA .

The opacity has units of cm^{-1} . It is often useful to define a specific opacity κ_ν as

$$\alpha_\nu = \kappa_\nu \rho. \quad (2.19)$$

In its most general form, the opacity has a directional dependency, which is however ignored here. The frequency dependence can be very strong, especially if absorption by atomic or molecular transitions are important. The integral over the opacity along a path is called the optical depth τ :

$$\tau_\nu(s_0, s_1) = \int_{s_0}^{s_1} \alpha_\nu(s) ds \quad (2.20)$$

The opposite effect of absorption is emission, described by an emissivity η :

$$dE = \eta_\nu(\mathbf{x}, \mathbf{n}, t) dl dA d\Omega d\nu dt, \quad (2.21)$$

which in its most general form has a dependency on position as well as direction. We usually consider isotropic emission here and ignore any directional dependence. The units of η are $\text{ergs cm}^{-3} \text{s}^{-1} \text{Hz}^{-1} \text{ster}^{-1}$.

Scattering can be viewed as a combination of an absorption and an immediate re-emission event. The direction and energy of a photon usually changes during a scattering event, and the difference in energy and momentum are balanced by the ambient medium. In many problems the absorption and re-emission is isotropic, but in the most general anisotropic case, scattering needs to be modelled by a redistribution function $R(\mathbf{n}', \nu', \mathbf{n}, \nu)$, giving the probability of a photon (\mathbf{n}', ν') being scattered into (\mathbf{n}, ν) . An important example of scattering is Thomson scattering by CMB photons on free electrons along their path to us, giving rise to the Sunyaev-Zel'dovich effect. In the following we will however not explicitly treat scattering processes as they are comparatively unimportant for the reionization problem.

Note that the relations above hold true only in the rest frame of the medium. A rapidly moving medium “sees” the radiation at a different frequency and thus a different value of the opacity applies. But the radiation field can always be transformed into the rest frame of the medium through a Lorentz transformation, where the source and sink terms are easier to evaluate, and then transformed back into the lab frame again. This approach or variants thereof have to be taken in problems of relativistic radiation hydrodynamics. The fluid velocities involved in cosmic reionization are however small enough to allow relativistic effects to be ignored.

2.4.2 The radiative transfer equation

The transfer equation of radiation follows from the Boltzmann equation (2.6), assuming all photons travel with constant speed of light c :

$$\left(\frac{1}{c} \frac{\partial}{\partial t} + (\mathbf{n} \nabla) \right) I_\nu(\mathbf{n}, s) = \alpha_\nu(s) (S_\nu(s) - I_\nu(\mathbf{n}, s)), \quad (2.22)$$

where $S_\nu = \eta_\nu/\alpha_\nu$ is the so-called source function. Scattering can be included by adding the photon loss due to scattering along a ray to the opacity α_ν and adding the photon gain due to scattering to the source function S_ν .

For a static configuration, the time derivative can be dropped and the radiative transfer equation simplifies to

$$\frac{dI_\nu(\mathbf{n}, s)}{ds} = \alpha_\nu(s) (S_\nu(s) - I_\nu(\mathbf{n}, s)), \quad (2.23)$$

along a ray in direction \mathbf{n} parametrized by s . The formal solution of this equation is given by

$$I_\nu(s) = I_{\nu,0} e^{-\tau_\nu(s_0,s)} + \int_{s_0}^s \eta_\nu(s') e^{-\tau_\nu(s',s)} ds'. \quad (2.24)$$

The initial value $I_{\nu,0}$ decays exponentially. The emission along the path is accumulated and attenuated by the remaining distance towards the point s .

2.4.3 Thermodynamic equilibrium

A radiation field in thermodynamic equilibrium with a medium has a radiation intensity described by the Planck function

$$B_\nu(T) = \frac{2h\nu^3}{c^2} \left(e^{\frac{h\nu}{k_B T}} - 1 \right)^{-1}, \quad (2.25)$$

with the Planck constant h , speed of light c and Boltzmann constant k_B . In thermodynamic equilibrium, emission and absorption must balance each other, thus using Equation (2.22) and putting the left hand side to zeros, one obtains

$$\eta_\nu = \alpha_\nu B_\nu(T), \quad (2.26)$$

which is Kirchhoff's law of thermal radiation.

The relation is in a strict sense only valid for a global thermodynamic equilibrium. If the gradients of the radiation field are small compared to the optical depth, the system can be considered to be in a local thermodynamic equilibrium (LTE).

In a medium with a thermal source function $S_\nu = B_\nu$, according to Equation (2.23) the radiative intensity changes until $B_\nu = I_\nu$. The decay length until this relation field approaches B_ν is given by the opacity α_ν . For frequencies near an atomic transition line, the intensity saturates after a very short distance. But even far away of lines, the opacity is extremely small but non-zero, and will eventually saturate at large distances. Thus, if the medium is optically thick enough, the radiation field leaving the medium has a Planck spectrum.

2.4.4 Moments of the transfer equation

Unlike the typical velocity distribution of a fluid, the photon distribution can be highly anisotropic. This can make moment-based approaches very inaccurate in some situations. The first moments of the radiation intensity are defined as

$$E_\nu = \frac{1}{c} \oint I_\nu(\mathbf{x}, \mathbf{n}, t) d\Omega \quad (2.27)$$

$$\mathbf{F}_\nu = \oint I_\nu(\mathbf{x}, \mathbf{n}, t) \mathbf{n} d\Omega \quad (2.28)$$

$$\mathbf{P}_\nu = \frac{1}{c} \oint I_\nu(\mathbf{x}, \mathbf{n}, t) \mathbf{n} \otimes \mathbf{n} d\Omega \quad (2.29)$$

Analogously bolometric quantities E , \mathbf{F} and \mathbf{P} are defined by integrating out the frequency dependence.

The time evolution equations for these moments are obtained by taking moments of the radiative transfer Equation (2.22) and integrating over the angular dependence:

$$\frac{\partial E_\nu(\mathbf{x}, t)}{\partial t} + \nabla \cdot \mathbf{F}_\nu(\mathbf{x}, t) = \oint \alpha_\nu(\mathbf{x}, \mathbf{n}, t) (S_\nu(\mathbf{x}, \mathbf{n}, t) - I_\nu(\mathbf{x}, \mathbf{n}, t)) d\Omega \quad (2.30)$$

$$\frac{1}{c^2} \frac{\partial \mathbf{F}_\nu(\mathbf{x}, t)}{\partial t} + \nabla \cdot \mathbf{P}_\nu(\mathbf{x}, t) = \frac{1}{c} \oint \alpha_\nu(\mathbf{x}, \mathbf{n}, t) (S_\nu(\mathbf{x}, \mathbf{n}, t) - I_\nu(\mathbf{x}, \mathbf{n}, t)) \mathbf{n} d\Omega \quad (2.31)$$

To solve this system of equations, either another moment equation for the radiation pressure tensor \mathbf{P}_ν , which in turn would include even higher moments, is needed, or a closure relation is required. When we discuss our numerical implementation in the next chapter we will introduce the so called M1 closure as one specific possibility for this.

2.5 Atomic processes

The electrons of atoms can interact with light. In bound-bound processes the electron changes from one bound energy level to another bound energy level of the atom. The process can either be stimulated by photons or happen through a spontaneous decay to a lower energy level. The transition probabilities are described by the Einstein coefficients. The probability per unit volume for a transition from energy level i to j stimulated by photons is given by

$$p_{ij} = B_{ij} n_i B_\nu, \quad (2.32)$$

with the Einstein coefficient B_{ij} for stimulated emission / absorption, the number density n_i of atoms with energy level i and spectral energy density B_ν at frequency ν . If the energy E_j of level j is higher than the energy of level i , the process involves the absorption of a photon with frequency $\nu = (E_j - E_i)/h$. In the opposite case

a photon with the energy difference ($E_j - E_i$) of the two energy levels is emitted. An alternative way of decaying from level j back to level i is through spontaneous emission of a photon. The probability for this process is

$$p'_{ji} = A_{ji}n_j, \quad (2.33)$$

where A_{ij} is the Einstein coefficient for spontaneous emission.

In thermodynamical equilibrium, the number density of atoms in energy levels i and j must be constant, thus the total probabilities for creation and destruction must be equal:

$$B_{ij}n_iB_\nu = A_{ji}n_j + B_{ji}n_jB_\nu. \quad (2.34)$$

Furthermore, the occupation number densities of energy levels i and j are related by the Boltzmann distribution

$$\frac{n_j}{n_i} = \frac{g_j}{g_i} \exp\left(-\frac{h\nu}{k_B T}\right), \quad (2.35)$$

with statistical weights g_i and g_j .

Combining equations (2.25), (2.34) and (2.35), it can be shown that the following relations must hold for the Einstein coefficients:

$$g_j A_{ji} = \frac{2h\nu^3}{c^2} g_i B_{ij}, \quad g_j B_{ji} = g_i B_{ij} \quad (2.36)$$

2.5.1 Photoionization and recombination

Photoionization and recombination are similar to excitation of atoms by photons, except that the state j is an unbound state. A photon is only able to ionize an atom if the photon energy is larger than the binding energy of the electron. The excess energy is put into kinetic energy of the released electron. The rate of ionization events is given by

$$\Gamma = \int_{\nu_0}^{\infty} c\sigma_\nu n_\gamma d\nu. \quad (2.37)$$

The ionization cross section can be determined by quantum electrodynamics (QED) computations. The cross section depends on the charge of the atom and the energy level from which the electron is removed. For hydrogen like atoms, ionization typically happens from electrons in the ground state. A parametrization of the cross section is given by

$$\sigma(\nu) = \frac{64}{3\sqrt{3}} \alpha \pi a_0^2 \frac{g(\nu)}{Z^2} \left(\frac{\nu_0}{\nu}\right)^3, \quad (2.38)$$

with fine structure constant α , Bohr radius a_0 and the charge of the residual ionized atom Z . The Gaunt factor $g(\nu)$ is very close to unity and tabulated values are available.

The photoionization and recombination cross sections are related by the Milne relation

$$\sigma_r(v) = \frac{g_i}{g_{i+1}} \left(\frac{h\nu}{m_e c v} \right)^2 \sigma(\nu), \quad (2.39)$$

with $\sigma_r(v)$ being the recombination cross section for an electron of velocity v and the statistical weights g_i and g_{i+1} of the atom in the i and $i+1$ times ionized states. The frequency ν and free electron velocity v are related by energy conservation through $\frac{1}{2}mv^2 = (\nu - \nu_n)h$, with ν_n corresponding to the energy of level n .

In local thermodynamical equilibrium, the electron velocities are distributed according to the Maxwell-Boltzmann distribution $f(v, T)$ with the electron temperature T . The recombination cross section to the energy level n is the velocity average of $\sigma_r(v, n)v$. The total recombination rate is then the sum of all recombinations to any energy level. Thus,

$$\alpha_A(T) = \sum_{n=1}^{\infty} \alpha_n(T) = \sum_{n=1}^{\infty} \int_0^{\infty} \sigma_r(v, n)v f(v, T) dv \quad (2.40)$$

is the so called Case A recombination coefficient. The recombination directly to the ground state will emit another ionizing photon, and if the medium is sufficiently optically thick this photon is immediately absorbed by another atom. Thus, the locally averaged ionization state of the medium is unchanged. It is therefore useful to consider the Case B recombination rate α_B , which considers only recombination events not leading to the emission of an ionizing photon, i.e. $\alpha_B = \alpha_A - \alpha_1$. This approximation is the so called ‘‘on the spot approximation’’ (OTSA).

The energy difference between the ionizing photon and the energy needed to free the electron provides a heating process to the medium. The heating rate can be written as

$$\mathcal{H} = \int_{\nu_0}^{\infty} h(\nu - \nu_0)n_{\text{HI}}n_{\gamma}(\nu)\sigma(\nu) d\nu, \quad (2.41)$$

only considering ionization from the ground state here. The opposite process of recombination is a cooling process to the medium. At low temperatures, the ionization-recombination process results in a net gain in thermal energy for the medium, as the recombination rate is higher for low velocity electrons.

2.5.2 Collisional ionization

An alternative way of ionizing an atom is by a collision with another particle. Of particular relevance are collisions with free electrons. Similar to the recombination rate, the collisional ionization rate can be parametrized as

$$\beta(T) = \int_0^{\infty} \sigma_c(v)v f(v, T) dv. \quad (2.42)$$

The velocity dependent collisional ionization cross section can be obtained from QED calculations. This process implies a net cooling of the gas, as thermal energy is removed to unbind electrons from atoms.

2.5.3 Collisional excitation

A similar cooling process is given by collisional excitation, where an atom is put into an excited state by a collision with another particle. The atom can then decay back into its ground state through the emission of a photon.

2.5.4 Bremsstrahlung

Bremsstrahlung radiation is a free-free process. When an electron collides with a proton, the electron is deflected and photons are emitted. The emissivity due to bremsstrahlung radiation is described by

$$\epsilon_{\text{ff}}(\nu) = n_i n_e \int P(v, \nu) f(v, T) dv \quad (2.43)$$

with radiative power $P(v, \nu)$. An expression for $P(v, \nu)$ can be obtained from electrodynamics. The resulting cooling rate due to bremsstrahlung is

$$\mathcal{C}_{\text{ff}} = \int \epsilon_{\text{ff}}(\nu) d\nu. \quad (2.44)$$

An approximate form of the cooling rate is given by

$$\mathcal{C}_{\text{ff}} \approx 1.4 \times 10^{-23} T_8^{1/2} \left(\frac{n_e}{\text{cm}^{-3}} \right)^2 \text{ ergs s}^{-1} \text{ cm}^{-3}, \quad (2.45)$$

with $T_8 = T/10^8$ and assuming $n_p = n_e$.

2.5.5 Compton scattering

Compton scattering is the inelastic scattering process of free electrons with photons. In the case of normal Compton scattering, energy is transferred from the photon to the electron. In the case of inverse Compton scattering, energy is transferred to the photon instead. The cross section for this process is given by the classical Thomson cross section

$$\sigma_{\text{th}} = \frac{8\pi}{3} \left(\frac{e^2}{m_e c^2} \right)^2. \quad (2.46)$$

If the temperature T_e of the electrons is larger than the temperature of the radiation field T_γ , energy is transferred to the radiation field. The rate of energy transfer in the limit of $T_e > T_\gamma$ is given by

$$\mathcal{C} = \frac{4k_B T_e}{m_e c^2} c \sigma_{\text{th}} n_e a_r T_\gamma^4. \quad (2.47)$$

An astrophysical important process is cooling due to Compton scattering off CMB photons whose temperature at redshift z given by $T_\gamma = 2.73(1+z)$ K.

Part II

Radiative Transfer and Cosmic Reionization

3

A GPU Based Radiative Transfer Solver for Simulating the Epoch of Reionization

3.1 Introduction

Ideally a radiative transfer method solves (an approximation of) the Boltzmann equation for the photon distribution function $I(\mathbf{x}, \mathbf{n}, \nu, t)$. The function I describes the number density of photons of frequency ν moving in the direction of the normal vector \mathbf{n} at position \mathbf{x} and time t . The time evolution of this distribution is described by

$$\frac{\partial I}{\partial t} + c\nabla \cdot (\mathbf{n}I) = \frac{\partial I}{\partial t}\Big|_{\text{source}} - \frac{\partial I}{\partial t}\Big|_{\text{sink}}, \quad (3.1)$$

with source and sink terms due to emission and absorption by ionization and recombination events. Instead of solving the full multi frequency equation, we will approximate the photon field as monochromatic. In this approximation one effective frequency bin of hydrogen ionizing UV photons is used. This approximation can be easily generalized to helium reionization by using three effective frequency bins instead. The frequency dependent ionization and recombination rates in the source and sink terms are replaced by frequency integrated averages weighted by the spectral energy distribution of photons in the bin. Equation (3.1) ignores the redshifting effect of photons. This approximation is equivalent to the assumption that photons travel only a short distance compared to cosmological scales before they are absorbed. In the context of reionization simulations, this is a well justified approximation.

3.2 Radiative transfer

The high dimensionality of $I(\mathbf{x}, \mathbf{n}, \nu, t)$ and the short time scales imposed by the speed of light make solving the left hand side of Equation (3.1) computationally expensive. Thus, numerous approximate numerical methods have been proposed in the literature. Our implementation is based on two different approaches: A cone-based advection scheme [Petkova and Springel, 2011a] and a moment-based method with an M1 closure for the Eddington tensor [Aubert and Teyssier, 2008; Rosdahl et al., 2013]. In the following we will describe both methods subsequently.

3.2.1 Cone-based advection method

This method was first proposed in Petkova and Springel [2011a]. The distribution function I is grouped in momentum space into cones of equal opening angle and one or more frequency bins. For each cone field, the left hand side of Equation (3.1) provides an independent advection equation. The centres of the cones are adopted as the central angular directions of a HEALPIX tessellation [Górski et al., 2005] of the sky. This is used largely for computational convenience; we make use of no other properties of the HEALPIX tessellation other than their equal solid angle coverage of the unit sphere. Any other tessellation with this property would also work equally in the context of our method.

The HEALPIX method provides tessellations at different, nested refinement levels n , with $N_{\text{pix}} = 12 \times 4^n$ cones each. Thus, in total we have to independently advect N_{pix} photon fields, $I_l(\mathbf{x})$. We define the total photon field I_{tot} as $I_{\text{tot}} = \sum I_l$. For each angular-decomposed photon field we have to solve the following equation in the free streaming limit:

$$\frac{\partial I_l}{\partial t} + c \nabla \cdot (\mathbf{n}_l I_l) = 0. \quad (3.2)$$

This equation represents an ordinary linear advection equation with an effective advection direction \mathbf{n}_l . This type of equation can be straightforwardly solved with a finite volume scheme.

The question remaining is how to choose \mathbf{n}_l . Obviously, \mathbf{n}_l has to point in the direction of the l -th cone at all time. At the same time, the full opening angle of the cone has to be illuminated. If \mathbf{n}_l was always chosen as the centre of the l -th HEALPIX cone and kept always fixed in the direction, the light cone emerging from a point source would eventually not be entirely filled. Instead, distinct outgoing light beams would eventually form. We can achieve homogeneously filled cones by choosing

$$\mathbf{n}'_l = -\frac{\nabla f_\gamma}{|\nabla f_\gamma|}, \quad (3.3)$$

instead and additionally limiting \mathbf{n}'_l to lie within the l -th cone. Therefore, a projection of \mathbf{n}'_l into the cone is performed if the angle between the cone centre \mathbf{n}_0 and \mathbf{n}'_l is larger than half the opening angle of the cone:

$$\phi = \arccos(\mathbf{n}_0 \cdot \mathbf{n}'_l) > \phi_{\max} \quad (3.4)$$

with

$$\phi_{\max} = \sqrt{4/N_{\text{pix}}}. \quad (3.5)$$

We note that the HEALPIX cones do not have a round spherical shape but are polygonal tiles. In principle, a projection back to the boundary of the HEALPIX cones would be possible. However, this would be computationally expensive without offering much gain, as we anyway want to make sure that there is enough overlap between different tessellation tiles to not produce any noticeable gridding structures in the angular light distribution. In fact, in order to guarantee such a seamless coverage of the unit sphere, we typically use a slightly larger opening angle of $\phi'_{\max} \approx 1.5\phi_{\max}$, which reduces the achieved angular resolution only slightly. Hence, if \mathbf{n}'_l falls outside the cone, it is projected back on the boundary of the cone by:

$$\mathbf{n}'_{l,\text{proj}} = \sin(\phi_{\max})\mathbf{m} + \cos(\phi_{\max})\mathbf{n}_0 \quad (3.6)$$

with

$$\mathbf{g} = \mathbf{n}_0 \times \mathbf{n}'_l \quad (3.7)$$

$$\mathbf{m} = \frac{\mathbf{g}}{|\mathbf{g}|} \times \mathbf{n}'_l \quad (3.8)$$

3.2.2 A moment-based method with an M1 closure

We have also implemented an alternative advection method to solve the left hand side of Equation (3.1), based on the first two moments. This second advection method enables us to assess the accuracy of the cone-based advection method and at the same time provides a computationally faster alternative. As a closure relation, we use the so-called M1 closure for the Eddington tensor.

The zeroth moment equation can be derived by taking Equation (3.1) and integrating over the angle \mathbf{n} . By multiplying Equation (3.1) with \mathbf{n} , the first moment equation is obtained instead. This leads to the following system of equations:

$$\frac{\partial N}{\partial t} + \nabla \cdot \mathbf{F} = 0, \quad (3.9)$$

$$\frac{\partial \mathbf{F}}{\partial t} + c^2 \nabla \cdot \mathbf{P} = 0, \quad (3.10)$$

with N denoting the photon density and \mathbf{F} the radiation flux vector.

For solving these equations we either need to introduce higher order moments or adopt a closure equation for the radiation pressure \mathbf{P} . The literature discusses

different possible choices for the closure. One of the simplest approaches is to choose \mathbf{P} as an isotropic pressure and to assume that \mathbf{F} is only slowly varying with time, allowing time derivatives to be ignored. This gives rise to the so-called flux limited diffusion methods. These methods require an additional limiter of the flux to prevent superluminal diffusion of photons in a optically thin regions.

A more sophisticated approach that is suitable for the reionization problem is the optically thin variable Eddington tensor approximation (OTVET) [Gnedin and Abel, 2001], which takes the distribution of the sources into account when estimating the local radiation pressure. One of the most accurate closures is given by the more general variable Eddington tensor (VET) method, which uses a time independent and relatively coarse short-characteristics method to compute the local Eddington tensor everywhere [Davis et al., 2012].

Here, we use the M1 method, which estimates the Eddington tensor based on local quantities only. The parametrization of the photon pressure with the M1 closure is given by:

$$\mathbf{P} = \left(\frac{1 - \xi}{2} \mathbf{I} + \frac{3\xi - 1}{2} \mathbf{n} \otimes \mathbf{n} \right) N, \quad (3.11)$$

with

$$\mathbf{n} = \frac{\mathbf{F}}{|\mathbf{F}|}, \quad \xi = \frac{3 + 4f^2}{5 + 2\sqrt{4 - 3f^2}}, \quad f = \frac{|\mathbf{F}|}{cN}. \quad (3.12)$$

The field f describes how strongly pointed the flux is by comparing the actual flux \mathbf{F} with the maximally allowed free streaming flux cN . The two limiting cases are radiation diffusion with $f = 0$ on one hand and free streaming with $f = 1$ on the other hand. The factor ξ interpolates smoothly between these two cases and can take values in the range of $1/3$ to 1 . In case of the lower limit, \mathbf{P} only contains the left part and is purely isotropic. In the other limiting case, the isotropic part of \mathbf{P} vanishes and a pure streaming term remains in Equation (3.11).

In practice, the results of M1 can be of surprisingly good accuracy. Nevertheless, the simplifications adopted here impose some limitations on the situations that can be represented well with the M1 method. For example, if one considers two intersecting light beams, an obvious shortcoming of the method emerges: By taking moments of the radiative transfer equation and integrating over the directional dependence of the photon distribution I , the collisionless photon field is essentially treated like a collisional fluid. At the intersection points this leads to an unphysical isotropic scattering of photons. However, in practical applications these special situations are rare and are often of little relevance. Ultimately, whether or not this is really the case is not clear a priori and can only be decided by comparing the results obtained with different methods against each other.

3.2.3 Ionization network

Next, we focus on the sink term on the right hand side of Equation (3.1) and the ionization network. The ionization state of hydrogen is influenced by absorption

of ionizing photons and recombination with free electrons. Additionally, collisional ionization is taken into account. These processes can be modelled by the following system of equations:

$$\frac{dn_\gamma}{dt} = -c\sigma n_{\text{H}} x_{\text{HI}} n_\gamma + (\alpha_{\text{A}}(T) - \alpha_{\text{B}}(T)) n_{\text{H}}^2 x_{\text{HII}}^2, \quad (3.13)$$

$$\frac{dx_{\text{HI}} n_{\text{H}}}{dt} = \alpha_{\text{A}}(T) n_{\text{H}}^2 x_{\text{HII}}^2 - \beta(T) n_{\text{H}}^2 x_{\text{HI}} x_{\text{HII}} - c\sigma n_{\text{H}} x n_\gamma, \quad (3.14)$$

with σ denoting the frequency averaged ionization cross section, n_{H} the hydrogen number density and x_{HI} the neutral hydrogen fraction. The case A recombination rate α_{A} , the case B recombination rate α_{B} , and the collisional ionization rate β are taken as fitting functions from Hui and Gnedin [1997]. The case B recombination rate considers only recombination events which do not result in the emission of an ionizing photon, while the case A recombination rate considers all recombination events.

In addition we have to keep track of the thermal energy state, which is modified by photoionization heating and various cooling terms:

$$\frac{du}{dt} = \mathcal{H} - \mathcal{C} = \Lambda, \quad (3.15)$$

with the heating rate

$$\mathcal{H} = \epsilon_\gamma c\sigma n_{\text{H}} x_{\text{HI}} n_\gamma \quad (3.16)$$

and the average thermal energy gain per photoionization event ϵ_γ . The cooling rate $\mathcal{C}(T)$ is composed of the following processes: collisional ionization (ζ), collisional excitation (ψ), recombination cooling (η), bremsstrahlung (θ) and Compton cooling off CMB photons (ω). The total cooling rate \mathcal{C} is given by:

$$\begin{aligned} \mathcal{C} = & (\zeta(T) + \psi(T)) n_{\text{e}} x n_{\text{H}} \\ & + (\theta(T) + \eta(T)) n_{\text{e}} (1 - x) n_{\text{H}} \\ & + \omega(T) n_{\text{e}} \end{aligned} \quad (3.17)$$

During a recombination event, either an ionizing photon or multiple non-ionizing photons can be emitted. The emission of ionizing photons due to recombination is essentially an additional photon source term for the frequency bin of ionizing photons. For example, ray tracing codes can only well resolve a limited number of photon sources. For these methods a continuous source field due to recombination would pose a potential problem. A solution often used is the so called ‘‘on the spot approximation’’, which assumes an instantaneous nearby ionization event, which immediately consumes those ionizing photons. Thus, recombination events with the emission of an ionizing photon can be ignored and do not change the local ionization state. This can be modelled by replacing the case A recombination rate α_{A} with the case B recombination rate α_{B} in Equation (3.14), removing the source term from Equation (3.13). Both of our advection methods are able to handle source fields from recombination radiation and thus our implementation can be used both with and without OTSA.

3.3 Numerical discretization

3.3.1 Photon advection for the cone-based method

The advection Equation (3.2) is solved using a finite volume approach. All N_{pix} photon fields are discretized on a homogeneous Cartesian mesh, which is advantageous for solving the radiative transfer equations using GPUs. The reason for this choice will be explored in more detail later in Section 3.4.2. We define the discretized photon field $N_l(\mathbf{x})$ as

$$N_{l,i}(\mathbf{x}) = \int_{V_i} I_l dV, \quad (3.18)$$

integrating over the volume of the discrete cell with centre \mathbf{x}_i and with $N_{l,i}$ being the photon density in the l -th bin in the i -th cell. Analogously, we define $N_{\text{tot},i} = \sum N_{l,i}$ as the total photon field used in the computation of the advection direction $\mathbf{n}_{l,i}$.

Applying a finite volume discretization to Equation (3.2) results in

$$\frac{\partial N_{l,i}}{\partial t} + c \int_{\partial V_i} N_{l,i} \mathbf{n}_{l,i} d\mathbf{A} = 0. \quad (3.19)$$

The volume integral of the second term was transformed into a surface integral using Gauss's theorem. The surface integral can be split into a contribution from each of the 6 surfaces of a cell. The integrand is assumed to be constant along each surface element. This results in a numerical flux $\mathcal{F}_{l,i} = cN_{l,i}\mathbf{n}_{l,i}\mathbf{n}_A$ with surface normal vector \mathbf{n}_A and advection direction $\mathbf{n}_{l,i}$ over each interface between neighbouring cells. The time derivative is discretized using a first order accurate finite difference approximation. This gives the following update step:

$$N_{l,i}^{n+1} = N_{l,i}^n + \Delta t \left((\mathcal{F}_{l,x^+} - \mathcal{F}_{l,x^-}) + (\mathcal{F}_{l,y^+} - \mathcal{F}_{l,y^-}) + (\mathcal{F}_{l,z^+} - \mathcal{F}_{l,z^-}) \right), \quad (3.20)$$

with surface positions x^-, x^+, y^-, y^+, z^- and z^+ . This equation is solved by directionally splitting the update step into three parts, solving the advection in one direction at a time only. This reduces the three dimensional problem into a set of independent one dimensional problems:

$$N_{l,i}^{n+1} = N_{l,i}^{n+1} + \Delta t (\mathcal{F}_{l,i+1/2} - \mathcal{F}_{l,i-1/2}). \quad (3.21)$$

The missing piece is how to obtain an approximation for the flux $\mathcal{F}_{l,i\pm 1/2}$ between adjacent cells. To obtain the advection direction at the interface position, we simply average ∇N_{tot} using the values of the left and right side of the interface. The gradient is computed by finite differencing N_{tot} . The averaged value of the gradient is used for limiting the direction vector to the l -th cone and to compute the advection direction $\mathbf{n}_{i\pm 1/2}$. Using an upwind approach, $\mathcal{F}_{i-1/2}$ is then given by

$$\mathcal{F}_{l,i-1/2} = \begin{cases} cN_{l,i}\mathbf{n}_{i-1/2}\mathbf{n}_A & \text{if } \mathbf{n}_{i-1/2}\mathbf{n}_A < 0 \\ cN_{l,i-1}\mathbf{n}_{i-1/2}\mathbf{n}_A & \text{otherwise,} \end{cases} \quad (3.22)$$

with surface normal vector n_A . A similar expression is used for $\mathcal{F}_{l,i+1/2}$. The obtained fluxes $\mathcal{F}_{l,i\pm 1/2}$ are formally only first order accurate. However, the flux computations and time integration can be extended to a second order accurate MUSCL-Hancock scheme by extrapolating the central values $N_{l,i}$ to the interface using a linear gradient estimation and temporal extrapolation.

3.3.2 Photon advection for the M1 method

The set of equations (3.9) and (3.10) can be combined into one vector equation with state vector $\mathbf{q} = (N, \mathbf{F})$ and flux tensor $\mathbf{F} = (\mathbf{F}, \mathbf{P})$:

$$\frac{\partial \mathbf{q}}{\partial t} + \nabla \cdot \mathbf{F}(\mathbf{q}) = 0. \quad (3.23)$$

Like for the cone-based advection method, the three dimensional problem is casted into a set of discrete one dimensional advection problems where the full 3D problem is solved by directional splitting:

$$\mathbf{q}_i^{n+1} = \mathbf{q}_i^n + \frac{\Delta t}{\Delta x} (\mathcal{F}_{i-1/2} - \mathcal{F}_{i+1/2}), \quad (3.24)$$

with $\mathcal{F}_{i\pm 1/2}$ being the flux through the left and right interface along one of the directions. We use the Global Lax Friedrich (GLF) function to obtain an approximation of $\mathcal{F}_{i\pm 1/2}$:

$$\mathcal{F}_{i-1/2} = \frac{\mathbf{F}_{i-1} \cdot \mathbf{n}_A + \mathbf{F}_i \cdot \mathbf{n}_A}{2} - \frac{c}{2} (\mathbf{q}_i - \mathbf{q}_{i-1}). \quad (3.25)$$

3.3.3 Solving the stiff thermochemical network

The non-equilibrium thermochemical network described by equations (3.13), (3.14) and (3.15) forms a coupled set of stiff ordinary differential equations local at each cell. The state within a cell is $\mathbf{U} = (n_\gamma, u, x_{\text{HI}})$. To guarantee stability and avoid invalid values for \mathbf{U} an implicit solver is desired. However, due to the non-linearity of the system of equations, a full implicit solver would not be very computationally efficient. Instead, we closely follow the approach taken by Rosdahl et al. [2013] and solve the system of equations in three steps. Instead of a direct update, only one component of \mathbf{U} is updated at a time. The values used for the other components are either the already updated values when available or the backward in time values. We first update the photon number n_γ , then the internal energy u , and finally the ionization state x_{HI} :

Photon number update

In case of the cone-based advection scheme the photon number density is given by $n_\gamma = \sum_l N_{l,i}/V_i$. The implicit photon number update step is done as follows:

$$\frac{n_\gamma^{n+1} - n_\gamma^n}{\Delta t} = C - n_\gamma^{n+1} D. \quad (3.26)$$

If the OTSA is not applied, C is non zero and given by the difference between the number of case A and case B recombination events:

$$C = (\alpha^A - \alpha^B) n_{\text{H}} x_{\text{HI}}^n (1 - x_{\text{HI}}^n). \quad (3.27)$$

The photon destruction rate D is given by

$$D = c\sigma n_{\text{H}} x_{\text{HI}}^n. \quad (3.28)$$

In the equations above, the old value at the end of the previous time step is used for x_{HI} .

Internal energy update

After the photon number n_{γ} is updated, an update of the internal energy u is carried out as follows:

$$\frac{u^{n+1} - u^n}{\Delta t} = \mathcal{H}(u^{n+1}) - \mathcal{C}(u^{n+1}) = \Lambda(u^{n+1}). \quad (3.29)$$

By Taylor expanding the heating and cooling rate Λ around u^n , one obtains the following update step for u :

$$u^{n+1} = u^n + \frac{\Lambda \Delta t}{1 - \frac{\partial \Lambda}{\partial u} \Delta t}, \quad (3.30)$$

with

$$\frac{\partial \Lambda}{\partial u} = \frac{\partial \Lambda}{\partial T} \frac{\partial T}{\partial u} = \frac{\partial \Lambda}{\partial \log T} \frac{1}{T} \left(\frac{(\gamma - 1) m_{\text{H}} \mu}{k_{\text{B}}} \right). \quad (3.31)$$

An expression for $\frac{\partial \Lambda}{\partial \log T}$ can be computed analytically by considering Equation (3.16) and (3.17). The derivatives of the cooling and heating rates are evaluated at $T = T(u^n)$. Thus, the update step is formally only semi-implicit in u . The coefficients of the cooling rates are precomputed and tabulated in $\log T$ space and are interpolated using the nearest two available values.

Updating the ionization state

The thermo-chemical update is completed by computing a new ionization state x_{HI} :

$$x_{\text{HI}}^{n+1} = x_{\text{HI}}^n + \Delta t \frac{x_{\text{HI}}^n (C + D) - C}{1 - J \Delta t}. \quad (3.32)$$

This expression is obtained by Taylor-expanding the right hand side of Equation (3.14). J is given by the following expression:

$$J = \frac{\partial \dot{x}_{\text{HI}}}{\partial x_{\text{HI}}} = -\frac{\partial C}{\partial x_{\text{HI}}} - (C + D) + x_{\text{HI}} \left(\frac{\partial C}{\partial x_{\text{HI}}} + \frac{\partial D}{\partial x_{\text{HI}}} \right), \quad (3.33)$$

with

$$\frac{\partial C}{\partial x_{\text{HI}}} = -\beta n_{\text{H}} + n_{\text{H}} x_{\text{HII}} \frac{\partial \beta}{\partial T} \frac{\partial T}{\partial x_{\text{HI}}} \quad (3.34)$$

$$\frac{\partial D}{\partial x_{\text{HI}}} = -\alpha n_{\text{H}} + n_{\text{H}} x_{\text{HII}} \frac{\partial \alpha}{\partial T} \frac{\partial T}{\partial x_{\text{HI}}} \quad (3.35)$$

and the temperature derivative

$$\frac{\partial T}{\partial x_{\text{HI}}} = \frac{T}{\mu} \frac{\partial \mu}{\partial x_{\text{HI}}} = T \mu X, \quad (3.36)$$

where X is the hydrogen fraction. Again, this update step is only semi-implicit in x_{HI} due to the use of x_{HII}^n .

An implicit scheme guarantees only stability but not necessarily accuracy. Thus, the full step from t^n to t^{n+1} can be subsampled by multiple smaller timesteps if needed. After each partial update step, we check whether the updated quantity changed by at most 10%. If the relative change is larger, the complete step is rejected and is repeated instead with steps of only half the size. If instead the maximum change in any quantity is less than 5%, the size of the next step is increased by a factor of two. This concludes the description of our thermochemical solver.

3.3.4 Time integration

The advection of the radiation field and the chemical network are coupled together by means of operator splitting. The multi dimensional advection operator itself is build out of one dimensional advection operators using a Strang-like directional splitting. Thus, a time step starts by first advecting the radiation fields in the x , in the y and then in the z -direction for half a timestep. Afterwards, source and sink terms are added by applying a half step of the source term, followed by a full step of the thermochemical network, again followed by a half step of the source term. The timestep is completed by half advection steps, but this time in reverse order, i.e. first advecting in the z -direction then in the y and x -directions. This then completes a full timestep.

3.4 Implementational details

From a technical point of view, GPUs are similar to machines with a wide vector unit. However, an application programmer is not required to formulate the algorithm in tedious vector instructions, but instead can specify the algorithms in a way which is more similar to multi threaded programming. These threads come in bundles of typically 32 threads, which is called a warp. The threads in the same warp can either execute the same instruction as the other threads in the warp in parallel and on different data, or do nothing during a clock cycle. In order to obtain maximum computational performance, we thus have to formulate every operation such that

it can be applied to 32 elements at the same time. To make things even more challenging, random or non-consecutive memory access by these 32 threads should be avoided. If the memory access pattern of threads in a warp is not contiguous and aligned, the memory access speed is substantially reduced and more memory access operations are required to retrieve the data for each thread. These requirements and limitations led to certain design decisions in the implementation of our radiative transfer code, which we now discuss in detail:

3.4.1 Domain decomposition and parallelization

To support a better parallelization, we split our computational domain into sub-cubes with a side length of $32 \times n$. Each compute kernel invocation handles one of these sub-cubes. These sub-cubes are combined to rectangular sub-domains. Each of these sub-domains is handled by one MPI task. Around each of these sub-cubes a layer of boundary information from the neighbouring sub-cubes is gathered. In order to efficiently transfer this boundary data from the GPU to the CPU side and communicate it via MPI, it has to be contiguous in memory. For a three dimensional cube, this is only the case in one direction. For the other two directions the data is gathered into an exchange buffer before it is transferred and communicated. The data transfer from the GPU back into host memory and vice versa can be handled asynchronously. The GPU can continue computing on one of the other sub-cubes while data is exchanged with the host or other MPI tasks. The organization of the domains into rectangular sub-domains enables a simple and regular communication pattern. Each MPI task has to exchange data with its direct neighbours only and expensive all-to-all communication patterns can be avoided.

Only during the advection step boundary information of the neighbouring sub-cubes is needed. In case of the cone-based advection method, for each photon field boundary information is needed in the current advection direction. However, to compute the advection direction \mathbf{n} , boundary information in all three directions for the total photon field N_{tot} is needed as well. As no three dimensional gradient has to be computed in case of the M1 advection method, only boundary information in the current advection direction is needed.

3.4.2 GPU parallelization

GPUs provide several types of memory associated with different access latencies and data access speed. The so called “shared memory” is rather small in size, but provides fast low latency access. At the beginning of an advection step, one line of data in the current advection direction is copied from the 3d array into shared memory. This copy process is fastest in the x -direction and slightly slower in the y -direction because the data is no longer contiguous in memory. Due to cache misses, the situation is even worse in the z -direction. Each thread is now assigned to a cell in the line. Next, each thread computes the flux $F_{l,i+1/2}$ through the interfaces to the right of its cell. After all threads have computed their flux, each thread applies

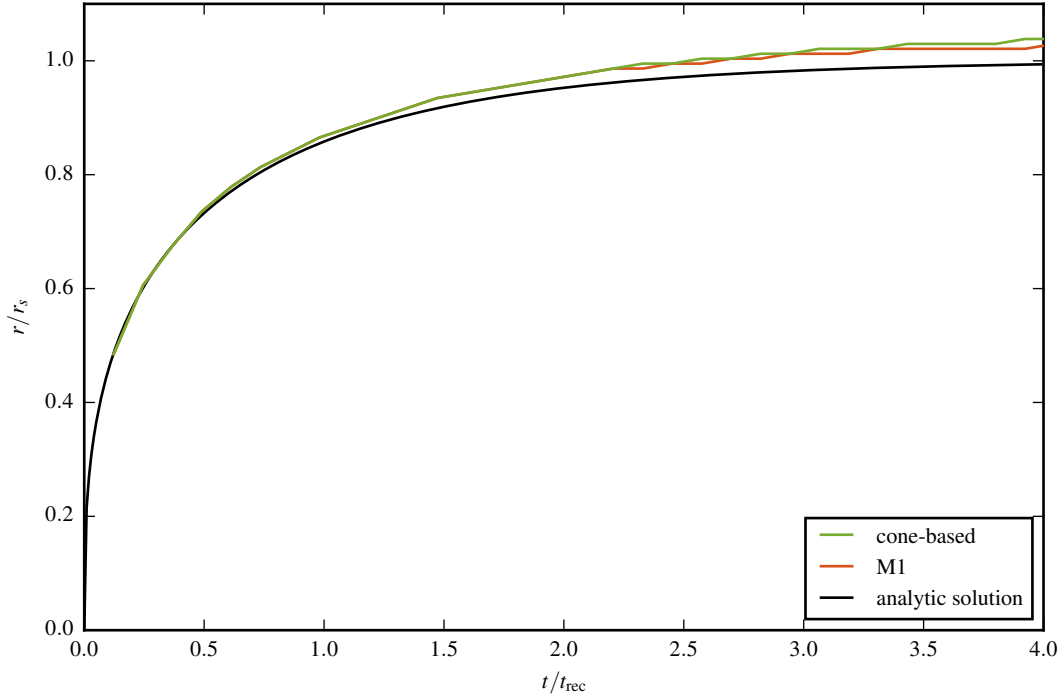


Figure 3.1: Test 1 – Time evolution of the Strömgren radius r_{eq} of the ionized region around the point source. The radius is in units of the Strömgren radius r_S and the time in units of the recombination time t_{rec} . We define the size of the ionized region as the radius at which the ionization fraction equals $x_{\text{HII}} = 0.5$. Both advection methods are almost indistinguishable from each other. As a reference we show the analytic approximation using Equation (3.42).

the flux to its own cell and afterwards to the neighbouring cell to the right. Then, all threads can move on to the next line. In case of the cone-based advection method, for each line, all photon fields are updated before the algorithm moves on to the next line. In case of the M1 method, N and \mathbf{F} are updated at the same time. Each line has $n \times 32 + 1$ interfaces, however only $n \times 32$ fluxes are computed. The missing flux is obtained from the neighbouring sub-cube and applied after the advection step.

The implementation of the thermochemical network solver needs only data of the local cell without any neighbour information. However, depending on the state \mathbf{U} , the execution path taken for updating the state can be very different for neighbouring cells. This leads to slight losses in performance due to thread divergence.

3.5 Test problems

In the following, we show results for standard test problems for ionization radiative transfer codes taken from the radiative transfer comparison project [Iliev et al., 2006a]. This enables us to assess the correctness and quality of the results obtained

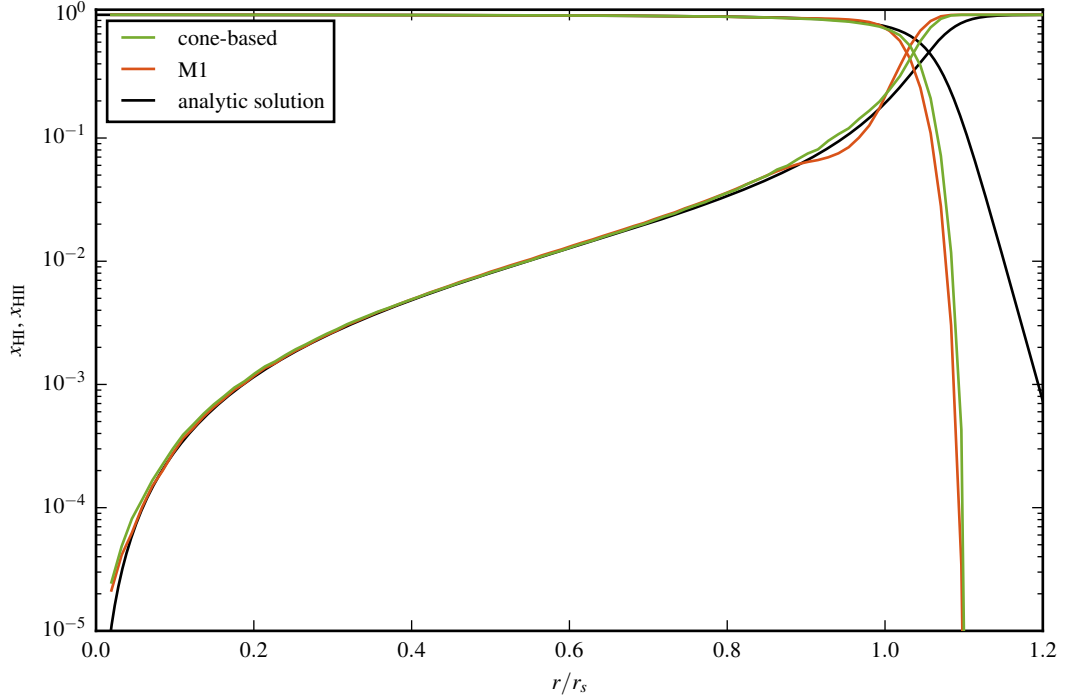


Figure 3.2: Test 1 – The radial profile of ionized and neutral fraction. The radius is shown in units of the Strömgen radius r_S . The profiles are obtained at the final time $t = 4t_{\text{rec}}$. For comparison we show the solution of Equation (3.38) as well. The size of the ionized region, where $x_{\text{HII}} = 0.5$, is expected to be $r = 1.058r_S$. Both of our simulation results produce a smaller ionized region than expected. The agreement of both advection methods with each other however is good. The M1 method shows a slightly steeper profile at around $r = 1$ than the cone-based method.

by our implementations. For each test we show results for both of our numerical advection methods.

3.5.1 Isothermal Strömgen sphere

The Strömgen sphere test consists of a single point source of ionizing radiation located in the centre of the simulation domain which is filled with neutral hydrogen. The ionizing radiation will drive an expanding sphere of ionized hydrogen. The equilibrium radius of that sphere is determined by a balance between the ionizing luminosity of the source and recombination within the ionized Strömgen sphere. Assuming a sharp transition from an ionized to a neutral medium and equating the ionization and recombination rates gives the so-called Strömgen radius r_S of

$$r_S = \left(\frac{3L}{4\pi\alpha_B n_{\text{H}}^2} \right)^{1/3}. \quad (3.37)$$

In the following we will define the actual Strömgen radius r_{eq} as the radius at which the ionization profile reaches $x = 0.5$. In reality, the transition from an ionized

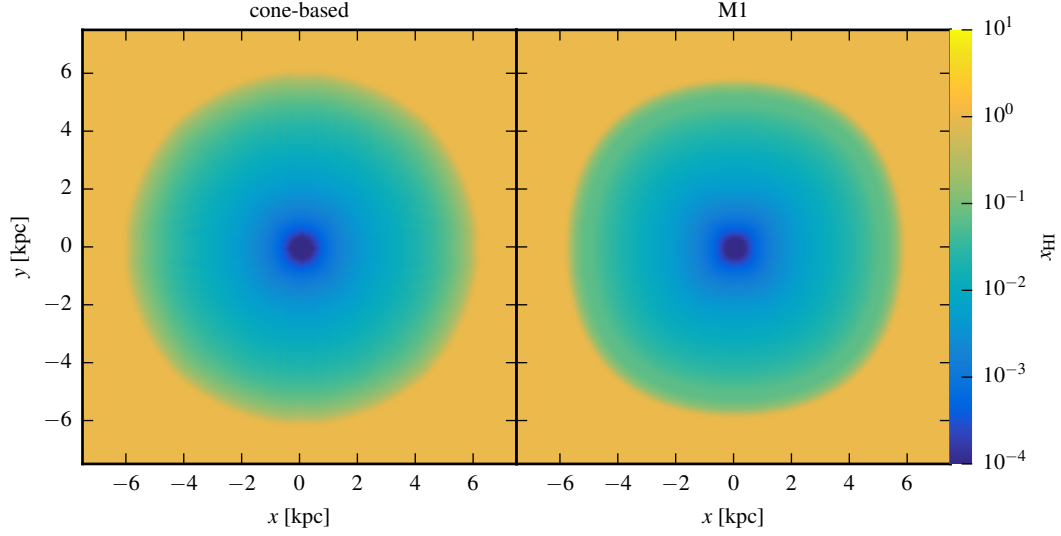


Figure 3.3: Test 1 – Slices through the mid plane of the simulations at $t = 4t_{\text{rec}}$. The figure shows the logarithm of the neutral fraction. Both advection methods can reproduce a round Strömgen sphere. The splitting of the photon field into individual cone fields produces no visible artifacts.

to a neutral medium will be rather smooth rather than abrupt, which alters the radius of the Strömgen sphere slightly compared to the estimate obtained from Equation (3.37). The correct equilibrium ionization profile $p(r)$ is given by solving

$$\frac{p(r)n_{\text{H}}L\sigma}{4\pi r^2} \exp^{-\tau(r)} = (1 - p(r))n_{\text{H}}^2\alpha_B, \quad (3.38)$$

with

$$\tau(r) = n_{\text{H}}\sigma \int_0^r dr' p(r') \quad (3.39)$$

for $p(r)$ [see Pawlik and Schaye, 2008]. This equation can be solved numerically and r_{eq} can be determined.

An approximation of the time evolution of the radius of the Strömgen sphere $r_{\text{I}}(t)$ can be obtained by solving

$$4\pi r_{\text{I}}^2 n_{\text{H}} \frac{dr_{\text{I}}}{dt} = L - \frac{4}{3}\pi r_{\text{I}}^3 \alpha_B n_{\text{H}}^2. \quad (3.40)$$

This equation can be written with dimensionless variables $\xi = r_{\text{I}}/r_{\text{S}}$ and $\tau = t/t_{\text{rec}}$. With the recombination timescale $t_{\text{rec}} = 1/(\alpha_B n_{\text{H}})$ one obtains the following equation:

$$\frac{d\xi}{d\tau} = \frac{1 - \xi^3}{3\xi^2}, \quad (3.41)$$

which is solved by

$$\frac{r_{\text{I}}(t)}{r_{\text{S}}} = \left(1 - \exp^{-t/t_{\text{rec}}}\right)^{1/3}. \quad (3.42)$$

Our computational domain has a side length of $L = 14$ kpc. The source has an ionizing luminosity of $\dot{N}_{\gamma} = 5 \times 10^{48}$ photons s^{-1} and is located at the centre of the computational domain. In this test, the ambient hydrogen medium has a number density of $n_{\text{H}} = 10^{-3} \text{ cm}^{-3}$ and the temperature is kept fixed at $T = 10^4$ K. The hydrogen ionization cross section is assumed to be $\sigma = 6.30 \times 10^{-18} \text{ cm}^2$ and a recombination rate of $\alpha_{\text{B}} = 2.59 \times 10^{-13} \text{ cm}^3 \text{ s}^{-1}$ is adopted. For the given choice of parameters this results in $r_{\text{S}} = 5.4$ kpc and an equilibrium radius of about $r_{\text{eq}} = 1.058 r_{\text{S}}$. The recombination timescale is $t_{\text{rec}} = 122.35$ Myr. We follow the simulation for more than $4 t_{\text{rec}}$ until $t = 500$ Myr.

In Figure 3.1, we show the time evolution of the radius of the Strömgen sphere. As a reference we show the expected analytic solution as well. Both of our radiation advection methods are in good agreement with each other and with results obtained by other methods. As discussed before, the final radius is slightly larger than r_{S} . Additionally, Figure 3.2 shows the final ionization profile at $t = 4 t_{\text{rec}}$ and the expected solution according to Equation (3.38).

In order to better assess the influence of the two implemented advection methods, Figure 3.3 shows thin slices through the middle of the Strömgen sphere, displaying the neutral fraction. The separation of the radiation field into individual cones does not introduce any artifacts or discontinuities at cone boundaries. Both methods are able to produce approximately equally good results and yield a nice round Strömgen sphere. Due to the high degree of symmetry of the problem at hand, the ability of the cone-based advection method to better resolve the angular dependence of the solution is not apparent in this test problem. By always producing a flux vector pointing radially outwards from the source (which is evidently correct), the M1 advection method can handle this test problem very well.

3.5.2 Non-isothermal Strömgen sphere

This test problem uses the same setup as in the isothermal case, except now the temperature evolution of the surrounding medium affected by the UV photons is included as well. Initially, the temperature of the ambient medium is set to $T = 100$ K.

In Figure 3.4 and 3.5, we compare both advection methods using slices through the neutral fraction and temperature fields in the mid-plane of the Strömgen sphere. Both methods are again able to reproduce a round and artifact free solution of the test problem.

Due to the decline of the recombination rate with increasing temperature the non-isothermal case produces a slightly larger Strömgen sphere than in the isothermal case. This can be clearly seen in Figures 3.6 and 3.7. Even though the initial evolution is rather similar to the isothermal case, the final Strömgen radius r_{S} is considerably

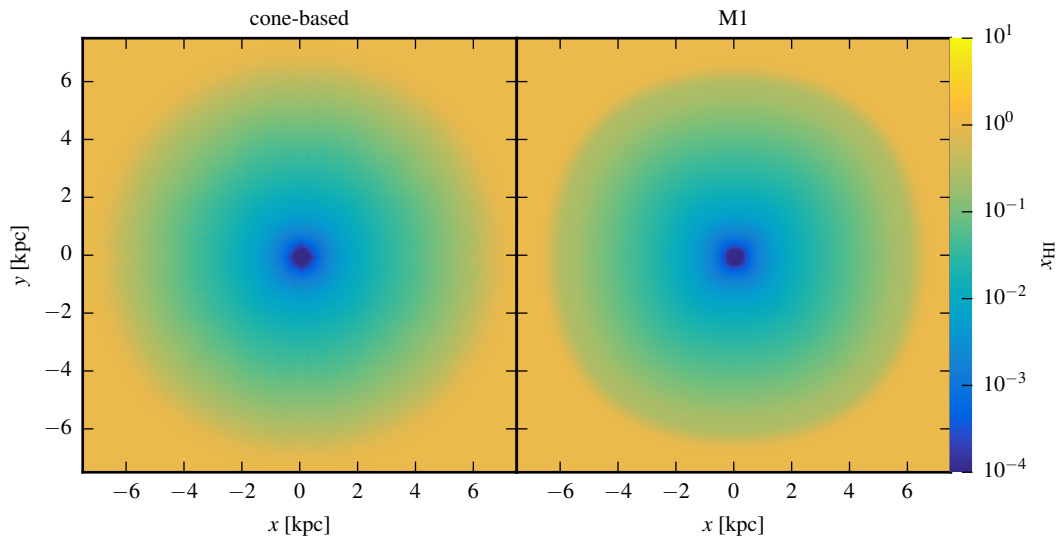


Figure 3.4: Test 2 – The same as Figure 3.3, for the non-isothermal case. The neutral hydrogen fractions are similar, however the Strömgren sphere reaches a slightly larger final radius.

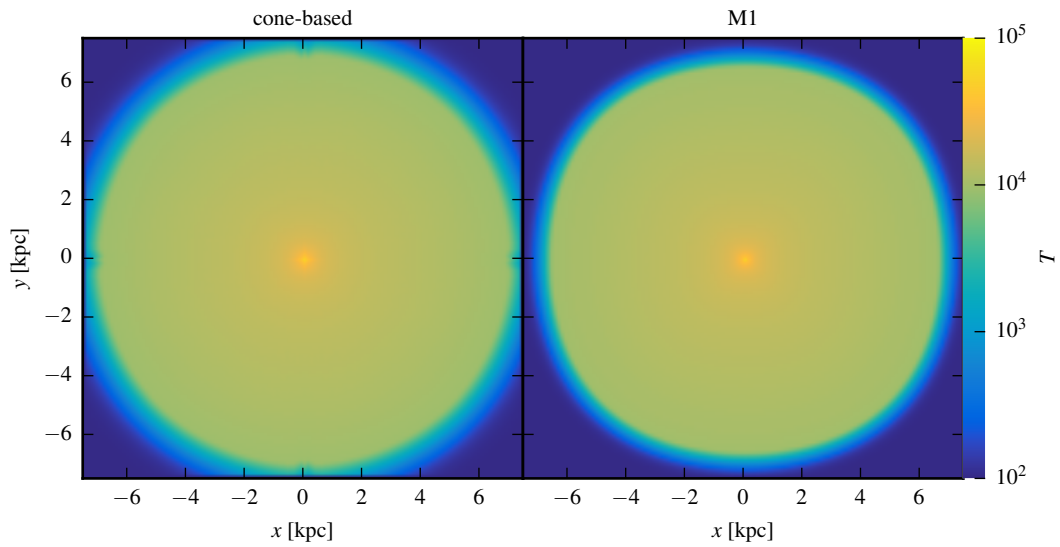


Figure 3.5: Test 2 – Slices through the middle of the Strömgren sphere for the non-isothermal case, showing the temperature at the final time $t = 4t_{\text{rec}}$.

3 A GPU Based Radiative Transfer Solver for Simulating the Epoch of Reionization

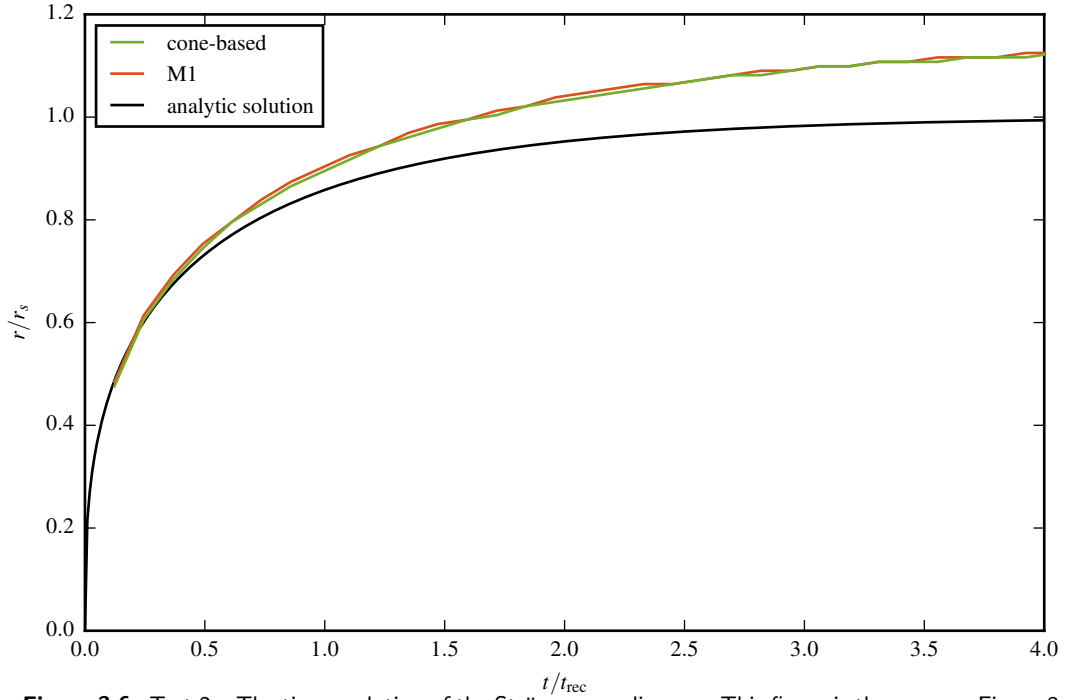


Figure 3.6: Test 2 – The time evolution of the Strömrgren radius r_{eq} . This figure is the same as Figure 3.1, but including ionization heating and cooling processes. The sphere reaches a substantially larger final radius than in the isothermal case. Both of our advection methods agree very well due to the high degree of symmetry of the problem.

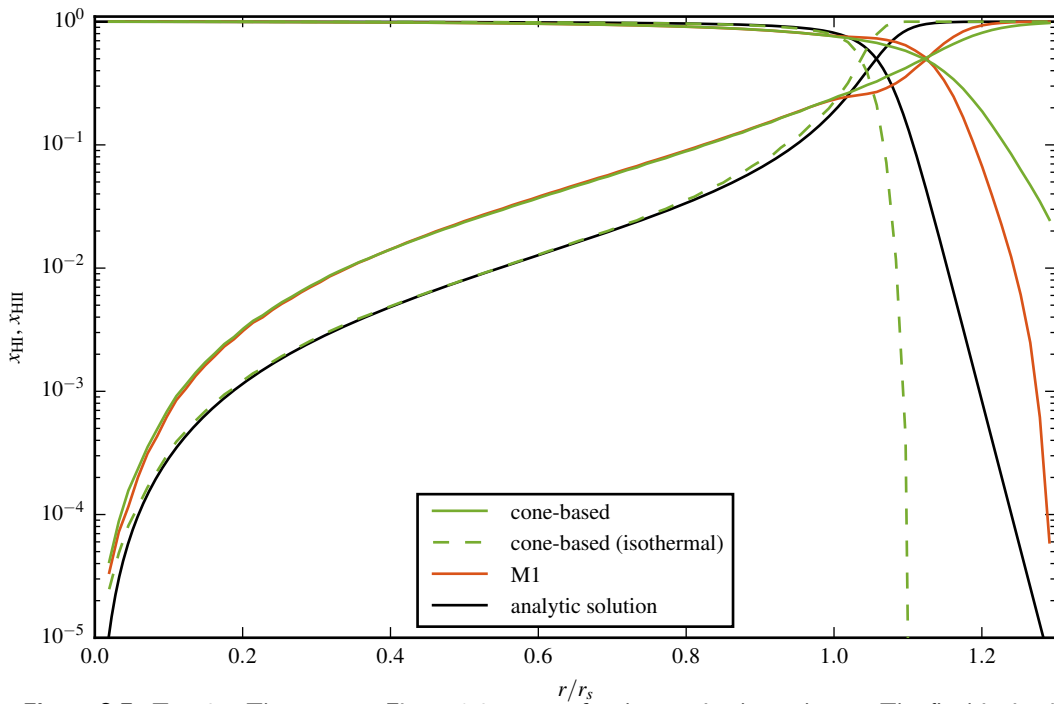


Figure 3.7: Test 2 – The same as Figure 3.2, except for the non-isothermal case. The final ionization profile is considerably larger than in the isothermal case with both advection methods. The isothermal solution for the cone-based advection method is shown as well.

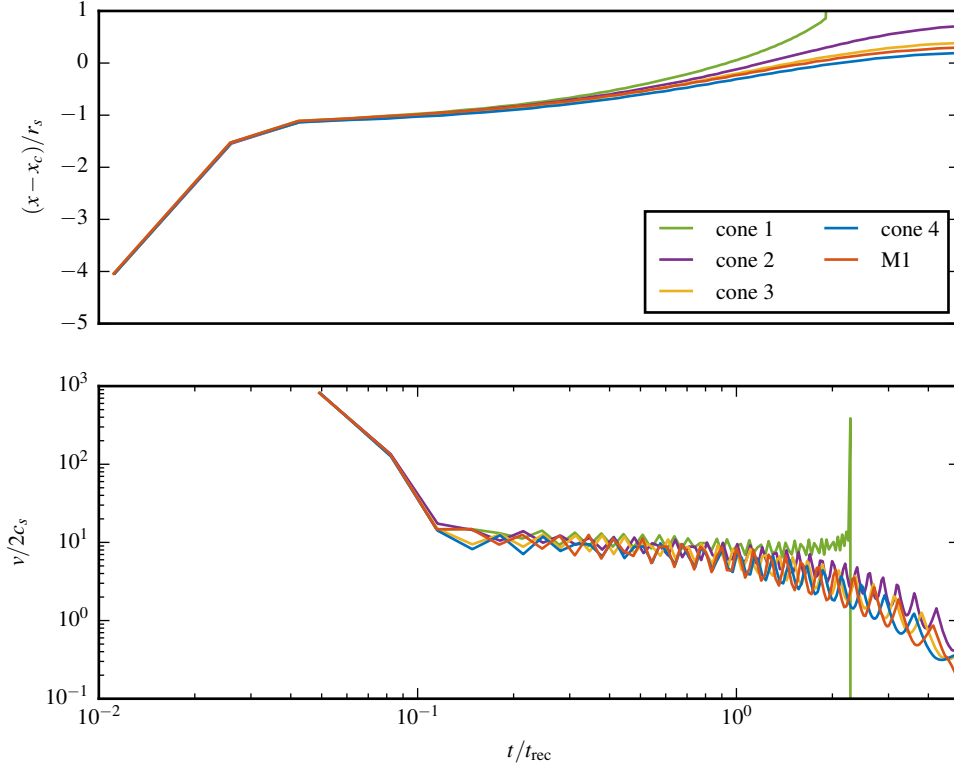


Figure 3.8: Test 3 – The upper panel shows the time evolution of the ionization front position along an axis through the centre x_c of the dense cold cloud in direction of the radiation flux in units of the Strömgen length of the cloud r_s . The time axis is in units of the recombination time t_{rec} . The lower panel shows the velocity of the approaching ionization front in units of twice the sound speed c_s .

larger than in the isothermal case. This is also apparent in the radial profile at the final time $t = 4 t_{\text{rec}}$, where we show the isothermal solution for comparison as well.

3.5.3 Trapping of an ionization front by a cold dense clump

In this test, a cold dense spherical clump with radius r_{clump} is placed into a hot ambient medium. A plane parallel ionizing radiation field approaching from the y -direction tries to evaporate the dense clump.

By balancing the number of ionizing photons with recombination events along a line of sight through the centre of the clump, the Strömgen length l_S is given by

$$l_S = \frac{F}{\alpha_B(T)n_{\text{H}}^2}, \quad (3.43)$$

3 A GPU Based Radiative Transfer Solver for Simulating the Epoch of Reionization

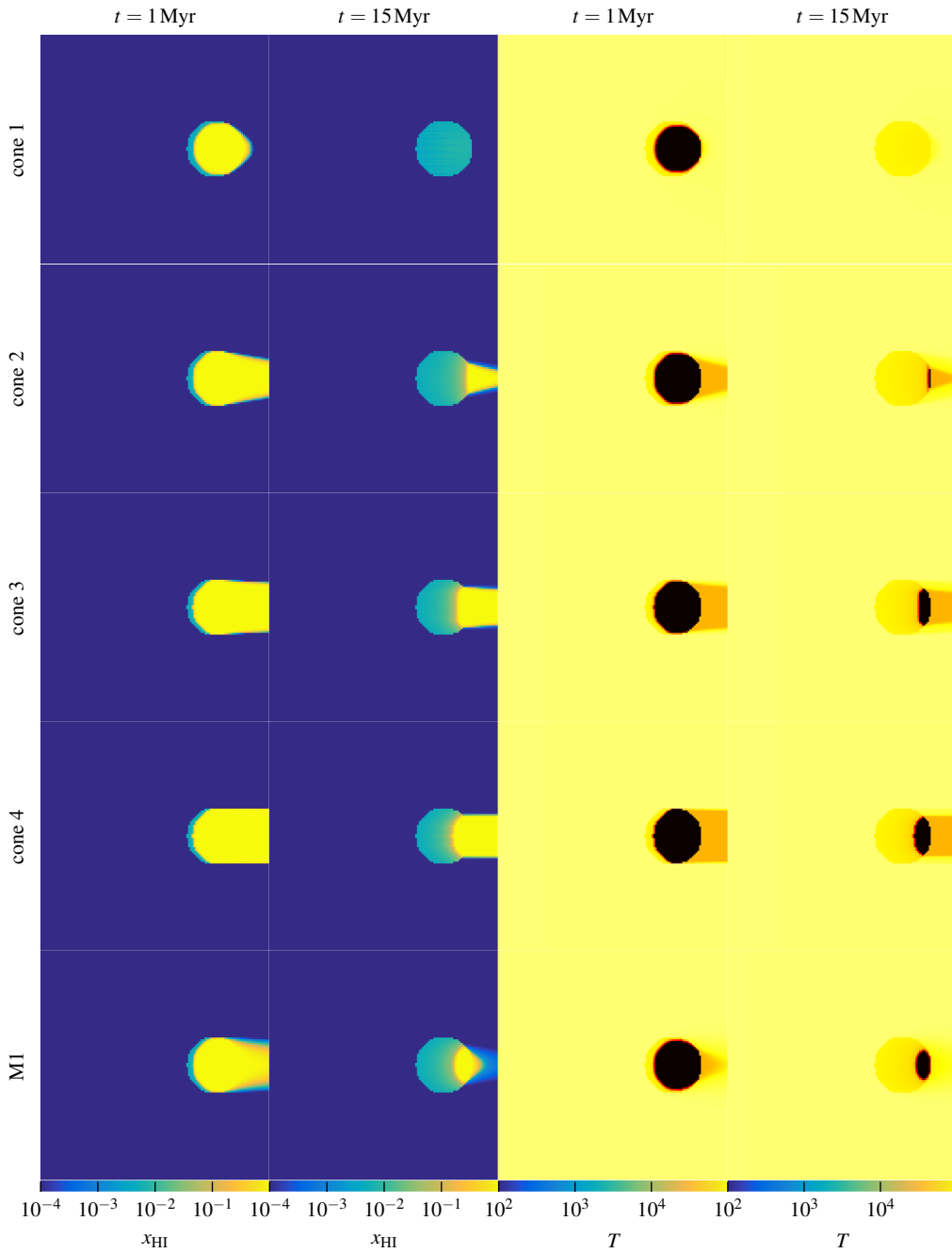


Figure 3.9: Test 3 – Thin slices through the mid plane of our box at $z = 1/2L$ of the neutral fraction x_{HI} and temperature T at $t = 1 \text{ Myr}$ and $t = 15 \text{ Myr}$. Over time, a large part of the cloud is photo ionized until the ionization front comes to rest roughly in the middle of the cloud. The cone-based method is able to produce a sharp shadow behind the dense clump if the angular resolution is high enough. In the case of the M1 advection method, most of the shadowed area is lost due to photons diffusing and scattering into the region. The shadowed region remains colder than the ambient medium.

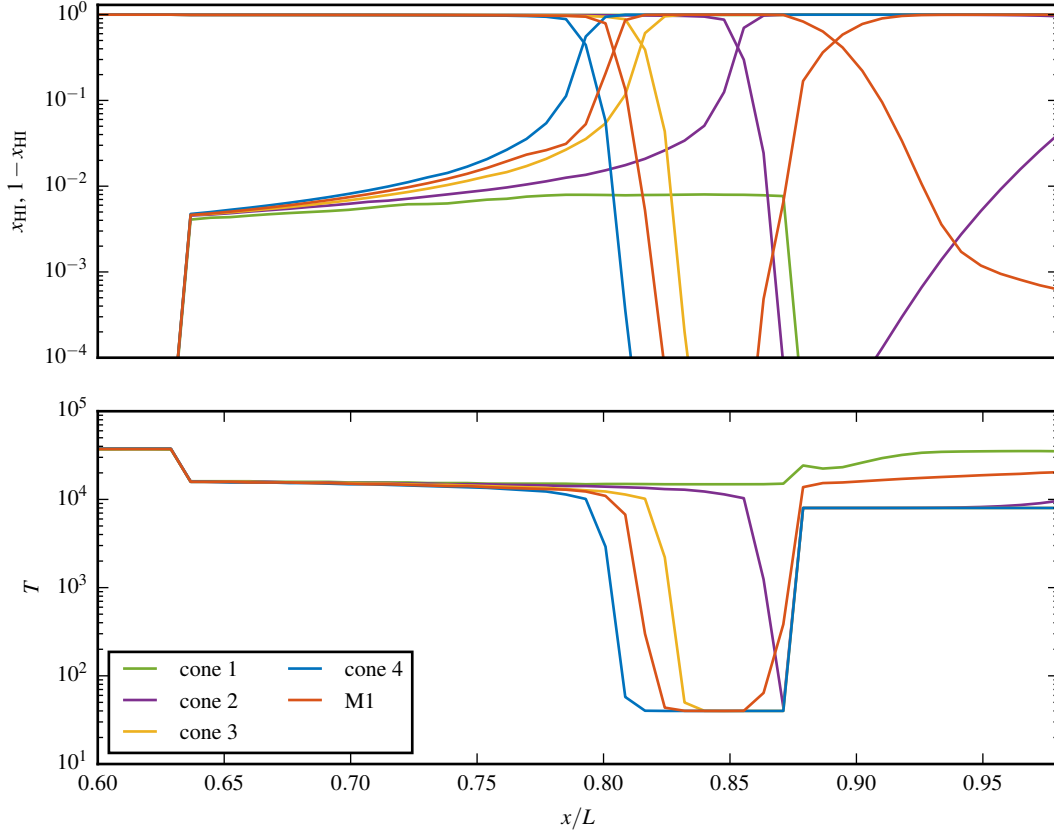


Figure 3.10: Test 3 – Profiles of the ionization state x_{HI} and x_{HII} and temperature T along an axis through the centre of the cloud parallel to the radiation flux at $t = 15 \text{ Myr}$. The x axis is in units of the size of the simulation domain L .

and following Iliev et al. [2006a], a Strömgren number can be defined as $L_S = 2r_{\text{clump}}/l_S$, resulting in

$$L_S = \frac{2r_{\text{clump}}\alpha_B(T)n_{\text{H}}^2}{F}. \quad (3.44)$$

If $L_S > 1$, the clump should be able to trap the approaching ionization front.

The computational domain has a side length of $L = 6.6 \text{ kpc}$. The ambient medium has a hydrogen number density of $n_a = 2 \times 10^{-4} \text{ cm}^{-3}$ and a temperature of $T_{a,0} = 8000 \text{ K}$. The cold dense clump is located at $\vec{x} = (5, 3.3, 3.3) \text{ kpc}$, has a radius of $r_{\text{clump}} = 0.8 \text{ kpc}$ and a hydrogen number density of $n_c = 200 \times n_a = 0.04 \text{ cm}^{-3}$ inside the clump. The temperature inside the clump is $T_{c,0} = 40 \text{ K}$. The radiation has a black body radiation field with $T = 10^5 \text{ K}$ and an ionizing flux of $F = 10^6 \text{ s}^{-1} \text{ cm}^{-2}$. The recombination time scale is $t_{\text{rec}} = 3.06 \text{ Myr}$. The simulation is run until $t = 15 \text{ Myr}$. We perform one run using the M1 advection method and four runs using our cone-based method. In case of the cone-based method, we inject only photons into the

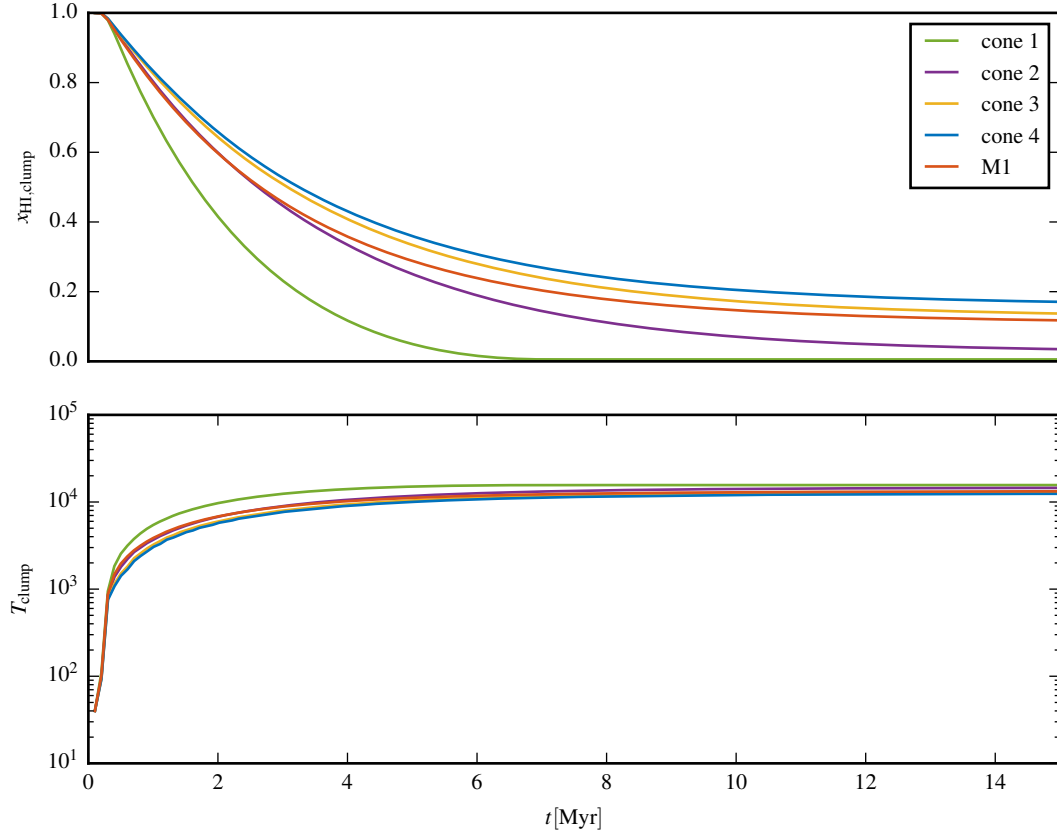


Figure 3.11: Test 3 – Average temperature and neutral fraction in the cold dense cloud over time t . The timespan ranges from the beginning of our simulation until 15 Myr afterwards. As soon as the ionization front hits the cloud, it gets heated up and after about one recombination time t_{rec} it reaches a final temperature of a few $\times 10^4$ K. The steady state ionization state averaged throughout the cloud is about $x_{\text{HI}} = 0.2$ for the run with the highest angular resolution using the cone-based method.

cone field pointing into the direction of the plane parallel radiation field. To study the impact of different angular resolution levels, we alter the opening angle of these cones. We consider the cases of an effective opening angle of $\phi_{\text{max}} = 4\pi/12$, $4\pi/\sqrt{240}$, $4\pi/240$, and $4\pi/12000$. For the given setup the Strömgen number is $l_S \approx 2.05 (T/10^4 \text{ K})^{-3/4}$ and thus the clump is expected to trap the approaching ionization front half way through the clump. Directly behind the clump a sharp shadow is supposed to form.

Slices through the mid plane of the clump at $t = 1$ Myr and $t = 15$ Myr are shown in Figure 3.9. The M1 method is able to form a slightly shadowed region behind the clump. However, the medium does not remain completely neutral in the shadowed region. This finding is broadly consistent with the result obtained in Rosdahl et al. [2013] for the RamsesRT GLF run, which is similar to our implementation. If we use only the coarsest angular resolution, the clump is completely ionized by the approaching ionization front. Due to the round shape of the clump, the optical depth

experienced by the photons is lower along the axis away from the centre of the clump. Thus, the large opening angle is able to scatter light into the centre of the cloud. However, with increasing angular resolution, the cone-based method is able to form a shadow behind the dense clump. The remaining neutral fraction within the clump rises as well with angular resolution.

This finding is shown in a more quantitative way in Figure 3.10, where we show profiles of the neutral fraction and temperature through the clump along the central axis. The profiles confirm our qualitative finding obtained from Figure 3.9. The cone-based method with the lowest angular resolution is not even able to keep parts of the clump neutral. The M1 and low resolution cone-based methods have difficulties forming a shadow and reionize the ambient medium behind the clump to a fraction of $10^{-3} - 10^{-1}$. However, if the angular resolution of the cone-based method is further increased, the shadow is being resolved and the ionizing front stops at around $x/L \sim 0.8$.

The neutral fraction averaged over the entire clump is shown in Figure 3.11 and shows a similar trend with increasing angular resolution. In Figure 3.8 the position of the ionization front is shown relative to the centre of the dense clump. The lower panel shows the corresponding velocity of the ionization front in units of twice the sound speed $c_s(T = 10^4 \text{ K}) = 2.35 \times 10^6 \text{ cm/s}$ of the ambient medium. Initially the ionization front propagates highly supersonically through the rarefied medium. As soon as the front hits the clump the front is severely slowed down.

3.5.4 Cosmological box

The last test we consider is reionization within a small cosmological box with stellar sources of ionizing photons placed at the centre of the most massive halos. We use the same static density field as in Iliev et al. [2006a]. The side length is $L = 0.5h^{-1} \text{ cMpc}$ at a resolution of 128^3 cells. The outer boundaries are transmissive to photons. The density field is obtained from a cosmological N-body simulation including gas dynamics performed using the PM+TVD code. The source population is given by the 16 most massive halos of the simulation. The static density field is taken at a redshift of $z = 7$. We assume an initial temperature of $T_0 = 100 \text{ K}$ throughout the entire box. The sources are modelled as black body sources with an effective temperature of $T_{\text{eff}} = 10^5 \text{ K}$. The emissivity is scaled with halo mass as

$$\dot{N}_\gamma = f \frac{M\Omega_b}{\Omega_0 m_p t_s}, \quad (3.45)$$

with $f = 250$ ionizing photons per baryon and M denoting the total halo mass. The cosmological parameters are given by $\Omega_0 = 0.27$, $\Omega_b = 0.043$, and $h = 0.7$. The sources are emitting ionizing radiation over a lifetime of $t_s = 3 \text{ Myr}$. All sources start to emit ionizing photons at the same time at the beginning of the simulation, which is evolved for a period of $t = 0.4 \text{ Myr}$. Here, we considered the M1 method and the cone-based method with $N_{\text{pix}} = 12$ (cone 1) and $N_{\text{pix}} = 48$ cones (cone 2). In all tests the OTSA is assumed.

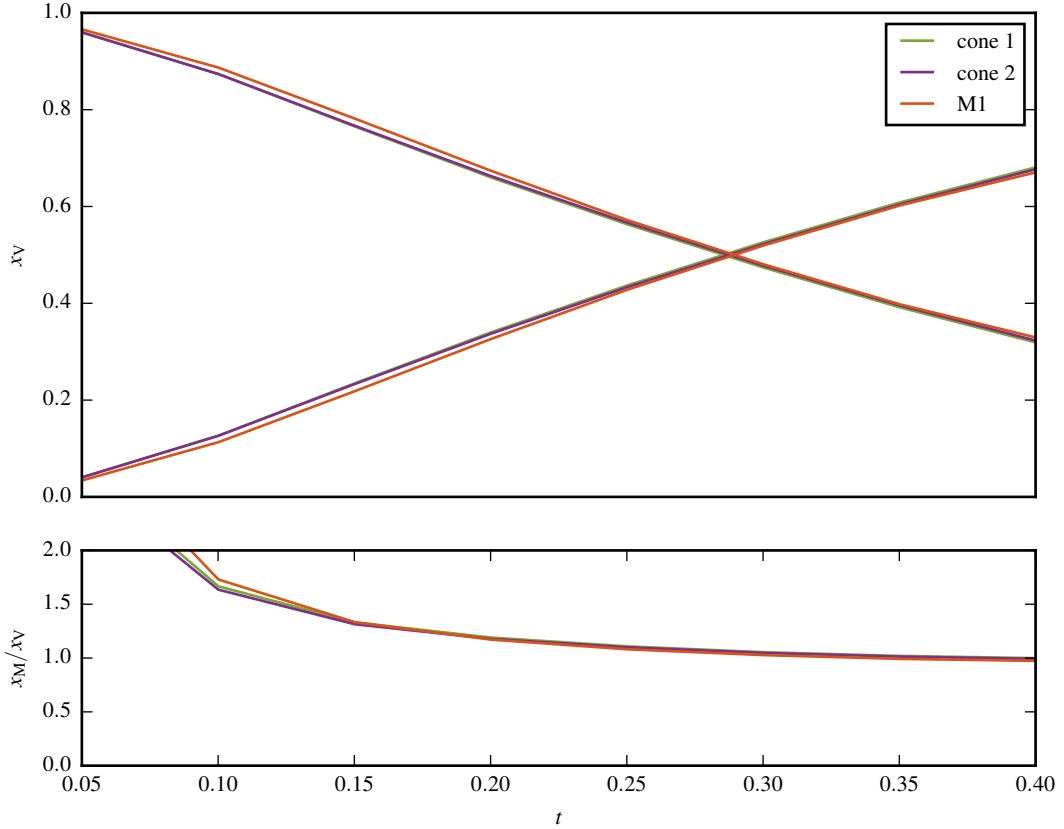


Figure 3.12: Test 4 – The upper panel shows the volume averaged ionization state in the box. The lower panel shows the ratio between mass and volume averaged ionization fraction. The three different choices for the advection method do not affect the reionization history. Initially $x_M/x_V > 1$, meaning the ionized regions are denser than the average density in the box. After $t = 0.4$ Myr the ionization fraction reaches about $x_{\text{HII}} = 0.7$.

In Figures 3.15 and 3.16 we show thin slices through the middle of our box at $z = 1/2L$ for the neutral fraction x_{HI} and temperature T . We show results for the three discussed advection methods at three output times. Generally, all three methods agree well with each other. The morphological differences between the cone-based methods at different angular resolution are minor. For example, the high angular resolution enables a better representation of a thin neutral filament in the lower right corner at the final output time, but this is arguably a detail. The M1 advection method on the other hand has more trouble representing the same feature.

The global ionization state of the test simulation is rather unaffected by the choice of our advection method. The reionization histories in Figure 3.12 are essentially indistinguishable from each other. The global ionization state is only influenced by how many photons are available to drive reionization. Even though the recombination rate is non-linearly dependent on the hydrogen density of the ionized medium, small

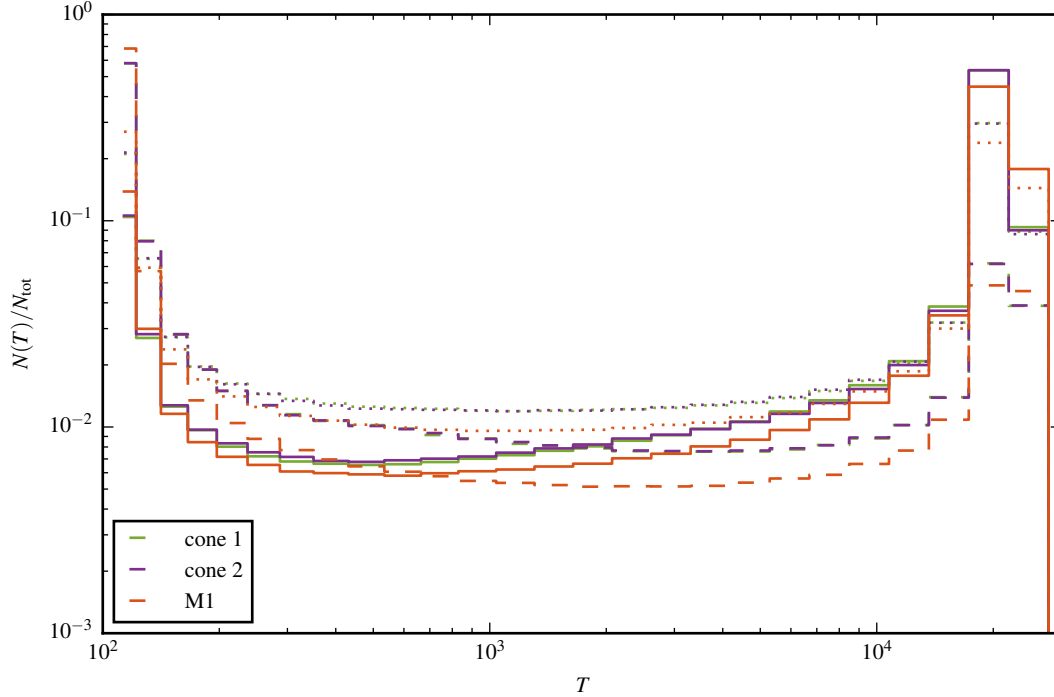


Figure 3.13: Test 4 – Temperature histogram at $t = 0.1$ Myr (dashed lines), 0.25 Myr (dotted lines) and 0.4 Myr (solid lines). Initially, only a small fraction of all cells have a temperature of $T = 4 \times 10^4$ K, but over time the distribution shifts towards higher temperatures. Note that a considerable fraction of all cells remain at the initial temperatures of about $T = 100$ K, because not the whole box is reionized in this test.

morphological differences are not able to alter the globally averaged ionization state much.

Figures 3.13 and 3.14 show histograms of the temperature and neutral fraction at three output times indicated by the line style. Even at the final time, a considerable fraction of all cells remains neutral and roughly at the initial temperature T_0 . Thus reionization is not completed everywhere throughout the duration of the test problem. In this measure, the M1 method shows some small differences compared with the cone-based advection method. These differences are largest at early times.

3.6 Discussion

In the last chapter we have used a number of test problems to validate our implementations. The cone-based method leads to considerably improved results over the M1 method if a sufficiently high angular resolution is used, which is however computationally more expensive. In the following, we will assess the performance characteristics of our radiative transfer implementation. Furthermore, we discuss how our GPU-based implementation can be dynamically coupled to a full cosmological

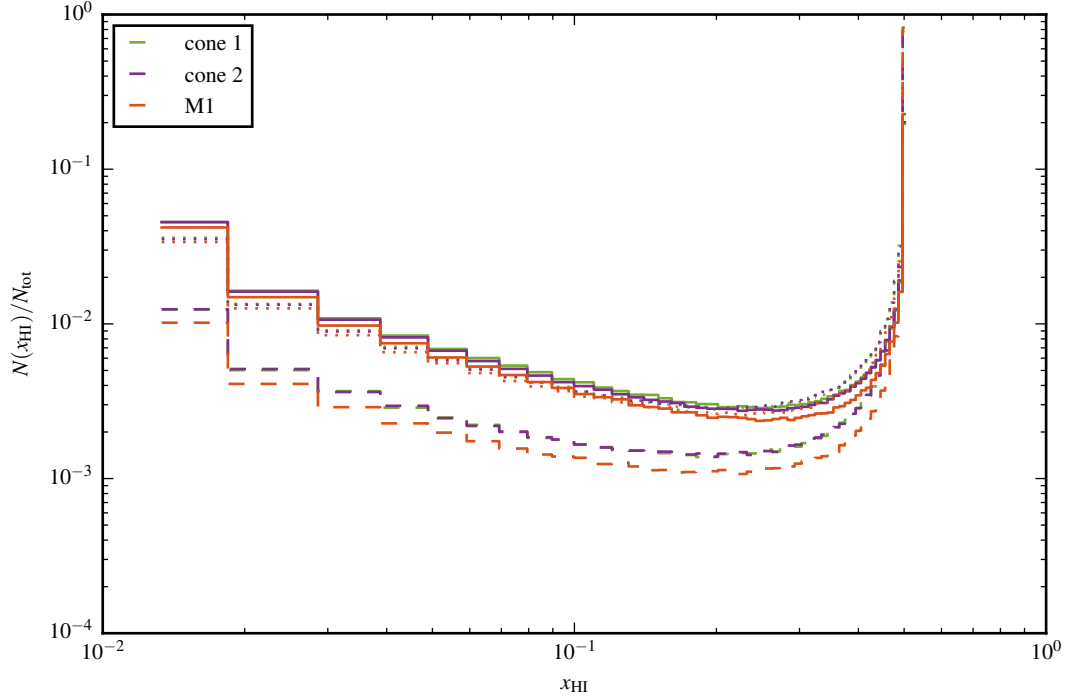


Figure 3.14: Test 4 – The same as Figure 3.13 but for the neutral fraction x_{HI} . Over time the initially neutral medium becomes ionized. However, throughout this test, a considerable fraction of all cells remain neutral.

hydrodynamics simulation code in the future. The performance impact on an Illustris type simulation [Vogelsberger et al., 2014a] is considered as well.

3.6.1 Performance characteristics

Our two advection methods have very different requirements in terms of memory usage and computational work load. For the M1 method we need to store 4 values for the radiation field per resolution element. In addition we need 3 more fields to store the density, thermal energy and ionization state. On the other hand, the cone-based advection method requires $12N_{\text{pix}} + 1 = 12 \times 4^n + 1$ values per resolution element to describe the cone fields $N_{l,i}$ and the sum of them N_{tot} . In principle, the last one could be avoided, but this would increase the computation time, as the sum over the cone fields is required multiple times. For realistically achievable resolution levels of $n = 0, 1, \text{ or } 2$ the memory requirements are about 2.3, 7.4 or 28 times higher than for the M1 method. These high memory requirements seem to make the cone-based advection method uninteresting, especially if the typically much lower available memory per GPU ratio is considered. However, in case of a large scale cosmological simulation, it is not necessarily required to simulate the radiative transfer on the same spatial resolution level or mesh as gravity, hydrodynamics and galaxy formation physics.

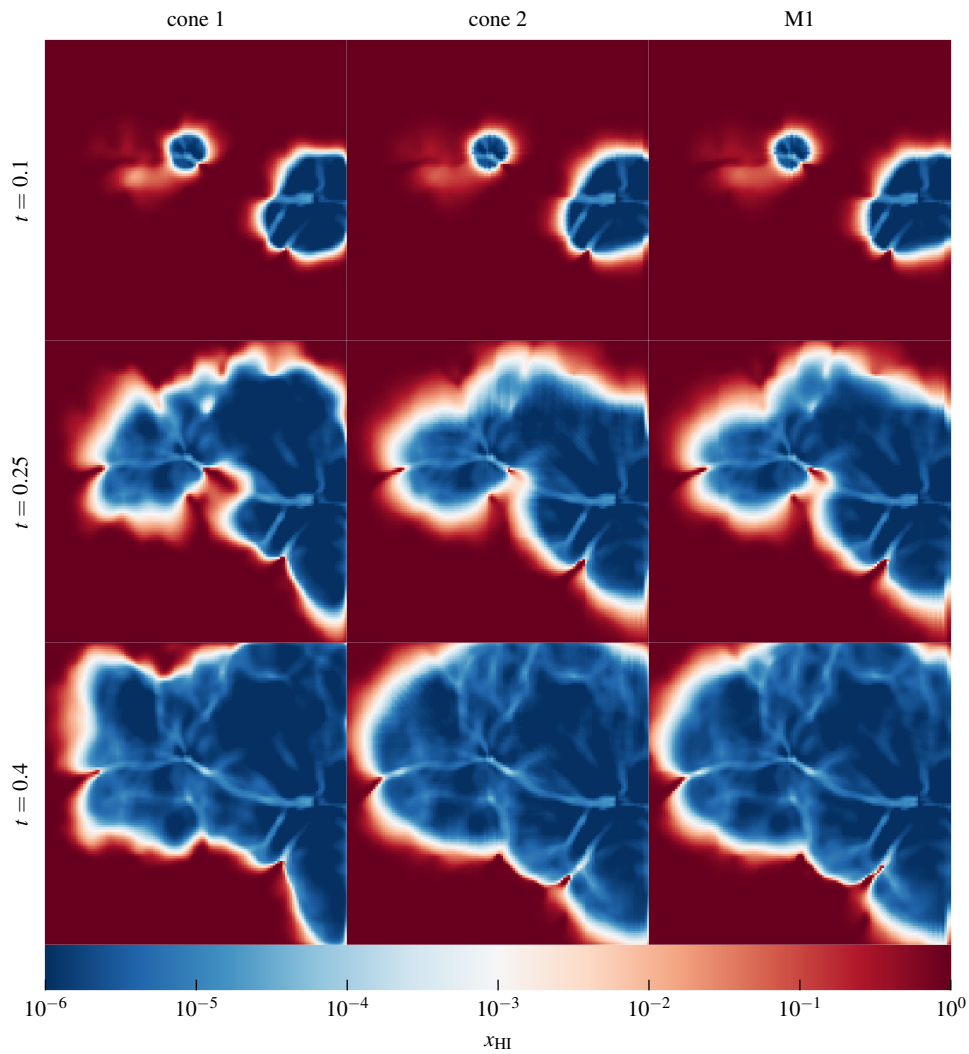


Figure 3.15: Test 4 – Thin slices through the middle of the computational domain at $z = 1/2L$. The figure shows the neutral fraction x_{HI} at three different output times for three advection methods. The cone-based methods show a rather similar morphology, while the morphology produced by the M1 closure is more different.

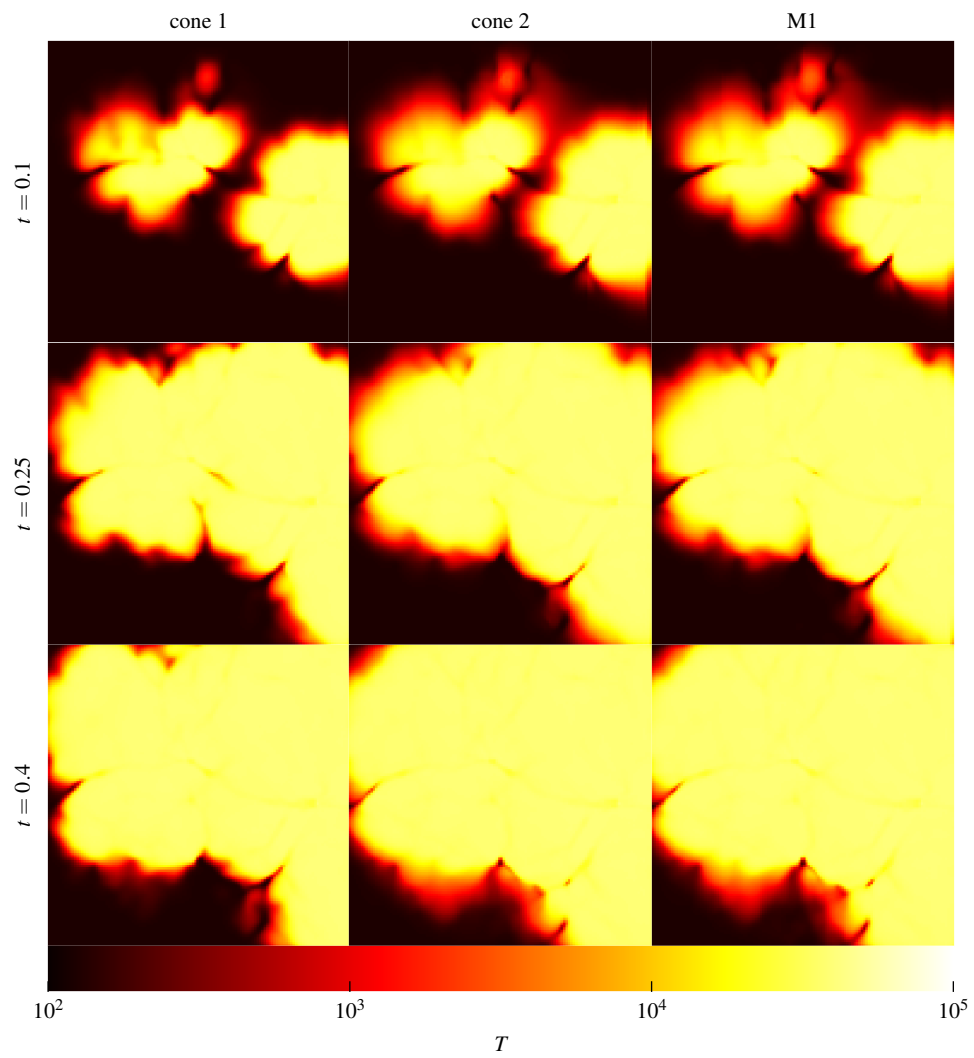


Figure 3.16: Test 4 – The same as in Figure 3.15, but temperature maps are shown here.

The higher memory requirements of the cone-based advection method correspond to a higher computational work load as well, as more data has to be processed. On the other hand, this makes GPU acceleration an interesting option. The GPU can take care of the radiative transfer, while the CPU handles the remaining parts of the simulation.

3.6.2 On the fly radiative transfer in a large cosmological simulations

Our current implementation is able to simulate reionization in post processing only. Any feedback effect on the gas through photoionization heating or a changed ionization state is thus ignored. Current cosmological simulations typically assume a globally tabulated UV background. Instead, it would be desirable to dynamically couple a reionization radiative transfer simulation to a large scale cosmological simulation. Ideally, in such a scheme our GPU-based implementation for radiative transfer could utilize the GPUs while at the same time the CPUs advance the other parts of the simulation forward in time.

As a worked example, we consider the Illustris simulation, which took about 735888 CPU hours to evolve the simulation from redshift $z = 21.8$ up to $z = 5$, using 8192 CPUs in parallel. This is a reasonable redshift range to consider for a self-consistent hydrogen reionization simulation. A post processing simulation of reionization covering the same timespan using 64 GPUs and the M1 advection method on a grid with 1024^3 resolution elements took about 11701 GPU hours in total. A resolution level of about 2048^3 resolution elements would be desirable for the radiative transfer. Assuming linear scaling and about 8 available CPUs per GPU would result in a comparable runtime for the radiative transfer and the remaining part of the cosmological simulation during the stated redshift interval. Even if the computations on the GPU and CPU cannot be run in parallel, the increase in total simulation time would be only be about a factor of 2. However, at least parts of the computations can be carried out simultaneously. Additionally, hydrodynamics requires much smaller timesteps at late time, while the timesteps for the radiative transfer actually increase due to cosmic expansion if the resolution is kept fixed. While the parallelization pattern described above allows for a very good scalability we note that this might not be the case up to arbitrary high numbers of CPU or GPU cores. In any case, it appears that the computational costs of the two calculational parts are quite well matched to make such a fully coupled cosmological simulation of reionization a realistic goal in the near future.

4

Hydrogen Reionization in the Illustris Universe

This chapter is based on Bauer et al. [2015]

4.1 Introduction

The cosmic microwave background radiation was released when the Universe recombined at a redshift of $z \sim 1100$, leaving behind only a tiny residual free electron fraction. Yet in the present Universe, it is well established that the intergalactic medium is highly ionized, as is inferred from the absence of Gunn and Peterson [1965] troughs in the absorption spectra of nearby quasars. Hence there must have been an ‘epoch of reionization’ (EoR) sometime in between, where photons emitted by stars and possibly quasars ionized the intergalactic hydrogen again [for reviews see Barkana and Loeb, 2001; Fan et al., 2006a; Morales and Wyithe, 2010]. This is believed to first happen to hydrogen at $z \sim 7 - 10$, with helium being ionized considerably later at $z \sim 3$ [McQuinn et al., 2009; Schaye et al., 2000] by the harder radiation of quasars.

Observations of distant quasars show unambiguously that reionization was complete not much later than $z = 6$ [Fan et al., 2006b]. Observations of Lyman- α emitters indicate rapid changes in their abundance at somewhat higher redshift [e.g. Caruana et al., 2014; Kashikawa et al., 2011; Ouchi et al., 2010]. Together with the relatively high optical depth to scattering on free electrons inferred from CMB observations [Bennett et al., 2013; Planck Collaboration et al., 2014] and the discovery of early

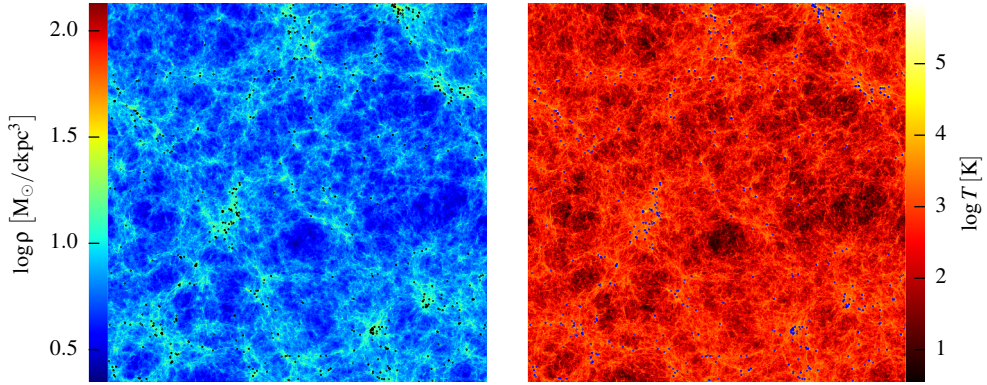


Figure 4.1: Projected slices of thickness 7.1 cMpc through the binned gas and temperature fields of the 106.5 cMpc wide Illustris simulation at redshift $z = 7$, just before the externally applied UV background raises the temperature of the diffuse gas (the unit ‘cMpc’ stands for comoving Mpc). The left panel shows the gas density field, with overlaid circles giving the locations of galaxies identified at this time by the group finder algorithm SUBFIND [Springel et al., 2001]. The right panel gives the corresponding mass-weighted temperature field; the heated regions around the galaxies are caused by shocks associated with virialization and feedback-driven outflows. In turn, the high temperature there leads to collisional ionization of the gas.

galaxies at $z \sim 7$ and higher [Bouwens et al., 2011; Oesch et al., 2014; Pentericci et al., 2011], this suggests that reionization likely started considerably earlier than $z \sim 7$. The duration of the transition process, and the nature of the source population ultimately responsible for reionization, remain however subject of much observational and theoretical research.

A particularly exciting prospect is that an observational breakthrough in this field may be imminent, in particular through a direct mapping of the EoR with 21-cm observations [see Zaroubi, 2013, for a recent review]. This has not yet been achieved, but impressive progress towards this goal has recently been made [e.g. Dillon et al., 2014; Parsons et al., 2014], and future instruments such as the Square Kilometre Array (SKA) or the James Webb Space Telescope (JWST) promise to revolutionize our understanding of the early universe, and of reionization in particular.

Numerous theoretical models for cosmic reionization have been constructed, often based on semi-analytic models of the reionization process or simple radiative transfer postprocessing of dark matter simulation outputs. Furlanetto et al. [2004] developed an excursion set approach to reionization that has seen widespread use in analytic and semi-numerical models of reionization [e.g. Alvarez and Abel, 2007; Battaglia et al., 2013; Mesinger et al., 2011; Zahn et al., 2011]. Many different numerical algorithms for direct radiative transfer simulations have also been developed over the years, in most cases however based on static density fields derived from dark matter only simulations or from simplified hydrodynamic simulations [e.g. Ahn et al., 2012; Aubert and Teyssier, 2010; Ciardi et al., 2003; Croft and Altay, 2008; Iliev et al.,

2006b; McQuinn et al., 2007b; Sokasian et al., 2001; Trac et al., 2008; Zahn et al., 2007].

Recently, full radiation hydrodynamics simulations that follow cosmic reionization and structure formation simultaneously and self-consistently have become possible. These calculations can in principle account for radiative feedback processes on forming galaxies, for example from inhomogeneous photoionization heating. Pioneering work of this type has been presented by Gnedin [2000], but only in recent years it has become possible to study approximately representative cosmological volumes in this way [e.g. Paardekooper et al., 2013; Petkova and Springel, 2011b].

Some of the most advanced studies of this kind include the simulations recently presented by Norman et al. [2013] and So et al. [2014], who use full radiative hydrodynamics simulations of cosmic structure formation on a uniform grid. A fixed spatial grid resolution does however not allow a proper resolution of internal galaxy structure, which compromises the ability of the simulations to reliably predict the build up of stellar mass. To remedy this problem, Gnedin [2014] and Gnedin and Kaurov [2014] employ adaptive mesh refinement techniques and simulate galaxy formation in cosmological volumes with high spatial and mass resolution. Similar work has recently been presented by Pawlik et al. [2015], based on hydrodynamical SPH simulations coupled self-consistently to the radiative transfer scheme TRAPHIC [Pawlik and Schaye, 2008]. However neither group evolves the simulations significantly past the EoR (let alone to $z = 0$) due to the high computational cost involved, so it is not yet clear whether these simulation models would also yield a plausible *present-day* galaxy population.

This body of theoretical works has made it clear that the source population primarily responsible for reionization is most likely star-forming small galaxies at high redshift. While so-called Pop-III stars may boost the high redshift photon production rate, the overall contribution of these “first star” sources is likely only of secondary importance [Paardekooper et al., 2013; Wise et al., 2014]. Similarly, another potential source of ionizing photons, active galactic nuclei, are not expected to be critical at high redshift due to their large mean separation [Faucher-Giguère et al., 2009; Hopkins et al., 2007] and still fairly limited cumulative luminosity. Instead, it is often argued that small proto-galaxies, with stellar masses just around $10^4 M_{\odot}$ or even lower may dominate the ionizing budget [Paardekooper et al., 2013]. Ahn et al. [2012] showed that these mini halos alone can not complete reionization, but significantly contribute towards an earlier onset of reionization and thus enhance the optical depth towards the last scattering surface. These small halo mass systems are further assisted by suggestions that the escape fraction may strongly rise towards small halo masses, as inferred by Wise et al. [2014] based on radiative hydrodynamics simulation of faint high redshift galaxies. Using this finding in a semi-analytic model for reionization, Wise et al. [2014] have also demonstrated that the first galaxies may plausibly constitute the reionizing sources, yielding an optical depth consistent with Planck Collaboration et al. [2014] without exceeding the UV emissivity constraints by the Ly- α forest.

It is interesting however to note that the cosmic star formation history inferred from observations is predicted to rapidly decline towards high redshift [e.g. Ellis et al., 2013]. This is also expected [Hernquist and Springel, 2003] and desirable on theoretical grounds [Scannapieco et al., 2012], because simulation models of galaxy formation need to resort to an extremely efficient suppression of high-redshift star formation in order to successfully describe present-day galaxy properties [e.g. Stinson et al., 2013]. A very low level of high redshift star formation is however quite the opposite of what seems necessary to explain early reionization and the comparatively high optical depth inferred from CMB experiments. This tension makes it difficult to attribute reionization entirely to young galaxies with more or less ordinary stellar populations. In Λ CDM models with low normalization σ_8 , or in alternative warm dark matter cosmologies, this problem is further exacerbated [Yoshida et al., 2003a,b], whereas in certain non-standard dark energy models that shift structure growth to earlier times, for example ‘early dark energy’ [Grossi and Springel, 2009; Wetterich, 2004], it may be alleviated.

Recently, cosmological hydrodynamic simulations of galaxy formation such as the *Illustris* [Vogelsberger et al., 2014a] or *Eagle* [Schaye et al., 2015] projects have advanced to a state where they produce realistic galaxy populations simultaneously at $z = 0$ and at high redshifts, throughout a representative cosmological volume. This is achieved with coarse sub-resolution treatments of energetic feedback processes that regulate star formation, preventing it from exceeding the required low overall efficiency. Ideally the process of reionization should be coupled dynamically to such a galaxy formation model. However, running several such reionization simulations for different escape fraction parameterizations at the resolution and size of *Illustris* would be computationally very expensive. Thus we have here reverted to study reionization in post processing only.

An important manifestation of feedback are galactic winds and outflows that substantially modify the distribution of the diffuse gas in the circumgalactic medium (CGM) and the intergalactic medium. This in turn also influences the gas clumping and the recombination in models of cosmic reionization. It thus becomes particularly interesting to test whether detailed models of galaxy growth such as *Illustris* are in principle also capable of delivering a successful description of cosmic reionization, and if so, what assumptions are required to achieve such a success.

This is exactly the goal of this paper. We use a sequence of snapshots with high time resolution of the high-resolution *Illustris* simulation and combine them with a radiative transfer scheme that is capable of accurately evolving ionizing radiation for an arbitrary number of sources. We are particularly interested in the question of whether the star formation history predicted by *Illustris* can reionize the universe early enough to be consistent with observational constraints, and how the reionization transition proceeds in detail in this scenario. Because we have implemented two different radiative transfer methods, we can also evaluate how well they intercompare, thereby providing an estimate for systematic uncertainties related to these radiative transfer methods. We also explicitly test the impact and accuracy of the often adopted reduced speed of light approximation.

4.2 Methods

4.2.1 The Illustris simulation

Recently, Vogelsberger et al. [2014a] introduced the Illustris simulation suite, an ambitious attempt to follow cosmological hydrodynamics and the feedback processes associated with galaxy formation in a sizeable region of the universe. The highest resolution simulation of the project employed 2×1820^3 particles and cells in a box 106.5 Mpc across, yielding a mass resolution of $1.26 \times 10^6 M_\odot$ in the baryons, and $6.26 \times 10^6 M_\odot$ in the dark matter. The cosmology adopted is given by $\Omega_m = 0.2726$, $\Omega_\Lambda = 0.7274$, $\Omega_b = 0.0456$, $\sigma_8 = 0.809$, $n_s = 0.963$, and $H_0 = 70.4 \text{ km s}^{-1} \text{ Mpc}^{-1}$, which is consistent with the most recent determinations from WMAP9 and Planck. The simulations employed the moving-mesh code AREPO [Springel, 2010], which is well-suited to applications in cosmic structure formation.

The physics model employed by Illustris includes radiative cooling, metal enrichment based on 9 elements, star formation, stellar evolution and mass return, supernova feedback by means of a kinetic wind feedback, and black hole growth and associated feedback processes in a quasar- and radio-mode. We refer to Vogelsberger et al. [2013] and Torrey et al. [2014] for a description of the full details and basic tests of the model. A number of different studies have analysed structure formation in Illustris, making it clear that many basic properties of the observed galaxy populations are approximately reproduced by the simulation model. This in particular includes constraints on the stellar mass function at different epochs [Genel et al., 2014; Vogelsberger et al., 2014b], the morphologies and spectra of galaxies [Torrey et al., 2015], the colours of satellite systems [Sales et al., 2015], the stellar halos of galaxies [Pillepich et al., 2014], the nature of high redshift, compact galaxies [Wellons et al., 2014], the galaxy-galaxy merger rate [Rodríguez-Gomez et al., 2015], the kinematics and metal abundance of damped Lyman-alpha absorbers [Bird et al., 2015], or the evolution of the black hole mass density and quasar luminosity function [Sijacki et al., 2014]. The galaxy formation predictions by Illustris are hence in broad agreement with observations, which adds additional motivation to ask whether they at the same time yield a plausible reionization history.

A self-consistent treatment of the UV background using radiative transfer was however not included in Illustris, as this is still beyond reach in such large cosmological simulations that are evolved to low redshift. Instead, an external, spatially uniform and time-dependent UV background was imposed based on the model of Faucher-Giguère et al. [2009], and dense gas is self-shielded from UV background radiation using a prescription derived from Rahmati et al. [2013]. A coarse treatment of an AGN proximity effect was included where accreting AGN modify the ionization balance of gas in their environment [Vogelsberger et al., 2013]. In this work, we therefore aim to study reionization through postprocessing of the Illustris simulation, making use of the significant number of output dumps [more than 128, with an output spacing as in the Aquarius project, Springel et al., 2008] stored for the calculation. This allows us to take the temporal information about the growth of cosmic structures

into account, avoiding the simplification of a static density field often adopted in past work. Another advantage of Illustris is the reasonably large box size of 106.5 Mpc. While a still larger volume would clearly be desirable, studies of cosmic variance of reionization have suggested that $\sim 100 h^{-1} \text{Mpc}$ corresponds to the minimum box size required to obtain a reliable mean reionization history [Iliev et al., 2014; Mesinger and Furlanetto, 2007]. The volume available in Illustris falls slightly short here, but is approximately still sufficient for hydrogen reionization. Studying HeII reionization with Illustris would be more problematic however due to the incomplete sampling of bright and rare quasars.

4.2.2 Reionization in post processing

In this work, we study the progress of cosmic reionization by following the time-resolved evolution of the density field and the source population of the Illustris simulation in postprocessing. The unstructured Voronoi mesh that stores the baryon distribution in the simulation outputs needs to be rebinned onto a regular Cartesian mesh to allow use of our GPU-based code. To this end, we assign the mass of each Voronoi cell onto the density grid using a spline-kernel assignment. This yields a less noisy and smoother density field than obtained, e.g., by using a clouds-in-cells (CIC) or nearest-grid-point (NGP) assignment kernel [Hockney and Eastwood, 1981]. The actual density field used in our reionization calculation is then continuously updated by linearly interpolating in time between the two nearest binned density grids available in $\log a$ space, where $a = 1/(1+z)$ is the cosmological scale factor. The Illustris outputs are spaced roughly 65 Myrs apart at the relevant redshift $z \sim 6$, allowing us to bin the density field in total 35 times between redshift $z = 21.8$ and $z = 4.9$. Using a set of small subboxes cut out from Illustris and stored with much higher time-resolution we have checked that the sparser time resolution of the main outputs is still reasonably accurate. It shifts the completion of reionization towards slightly earlier times, but the uncertainty in our results is still dominated by the parametrization of the escape fraction. Initially we start with a uniform temperature field with $T = 100 \text{ K}$ and then follow the temperature evolution using Equation (3.15), ignoring the intrinsic temperature evolution of the underlying Illustris simulation. We note that in this paper we consider hydrogen reionization only.

4.2.3 Escape fraction

Of all ionizing photons emitted by stars, only a fraction f_{esc} reaches the IGM, while the other photons are absorbed by the denser interstellar medium (ISM) or by dust. In principal, the escape fraction depends on individual halo properties like halo mass or dust content. Unfortunately, only little is known about the real values of the escape fractions, especially at high redshifts, making this parameter one of the primary uncertainties in studying the EoR. However, theoretical models have started to constrain the escape fraction, albeit with large systematic uncertainties. For

Overview of radiative transfer simulation models				
Name	Resolution	f_0	κ	advection method
V1_X_CONE	256 ³ ... 512 ³	0.04	4	cone-based method
V5_X_CONE	256 ³ ... 512 ³	0.04	3.6	cone-based method
C2_X_CONE	256 ³ ... 512 ³	0.2	0	cone-based method
V1_X_M1	256 ³ ... 1024 ³	0.04	4	M1 method
V5_X_M1	256 ³ ... 1024 ³	0.04	3.6	M1 method
C2_X_M1	256 ³ ... 1024 ³	0.2	0	M1 method

Table 4.1: Overview of the different radiation transfer calculations performed for this study. We carried out runs with a resolution ranging from 256³ up to 1024³ cells, which is indicated by replacing the placeholder ‘X’ with the number of cells per dimension in the actual run name. We compare different escape fraction parameterizations, characterized by f_0 and κ . The three different choices we adopted for this are labeled ‘V1’, ‘V5’ and ‘C2’ in the simulation names. Finally, for each of the models we compare two different advection schemes for the radiation, one based on the M1 closure relation, the other on an explicit discretization of the solid angle (‘cone-based’).

example, the simulations of Wise et al. [2014] suggest a sharp increase of the escape fraction towards smaller masses, reaching 50% at halo masses of 10⁷ M_⊙.

The simplest model is evidently to adopt a globally constant escape fraction that is the same for all galaxies at a given epoch. This is what we shall assume here, because one may well argue that in light of the many other uncertainties adopting a more complicated model would not be justified [see also the discussion in Pawlik et al., 2015]. As a default choice for the constant escape fraction model we have considered $f_{\text{esc}} = 0.2$ (C2 model). This almost certainly constitutes an overestimate for low redshift galaxies, but is perhaps not overly optimistic at high redshift.

Besides such a globally constant escape fraction, we also consider an evolution of the f_{esc} value with time. To this end, we use the model of Kuhlen and Faucher-Giguère [2012] who proposed an evolution of the escape fraction as a function of redshift according to:

$$f_{\text{esc}} = \min \left[1, f_0 \left(\frac{1+z}{5} \right)^\kappa \right]. \quad (4.1)$$

Our default choices for the parameters f_0 and κ are $f_0 = 0.04$ and $\kappa = 4$, implying a rise of the escape fraction with redshift (V1 model). We have also calculated results for a variety of other fiducial parameter choices as well. For an overview see Table 4.1.

We stress again that the escape fraction is essentially a free parameter in our treatment. Its interpretation is complicated by the fact that the absorbing ISM is not totally absent in our reionization simulations. It is just severely under-resolved, and thus some part of the boost in recombination rates due to a highly clumped environment is missing. However, photons are still consumed for (repeatedly) ionizing the material in these high density regions. Unresolved small galaxies and thus missing UV photons might be compensated by a slightly larger escape fraction than otherwise would be needed.

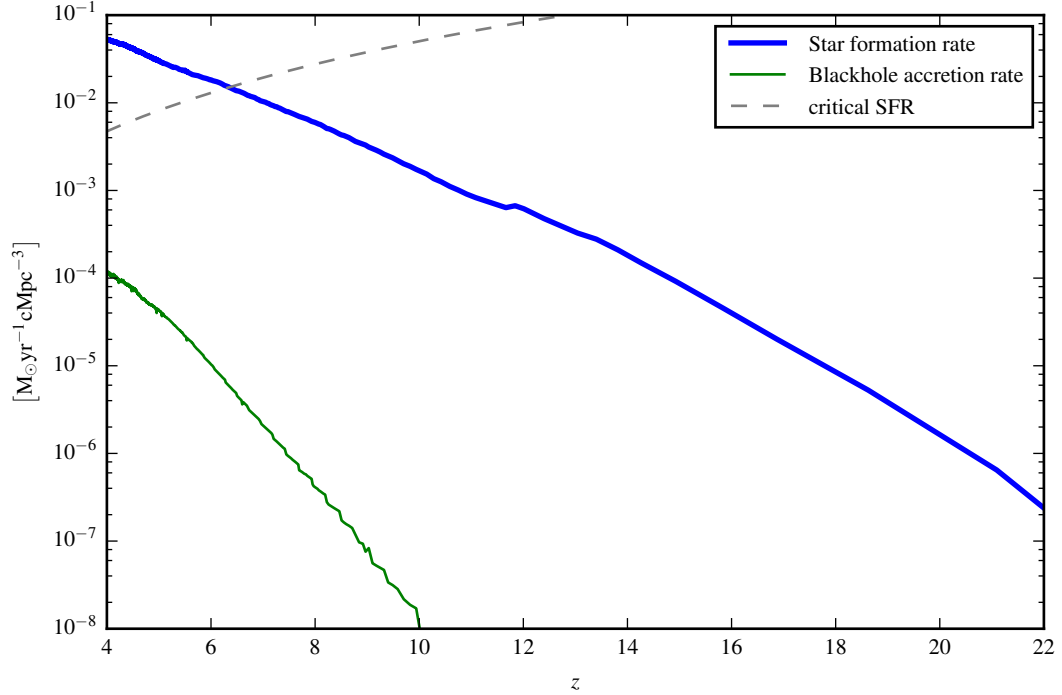


Figure 4.2: The rise of the total comoving star formation and black hole accretion rate densities (solid lines) as a function of redshift in the Illustris simulation. We see that the black hole accretion drops more rapidly towards very high redshift than the star formation rate, making it an insignificant contributor to the first phases of cosmic reionization. The dashed line gives a simple estimate for the required star formation rate to keep the Universe ionized if the clumping factor is $C = 5$ with a constant escape fraction of $f_{\text{esc}} = 0.2$ and a Chabrier IMF is assumed [Pawlik et al., 2015]. (see also Section 4.4.6). The fact that the star formation rate does cross this line at $z \sim 7 - 8$ indicates that reionization could happen roughly at this epoch provided the actual clumping in Illustris is not very different.

4.2.4 Source modelling

The main source of ionizing photons considered in our model are ordinary stellar populations in young stars, which arguably appear to be the most likely source responsible for reionization. In this work we are mainly interested in testing this hypothesis based on directly adopting the stellar populations forming in the Illustris simulation. Their ionizing luminosities as a function of stellar age and metallicity are taken from STARBURST-99 [Leitherer et al., 1999]. Figure 4.1 gives a visual impression of the binned gas density field in Illustris at $z = 7$, and of the clustered galaxy population that represents our source population. Because the local ionization rate can change on much shorter timescales than the density, we bin the luminosity field with much finer time resolution than the density field. In our default set-up, we binned it 200 times during the duration of the reionization simulation including the actual birth time of the stellar sources. The actual luminosity used in the simulation to integrate the source terms is then again interpolated in $\log a$ space from this large

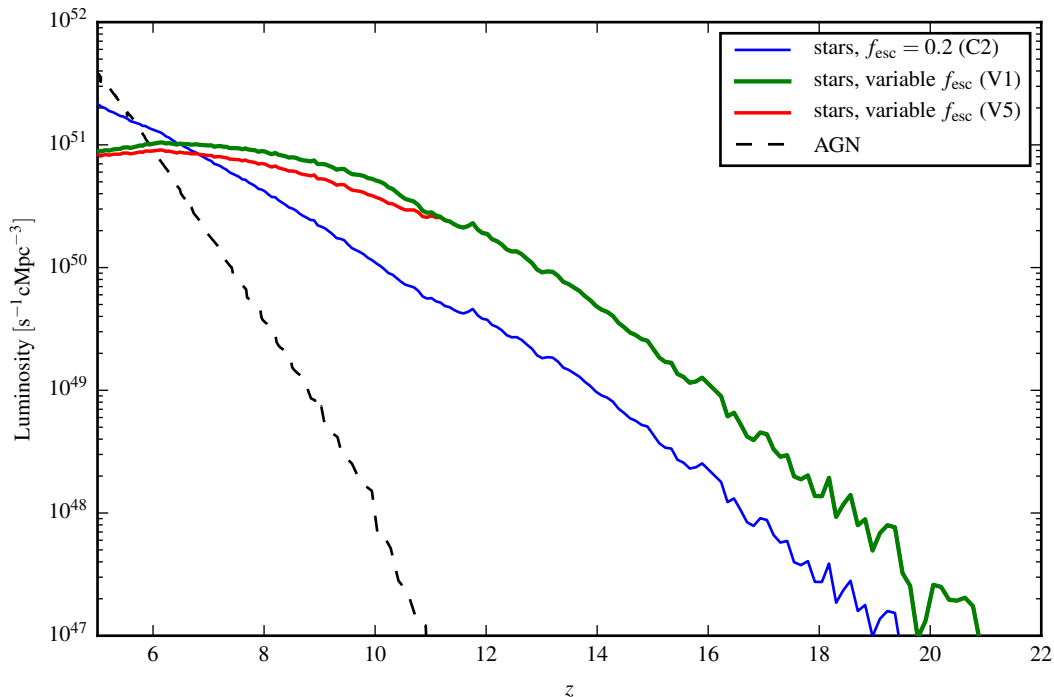


Figure 4.3: Time evolution of the total ionizing luminosity resulting for our different escape fraction models. The model with a constant escape fraction (blue lines) tracks the shape of the cosmic star formation history. Our default models with a redshift dependent escape fraction are given by the green and red lines. For comparison, we also include the ionizing luminosity implied by the quasars included in our simulation (dashed black line), adopting a simple conversion of quasar accretion rate to ionization radiation output. This demonstrates that the quasar contribution picks up too late to cause the initial hydrogen reionization, but it may play a role in keeping the universe ionized at later times, as well as for completing late-time helium reionization.

grid of luminosity density fields. The ionizing luminosity of a single stellar source is always distributed in a photon conserving way to the radiation grids. The assignment of the luminosity is done using a CIC interpolation scheme.

As a global overview, Figure 4.2 shows the time evolution of the star formation rate density and the black hole accretion rate density in the main Illustris simulation. These are the sources we mainly have at our disposal from this simulation. Additional sources, especially at early times, could be primordial Pop-III stars. Their relative importance for the build-up of high-redshift galaxies is still a matter of debate, but their overall contribution for ionizing the universe is likely subdominant, hence we only consider the ordinary stellar populations followed by Illustris.

The ionizing sources we have at our disposal from the main Illustris simulation are related to the star formation rate and black hole accretion rate densities. The corresponding time evolution of the net ionizing luminosity density is shown in Figure 4.3, together with different scenarios for the escaping luminosity according to our escape fraction models. The blue line shows our constant escape fraction

model (C2 model), while the green line is our default model for a time-varying escape fraction (V1 model). The red line (V5 model) represents a variable escape fraction model with a different value for the exponent κ than in the V1 model. These models rapidly rise for some time, but at around a redshift of $z \simeq 8$, the escaping radiation actually reaches a maximum and then starts to slowly decline again. Here the strong decrease of the escape fraction from 1 to 0.04 marginally over-compensates the further increase of the star formation density and the raw ionizing luminosity. We note that the maximum coincides with the epoch where we expect most of the hydrogen to be reionized.

An alternative source of ionizing radiation is in principle provided by AGNs. We assume a bolometric AGN luminosity described by

$$L_{\text{bol}}^{\text{AGN}} = (1 - \epsilon_f) \tilde{\epsilon}_r \dot{M}_{\text{BH}} c^2, \quad (4.2)$$

with a radiative efficiency of $\epsilon_r = 0.2$ and an energy fraction of $(1 - \epsilon_f) = 0.95$ available for radiation. The luminosity is converted into a rate of ionizing photons assuming a parameterized AGN SED [Korista et al., 1997] equal to

$$f^{\text{AGN}}(\nu) = \nu^{\alpha_{\text{UV}}} \exp\left(-\frac{h\nu}{kT_{\text{BB}}}\right) \exp\left(-\frac{10^{-2}\text{Ryd}}{h\nu}\right) + a\nu^{\alpha_x}, \quad (4.3)$$

with a suppression of the UV component at a temperature of $T_{\text{BB}} = 10^6$ K, a UV component slope of $\alpha_{\text{UV}} = -0.5$ and an X-ray component slope of $\alpha_x = -1$. To obtain an approximation for the maximum contribution to reionization, we assume an escape fraction of $f_{\text{esc,AGN}} = 1$. For comparison, we show the AGN ionizing luminosity as a dashed black line in Figure 4.3. The AGN contribution only becomes relevant at around $z = 6$, but by then most of the hydrogen must already be ionized, making it unlikely that AGNs are significantly contributing to the initial EoR transition. However, they might play a role in keeping the universe ionized at a later time, and almost certainly are important for completing helium reionization at lower redshift, thanks also to their harder spectrum. As we only study hydrogen reionization, in the following only stellar emission is considered as sources of ionizing photons.

4.3 Simulation results

An overview of the various reionization simulations carried out in this work is given in Table 4.1. To examine resolution dependences, we computed several of our models with grid resolutions of up to 1024^3 cells. We considered two different models with a time-variable escape fraction and contrasted them with one model with a fixed escape fraction. In order to assess the impact of different radiative transfer methods we performed most of our simulations both with our default cone-based approach as well as with the moment-based method with M1 closure.

The progress of reionization in different environments is visually shown in Figure 4.4, where we compare two regions around very massive halos with a more average

environment around a typical medium-sized halo, and an underdense region. The different projections show the four regions at six different output times. Reionization starts inside the most massive halos first, and then quickly ionizes the surrounding regions. Compared to such a high-density environment, the onset of reionization is considerably delayed around a medium mass halo. More drastically, the underdense region only begins to be reionized once the denser regions have almost completed their reionization transition. The visual impression is thus qualitatively consistent with an inside-out reionization scenario in which halos in high-density regions are affected first and lower density voids are reionized rather late, for the most part after overdense gas been reionized [Razoumov et al., 2002]. This contrasts with suggestions that low density regions are reionized quite early and only then the reionization fronts progress to ionize filaments and gas in halos [Gnedin, 2000].

4.3.1 Reionization history

In the upper panel of Figure 4.5, we show the volume weighted ionization fraction $1 - x_V$ as a function of time for three of our high-resolution radiative transfer calculations. We see a rapid, exponential rise at high redshift, and an approach to unity at around $z \simeq 6 - 8$. The end of reionization and the rapid phase transition to a reionized universe is better visible in displaying the neutral fraction x_V , which is also included in the figure. For comparison, we also show observational constraints derived by Fan et al. [2006b] from quasar absorption lines (symbols with error bars). Especially our model V1_1024_M1 reproduces the suggested end of reionization in this data quite well, although the residual neutral fraction comes out slightly low.

In the lower panel of Figure 4.5, we consider the evolution of the ratio between mass- and volume-weighted ionization fractions, $(1 - x_M) / (1 - x_V)$. This quantity is the average density of the ionized hydrogen compared to the average hydrogen density of the full box:

$$\frac{1 - x_M}{1 - x_V} = \frac{V_{\text{tot}} (1 - x_M) M_{\text{tot}}}{M_{\text{tot}} (1 - x_V) V_{\text{tot}}} = \frac{1}{\langle \rho \rangle_{\text{tot}}} \frac{M_{\text{ionized}}}{V_{\text{ionized}}} = \frac{\langle \rho \rangle_{\text{ionized}}}{\langle \rho \rangle_{\text{tot}}}. \quad (4.4)$$

This ratio stays at or above unity for all time, which can be interpreted as a signature of an inside-out character of reionization [Iliev et al., 2006b]. Overdense environments around our sources ionize first, so that the ionized volume is always overdense on average. Interestingly, the evolution of the mean overdensity of ionized regions with time also differs for our different escape fraction models. The run assuming a constant escape fraction model starts reionization later but then progresses somewhat more rapidly. This model maintains the highest value of $(1 - x_M) / (1 - x_V)$ for most of the simulated timespan. Here reionization is particularly biased to overdense regions and is stuck there for a comparatively long time, until the final reionization transition occurs on a short timescale and the IGM at mean density is ionized as well. Interestingly, even though the variable escape fraction models show some variety in the time of the onset of reionization and the remaining neutral fraction, the evolution of $(1 - x_M) / (1 - x_V)$ is still rather similar among these models. They

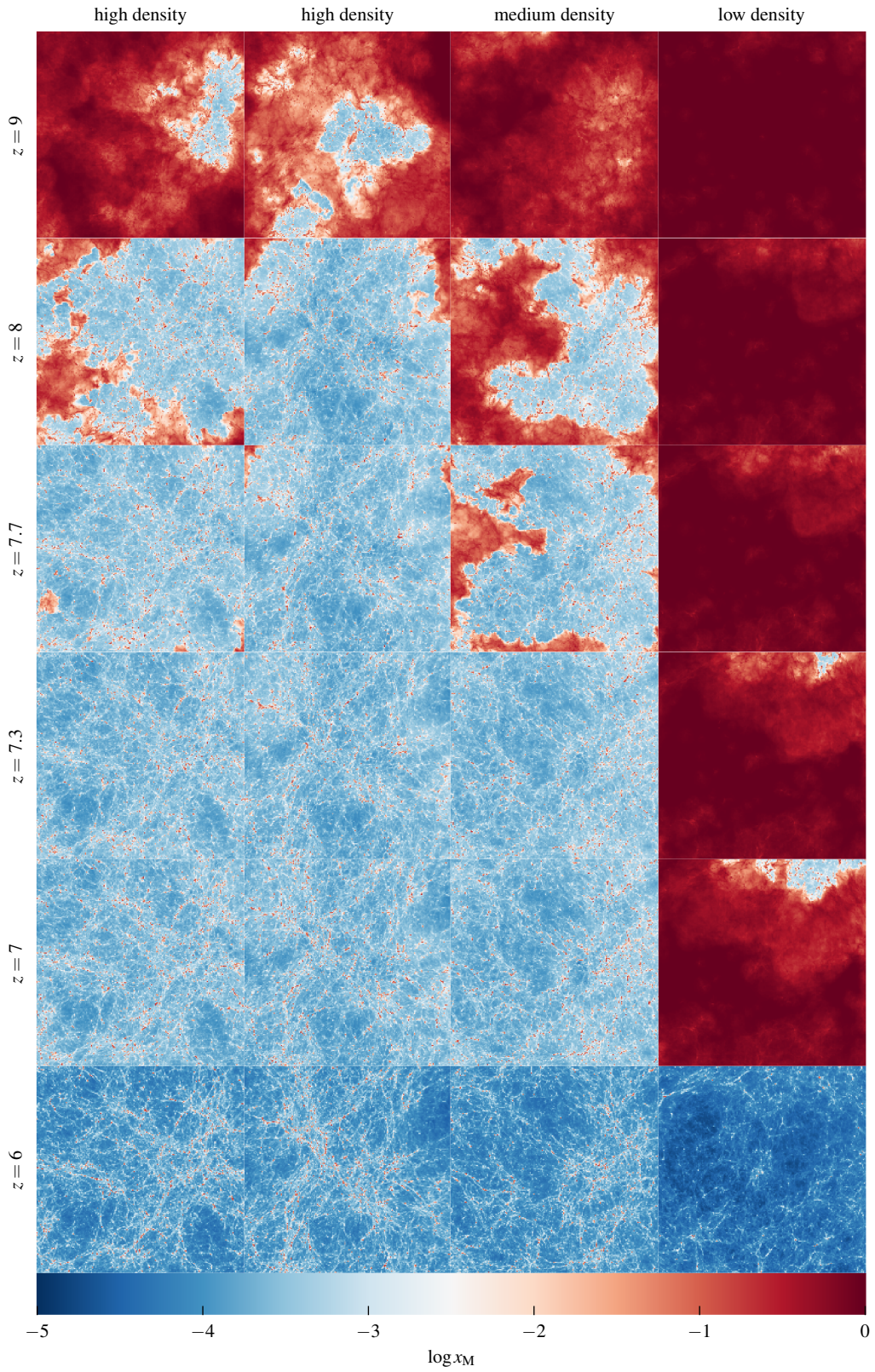


Figure 4.4: Progression of reionization as seen in the neutral hydrogen fraction in slices through selected sub-volumes in Illustris, each with a side-length of 21.3 cMpc. Each column shows the time evolution of a different, randomly selected environment in our V1_1024_M1 model; the two columns on the left correspond to an average density higher than the mean, the other columns have medium and low mean density, as labeled. Each row gives a different redshift, from $z = 9$ (top) to $z = 6$ (bottom).

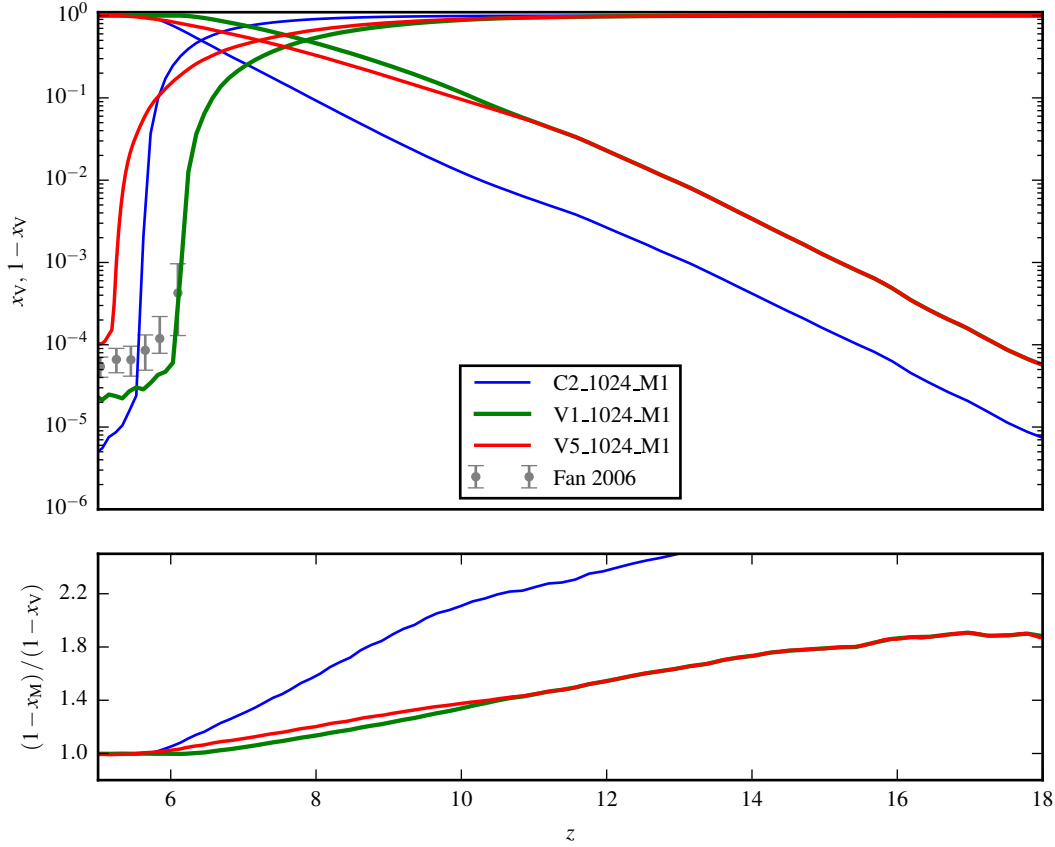


Figure 4.5: The ionization history for different escape fraction parameterizations. The upper panel shows the evolution of the volume weighted ionization fraction (solid lines rising to low redshift) and the neutral hydrogen fraction (lines dropping towards low redshift), as a function of redshift. For comparison, observational constraints by Fan et al. [2006b] are shown as symbols with error bars. The lower panel shows the ratio between mass- and volume-weighted ionization fractions $(1 - x_M)/(1 - x_V)$ for the different models.

begin reionization earlier and thus generally have low mean overdensities of the ionized volume at any given time.

That the character of the reionization process is best described as an inside out transition can be seen in more detail in Figure 4.6, where the time evolution of the average neutral fraction is shown for regions of a fixed given overdensity. Highly overdense regions start to become ionized quite early on, assisted by collisional ionization in virialized halos. As a result, the reionization process for high density regions is also considerably less sudden than for lower density gas. After reionization is essentially completed, the behaviour however reverses; now overdense regions show on average a final ionization degree that is considerably lower than for lower density regions. This can be understood as a result of the higher recombination rate in the denser regions, shifting the equilibrium value of the ionized fraction in a given UV

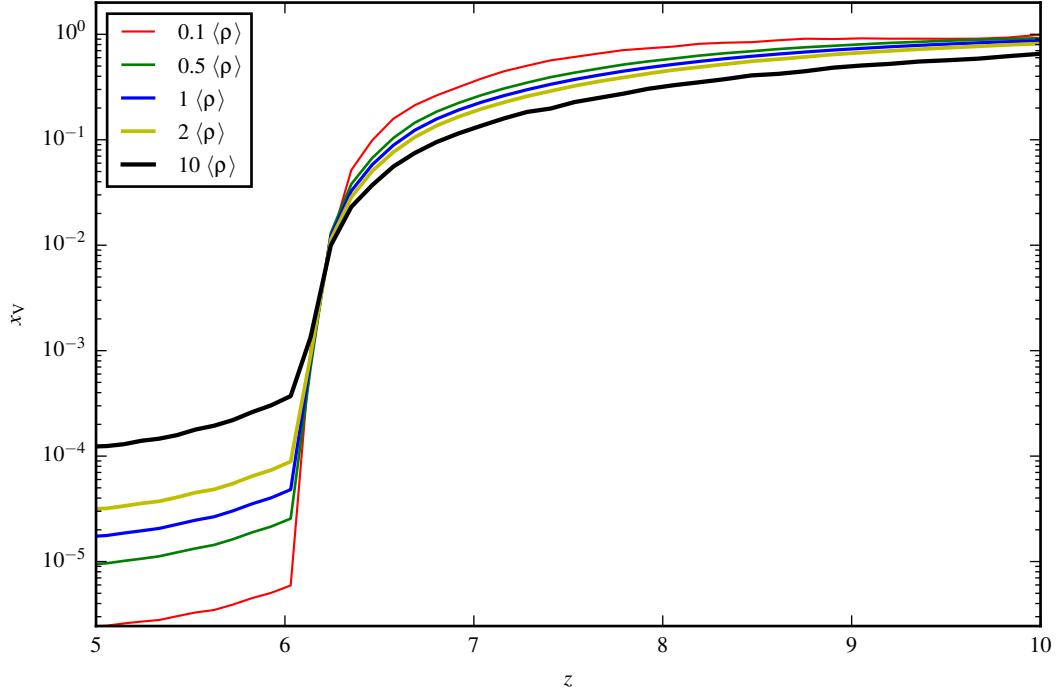


Figure 4.6: Time evolution of the neutral hydrogen fraction at given gas overdensities. Each of the lines shows the result for a small density range around a nominal comoving density threshold, as labeled, for our model V1_1024_M1. We see that the ionization of dense gas begins earlier, but this gas also ends up with a higher residual neutral fraction once reionization is completed.

background. Generally speaking, we find that denser regions start to ionize earlier but keep a higher neutral fraction than underdense regions.

Reionization is clearly not an instantaneous transition but requires a certain amount of time. It is hence interesting to characterize the epoch of reionization not only with a single redshift but also to ask how long the duration to a reionized universe takes. To this end we define the duration Δz as the interval in redshift space during which the volume-weighted neutral fraction drops from 80% to 20%. Our fiducial model V1_1024_M1 leads to an extent of $\Delta z = 2.28$ for the epoch of reionization, corresponding to a timespan of $\Delta t = 251.2$ Myr for this period. The V5_1024_M1 model shows a slightly longer duration of reionization with $\Delta z = 2.61$ and $\Delta t = 341.3$ Myr. Reionization lasts only over a span of $\Delta z = 1.13$ or $\Delta t = 190.0$ Myr in our C2_1024_M1 model. Thus our models with a variable escape fraction show a more extended epoch of reionization compared to the model with a constant escape fraction. In the models with a variable escape fraction, the ionizing luminosity is initially higher, but once most of the ionizing luminosity has become available, the variable escape fraction gradually begins to limit the amount of escaping UV radiation, resulting in a more prolonged epoch of reionization.

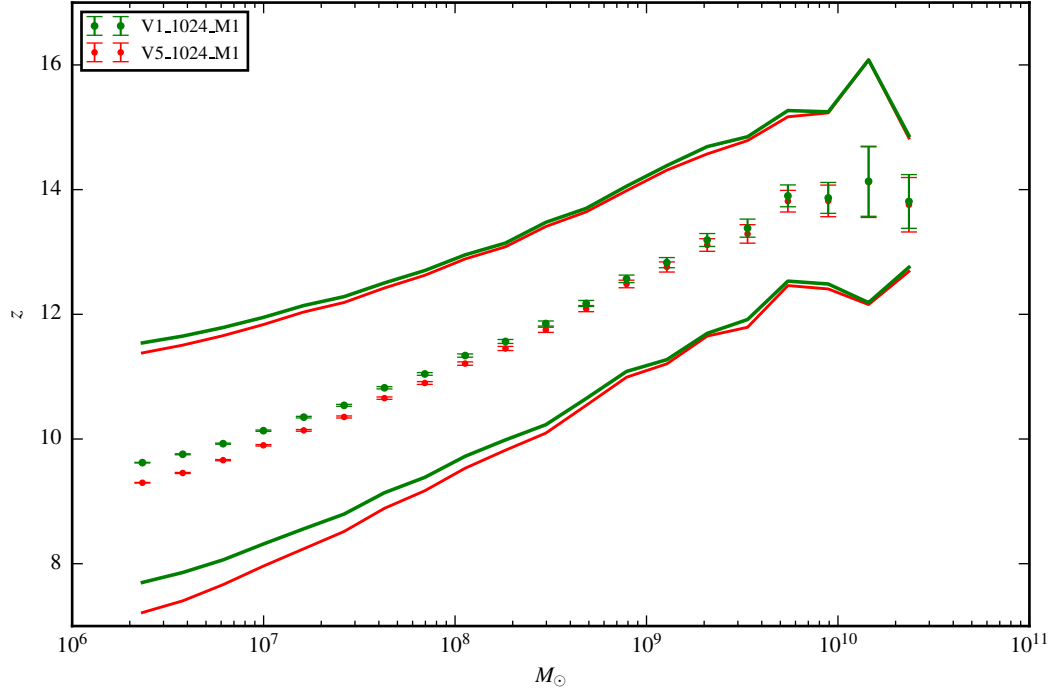


Figure 4.7: Mean reionization redshifts of the immediate surroundings of galaxies as a function of their $z = 6$ stellar masses for our highest resolution run of the V1 and V5 models. The symbols give the means in each mass bin, with the error bars showing the statistical error of the mean. The solid lines illustrate the $\pm 1\sigma$ variance in each mass bin.

One can also ask whether galaxies of different stellar mass are all ionized at the same time, or whether there are significant systematic trends of the mean reionization epoch as a function of galaxy size. To this end, we have considered the sample of all $z = 6$ galaxies in Illustris and then checked at what redshift the average ionized fraction in a sphere of radius 150 kpc around them (taking their $z = 6$ positions) reached 50% for the first time. The results of this analysis are shown in Figure 4.7, binned as a function of stellar mass. There is a clear trend for an earlier reionization around more massive galaxies. Interestingly, the spread in the reionization times slightly increases towards smaller stellar masses, indicating that dwarf galaxies are expected to show larger diversity in their reionization histories. Also, these low mass galaxies are more sensitive to the adopted parametrization of the escape fraction and tend to reionize later in our V5 model.

4.3.2 UV background

In Figure 4.8, we consider the time evolution of the volume averaged photoionization rate for models calculated with different escape fractions and grid resolutions, and compare to different models in the literature for the evolution of the cosmic UV

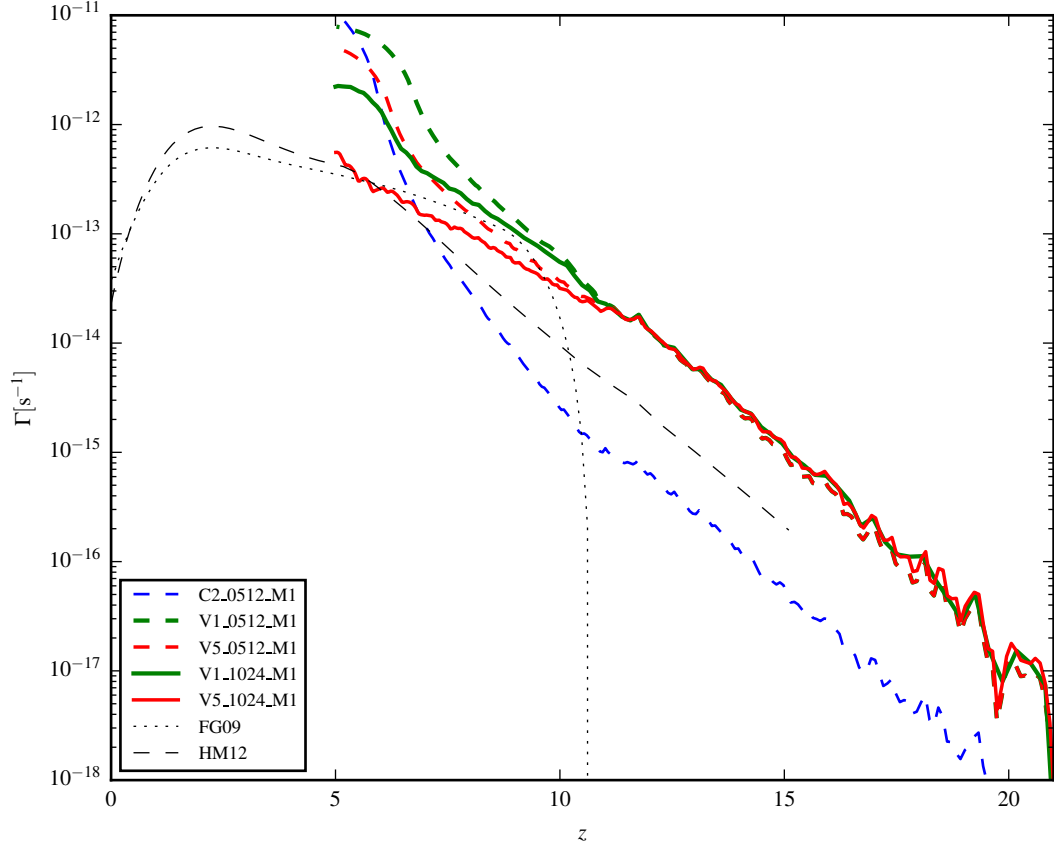


Figure 4.8: Average photoionization rate Γ as function of redshift for models calculated with different escape fractions and grid resolutions. For comparison, we also include two widely used theoretical models for the UV background evolution: FG09 [Faucher-Giguère et al., 2009, we show the updated version from Dec. 2011] and HM12 [Haardt and Madau, 2012]. The V5_1024_M1 model is in particularly good agreement with FG09, at least for $z < 10$.

background [Faucher-Giguère et al., 2009; Haardt and Madau, 2012]. At high redshift, the background builds up exponentially with redshift, similar to the growth of the volume weighted ionization fraction, with an overall amplitude that varies with the escape fraction model. Our variable escape fraction models and our fixed escape fraction model bracket the scenario of HM12. Interestingly, our scenario V5_1024_M1 follows the model of Faucher-Giguère et al. [2009] very closely, except that after reionization is completed, our calculations tend to overshoot the model predictions. We note that a very similar behaviour is also seen in the recent radiative transfer simulations of Pawlik et al. [2015], where this effect is even more pronounced. A more realistic variable escape fraction model than the rather simple parametrization employed might help resolving this issue.

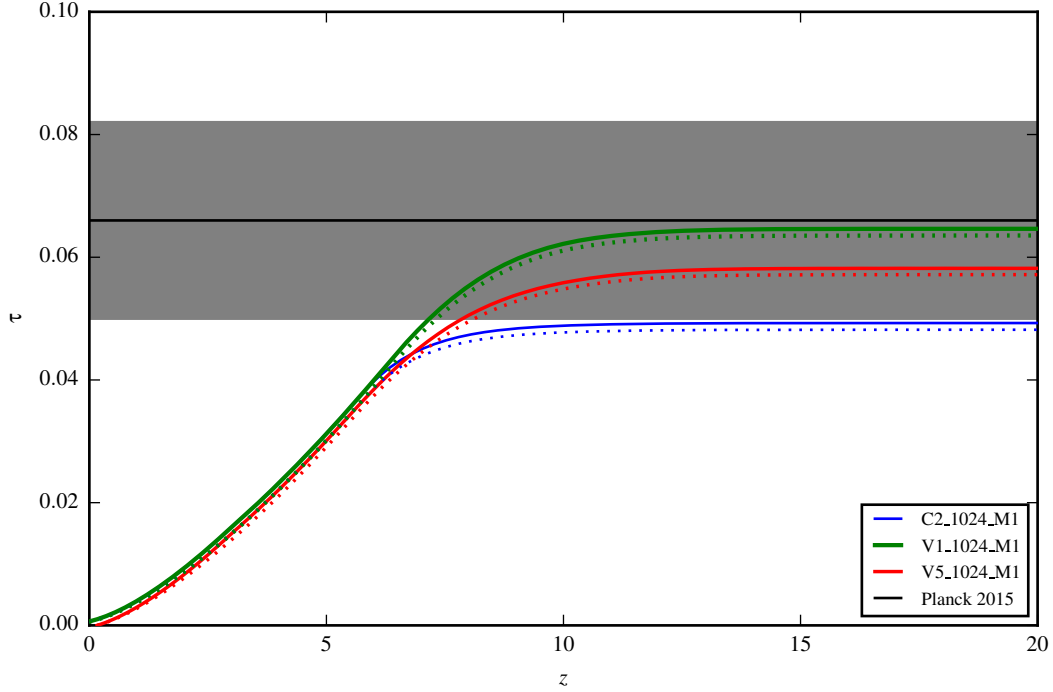


Figure 4.9: Cumulative optical depth for Thomson scattering on free electrons, integrated out to the redshift specified on the horizontal axis. Solid lines include electrons from doubly ionized helium (assuming that they contribute for $z < 3$), while dotted lines assume hydrogen and one helium electron only. The horizontal line with $\pm 1\sigma$ uncertainty region (shaded) marks the newest 2015 constraints $\tau = 0.066 \pm 0.016$ by the Planck Collaboration et al. [2015a]. Our fiducial model V1_1024_M1 is in very good agreement with optical depth inferred from these precision measurements of the CMB. Our other models lie slightly lower, however their value is still consistent. Interestingly, the previous determination by Planck based on their first 2013 data analysis had given a considerably higher value for τ . The tension with this result is now resolved.

4.3.3 Optical depth τ

Starting with the onset of reionization, CMB photons will Thomson scatter off the free electrons again. This effect can be quantified by measuring the cumulative optical depth τ seen by CMB photons along their path towards us. This optical depth is given by

$$\tau = c\sigma_{\text{th}} \int_{z_0}^0 n_e(z) \frac{dt}{dz} dz, \quad (4.5)$$

where σ_{th} is the Thomson cross section, and n_e the number density of free electrons. In this work, we only consider hydrogen reionization for simplicity. Given that the first ionization potential of helium is very close to the ionization potential of hydrogen,

we assume that HeII is created in proportion the HII. The free electron density is then given by

$$n_e = \left[1 + \frac{1 - X}{4X} \right] (1 - x_M) n_H \approx 1.079 (1 - x_M) n_H, \quad (4.6)$$

where $X = 0.76$ is the hydrogen mass fraction. At late times, helium reionization will eventually be completed, increasing the optical depth slightly compared to the above estimate. Adopting the common assumption that helium becomes doubly ionized at $z = 3$ [e.g. Iliev et al., 2005], the free electron density increases by $\Delta n_e = (1 - X)/(4X)(1 - x_M) n_H \simeq 0.079 (1 - x_M) n_H$ compared to the estimate above, and hence the optical is enlarged by

$$\Delta\tau = c \sigma_{\text{th}} \int_3^0 \Delta n_e(z) \frac{dt}{dz} dz = 0.0011, \quad (4.7)$$

which is a very small correction given the other uncertainties.

The optical depth τ for a specific reionization history can be converted into an effective reionization redshift z_{reion} assuming a fiducial scenario in which the reionization transition is instantaneous at this epoch. The latest WMAP9 results find a best-fit value of $\tau = 0.088 \pm 0.013$, corresponding to $z_{\text{reion}} = 10.5 \pm 1.1$ [Hinshaw et al., 2013], quite a bit lower than the value of $\tau = 0.17 \pm 0.08$ WMAP1 had initially estimated. The results of the PLANCK mission in its 2013 data release [Planck Collaboration et al., 2014] favour a very similar, slightly larger value for the optical depth, $\tau = 0.089 \pm 0.032$, corresponding to an even earlier reionization redshift of $z_{\text{reion}} = 10.8$. However, the latest PLANCK data release of 2015 [Planck Collaboration et al., 2015a] prefers a much lower optical depth of $\tau = 0.066 \pm 0.016$ and a corresponding redshift of reionization of $z_{\text{reion}} = 8.8_{-1.4}^{+1.7}$. A similar low optical depth of $\tau = 0.063 \pm 0.013$ has been found in Finkelstein et al. [2014] based on a UV luminosity function derived from Hubble Ultra Deep Field and Hubble Frontier Field data.

In Figure 4.9, we show the optical depth of our reionization simulations as a function of the integration redshift z for three of our models. The most recent 2015 constraint from PLANCK is shown as a horizontal line, together with the $\pm 1\sigma$ uncertainty region (shaded). Our models with a variable escape fraction are comfortably compatible within the error bars with the 2015 Planck results. Our fiducial model V1_1024_M1 predicts an optical depth of $\tau = 0.065$ which is in very good agreement with the most recent Planck 2015 data. However all of our other models prefer the low side of the range determined by Planck. Still, it is very promising that the former tension between galaxy formation simulations and optical depth inferred from CMB measurements seems nearly resolved with the 2015 Planck data. A similar finding has been reported in Robertson et al. [2015] based on Hubble observations of distant galaxies. Allowing for additional high redshift star formation could easily close the small remaining gap if needed, but we note that constraints from galaxy formation disfavour this solution. For example, Illustris already tends to overshoot estimates

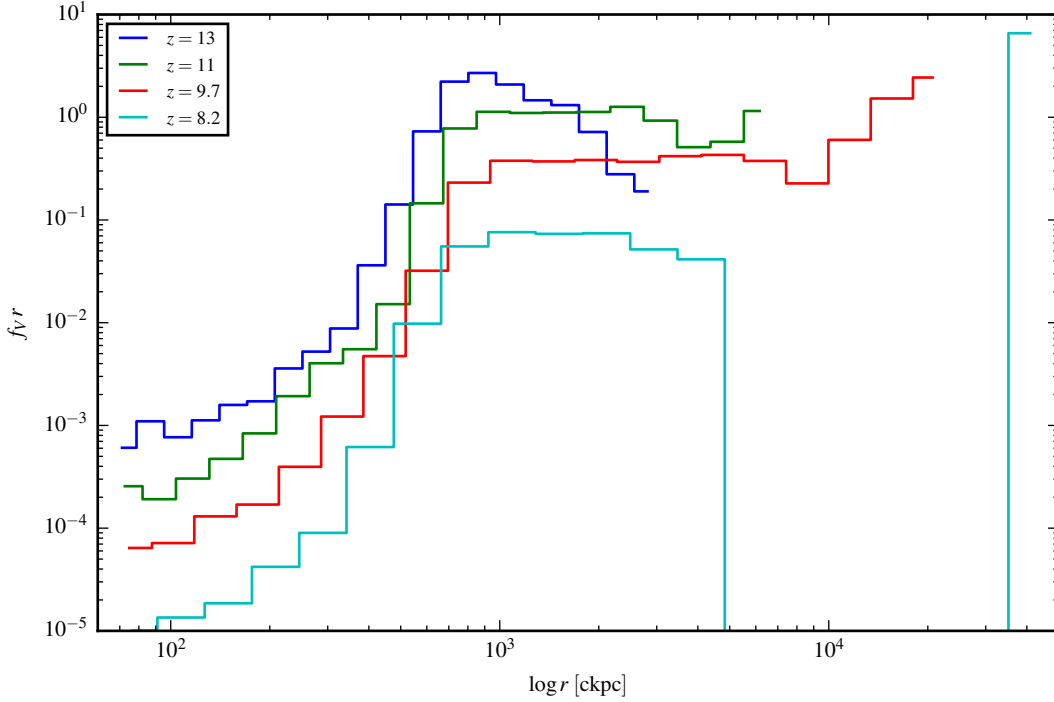


Figure 4.10: Distribution of the characteristics radius of ionized regions at four different redshifts, in our fiducial model V1_1024_M1. The integral over the distributions is normalized to unity for each of the measurements, and a horizontal line corresponds to equal volume fraction per logarithmic size interval. Initially, small bubbles dominate but over time the distribution shifts to ever larger bubbles until only one large region dominates.

for the stellar mass function of small galaxies, at late and early times alike [Genel et al., 2014; Vogelsberger et al., 2014b]. Resolving these problems seems to call for reduced high redshift star formation and not the opposite, highlighting the difficulty to reconcile high optical depths values from CMB experiments with detailed galaxy formation models.

4.3.4 Bubble size statistics

Mapping the epoch of reionization more directly than possible thus far, for example through 21cm imaging, is an exciting observational prospect. Once this becomes possible with future radio telescopes such as the SKA, quantitative measures of the geometry of the ionized regions, such as their topology, promise to be a powerful probe of theoretical models for reionization. Radiation transfer models like those calculated herein are the method of choice to make the required detailed predictions about how these morphological measures evolve in time. To illustrate this, we here compute a few basic statistical measures that quantify the number and size of ionized

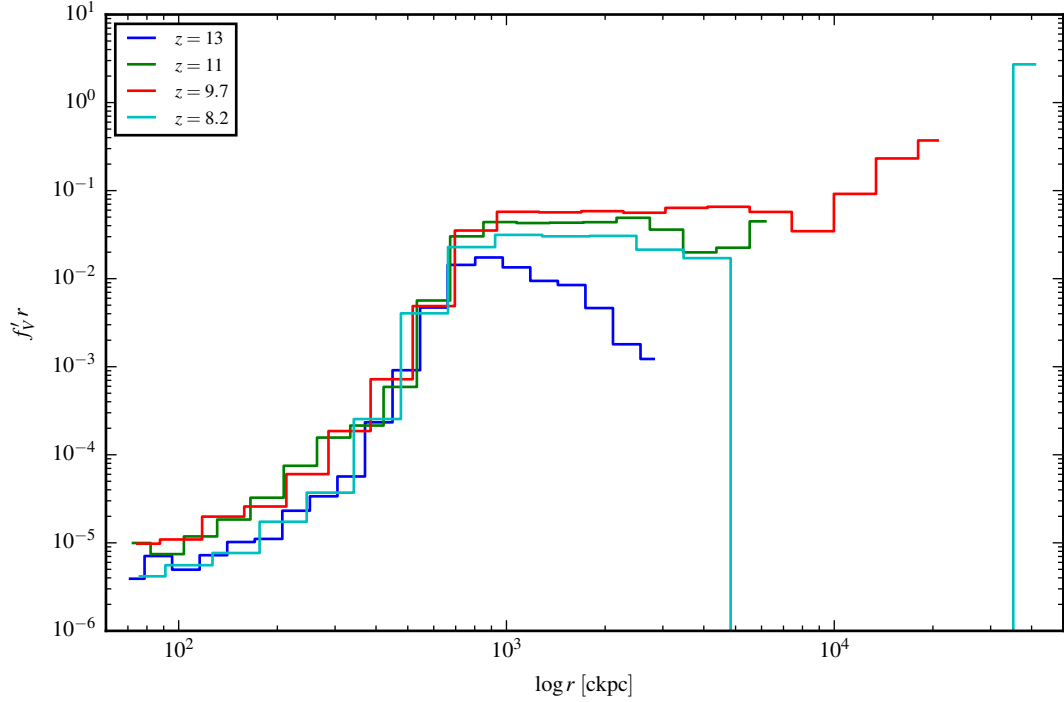


Figure 4.11: The same information as in Figure 4.10, except with a different normalization. Here the integral is normalized by the constant comoving box volume so that the area under the distributions gives the total ionized volume fraction. This is informative because the relative constancy of the size distributions for small bubble sizes suggests that the growing bubbles are replenished by new small bubbles just at the right rate to achieve this balance. Interestingly, the volume occupied by small bubbles stays hence roughly the same for the whole duration of reionization, even slightly beyond bubble percolation where a dominating single large ionized region forms.

regions as a function of time, which may also serve as a useful comparison against other theoretical reionization models.

We start by tagging cells as ionized if their ionization fraction exceeds $1 - x_M > 0.5$. Based on the resulting grid of binary values, ionized regions are then identified using a friends-of-friends algorithm that links adjacent ionized cells [Chardin et al., 2012; Iliev et al., 2006b]. We let cells belong to the same group if they share at least one corner, or in other words, if any of the 26 neighbours of an ionized cell is also ionized, both cells are put into the same group. For each ionized island identified in this way, we compute an effective radius as $r = [3/(4\pi V)]^{1/3}$, where V is the cumulative volume of the cells making up the group. Finally, we consider the distribution function f_V of the ionized volume fraction contained in regions of a given bubble radius.

In Figure 4.10, we show the resulting distribution function when the convention of Zahn et al. [2007] is followed and the distribution is normalized such that

$$\int f_V r \, d \log r = 1, \quad (4.8)$$

i.e. we only consider the ionized volume of the box. The results show that at early times, when only a small fraction of the volume is ionized, the ionized volume is comprised of disjoint regions of characteristic size $r \simeq 2$ cMpc. While reionization progresses, ever larger bubbles appear, with a flat distribution as a function of size, i.e. roughly the same amount of ionized volume is contained per logarithmic interval in bubble size, up to bubble sizes of order $r \simeq 20$ cMpc. Eventually, the bubbles start to percolate and one dominating region containing a substantial fraction of the simulation volume is formed ($z = 8.2$). There is then still a population of smaller ionized regions left, with a constant volume fraction per unit $\log r$ over a dynamic range of about ~ 5 in size.

An alternative normalization for the size distribution is used in Gnedin and Kaurov [2014], who consider the whole box thus that integrating over f_V gives the ionized volume fraction:

$$\int f'_V r \, d \log r = 1 - x_V. \quad (4.9)$$

It is instructive to plot the corresponding distributions also with this normalization, which is shown in Figure 4.11. Now the area under the distribution function grows with redshift, reflecting the increase of the ionized volume fraction. Interestingly, we see in this representation that the bubble size distribution is fairly constant with time, especially for the small bubble sizes. Even though these bubbles grow individually in size with time, the fact that the abundance of bubbles of a given size stays approximately constant in time (once the first bubbles of this size have formed), suggests that small bubbles are reformed just at the right rate to compensate for the loss of bubbles of a given size due to the growth or coalescence of bubbles.

4.3.5 Distribution function of neutral volume fraction

In Figure 4.12, we show the distribution function $f(x_V) = dV/dx_V$ of the volume fraction that is found at a given neutral fraction. We compare our two different variable reionization scenarios, in the form of V1_1024_M1 (top panel) and V5_1024_M1 (bottom panel), and give results for different redshifts in each case. Note that we plot $x_V f(x_V)$ on the vertical axis versus the log of x_V , i.e. the area under the curves is proportional to the volume fraction at the corresponding range of neutral fractions.

Progress in reionization is associated with a large increase in the volume fraction found at low neutral fractions, as is of course expected. Interestingly, the differential distribution of volume at a given neutral fraction is however fairly broad while reionization is not completed, with a peak at a characteristic neutral fraction that shifts progressively to lower values. For example, at redshifts $z \simeq 11$, most of the volume is either still neutral or at a neutral fraction of $x_V \sim 10^{-3}$. At around redshift $z \sim 7$, the characteristic neutral fraction where most of the volume is found has dropped to $x_V \sim 10^{-4}$. Finally, post reionization, the two models start to differ more prominently. Here V1_1024_M1 shows a low neutral fraction of $x_V \sim 10^{-5}$ or lower for most of its volume, which corresponds also to the strong rise in the predicted UV

4 Hydrogen Reionization in the Illustris Universe

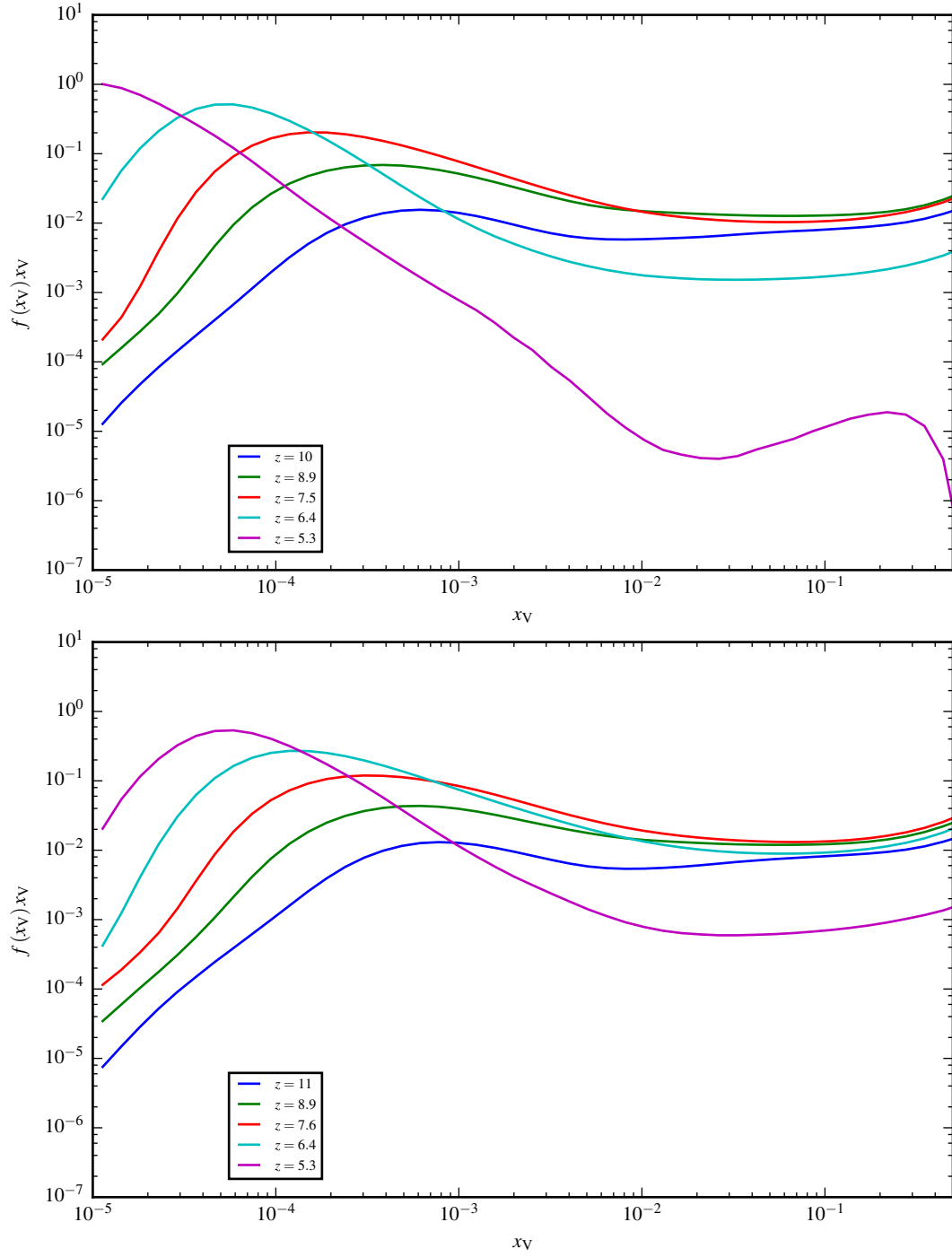


Figure 4.12: Degree of ionization level PDFs at different redshifts. The top panel shows the results for the V1_1024_M1 model, whereas the bottom panel is for the V5_1024_M1 model. Compare to Figure 4.8, where the V1 run shows a strong upturn in the UV flux, which is here expressed as a shift of ionized cells down to $n_{\text{HI}} = 10^{-5}$ at around $z = 5.3$, which does not happen in the V5 run.

background seen in this model in Figure 4.8. In contrast, the model V5_1024_M1, which shows good agreement with the UV background model of Faucher-Giguère et al. [2009] at this epoch, yields a markedly different distribution of the neutral fraction, with most of the volume having neutral fractions around $x_V \simeq 5 \times 10^{-5}$.

4.4 Caveats and discussion

The accuracy and reliability of our results is influenced by many numerical aspects as well as physical uncertainties. In the following we discuss a number of these aspects, focusing primarily on those pertaining to the radiative transfer modelling itself. We note however that there are in principle additional uncertainties related, for example, to the treatment of star formation and the associated feedback processes in the underlying Illustris simulation, or to the cosmological background model that we use. These are arguably subdominant compared to the uncertainties related to the reionization calculation itself (such as escape fraction, radiative transfer solver, etc.), and in any case are beyond the scope of this paper [a discussion of the uncertainties in the galaxy formation model can be found in Vogelsberger et al., 2014b].

4.4.1 Reionization feedback

Due to the fact that we simulate reionization only in post-processing, any back reaction onto the gas due to photoionization heating and potentially radiation pressure is not taken into account self-consistently. The Illustris simulation assumes a uniform global UV background, hence the *average* back reaction on star formation due to photo-ionization is approximately accounted for, but any local modulation of the corresponding effects is of course ignored. This limitation could only be overcome by dynamically coupling the radiative transfer solver to a hydrodynamical code and doing full radiation-hydrodynamics simulations of galaxy formation. Recently, impressive progress has been made in this direction [Gnedin, 2014; Gnedin and Kaurov, 2014; Pawlik et al., 2015], but the achieved cosmological volumes are still severely limited due to the demanding computational cost of radiative transfer, and in general, these calculations have not been evolved to redshift $z = 0$, thus it is unclear whether they are successfully reproducing the observed galaxy population.

Besides photo-heating, the ionizing radiation of young stars could also exert significant feedback effects through radiation pressure, particularly in dusty gas where infrared radiation may be trapped [Agertz et al., 2013; Hopkins et al., 2012; Murray et al., 2010]. However, the effectiveness of this mechanism is debated, with a number of recent studies arguing that photo-heating is likely the dominant feedback channel on the scale of galaxies, with radiation pressure being comparatively unimportant [Rosdahl et al., 2015; Sales et al., 2014]. We thus consider the omission of radiation pressure effects in our reionization calculations to be comparatively unimportant.

4.4.2 Moment-based vs cone-based RT method

Our radiative transfer implementation supports two different transport methods, allowing us to compare them against each other with no changes in any other aspect of the modelling. In the case of the cone-based method, we have to store and process 48 radiation intensity fields, one for each advection direction. On the other hand, the moment-based M1 scheme only requires 4 fields, one for the photon number density and 3 for the flux vector. This difference makes the cone-based advection scheme much more expensive in terms of computational cost as well as in terms of (GPU) memory requirements.

If we compare the ionization histories predicted by these different radiative transfer methods in terms of the ionized volume fraction, no appreciable differences are detected. In fact, the agreement of the evolution of the ionized volume fractions is so good that we refrain from showing the corresponding comparison in a dedicated plot. But this consistency is perhaps not too surprising. The ionization history mainly depends on the source population that injects ionizing photons, as well as on the density evolution of the gas, as the latter sensitively determines the recombination rate. Given that the photon injection rates and the density structure are exactly equal in our comparison, and given the fact that both radiative transfer algorithms are manifestly photon conserving, any difference between the cone-based and the M1-closure methods can only be induced by differences in the photon transport directions. These are apparently subtle enough that they do not matter much for global statistics of the reionization transition.

However, despite this good agreement in global averages, the two methods still show differences in the detailed morphology of the ionized bubbles when examined in detail. In Figure 4.13, we compare the morphology of the ionized regions around a typical galaxy at redshifts $z = 8$ and $z = 8.5$. While there is clearly a great deal of similarity, the detailed locations of the ionization fronts differ substantially, highlighting that the radiative transfer solvers do not behave identically after all. This is also borne out by a higher order quantitative comparison of the neutral hydrogen fraction fields predicted by the two methods. This can for example be done by computing the mass-weighted standard deviation of the difference between the neutral hydrogen densities obtained by our two radiative transfer schemes:

$$v = \text{var}(\rho(x_{\text{M1}} - x_{\text{CONE}})) / \langle \rho \rangle. \quad (4.10)$$

For our V1_0512 models, we find that this quantity rises with decreasing redshift until a maximum of $v = 0.2$ is reached at $z = 7.5$. Afterwards, the full volume is quickly reionized and the variance of the difference field rapidly declines again. We note that the cone-based method should be the more accurate approach in this comparison, as it can avoid certain inaccuracies of the M1 approach, in particular when the ionization bubbles of two or more sources overlap.

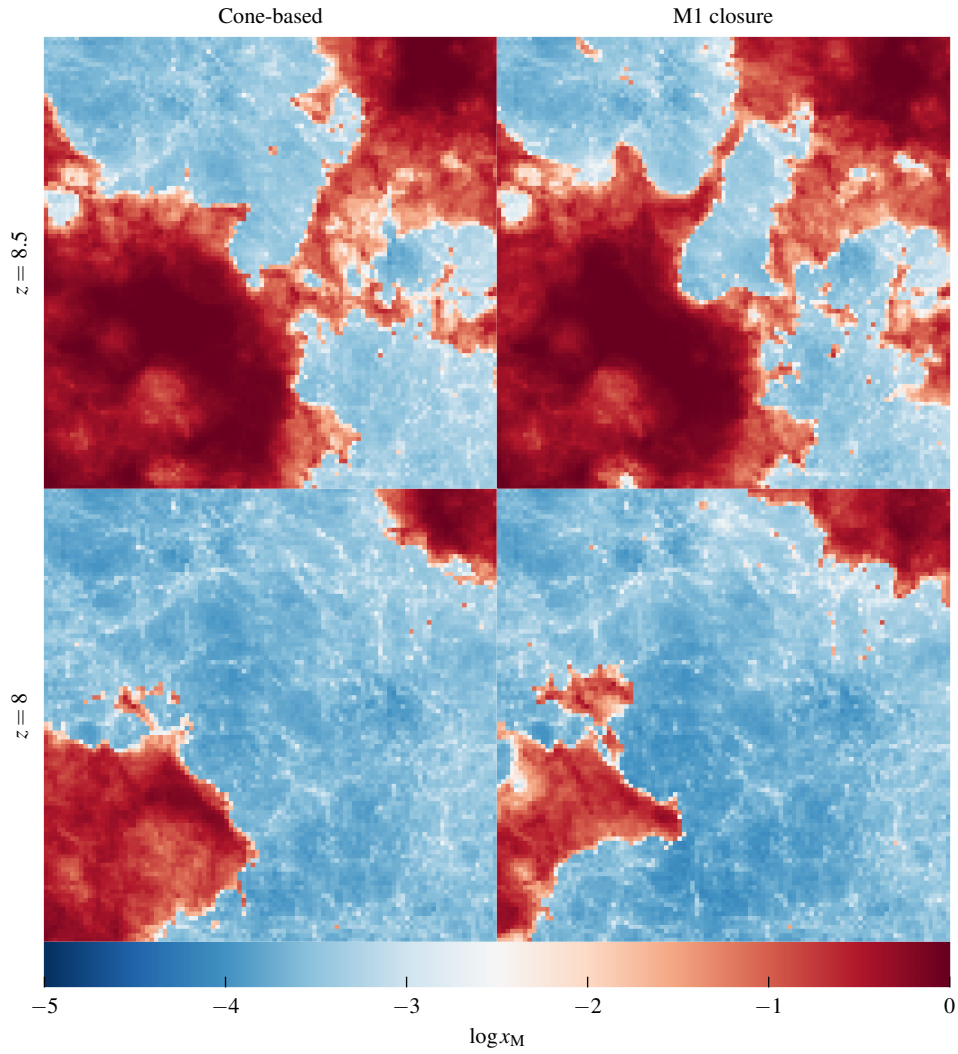


Figure 4.13: Visual comparison of our two different radiation advection methods at two instances in time. All panels show a thin slice through the box with a side length of 21.3 cMpc. The top row compares the neutral hydrogen fraction at $z = 8.5$ for the cone-based method (left) and the moment-based method with M1 closure (right). Similarly, the bottom row shows this comparison for redshift $z = 8$.

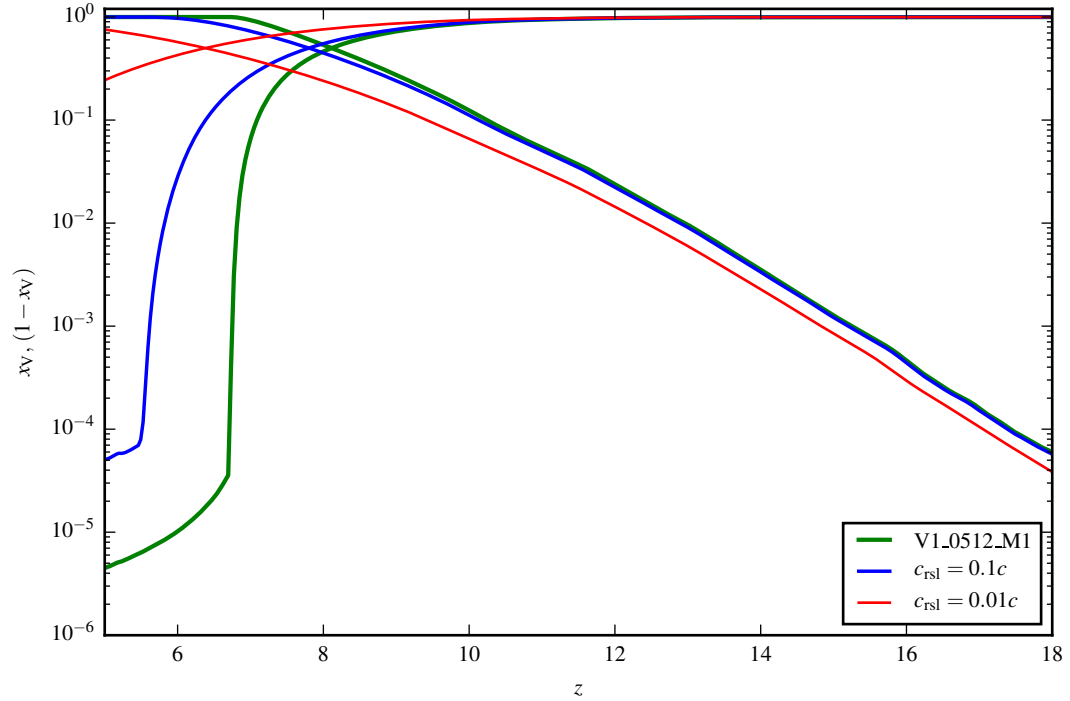


Figure 4.14: Impact of the reduced speed of light approximation on the evolution of the neutral and ionized volume fractions. Reducing the speed of light by a factor of 10 (blue line) or 100 (red line) relative to our default calculation with a physical speed of light (green line) causes a later reionization of the universe.

4.4.3 How accurate is the reduced speed of light approximation?

As long as the medium is dense enough, the propagation speed of the ionization fronts is determined by the rate at which new ionizing photons arrive at the edge of neutral gas, and not how fast they get there. This motivates the idea of the so-called reduced speed of light approximation [Aubert and Teyssier, 2008; Gnedin and Abel, 2001], in which the physical value of c is artificially reduced. The computational advantage of a reduced speed of light is that a much larger Courant time step is allowed in schemes where photon transport is followed with explicit time integration. Rosdahl et al. [2013] report that the reduced speed of light approximation describes the solution of Strömberg sphere well after an effective crossing time $t_{\text{cross}} = r_S/c$, where r_S is the radius of the corresponding Strömberg sphere and c the (reduced) speed of light. Before $t_{\text{cross}} = r_S/c$, however, the numerical solution necessarily always falls behind the correct one. Considering the relevant time scales that have to be resolved in cosmic reionization, this yields a criterium for the maximum allowed reduction of the speed of light. The conclusion of Rosdahl et al. [2013] is that there is not much room for applying the reduced speed of light approximation if accurate reionization simulations of the IGM are desired.

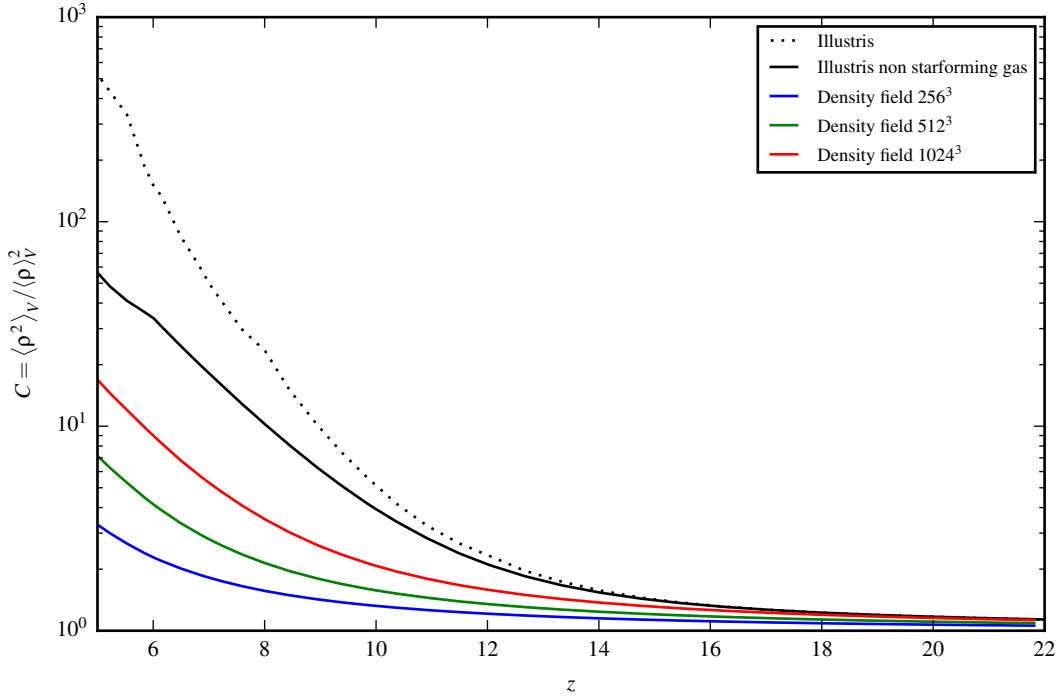


Figure 4.15: Clumping factor of the gas computed in different ways. The upper solid line shows the intrinsic clumping factor of all non star-forming gas (with density below the star formation threshold), based on the Voronoi tessellation of the Illustris simulation volume. The dotted line gives the intrinsic clumping factor of all the gas in the simulation. For comparison, we also show the clumping factor of all the non star-forming gas when this is obtained for different mesh resolutions after mapping the simulation volume to a grid with fixed spatial resolution.

It is interesting to use our independent radiative transfer code to check this assessment. In Figure 4.14, we show the impact of the reduced speed of light on the obtained reionization history, based on a reduction of the physical speed of light by factors of 10 or 100, respectively. Consistently with the findings of Rosdahl et al. [2013], the reduction of the speed of light leads to a significant delay in the resulting epoch of reionization, amounting to $\Delta z \sim 1 - 1.5$ for the factor of 10 reduction, and much larger for a factor of 100. The size of this error unfortunately implies that this numerical trick can induce unacceptably large distortions in the reionization predictions, hence we have refrained from using it throughout the study.

4.4.4 Clumping factors

The degree of gas clumping is a critical factor in models of reionization, as it directly determines the recombination rate and hence the amount of photons required to reionize the universe and to keep it ionized. Full hydrodynamical simulations of galaxy formation are a particularly powerful tool to realistically predict the non-linear

4 Hydrogen Reionization in the Illustris Universe

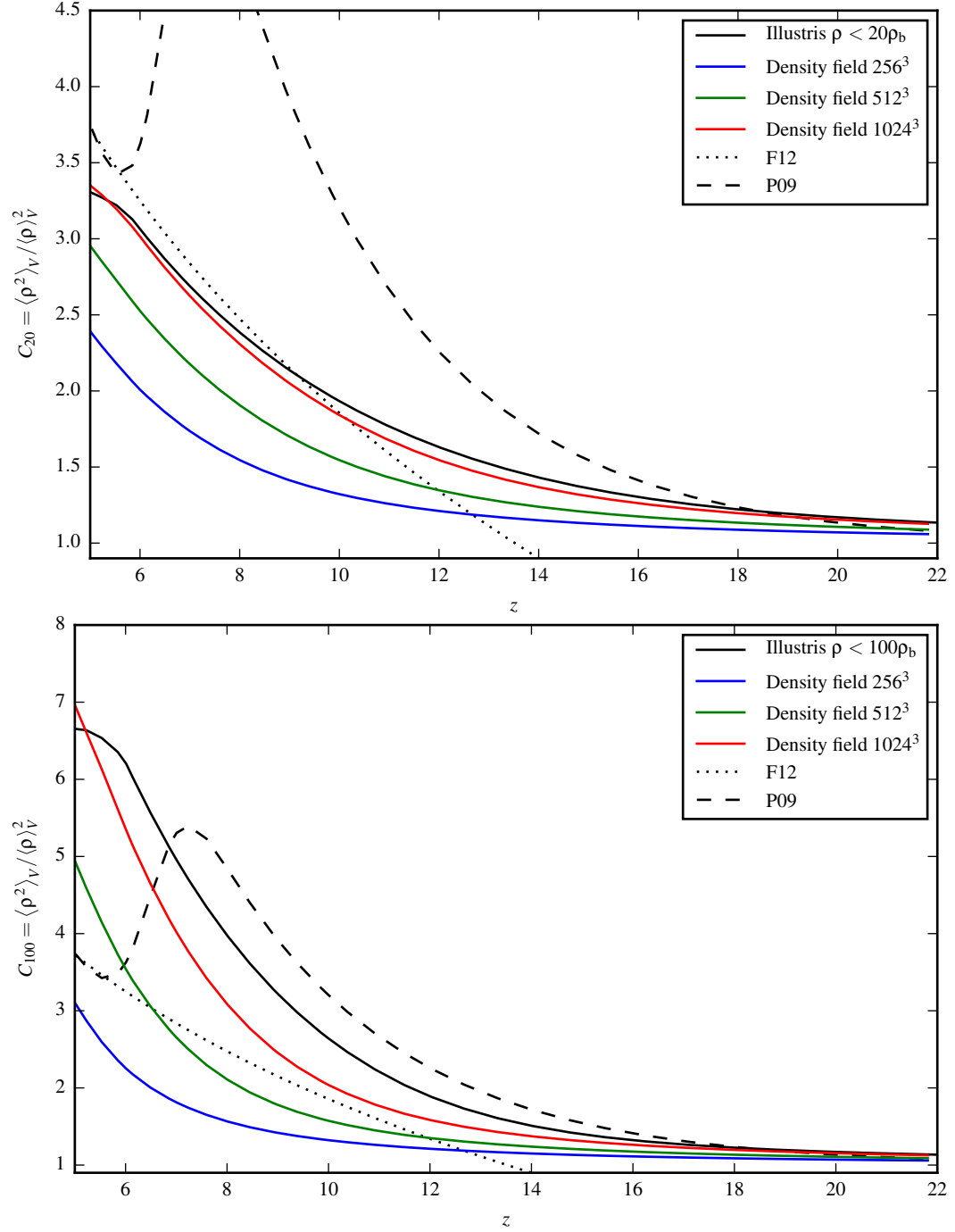


Figure 4.16: Gas clumping factors measured for gas below a certain characteristic gas overdensity. The top panel shows C_{20} , with the solid black line giving the result for the actual Voronoi tessellation used in the Illustris simulation for the hydrodynamical calculations. The other solid lines give the corresponding result for the binned density field when grids with resolution from 256^3 to 1024^3 are used, as labeled. The lower panel gives the same results for C_{100} , where instead a density threshold of 100 times the mean baryonic density is adopted. For reference, we also show fitting models by Finlator et al. [2012, F12] and [Pawlik et al., 2009, P09], which give the clumping factor of ionized gas or gas below a overdensity threshold of 100 (their $z \sim 7.5$ reionization case), respectively.

density structure of the gas, and hence to quantify the gas clumping. In Figure 4.15, we show the *full* clumping factor C of all the gas, defined in the standard way as

$$C = \frac{\langle \rho^2 \rangle}{\langle \rho \rangle^2}, \quad (4.11)$$

where the averages are volume averages for the full simulation box. The black lines represent the clumping factor obtained directly from the Voronoi cells of the underlying Illustris simulation, which is hence accounting for all structure resolved by the more than 6 billion cells of the simulation. We give results for the complete density field (dotted line) as well as for cells constrained to not lie on the effective equation of state of star forming gas (solid black line). The former result includes the collapsed gas that corresponds to the ISM and is star-forming, whereas in the latter this phase is excluded. The clumping factor is obviously much higher when this star-forming gas is included, but as the sub-grid model used by Illustris glosses over the true multi-phase nature of the ISM, the resulting clumping factor for all the gas is still an underestimate. However, we are here really only interested in the non-starforming gas, because the recombinations and absorptions inside the star forming regions are collectively accounted for by the escape fraction, which in part may be viewed as parameterizing our ignorance of the detailed gas structure on ISM scales.

The solid red, green and blue lines in Figure 4.15 show the clumping factor of all gas after binning it on radiation transfer grids with different resolution. Clearly, even for the 1024^3 grid we lose almost a factor of two in the total clumping due to the smoothing of this grid. However, as cosmic reionization is a volume filling process and the densest gas occupies only a tiny fraction of the value, it makes more sense to refer the escape fraction to a somewhat lower density threshold than the star-formation threshold. We are hence really interested in the clumping factor of gas up to some limited overdensity value, for example up to 20 or 100 times the mean baryonic density. Since both of these fiducial values have been used in the literature, we show in Figure 4.16 our results for C_{20} and C_{100} (in the top and bottom panels, respectively), where only gas cells which have a density of at most $20 \times \rho_b$ or $100 \times \rho_b$ have been included, respectively, with $\rho_b = \Omega_b \rho_{\text{crit}}$ denoting the mean baryon density. As before, we show results for the underlying Voronoi tessellation as well as reionization grids between 256^3 to 1024^3 resolutions. Note that in these plots a linear scale for the clumping factor has been used.

Our high resolution radiative transfer grid under-predicts the C_{20} clumping a bit due to the smoothing effects of the binning, but the effect is minor. The situation is a bit worse if one also wants to get the correct clumping factor for gas up to an overdensity of 100. Here some of this additional clumping is not resolved by the 1024^3 grid, as the results in the bottom panel of Figure 4.16 show. Given the trend with increasing resolution, using a 2048^3 grid instead (which we unfortunately cannot carry out due to memory constraints on the GPU system we have presently access to) should however be able to fully recover the C_{100} clumping of this gas. As we

discuss in more detail below, this resolution problem for the C_{100} quantity affects cosmic reionization however only mildly and is hence comparatively benign.

It is interesting to compare our clumping factors with those inferred from other works. Finlator et al. [2012] has pointed out that different definitions of the clumping factor can produce substantial differences in the results. It is thus important to base any such comparison on the same definition, which sometimes corresponds to considering the clumping of all the gas below a certain density threshold (to separate collapsed and diffuse gas), or to restricting the evaluation of the clumping factor to ionized gas. Note that the latter depends both on the detailed reionization model and the gas distribution. To get a sense of how well the gas distributions compare, it is thus arguably best to compare the total gas clumping factor. For the Illustris simulation at $z = 8$, we measure for the clumping of the non-starforming gas 10.2, slightly higher than the value reported by Finlator et al. [2012]. However, our value is significantly higher than the total gas clumping factor of $C \sim 3$ at $z = 8$ reported by Jeon-Daniel et al. [2014], which makes it considerably easier to achieve reionization in their model. When the baryon density is restricted to lie below an overdensity of 100, we find a clumping factor of about 4 at $z = 8$, somewhat larger than what was found in Pawlik et al. [2009] for their models reionizing at or before $z = 9$, but a bit lower than their model reionizing at $z = 7.5$. For a yet lower overdensity threshold of 20, Wise et al. [2014] report a value of 6.5, which is above our measurement of $\simeq 2.4$ for C_{20} at redshift $z = 8$. This likely reflects the higher mass resolution of their simulation, which has a boxsize of just 1 Mpc, but it could also be affected by the different feedback models in the two simulations.

4.4.5 Spatial resolution and convergence

Because the recombination rate depends nonlinearly on the density in a cell, the smoothing of density fluctuations (for example as a result of binning) causes an underestimate of recombination events and hence biases reionization towards higher redshift. Our results for the clumping factor indicate that our radiative transfer calculations clearly suffer from this effect to some degree. However, it is not obvious whether the size of the bias is quantitatively significant in the end, because the clumping of the volume-filling gas (which has comparatively low overdensity) is captured well by our high-resolution grid. If reionization would mostly occur ‘outside-in’, with low density regions ionized early, one may hope that this is already sufficient for allowing converged predictions of the reionization redshift even if density peaks are washed out. However, given that our results have confirmed that dense regions tend to be ionized earlier, this may largely be wishful thinking.

Indeed, this is borne out by our convergence tests for the reionization history of models V1 and V5 shown in Figure 4.17. Evidently, as the resolution of the grid for the radiative transfer simulation is increased, reionization happens progressively somewhat later, as a result of the smaller degree of suppression of the true underlying clumpiness of the gas. This prevents us from achieving a formal numerical convergence for our reionization histories. We note however that full radiation hydrodynamics

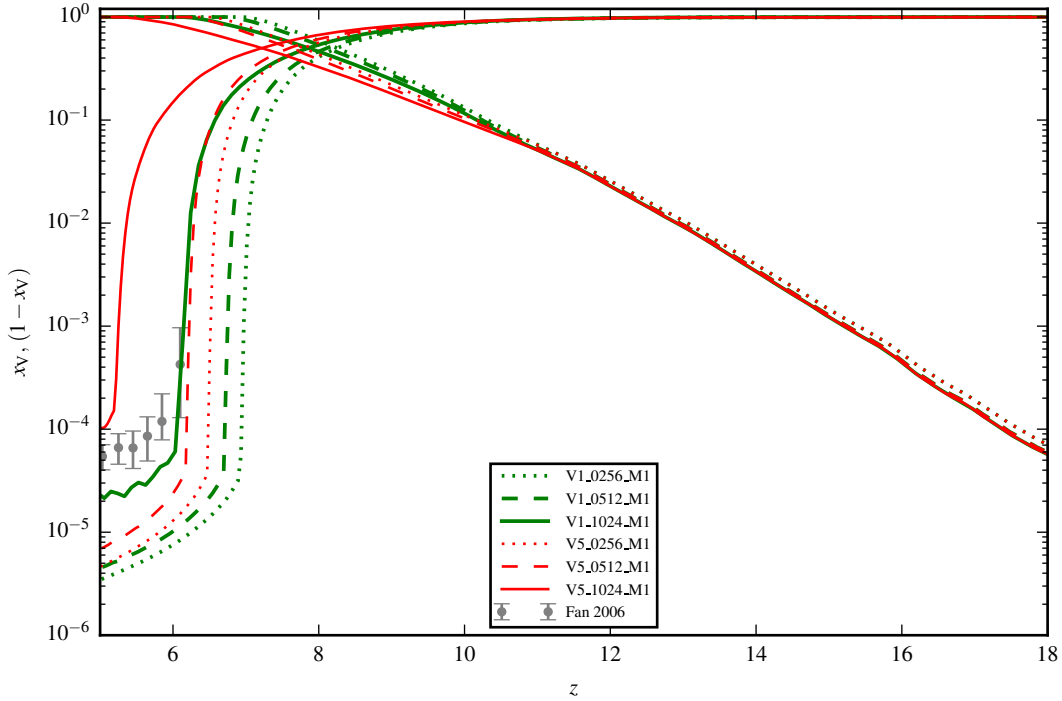


Figure 4.17: Convergence study for the neutral and ionized volume fractions for our reionization simulations based on the M1 method. The green and red lines are for the two different variable escape fraction models we considered. There are significant residual trends with resolution due to the smoothing effects a coarse grid has on the clumpy gas distribution. As a result, the highest resolution simulation tends to reionize slightly later than predicted by calculations at lower resolution.

simulations will counter this drift by physically inducing a reduction of the clumpiness of the gas [Pawlik et al., 2009], due to the photo-heating and the resulting pressure smoothing. This effect is not included in our simulations prior to redshift $z = 6$, when reionization happens due to the externally imposed UV background. We thus expect that our 1024^3 and 512^3 grids may well bracket the true behaviour of the clumping in a self-consistent simulation with full radiation hydrodynamics. This then also means that a 2048^3 calculation *without* taking this effect into account may well produce a less accurate result than the 1024^3 grid we used.

4.4.6 Comparison with a global reionization model

Instead of doing a full 3D radiative transfer calculation, the global evolution of the volume-weighted ionization fraction can be estimated with a simple model that considers only the global balance of the average ionization and recombination rates

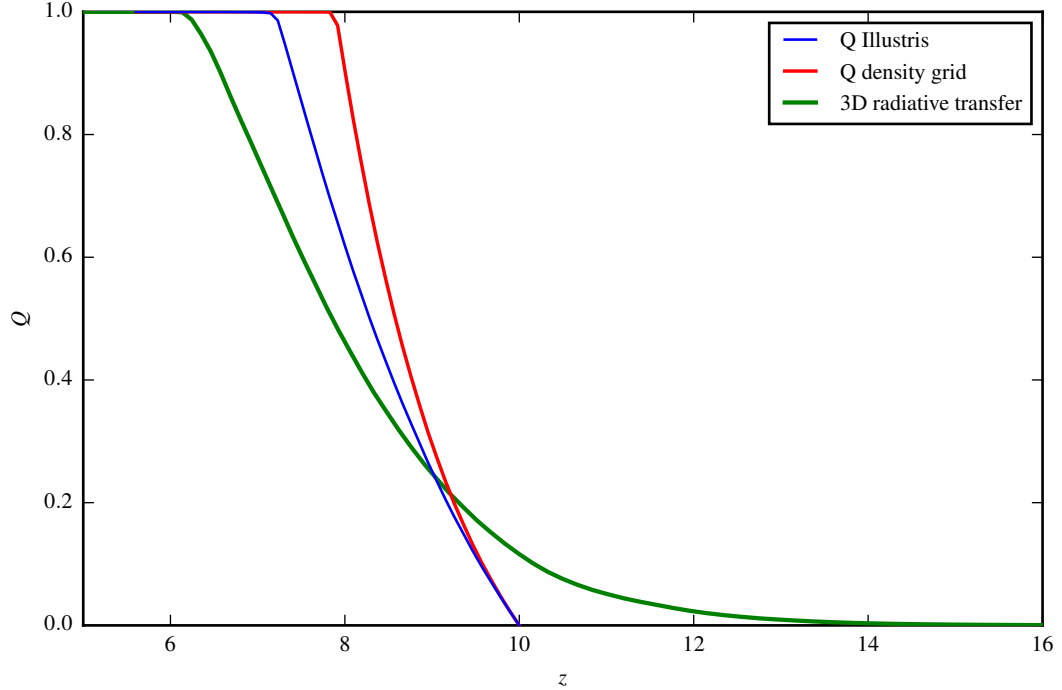


Figure 4.18: Comparison of different approaches for calculating the redshift evolution of the volume filling factor Q of ionized regions. The blue line assumes an evolution of the gas clumping factor according to the non star-forming gas of the Illustris simulation. The red line instead uses the effective clumping factor of the binned density field used for the reionization simulations. Finally, the evolution of the volume-weighted ionization fraction for our self-consistent radiative transfer simulation (V1_1024_M1) is shown in green. We see that the latter produces a more extended reionization history, whereas the simple semi-analytic treatments yield an artificially rapid reionization transition.

[Madau et al., 1999]. The time evolution of the ionized volume fraction Q can then be approximated by

$$\frac{dQ}{dt} = \frac{\dot{n}_{\text{ion}}}{n_{\text{H}}} - \frac{Q}{t_{\text{rec}}}, \quad (4.12)$$

where t_{rec} is given by $t_{\text{rec}} = [(1 + 2\chi)n_{\text{H}}\alpha_B C]^{-1} = 509.73 \frac{a^3}{C(a)} \text{Gyr}$. Strictly speaking, C is here the clumping factor of ionized gas only. This differential equation thus describes the average growth of the ionized volume in terms of the rate at which ionizing photons become available minus the rate at which ionized gas is lost due to recombinations, ignoring second-order effects like local density fluctuations, correlations between sources, and so on. A model of this kind has been used, among others, by Springel and Hernquist [2003], Paardekooper et al. [2013], and Wise et al. [2014], for simple reionization models.

It is interesting to check how such a model compares to the full radiative transfer treatment. To this end we use the clumping factor of non-starforming gas, which is different especially at earlier times, as denser gas ionizes first. The resulting time

evolution of Q is shown in Figure 4.18. The solid lines are obtained by solving Equation (4.12), while our fiducial reionization simulation (V1_1024_M1) is shown as a green line, for comparison. It is reassuring that the global reionization model reproduces the same trend as our full 3D simulation. However, the full radiative transfer simulation predicts a much more extended epoch of reionization, highlighting the limitations of the global model. But given that such a simplified global treatment is of course not expected to reproduce finer effects such as patchiness of the epoch of reionization, the agreement is still reasonably good, allowing in particular a rough estimate of the redshift of reionization, defining this as $Q(z_{\text{reion}}) = 0.5$, good to about $\Delta z \sim 1$. This is remarkable given the huge simplifications made in Equation (4.12).

4.5 Conclusions

In this work, we considered only hydrogen reionization and focussed on ordinary high-redshift star formation as the primary source of ionizing photons. Other populations may in principal contribute to reionization, in particular primordial population-III stars, AGN, or exotic sources such as annihilating dark matter. While Pop-III stars may be important for the onset of reionization, most estimates for their relative contribution to global star formation suggest that neglecting them for reionization is justified. Still, accounting for them in future models would be clearly desirable, if only for completeness. Our neglect of AGN radiation for hydrogen reionization is however quite well justified because their ionizing luminosity is overwhelmed by star formation at high redshift. AGN become important at intermediate redshifts, however, where they likely play an important role in HeII reionization.

Even with these simplifying assumptions, calculating the ionizing flux that becomes available for reionization is affected by a substantial number of uncertainties. This includes the stellar population synthesis model we have used, and in particular, the adopted stellar initial mass function, where we used a Chabrier IMF and assumed that there are no significant IMF variations as a function of environment. Another major uncertainty lies in the escape fraction, which is physically uncertain and is in large part a phenomenological parameter in our models, absorbing uncertainties due to the treatment of dense gas and the limited spatial resolution. Finally, there are also numerical limitations related to the radiative transfer solver, the finite angular and spatial resolution employed in the radiative transfer, and the lack of self-consistently accounting for local feedback effects by the radiation field.

Fortunately some of these uncertainties can be greatly reduced by matching key observables such as the total optical depth for electron scattering or the amplitude of the metagalactic ionizing UV background after completion of reionization [e.g. Faucher-Giguère et al., 2008a,b]. Our radiative transfer models for Illustris then basically test whether cosmic reionization does occur for reasonable assumptions about the escape fraction, based on a galaxy population that yields a successful description of a slew of other observational data both at high and low redshift. To the extent this works, it provides reassurance for the cosmological consistency of

our galaxy formation and reionization models, and it shows that they are physically meaningful. Importantly, they can hence be used to learn more about the reionization transition itself. Our main findings can be summarized as follows:

1. The star formation history predicted by the Illustris simulation combined with its high-resolution gas density field allows cosmic reionization with an optical depth of $\tau = 0.065$, consistent with the latest Planck 2015 results as well as constraints from high-redshift quasars. This relies on ordinary stellar populations only, but requires optimistic assumptions for a high escape fraction at high redshift.
2. Previous tensions between the high optical depth favoured by CMB results and the low level of high redshift star formation required by successful galaxy formation models are thus essentially resolved with Planck 2015.
3. Using a suitable variable escape fraction model, we can approximately reproduce the expected UV background after reionization is completed, but most of our models tend to then overshoot the ionization rate and yield a slightly lower neutral fraction than inferred from quasar absorption lines. A fine-tuned model may plausibly yield an improved match.
4. Reionization proceeds inside out in our model, with overdense regions being ionized earlier on average than lower density regions.
5. The size distribution of ionized regions shows a remarkable constancy with time for small bubble sizes, suggesting that during reionization new small bubbles are formed roughly at the rate at which they are removed by size growth or coalescence with other regions. The characteristic size of bubbles grows with time, but there is a fairly flat distribution of sizes between $r \sim 2$ cMpc and $r \sim 20$ cMpc with about equal volume fraction per logarithmic size interval just before reionization is completed.
6. The duration of the reionization transition varies with the escape fraction model, and we find transition times for a drop of the neutral fraction from 80% to 20% between 190 Myr and 340 Myr, depending on the model.
7. The distribution of volume with respect to neutral fraction is quite broad but shows a peak that progresses to ever smaller neutral fraction with time. For models that successfully match the UV background constraints after reionization, the characteristic neutral fraction is 5×10^{-5} , with the lowest amount of volume found at neutral fractions of 2×10^{-2} .

In future work based on our methodology it would be particularly interesting to study HeII reionization. Due to the two ionization levels of helium with different ionization thresholds, the computational cost rises by at least a factor of about three, as more spectral bins have to be tracked instead of just one for hydrogen.

Additionally, a much longer physical time down to $z \sim 3$ has to be followed. This would still be possible in postprocessing with a future Illustris type simulation with a larger box size, containing an evolving AGN population including contributions from the brightest objects. Simulating this much physical time is extremely challenging for direct radiation-hydrodynamics simulations, much more so than hydrogen reionization simulations that can be stopped at $z \simeq 6$. This makes postprocessing approaches the only practical radiative transfer method to study HeII reionization in the near term.

5

Flux Limited Diffusion in AREPO

5.1 Flux limited diffusion

Radiation hydrodynamics (RHD) is the combination of the Euler equations coupled to transport equations for the radiation field. Coupling radiation and hydrodynamics constitutes a challenging problem. The radiation time scales are typically much shorter than the hydrodynamic time scales. Additionally, optically thin and thick regions have to be handled at the same time. The RHD equations can therefore usually only be solved in an approximate way.

A rather crude but still effective approximation is given by the so-called flux limited diffusion method, which we consider below. The diffusion approximation is valid in optically thick regions, but in general fails in optically thin regions where the radiation flow is freely streaming. However, in many problems the errors arising in optically thin regions remain subdominant, making radiation diffusion methods a competitive approach.

In radiation hydrodynamics, the Euler Equations (2.12) are extended by source terms that account for the interaction of radiation with matter. Here, we integrate over the frequency dependence of the moment equations (2.30) and (2.31), which

gives the so-called grey radiative transfer approximation. This leaves gives us with the following system of equations:

$$\frac{\partial \rho}{\partial t} + \nabla(\rho \mathbf{v}) = 0 \quad (5.1)$$

$$\frac{\partial \rho \mathbf{v}}{\partial t} + \nabla(\rho \mathbf{v} \mathbf{v} + P) = -\mathbf{G} \quad (5.2)$$

$$\frac{\partial \rho e}{\partial t} + \nabla((\rho e + P)\mathbf{v}) = -G \quad (5.3)$$

$$\frac{\partial E(\mathbf{x}, t)}{\partial t} + \nabla \mathbf{F}(\mathbf{x}, t) = G \quad (5.4)$$

$$\frac{1}{c^2} \frac{\partial \mathbf{F}_\nu(\mathbf{x}, t)}{\partial t} + \nabla \cdot \mathbf{P}_\nu(\mathbf{x}, t) = \mathbf{G}, \quad (5.5)$$

where the source terms – the radiation force four vector (G, \mathbf{G}) – are defined as

$$G = \int_0^\infty d\nu \oint \alpha_\nu(\mathbf{x}, \mathbf{n}, t) [B_\nu(\mathbf{x}, T) - I_\nu(\mathbf{x}, \mathbf{n}, t)] d\Omega, \quad (5.6)$$

$$\mathbf{G} = \frac{1}{c} \int_0^\infty d\nu \oint \alpha_\nu(\mathbf{x}, \mathbf{n}, t) [B_\nu(\mathbf{x}, T) - I_\nu(\mathbf{x}, \mathbf{n}, t)] \mathbf{n} d\Omega. \quad (5.7)$$

These equations for the source terms are only valid in the rest frame of the fluid. However, Equations (5.1) - (5.5) require the source terms in the laboratory frame, which can be obtained by evaluating Equations (5.6) and (5.7) in the fluid rest frame and applying a Lorentz boost to the laboratory frame.

In case of flux limited diffusion, the flux vector \mathbf{F} is assumed to be

$$\mathbf{F} = -\frac{c\lambda(R)}{\alpha_R} \nabla E, \quad (5.8)$$

with flux limiter function $\lambda(R)$ and Rosseland mean opacity α_R . In Levermore and Pomraning [1981] the following form of the flux limiter is proposed:

$$\lambda(R) = \frac{1}{R} \left(\coth R - \frac{1}{R} \right), \quad R = \frac{|\nabla E|}{\alpha_R E}. \quad (5.9)$$

Other functions for $\lambda(R)$ are discussed in the literature as well. A common key property is their behaviour in the limit of optically thick and thin media. If $R \rightarrow 0$, i.e. in an optically thick medium, the flux limiter behaves as $\lambda \rightarrow 1/3$ and the flux reproduces the correct diffusion limit. In the opposite case of an optically thin medium $\lambda \rightarrow -(1/R)\mathbf{n}$, with normal vector \mathbf{n} , it reproduces the streaming limit.

We define the following averaged opacities:

$$\alpha_{\text{P}} = \frac{\int_0^\infty d\nu \alpha_\nu B_\nu(T)}{B(T)}, \quad (5.10)$$

$$\alpha_{\text{E}} = \frac{\int_0^\infty d\nu \alpha_\nu E_\nu}{E}, \quad (5.11)$$

$$\alpha_{\text{F}} = \frac{\int_0^\infty d\nu \alpha_\nu \mathbf{F}_\nu}{\mathbf{F}}, \quad (5.12)$$

$$\alpha_{\text{R}}^{-1} = \frac{\int_0^\infty d\nu \alpha_\nu^{-1} [\partial B_\nu(T)/\partial T]}{\int_0^\infty d\nu [\partial B_\nu(T)/\partial T]}, \quad (5.13)$$

where α_{P} is the Planck mean opacity, α_{E} is the energy mean opacity, α_{F} gives the flux mean opacity, and α_{R} denotes the Rosseland mean opacity. If the radiation field is close to a Planck spectrum, $\alpha_{\text{E}} = \alpha_{\text{P}}$, and in the case of high opacities, the flux limited diffusion approximation relates the flux to $\mathbf{F} = -[\partial B_\nu(T)/\partial T] \nabla T / \alpha$, thus $\alpha_{\text{R}} = \alpha_{\text{F}}$.

Note that in FLD the radiation momentum update Equation (5.5) is dropped. While the conservation of total energy is still exact through the matching energy source terms of Equations (5.3) and (5.4), momentum is now only implicitly conserved, as there is no explicit conservation law for photon momentum anymore.

The full form of the radiative transfer equations including source terms accurate up to first order in v/c is given in Krumholz et al. [2007]:

$$\begin{aligned} \frac{\partial}{\partial t}(\rho e) + \nabla \cdot ((\rho e + P)\mathbf{v}) = & -\alpha_{0\text{P}}(4\pi B(T) - cE) \\ & + \lambda \left(2 \frac{\alpha_{0\text{P}}}{\alpha_{0\text{R}}} - 1 \right) \mathbf{v} \nabla E, \end{aligned} \quad (5.14)$$

$$\begin{aligned} \frac{\partial}{\partial t} E - \nabla \cdot \left(\frac{c\lambda}{\alpha_{0\text{R}}} \nabla E \right) = & \alpha_{0\text{P}}(4\pi B(T) - cE) \\ & - \lambda \left(2 \frac{\alpha_{0\text{P}}}{\alpha_{0\text{R}}} - 1 \right) \mathbf{v} \nabla E - \nabla \cdot \left(\frac{3 - R_2}{2} \mathbf{v} E \right), \end{aligned} \quad (5.15)$$

with $R_2 = \lambda + \lambda^2 R^2$.

5.2 Numerical implementation and implicit formulation

We solve Equations (5.14) and (5.15) by means of operator splitting. First, the terms from the Euler equation and the radiation advection term $-\nabla \cdot ((3 - R_2)/2 \mathbf{v} E)$ are solved using an explicit finite volume approach. Then, the contributions due to the diffusion term $\nabla \cdot \left(\frac{c\lambda}{\alpha_{0\text{R}}} \nabla E \right)$ and the thermal coupling term $\pm \alpha_{0\text{P}}(4\pi B(T) - cE)$ are solved implicitly. Finally, the remaining source terms are solved explicitly.

The temperature T and the internal energy e are related through the specific heat $c_{\text{v}} = \frac{\partial e}{\partial T}$. For an ideal gas, c_{v} is constant and thus $e = c_{\text{v}} T$. The frequency integrated

Planck function is given by $4\pi B(T) = ca_{\text{R}}T^4$ with the radiation constant a_{R} , which turns equations (5.14) and (5.15) into a non-linear system making a direct implicit solver very difficult.

The terms of equations (5.14) and (5.15) which are solved implicitly can be written as

$$0 = \rho c_{\text{v}}(T^0 - T) - K(E, T) \quad (5.16)$$

$$0 = (E^0 - E) + \Delta t \nabla D \nabla E + K(E, T), \quad (5.17)$$

with the coupling term

$$K(E, T) = a [B(T^*) + B'(T^*)(T - T^*) - E], \quad a = \Delta t c_{\text{p}} \alpha_{\text{P}}, \quad (5.18)$$

where the Planck function has been Taylor-expanded around an intermediate temperature state T^* . Equation (5.16) is equivalent to

$$\delta^{-1}(T - T^*) = \rho c_{\text{v}}(T^0 - T^*) - a(B(T^*) - E), \quad (5.19)$$

with a ‘‘pseudo time step’’ size

$$\delta^{-1} = \rho c_{\text{v}} + aB'(T^*). \quad (5.20)$$

Using Equation (5.17) and inserting Equation (5.19), the update of the photon energy E leads to the following linear matrix equation

$$[-\Delta t \nabla D \nabla + (1 + a) - a^2 B' \delta] E = E^0 + a(B + B' \delta (\rho c_{\text{v}}(T^0 - T^*) - aB)), \quad (5.21)$$

where the right hand side is a vector independent of E . The only off-diagonal elements of the matrix [...] are due to the diffusion operator $\nabla D \nabla$. Initially, the intermediate temperature is set to $T^* = T^0$. Using equations (5.19) and (5.21), new values for (T, E) are computed. If the result is converged, the update step ends here, otherwise T^* is reset to the current value of T , and (T, E) are updated again until convergence is reached.

5.2.1 Discretization of the diffusion operator

A discretized version of the diffusion operator $\nabla D \nabla$ on an arbitrary mesh is obtained by a straight forward finite volume discretization:

$$\nabla D \nabla E = \frac{1}{V_i} \int \nabla D \nabla E \, dV \quad (5.22)$$

$$= \frac{1}{V_i} \oint D(\nabla E) \, d\mathbf{A} \quad (5.23)$$

$$= \frac{1}{V_i} \sum_{j \in \text{NGB}(i)} A_{ij} D_{ij} (\nabla E)_{ij} \mathbf{n}_{ij} \quad (5.24)$$

$$= \frac{1}{V_i} \sum_{j \in \text{NGB}(i)} \frac{A_{ij}}{r_{ij}} D_{ij} (E_j - E_i), \quad (5.25)$$

with A_{ij} denoting the area of the interface between cells i and j , r_{ij} giving the distance vector of the cells, and \mathbf{n}_{ij} the face normal vector. The average of the diffusion coefficient D_{ij} is given by $D_{ij} = c\lambda(R_{ij})/\alpha_{ij}$, where $\alpha_{ij} = 2\alpha_i\alpha_j/(\alpha_i + \alpha_j)$ is the geometrically averaged diffusion coefficient. We use backward in time arithmetic averages for E_{ij} and $|\nabla E|_{ij}$ in $R_{ij} = |\nabla E|_{ij}/\alpha_{ij}E_{ij}$.

5.2.2 Matrix solver

The matrix [...] given in Equation (5.21) is a sparse matrix, because the off-diagonal elements are only non-zero for neighbouring cells. Many efficient methods are known to numerically solve a sparse matrix problem. We choose a so-called multigrid method. Instead of implementing our own matrix solver, we make use of the implementation provided by the HYPRE library [Falgout et al., 2006].

A multigrid method is an iterative sparse matrix solver, working on a hierarchy of meshes. The error of an initial guess of the solution vector on a given mesh can be reduced by applying a smoothing operator. A possible choice for a smoothing operator is for example given by the Jacobi iteration. An improved solution vector can then be obtained by iteratively updating the solution vector. While such a smoothing operator improves the solution with each iteration, unfortunately only small scale errors are improved quickly. To achieve global convergence and a damping of large scale errors, many iterations would be required. This problem is solved in multigrid approaches by mapping the residuum to a coarser mesh, recursively calling the solver for the coarser mesh and afterwards using the solution on the coarser mesh to improve the solution on the finer mesh. The damping of small scale errors on the coarser mesh corresponds to the damping of larger scale errors on the finer mesh, which is the reason why multigrid methods are so effective. These steps can be recursively repeated until the mesh is coarse enough to enable a direct solution of the remaining matrix equation. Usually just one or a few of these multigrid cycles are then sufficient to reach convergence.

Due to the non-constant diffusion coefficients in our problem, we use a so-called semi coarsening multigrid method. Instead of coarsening the grid in all dimensions at the same time per recursion step, the grid is only coarsened in one dimension. This leads to grids with rectangular cells. Once only one or a few cells remain in that dimension, the procedure is repeated for the remaining dimensions.

5.3 Marshak test

The Marshak test consists of an inflowing radiation flux into a background medium with uniform density kept at rest. The radiation field is inflowing in $+z$ direction with radiative flux \mathbf{F}_{inc} . The medium has a temperature dependent heat capacity of $c_V = \alpha T^3$, which means $e = 1/4\beta T^4$, i.e. the specific internal energy becomes proportional to the emissivity of the medium with proportionality constant β . The initial temperature is set to $T = 0$ throughout the medium. We define $\epsilon = 4a_R/\beta$ which simplifies the emission term to $S = c\alpha\epsilon e$. Instead of integrating the temperature

T , we choose to integrate the specific internal energy e for this test problem. This modifies equations (5.19) and (5.21) to

$$e = e^* \rho \delta (e^0 - e^*) - a \delta (\epsilon e^* - E), \quad (5.26)$$

$$[-\Delta t \nabla D \nabla + (1 + a) - a^2 \epsilon \delta] E = E^0 + a(\epsilon e^* + \epsilon \delta (\rho (e^0 - e^*) - a \epsilon e^*)), \quad (5.27)$$

with $a = \Delta t c \alpha$ and $\delta^{-1} = (\rho + a \epsilon)$. In the following, we will use $\rho = 1$, $\alpha = 1 \text{ cm}^{-1}$, $\epsilon = 0.5$ and $\mathbf{F} = c/4 \mathbf{n}_z$. The simulation domain is 16 cm long in the z -direction and resolved by 1024 cells. This problem primarily tests the diffusion solver rather than the full non-linear solver including the T^4 dependency of the source term.

5.3.1 Marshak boundary condition

We require boundary conditions for the left and right end of the simulation domain. At $z = 0$ a Marshak boundary condition is enforced. Given an incoming flux \mathbf{F}_{inc} , this leads to the following boundary condition at the leftmost interface:

$$cE(0, t) - 2\mathbf{n}\mathbf{F}(0, t) = 4\mathbf{n}\mathbf{F}_{\text{inc}}, \quad (5.28)$$

with surface normal vector \mathbf{n} pointing into the positive z -direction.

In the following, we will replace vector quantities by the scalar component pointing in the $+z$ direction. The boundary condition evaluated using discrete values can be written as

$$cE_{-1/2} + 2F_{-1/2} = 4F_{\text{inc}}. \quad (5.29)$$

The total flux $F_{-1/2}$ at the boundary is discretized as

$$F_{-1/2} = -\frac{2c}{3\alpha} \frac{E_0 - E_{-1/2}}{\Delta z}, \quad (5.30)$$

with the cell centred radiation energy E_0 and boundary value $E_{-1/2}$. Combining these two equations and solving for the flux at the boundary surface gives

$$F_{-1/2} = \frac{2c}{3\alpha \Delta z + 4} \left(\frac{4}{c} F_{\text{inc}} - E_0 \right), \quad (5.31)$$

which is put into the finite volume discretization of the diffusion operator matrix. In summary, for cells next to the boundary this leads to a contribution to the diagonal element of the diffusion matrix and a source term on the right hand side.

5.3.2 Results

We compare our numerical results to an analytic solution obtained in Su and Olson [1996]. To be able to do a direct comparison we introduce the dimensionless radiation energy density $\tilde{E} = \frac{c}{4} \frac{E}{F_{\text{inc}}}$ and thermal energy density $\tilde{e} = \frac{c}{4} \frac{a_{\text{R}} T^4}{F_{\text{inc}}} = \frac{\epsilon e}{F_{\text{inc}}}$. Figures 5.1 and 5.2 show the dimensionless radiation and thermal energy densities in comparison

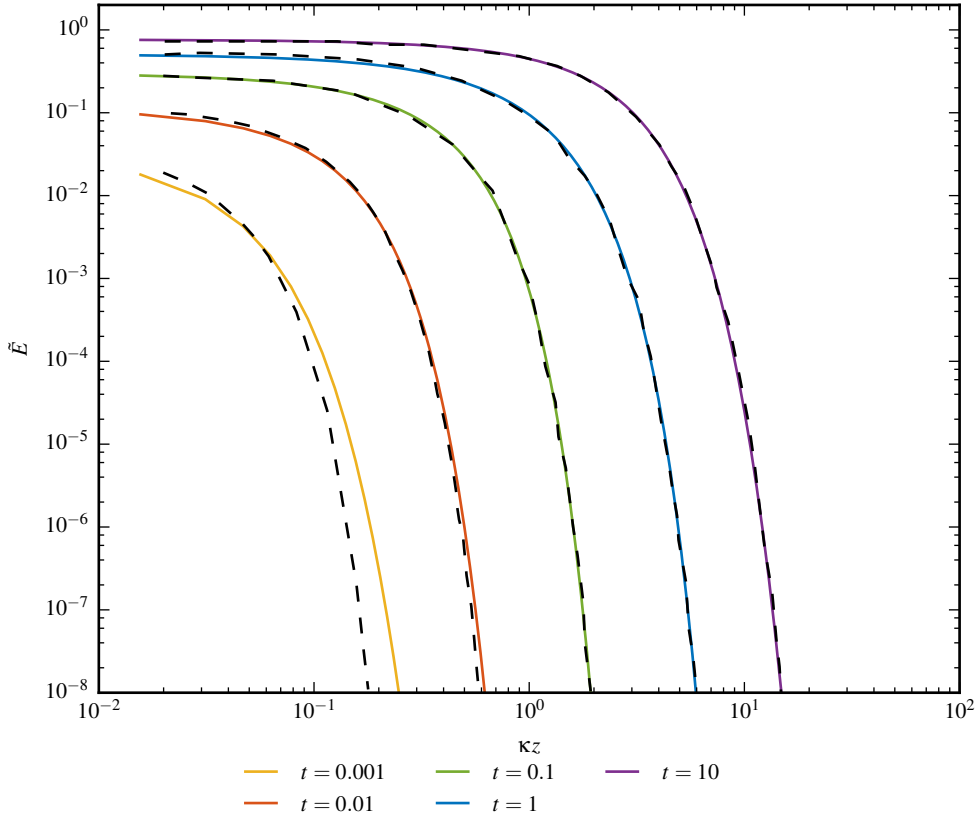


Figure 5.1: The figure shows the dimensionless radiation energy density at five output times. The dashed lines show the reference solution taken from Su and Olson [1996]. After $t = 0.01$ the agreement of our solutions with the expected results is very good.

to the expected solution. At early times around $t = 0.001$ the agreement with the exact solution is not perfect. Initially, the numerical solution progresses faster than expected into the medium. At later times the agreement is however very good. A similar effect was found in Krumholz et al. [2007]. In fact, the degree of accuracy is similar in both quantities considered here. We also found that using a higher numerical resolution the initial disagreement can be further reduced. This test hence mainly confirms the accuracy and stability of our diffusion solver in a simple test problem. However, the thermal coupling is simpler than in the full RHD problem due to the linear scaling of the emissivity with specific thermal energy. This motivates us to also consider more demanding test problems.

5.4 Levitation test

This test consists of a stable isothermal atmosphere which is irradiated from the bottom. The setup hence resembles a Rayleigh-Taylor instability test. Such a

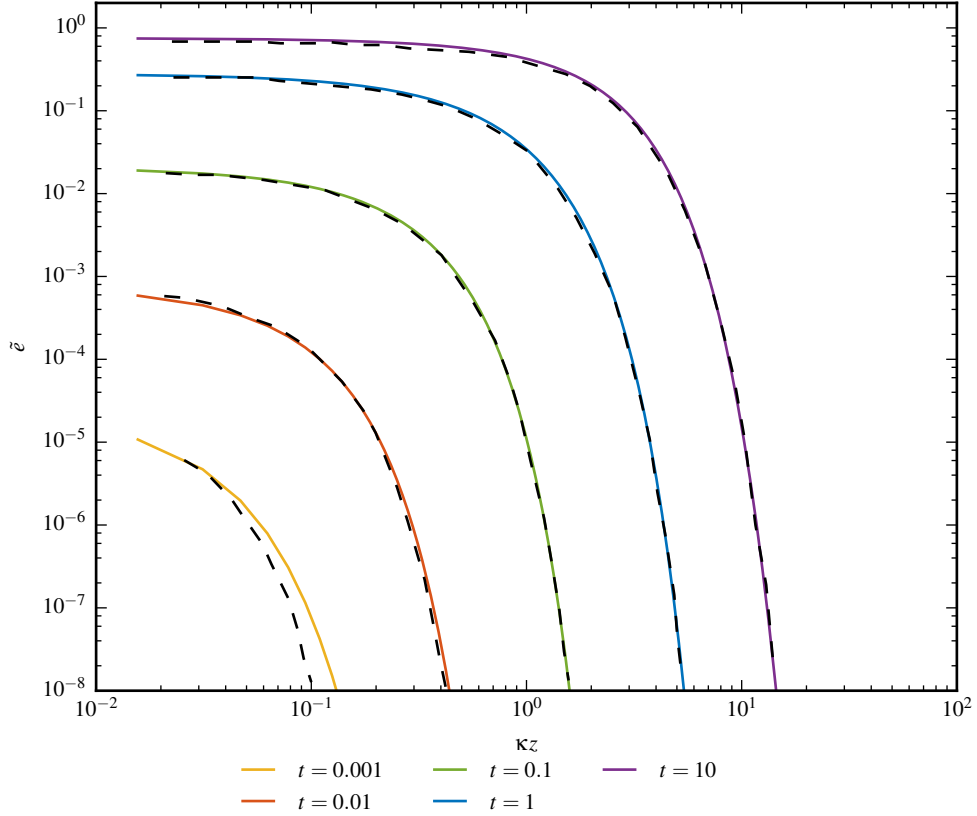


Figure 5.2: The same as Figure 5.1, but for the dimensionless specific internal energy. Again, after $t = 0.01$ the agreement with the dashed reference solutions with our results is very good.

situation is encountered for example in an environment of rapidly forming stars as in a ultra luminous infrared galaxies. The specific test considered here was first studied in Krumholz and Thompson [2012]. The same setup was also studied in Davis et al. [2014] using a more accurate VET radiative transfer method. Interestingly, these authors reported considerable differences between both radiative transfer methods. The radiation field obtained with the VET method managed to continuously lift some gas upwards through radiation pressure, whereas the FLD simulations showed a fallback of the gas and a turbulent end state. In Rosdahl et al. [2015], another radiative transfer scheme based on the M1 closure was introduced. Overall, their method produced a result more similar to FLD, even though some aspects of the outcome also resembled the VET method. A particularly interesting aspect of this test is hence that different radiative transfer approximations produce qualitatively different answers for it, blow-out or fall back, with the correct answer being uncertain at this point.

5.4.1 Setup

Gas and dust are assumed to be strongly coupled and the Planck and Rosseland mean opacities are given by

$$\alpha_{\text{P}} = 0.1 \left(\frac{T}{10 \text{ K}} \right)^2 \text{ cm}^2 \text{ g}^{-1}, \quad (5.32)$$

$$\alpha_{\text{R}} = 0.0316 \left(\frac{T}{10 \text{ K}} \right)^2 \text{ cm}^2 \text{ g}^{-1}. \quad (5.33)$$

The parametrization is compatible with Semenov et al. [2003] and strictly valid only for $T < 150 \text{ K}$, assuming the temperature of the radiation field and gas field are roughly equal. The gravitational field is pointing downwards with gravitational acceleration g . The inflowing radiation field has a net flux of F_{\star} , which corresponds to a temperature $T_{\star} = (F_{\star}/a_{\text{R}}c)^{1/4}$. This allows the definition of a characteristic sound speed $c_{\star}^2 = kT_{\star}/\mu m_{\text{H}}$, scale height $h_{\star} = c_{\star}^2/g$, and sound crossing time $t_{\star} = h_{\star}/c_{\star}$. In Krumholz and Thompson [2012] the temperature and mean molecular mass were chosen as $T_{\star} = 82 \text{ K}$ and $\mu = 2.33$. This results in a flux of $F_{\star} = 2.54 \times 10^{13} \text{ L}_{\odot} \text{ kpc}^2$. The Rosseland mean opacity at T_{\star} is $\alpha_{\text{R},\star} = 2.13 \text{ cm}^2 \text{ g}^{-1}$. Instead of specifying the gravitational acceleration g and surface density Σ directly, it is more convenient to define the dimensionless Eddington ratio $f_{\text{E},\star}$ and optical depth τ_{\star}

$$f_{\text{E},\star} = \frac{\alpha_{\text{R},\star} F_{\star}}{gc}, \quad (5.34)$$

$$\tau_{\star} = \alpha_{\text{R},\star} \Sigma. \quad (5.35)$$

Our simulations are using a 2D Cartesian grid in the (x, z) plane. Initially, we set the radiation field to $E = aT_{\star}^4$ everywhere. The density is given by

$$\rho = (1 + A \sin(2\pi x/\lambda)) \begin{cases} \rho_{\star} \exp(-z/h_{\star}), & \exp(-z/h_{\star}) > 10^{-10} \\ 10^{-10} \rho_{\star}, & \exp(-z/h_{\star}) \leq 10^{-10} \end{cases}, \quad (5.36)$$

with $\rho_{\star} = \Sigma_{\star}/h_{\star}$. Through A and λ an initial perturbation is added, for which we use $A = 0.25$ and $\lambda = 256h_{\star}$ in all runs. Additionally, we have added small random fluctuations in some of our runs. The initial temperature is set to $T = T_{\star}$, and the gas velocity to $\mathbf{v} = \mathbf{0}$.

We impose reflective boundary conditions for the fluid at the lower boundary and transmissive boundaries at the upper end. The transmissive boundaries are realized by forcing the density, temperature and velocity of the topmost row of cells to a fixed value of $\rho = 10^{-13} \rho_{\star}$, $T = 10^3 T_{\star}$ and $\mathbf{v} = \mathbf{0}$. For the radiation field, we impose a von Neumann boundary at the bottom and a Dirichlet boundary at the top end with $E = aT_{\star}^4$. The boundaries in the x -direction are periodic for both, the radiation field and the gas flow.

The gravitational field is constant throughout the domain and pointing in the $-z$ direction. Table 5.1 summarizes our runs and states the numerical resolution as well

Overview of Levitation tests				
Label	τ_\star	$f_{E,\star}$	$(L_x \times L_z)/h_\star$	$N_x \times N_z$
F0.02_TAU10.0	10.0	0.02	512×256	1024×512
F0.5_TAU3.0	3.0	0.5	512×1024	1024×2048
F0.5_TAU10.0	10.0	0.5	512×2048	1024×4096

Table 5.1: Overview of our Levitation test runs. The first run F0.02_TAU10.0 is in the stable regime, where the radiation is not able to lift the gas considerably. The two other runs F0.5_TAU3.0 and F0.5_TAU10.0 are in the unstable regime, where the radiation field can initially drive an outflow, which quickly becomes unstable and starts to fall back.

as the used box sizes. These runs are a subset of those studied in Krumholz and Thompson [2012]. The run F0.02_TAU10.0 represents the stable case, in which the radiation force is not able to drive a strong upward outflow. The other two runs, F0.5_TAU3.0 and F0.5_TAU10.0, have parameters in the more interesting unstable regime, where in principle such an outflow is possible.

5.4.2 Results

Stable regime

We will first analyse the F0.02_TAU10.0 run. Due to the low Eddington ratio of only $f_{E,\star} = 0.02$, the simulation should not show any outflow. Figure 5.3 shows the gas density at four instances in time. The corresponding radiation temperature is shown in Figure 5.4. The initial low Eddington ratio should not allow any significant lift of the gas. However, the high opacity of $\tau_\star = 10$ leads to trapping of the radiation, which results in a temperature increase, which in turn leads to a strong rise of the opacity through the $\propto T^2$ dependency of the opacity. Thus, the density profile is lifted slightly. Due to the higher opacity in the denser regions of the sine profile, the lift is stronger there. This leads to a distortion of the initial density perturbation. However, after some time, due to the decrease in density caused by the upwards motion, the atmosphere falls back and settles in a steady state.

This is shown in a more quantitative way in Figures 5.5 and 5.6. We define the mass-weighted velocity dispersion in the x and z -directions as

$$\sigma_{x,z} = \left(\frac{\int \rho (v_{x,z} - \bar{v}_{x,z})^2 dV}{\int \rho dV} \right)^{1/2}, \quad (5.37)$$

with

$$\bar{v}_{x,z} = \frac{\int \rho v_{x,z} dV}{\int \rho dV}, \quad (5.38)$$

and the total velocity dispersion as $\sigma = (\sigma_x^2 + \sigma_z^2)^{1/2}$. The velocity dispersion reaches about the sound speed during the initial upward motion, but then continuously

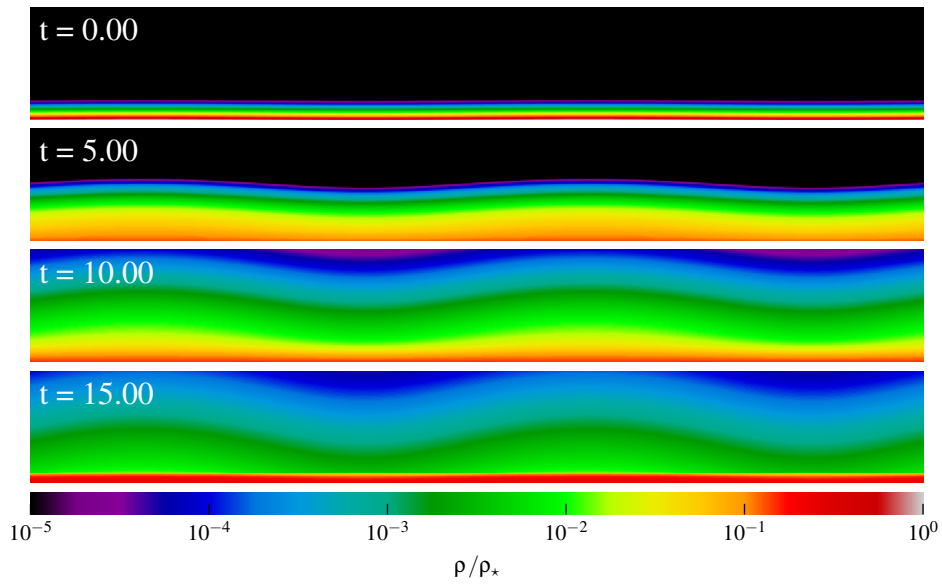


Figure 5.3: Density slices of the F0.02_TAU10.0 simulation at four instances in time. The initial exponential density profile is driven upwards by the inflowing radiation, but quickly starts to fall back as the radiation is not strong enough to drive an outflow.

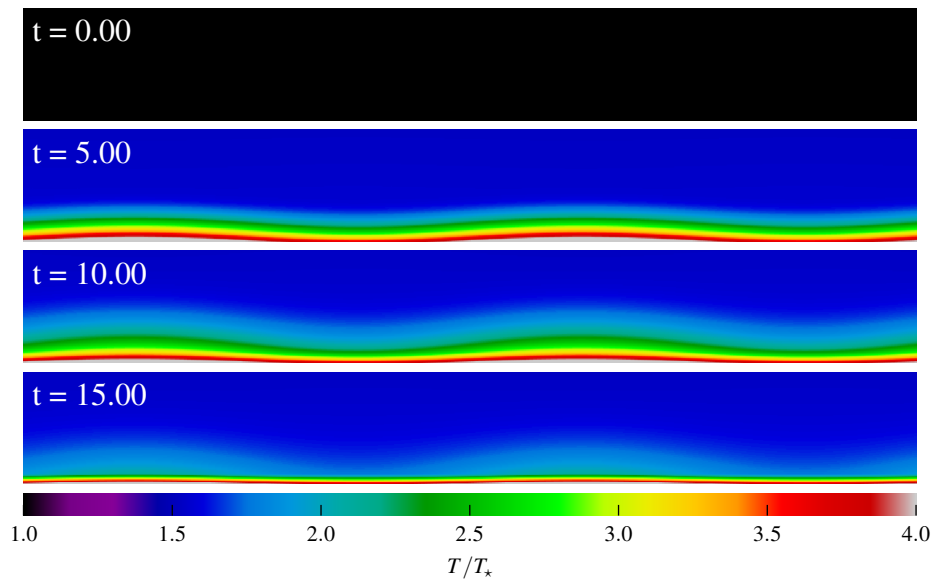


Figure 5.4: The same as Figure 5.3, but for the radiation temperature of the F0.02_TAU10.0 run.

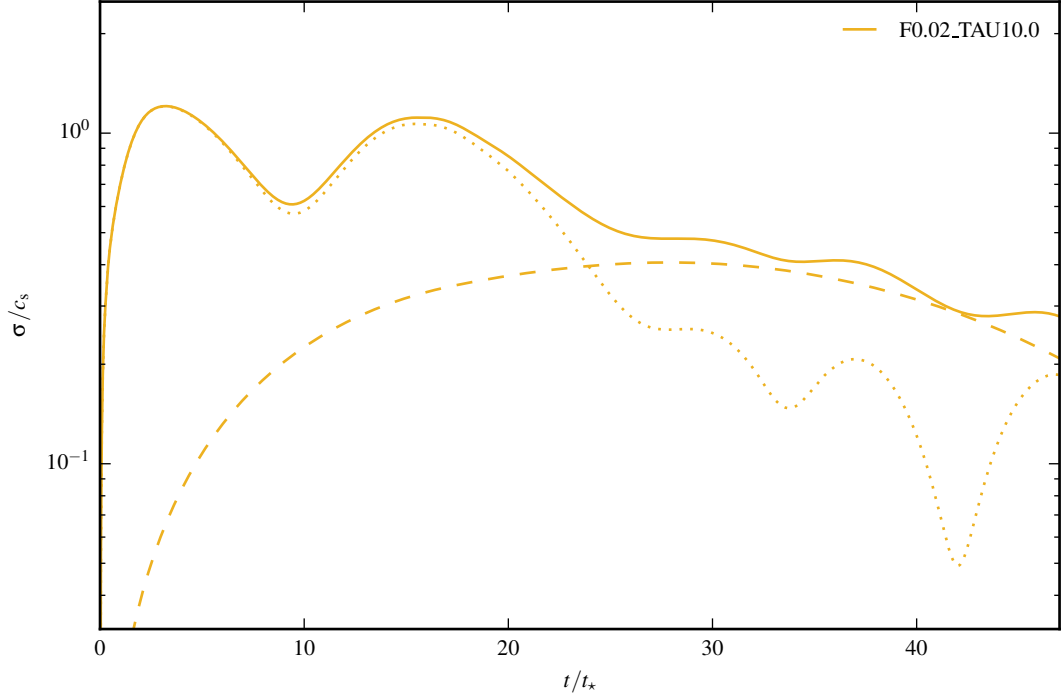


Figure 5.5: The velocity dispersion over sound speed for the F0.02_TAU10.0 run over time. The solid line shows the full velocity dispersion, while the dashed line shows the x -component and the dotted line shows the z -component of the velocity dispersion.

declines to about $0.3 c_s$. The horizontal velocity dispersion only slowly starts rising, while the vertical velocity dispersion changes much more quickly. This is not surprising, as the driving radiation force is mainly in the upward z -direction and horizontal motions only develop due to the sinusoidal density profile.

The mean Eddington ratio characterizes the balance between uplifting radiation forces and downdriving gravitational forces. The mean radiation force is

$$\langle f_{\text{rad},z} \rangle = \int \mathbf{f}_{\text{rad}} \mathbf{n}_z dV = \int \frac{\alpha_R \rho \mathbf{F}}{c} \mathbf{n}_z dV = \int (-\lambda \nabla E) \mathbf{n}_z dV, \quad (5.39)$$

thus the mean Eddington ration is given by

$$\langle f_E \rangle = \frac{\langle f_{\text{rad},z} \rangle}{\int \rho g dV}. \quad (5.40)$$

The Eddington ration shows a quick initial rise, but then falls back to $f_E = 0.2$ and remains there until the end of the simulation, which is in agreement with the lack of any outflow visible in the density slices.

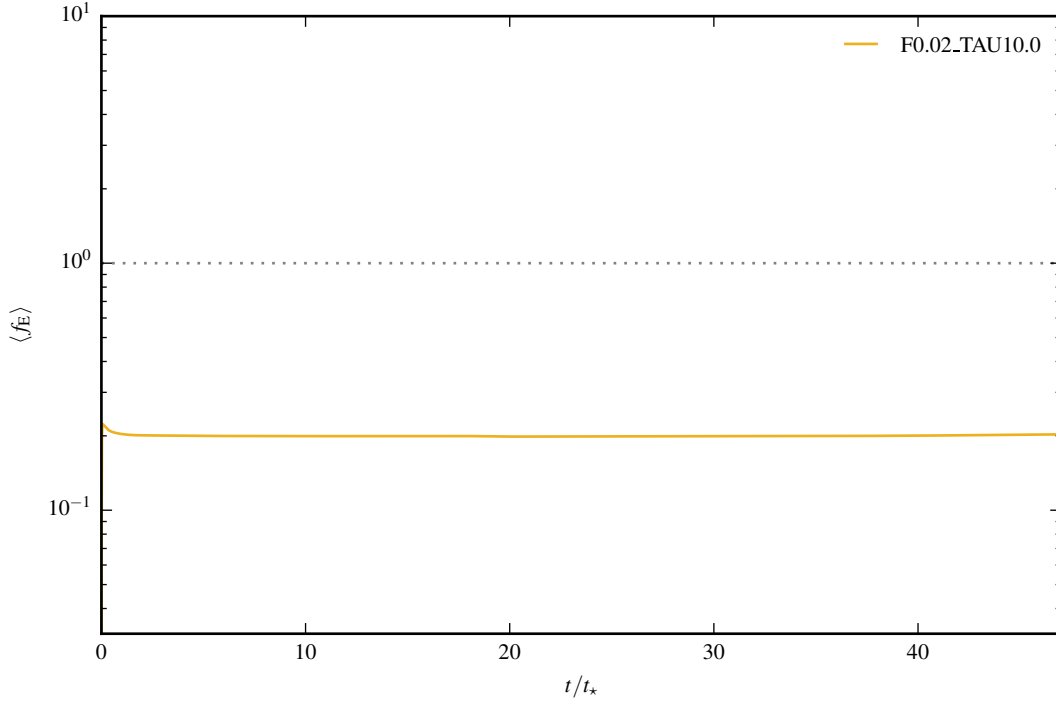


Figure 5.6: The Eddington ratio over time for the F0.02_TAU10.0 run. The grey dotted line marks $f_E = 1$, which is roughly required to drive an outflow. For this run the Eddington ratio stays below that value at all times.

Unstable regime

Now we focus on the runs in the unstable regime. Both have a larger initial Eddington ratio of $f_{e,\star} = 0.5$. They only differ in the initial optical depth τ_\star . The density and radiation temperature slices are shown in Figures 5.7 and 5.8 for the $\tau_\star = 3$ run and in Figures 5.9 and 5.10 for the $\tau_\star = 10$ run, respectively. In both runs, the radiation field initially manages to drive an upward motion. The heating of the gas leads to an increased opacity, which is responsible for the strong initial upward motion. However, at about $t/t_\star = 16$ ($\tau_\star = 3$ run) and $t/t_\star = 11.6$ ($\tau_\star = 10$ run), the density field starts to form buckles. At around the same time, radiation manages to escape through cavities and the temperature drops significantly. This in turn drastically reduces the upwards driving force. The gas develops a Rayleigh-Taylor instability and the down falling buckles seed turbulent motions.

This can be more clearly seen in Figure 5.11, showing the velocity dispersion of both runs. The final velocity dispersion is highly supersonic and reaches about $10 c_s$. Figure 5.12 clearly shows the drop in the uplifting force. Even though the Eddington ratio approaches unity, no large-scale outflow is established. Only a small fraction of the gas manages to reach the upper boundary. This finding is in agreement with the results obtained by Krumholz and Thompson [2012]. However, Davis et al. [2014]

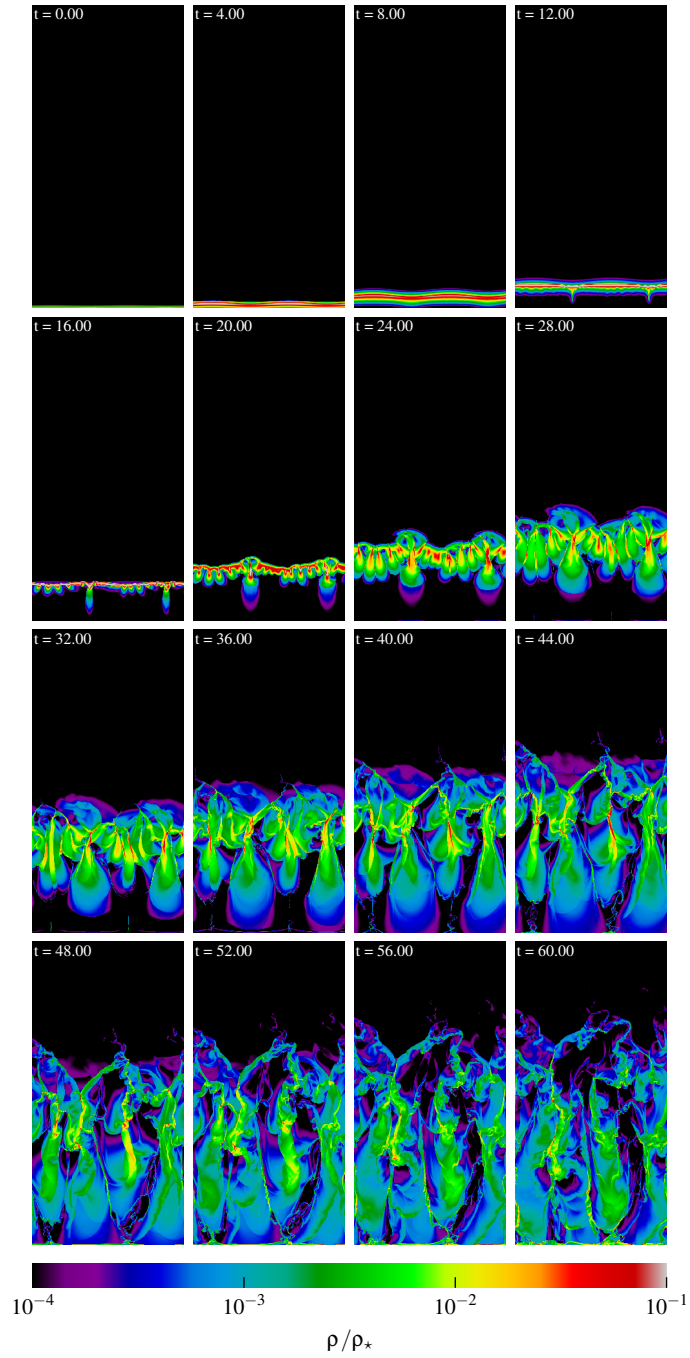


Figure 5.7: Density slices at 16 instances in time for the F0.5_TAU3.0 run. The inflowing radiation initially drives an upward motion. After some time the flow becomes turbulent and starts to fall back.

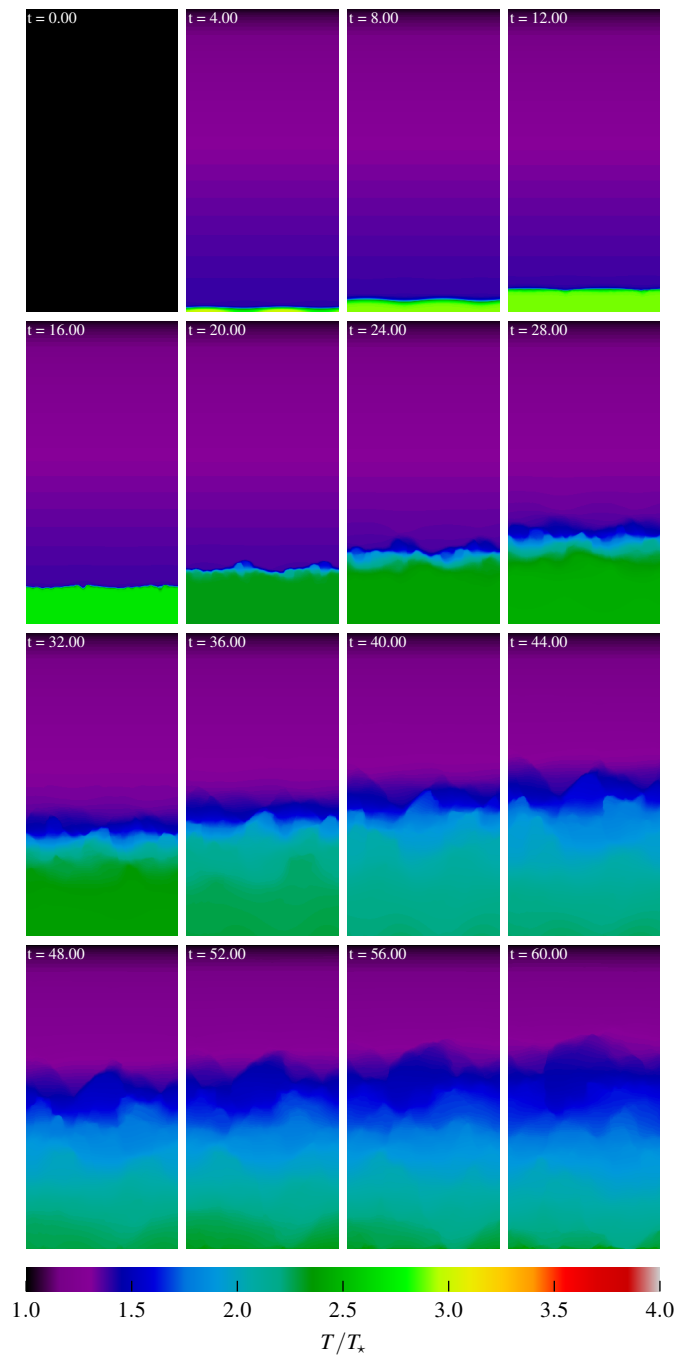


Figure 5.8: The same as in Figure 5.7, but for the radiation temperature.

5 Flux Limited Diffusion in AREPO

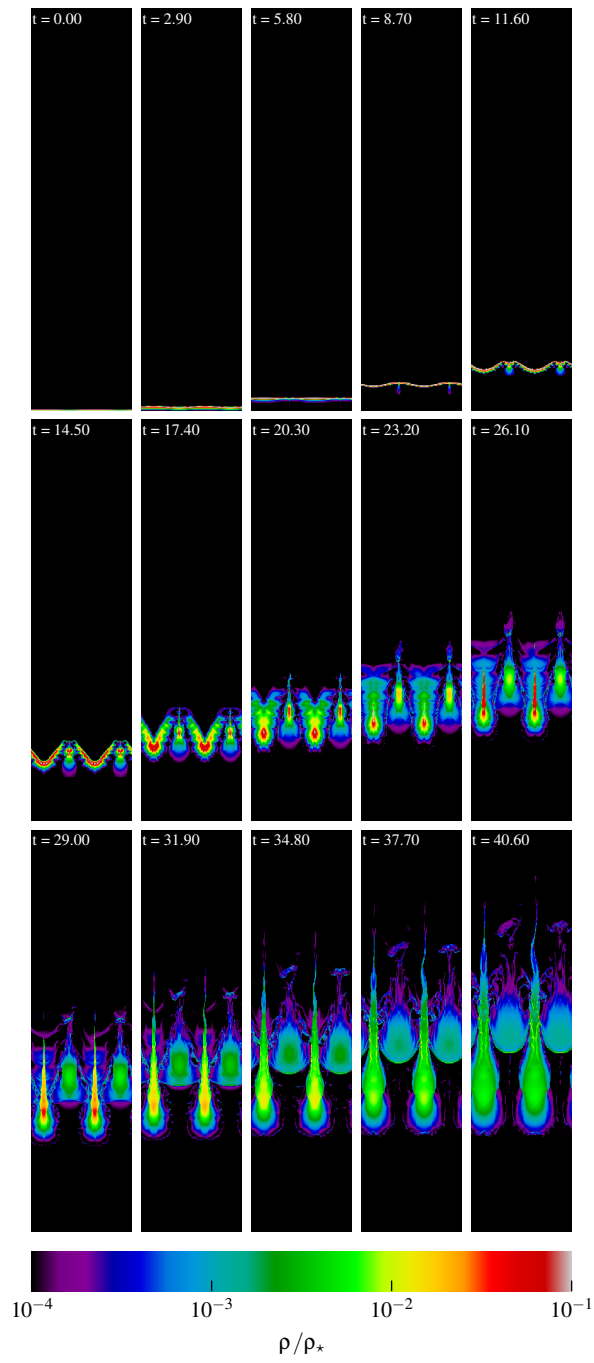


Figure 5.9: Density slices at 15 instances in time for the F0.5_TAU10.0 run. Initially, the gas starts to rise due to the incoming radiation. The high density regions start to buckle and the radiation field is no longer able to provide support against gravity, resulting in a back flow.

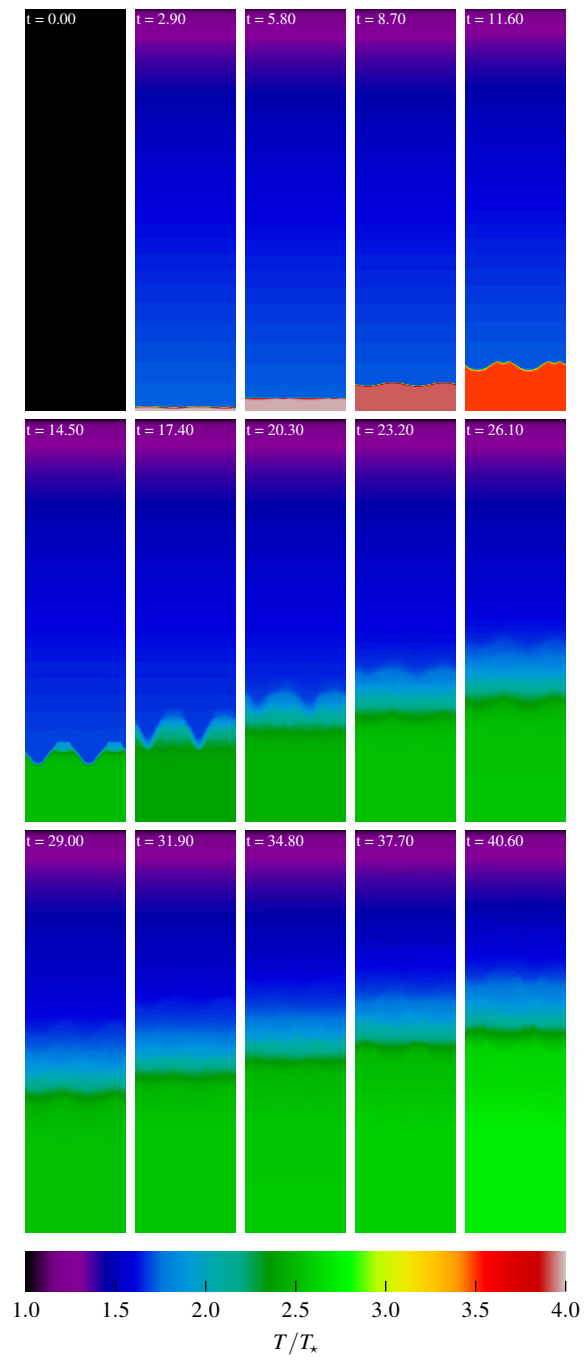


Figure 5.10: The same as in Figure 5.9, but for the radiation temperature.

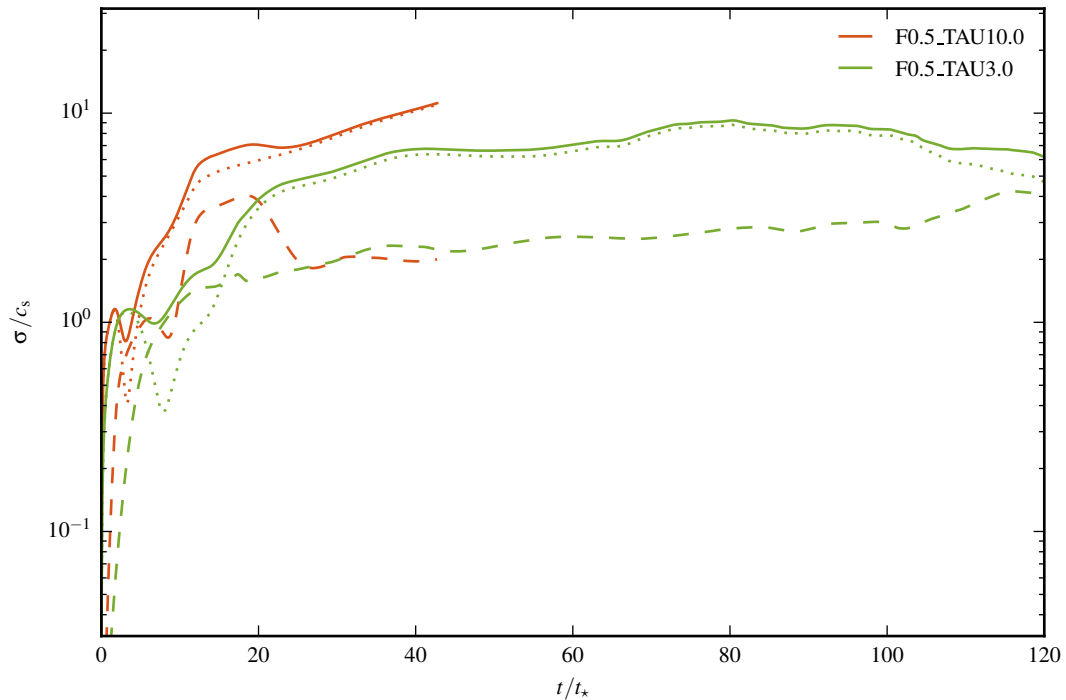


Figure 5.11: The velocity dispersion over sound speed for the F0.5_TAU3.0 and F0.5_TAU10.0 runs over time. The solid lines shows the full velocity dispersion, while the dashed line shows the x -component and the dotted line shows the z -component of the velocity dispersion.

report different results based on their VET method. For the same set of simulation parameters, they find an outflow and attribute the qualitative difference to the radiative transfer method and the inability of the FLD method to correctly describe the radiation flux in optically thin regions, possibly leading to a loss of radiation and an overly strong reduction of the uplifting force. Whether or not this claim is correct can unfortunately not easily be decided. Given the complexity of radiation hydrodynamics codes, an independent verification by another VET code will be necessary to shed more light on this interesting discrepancy between the different methods.

5.5 Discussion

We presented an implementation of flux limited diffusion in AREPO. Even though we have shown tests on Cartesian meshes only, a generalization of our implementation to an arbitrary Voronoi mesh is straightforward as the diffusion operator can be readily evaluated over the faces of a Voronoi cell. The remaining parts of the matrix equation are identical. The geometric multigrid solver would however have to be replaced by an algebraic multigrid solver. An algebraic multigrid solver makes no assumptions

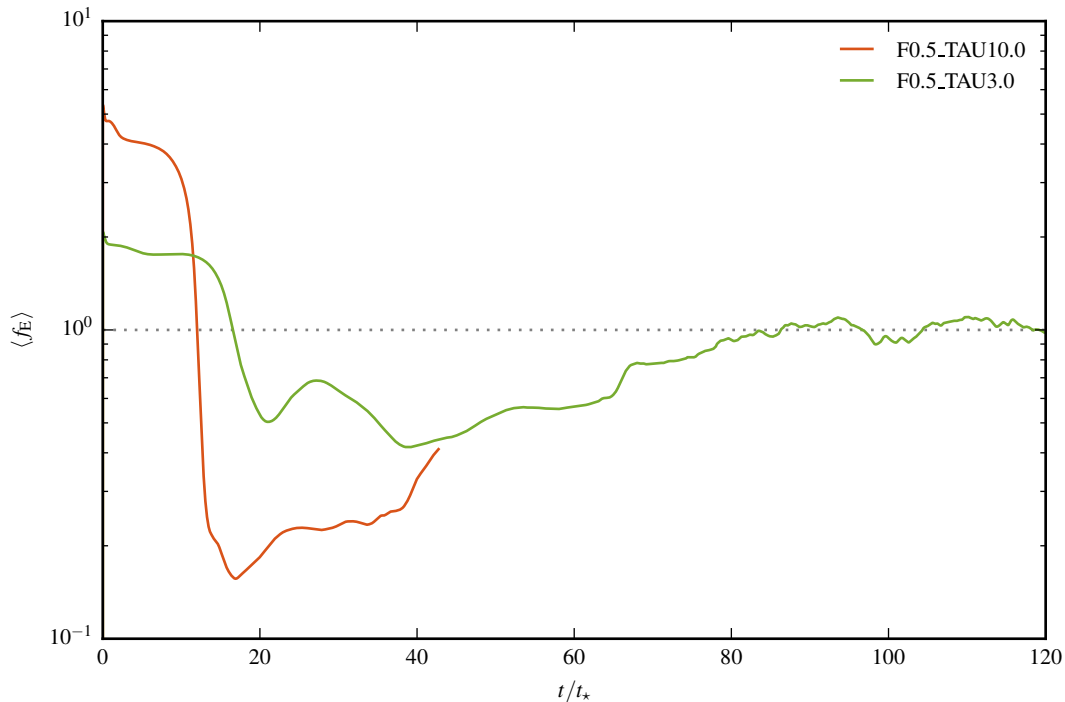


Figure 5.12: The Eddington ratio over time for the F0.5_TAU3.0 and F0.5_TAU10.0 runs. The initial high Eddington ratio drops significantly and stays at around unity. However, no significant outflow is found.

about the underlying mesh connectivity in deriving coarse grained meshes. Thus, a matrix with an arbitrary sparse pattern can be solved. The HYPRE library provides such an algebraic multigrid solver as well, which would then need to be employed instead of the geometric multigrid solver used thus far.

Furthermore, we have shown that our implementation is able to reproduce the non-trivial Marshak and Levitation test cases. Our results in the Levitation test agree well with those of Krumholz and Thompson [2012] and Rosdahl et al. [2015]. However, given the conflicting results by Davis et al. [2012] this also means that they may be affected by systematic inaccuracies of FLD. While flux limited diffusion provides a simple and fast approximation for radiation hydrodynamics, this also emphasizes that it should only be used for a subset of problems were it is demonstrated to be sufficiently accurate.

Part III

Towards Novel Numerical Methods

6

An AMR Module for Arepo

6.1 Introduction

The moving mesh code AREPO discretizes the Euler equations on a moving Voronoi mesh. Each Voronoi cell is constructed around a so called mesh generating point. The Voronoi mesh is defined such that every cell contains the volume closer to its mesh generating point than to any other mesh generating point. The ability to use an almost arbitrary set of points to construct a Voronoi mesh has the big advantage of a very flexible mesh than can be nearly perfectly adopted to the problem of interest. This is especially helpful if a huge density contrast has to be simulated and no geometric symmetries can be exploited, as encountered for example in cosmological simulations. Here, dense regions can be conveniently resolved with more mesh generating points, resulting in an adaptive resolution. Additionally, Voronoi cells have generally a roundish shape without preference for any spatial direction. The advantage over schemes like SPH, which also easily adapts to huge density contrasts, is that the mesh can also be refined on arbitrary other quantities, and not just on the mass enclosed within a cell. However, a significant disadvantage of a Voronoi tessellation lies in the complicated grid construction routines and the associated computational overhead.

Most other mesh codes used in astrophysics employ structured meshes that can be combined with an adaptive mesh refinement strategy. Often, they use a regular Cartesian mesh and split a cell of edge length Δx into 2^d smaller cells of size $\Delta x/2$, where d is the number of space dimensions. The resulting mesh is a more regular mesh composed of cubic cells. The regularity makes the mesh management routines a lot simpler and considerably reduces the computational cost. Many performance optimizations are easier to achieve on an AMR mesh than on an unstructured Voronoi mesh. Deriving discretized versions of differential operators for a regular grid is easier

as well, making exploring new physical processes, which require discretized versions of new equations, a lot easier and faster than on a Voronoi mesh.

Two general classes of methods for organizing the mesh are discussed in the literature: Tree-based [see e.g. Kravtsov et al., 1997; Teyssier, 2002] and block structured [see e.g. Bryan et al., 2014; Fryxell et al., 2000; Mignone et al., 2012] AMR methods. The block structured methods do not refine single cells, but instead larger regions are resolved by a finer grid encompassing many cells. This makes these codes a bit less adaptive. However, each patch can be stored continuously in memory, allowing for a better cache optimization. An alternative approach is to allow arbitrary cell refinements as in the tree-based methods. A tree like data structure is then used to manage the mesh. However, also here the mesh has to fulfill certain level jump conditions for stability reasons, which we will discuss below.

Implementing an alternative AMR mesh into the code AREPO is interesting for mainly two reasons. First, it allows a more direct comparison of results obtained with the moving-mesh Voronoi method against results obtained with a traditional AMR code. In particular, these comparisons can extend also to complex applications like galaxy formation where many additional physics available in AREPO needs to be used. Second, it provides a toolbox to quickly implement new numerical methods like flux limited diffusion or discontinuous Galerkin hydrodynamics approaches as discussed in Chapters 5 and 7.

Ideally, the AMR module should reuse as many parts of the AREPO code as possible to simplify the method comparisons. The Voronoi mesh construction already needs a tree like data structure for a fast neighbour search. Thus, implementing a tree-based AMR code is a natural choice. As many data structures filled out by the Voronoi mesh construction are reused. As a result, most other parts, which do not depend on the type of mesh used, need no adjustment.

6.2 AMR mesh generation

The main task of the mesh generation module is to generate a list of all active interfaces between cells containing their area, and to provide a mechanism to split or merge cells into smaller or larger ones.

A tree like data structure consists of two entity types: Internal nodes and leaf nodes. An internal node has up to 2^d child nodes. In order to obtain a volume filling AMR tessellation, we always require full occupancy of all 2^d children in an internal node, otherwise gaps would occur. In our case leaf nodes are associated with the AMR cells. Each internal and leaf node knows its parent node.

The root node is spanning the entire simulation domain. Each child of a node with volume V has a volume of $V/2^d$ and fills one of the octants¹. Each node has an associated level l , with $l = 0$ denoting the root node. An example of an AMR mesh in 1D is shown in Figure 6.1. The tree is distributed among the MPI tasks. Each

¹or quadrant in 2D, for brevity we will only discuss the 3D case here

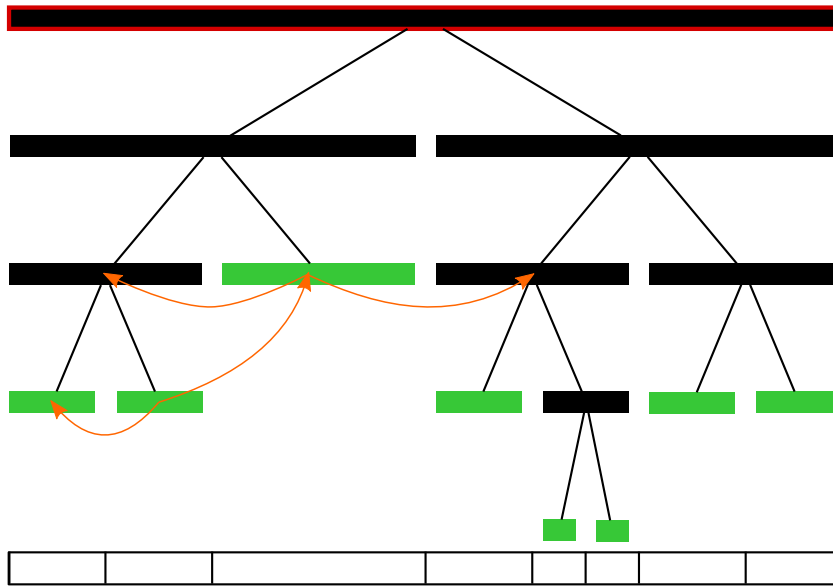


Figure 6.1: Example of an AMR tree in 1D. The top node represents the root node spanning the entire box. Internal tree nodes are shown in black and AMR cells or leaf nodes in green. The corresponding mesh is shown at the bottom. Orange arrows show neighbour relations.

process has a top tree, which is the same on all tasks. The part of the tree containing the local domain is stored along with a ghost layer for neighbouring domains.

Along with each node a list of the $2d$ direct neighbours in the d directions is stored. Neighbours in diagonal directions are not explicitly stored, but they can be easily obtained through neighbour of neighbour relations. For stability reasons, the level among neighbouring cells might jump at most by ± 1 in any direction including the diagonal directions. Thus, a cell of level l can either have four cells at level $l + 1$, one cell at the same level l , or a cell at level $l - 1$ as a neighbour. The neighbour node of an internal or leaf node at level l can either be an internal node or leaf node at the same level or a leaf node at level $l - 1$. A cell with split neighbour cells has an internal node as a neighbour in that direction.

Fluxes are computed between cells, always using the smaller interface. A cell can thus receive contributions from up to four other cells in any given direction. A node stores the averaged hydro state of all leaf nodes below that node as well. These averaged quantities are required to provide necessary boundary information at interfaces with a level jump. These averaged quantities can be easily computed in a recursive algorithm by first computing the averaged state of all children and then computing the averaged state of a node.

Now we need to ensure the level jump condition. For a cell at level l , we need to check the neighbours in all 26 directions. If they are a cell, they are either at the same level l , or at a smaller level $l - 1$. We do not need to check the other case of a node at level l with cells on level $l + 1$, as we go through the mesh level by level starting from the level with the smallest cells. Any violation of the level jump condition induced by this node and its cells would already have been detected and repaired. Along the inner directions towards the centre of an internal node, the level jump condition is always fulfilled. Fulfilling the level jump condition towards the outer direction requires the parent node to have either a cell at level $l - 1$, which is the same level as the parent node, or an internal node as a neighbour. This condition is equivalent to requiring that the grandparent node at level $l - 2$ has a node as a neighbour in that direction. Thus, it is more convenient to enforce the level jump condition on the level $l - 2$ of the grandparent: If a child of a node is either an internal node or a flagged cell (which will turn into a node after refinement), we need to check all surrounding neighbours and flag them as well, turning cells on level $l - 2$ into cells with level $l - 1$. Afterwards, the routine repeats on the next level.

To generate a more stable mesh, we additionally apply an optional mesh smoothing: This means that an additional buffer region of refined cells around cells refined based on a physical condition is generated. This is done by executing the refinement map routine multiple times. In these extra runs, refinement of a cell is triggered if a neighbouring cell or node is flagged for refinement. After the refinement map has been built, flagged cells will be split and un-flagged nodes will be merged to a single cell.

6.4 Gradient estimation

The reconstruction step of the finite volume flux computation requires a local gradient estimator. Such a gradient estimator can be obtained using finite difference operators. We use a symmetric first order accurate estimator for the derivative. A derivative estimate for a function f is given by

$$\left. \frac{df}{dx} \right|_{x_i} = \frac{f(x_{i+1}) - f(x_{i-1}))}{2h_i}, \quad (6.1)$$

where h_i is the length of the AMR cell and $f(x_i)$ the value at the discrete position x_i . The full gradient is determined by applying the finite difference formula in all directions.

At a level jump, boundary information is required. On each internal node we store averaged data of all cells below that internal node. If the neighbouring cells are on a finer level, the value stored on the internal node is used instead. In the opposite case of a larger neighbour cell, the central value of the larger cell is interpolated to the position of a corresponding neighbour cell on the same level. This requires a computation of the gradient estimates level by level, starting at the coarsest root level.

6.5 Finite volume method

The Euler equations can be written in integral form as

$$\frac{d}{dt} \int_{V_i} \mathbf{q}(\mathbf{x}, t) dV = \int_{\partial V_i} \mathbf{F}(\mathbf{q}(\mathbf{x}, t)) d\mathbf{A}, \quad (6.2)$$

with the state (vector) \mathbf{q} , infinitesimal surface normal $d\mathbf{A}$, and flux tensor \mathbf{F} . The left integral goes over the control volume V_i , while the integral on the right side extends over the surface of that volume. The control volume V_i is given by the AMR cells. We define the volume integrated values inside a cell with centre \mathbf{x}_i and at time t^n as

$$\mathbf{Q}(\mathbf{x}_i, t^n) = \int_{V_i} \mathbf{q}(\mathbf{x}, t^n) dV. \quad (6.3)$$

The discretized update step for Q is then

$$\mathbf{Q}(\mathbf{x}_i, t^{n+1}) = \mathbf{Q}(\mathbf{x}_i, t^n) - \Delta t \sum_j A_{ij} \mathcal{F}(\bar{\mathbf{q}}_L(\mathbf{x}_{ij}, t^{n+1/2}), \bar{\mathbf{q}}_R(\mathbf{x}_{ij}, t^{n+1/2}), \mathbf{n}_{ij}), \quad (6.4)$$

with timestep size Δt , surface area A_{ij} and surface normal vector \mathbf{n}_{ij} . The sum extends over all surfaces elements of the i -th cell with corresponding neighbour cell j . The intercell flux \mathcal{F} is evaluated using time and spatially extrapolated states $\bar{\mathbf{q}}_L(\mathbf{x}_{ij}, t^{n+1/2})$ and $\bar{\mathbf{q}}_R(\mathbf{x}_{ij}, t^{n+1/2})$ at the interface. Here $\bar{\mathbf{q}}_L$ is the extrapolated value from the left based on the i -th cell, while $\bar{\mathbf{q}}_R$ is the extrapolated value from the right for the j -th cell. The spatial extrapolation is done using the local gradient estimate,

$$q_{L/R}(\mathbf{x}_{ij}, t^n) = q(\mathbf{x}_{i/j}, t^n) + \Delta \mathbf{x}_{L/R} \nabla q, \quad (6.5)$$

with $\Delta \mathbf{x}_{L/R}$ being the vector connecting the centre of the cell with the centre of the interface. The time extrapolation is done by applying a forward Euler step to the state vector using the differential Euler equations:

$$\bar{\mathbf{q}}_{L/R}(\mathbf{x}_{ij}, t^{n+1}) = \mathbf{q}_{L/R}(\mathbf{x}_{ij}, t^n) - \Delta t \mathbf{F}(\mathbf{q}_{i/j}) \cdot \nabla \mathbf{q}_{i/j}. \quad (6.6)$$

The flux function $\mathcal{F}(\bar{\mathbf{q}}_L, \bar{\mathbf{q}}_R, \mathbf{n})$ is given by the solution of the corresponding Riemann problem. The Riemann problem assumes constant left and right states $\bar{\mathbf{q}}_L$ and $\bar{\mathbf{q}}_R$ at the interface with surface normal vector \mathbf{n} . Various approximate Riemann solvers are discussed in the literature. We use an exact Riemann solver here, which calculates the exact analytical solution.

6.5.1 Slope limiting

In smooth parts of the flow, our scheme is formally second order accurate. However, at strong gradients or discontinuities spurious oscillations then invariably appear.

This follows from Godunov's theorem which states that any linear scheme free from generating new extrema can only be of first order accuracy. The goal is then to construct a high resolution scheme, which is of second order accuracy in smooth parts, but can still resolve sharp discontinuities without introducing spurious oscillations. This is only possible for non-linear schemes.

The total variation (TV) of a scalar quantity q is defined as

$$\text{TV}(q) = \frac{1}{2} \sum_i \sum_{j \in \text{NGB}(i)} |q_j - q_i|, \quad (6.7)$$

and a scheme is said to be total variation diminishing (TVD) if

$$\text{TV}(q^j) \leq \text{TV}(q^i) \quad \forall j \geq i. \quad (6.8)$$

It can be shown that TVD is an essential property needed to prove convergence of a non-linear scheme. In the case of a scalar linear advection equation, various criteria for TVD schemes can be derived and proven. The situation is a bit less clear for non-linear partial differential equations like the Euler equations. Here, it is common practice to simply employ methods adapted from linear advection equations. Results obtained with these methods for non-linear schemes are usually found to be oscillation free in practice, even though formal proofs are often unavailable.

One possibility is to replace the estimated gradients (∇q) by so-called slope limited gradients

$$(\nabla q)' = \psi(r)(\nabla q), \quad (6.9)$$

with a slope limiter $\psi(r)$ and $r = (q_i - q_{i-1})/(q_{i+1} - q_i)$. The slope limiter ψ has to remain inside a so called TVD region described by

$$\psi(r) = 0 \quad \text{for } r \leq 0, \quad (6.10)$$

$$0 \leq \psi(r) \leq \min(\psi_L(r), \psi_R(r)) \quad \text{for } r > 0, \quad (6.11)$$

with

$$\psi_L(r) = \frac{2r}{1+r}, \quad (6.12)$$

$$\psi_r(r) = \frac{2}{1+r}. \quad (6.13)$$

The slope limiter is applied for each component of \mathbf{q} and for each direction independently. For comparison, we have implemented several slope limiter functions ψ discussed in the literature in our code:

- A Superbee type limiter:

$$\psi(r) = \begin{cases} 0 & \text{if } r \leq 0 \\ 2r & \text{if } 0 \leq r \leq 1/2 \\ 1 & \text{if } 1/2 \leq r \leq 1 \\ \min(r, \psi_R(r), 2) & \text{if } r > 1 \end{cases} \quad (6.14)$$

- A van Leer type limiter:

$$\psi(r) = \begin{cases} 0 & \text{if } r \leq 0 \\ \min\left(\frac{2r}{1+r}, \psi_R(r)\right) & \text{if } r \geq 0 \end{cases} \quad (6.15)$$

- A van Albada type limiter:

$$\psi(r) = \begin{cases} 0 & \text{if } r \leq 0 \\ \min\left(\frac{r(1+r)}{1+r^2}, \psi_R(r)\right) & \text{if } r \geq 0 \end{cases} \quad (6.16)$$

- A Minbee type limiter:

$$\psi(r) = \begin{cases} 0 & \text{if } r \leq 0 \\ r & \text{if } 0 \leq r \leq 1 \\ \min(1, \psi_R(r)) & \text{if } r \geq 1 \end{cases} \quad (6.17)$$

An alternative approach to limit the slope was proposed in Springel [2010]:

$$\psi = \min(1, \psi_{ij}) \quad (6.18)$$

with

$$\psi_{ij} = \begin{cases} (q_i^{\max} - q_i)/\Delta q_{ij} & \text{for } \Delta q_{ij} > 0 \\ (q_i^{\min} - q_i)/\Delta q_{ij} & \text{for } \Delta q_{ij} < 0 \\ 1 & \text{for } \Delta q_{ij} = 0, \end{cases} \quad (6.19)$$

$\Delta q_{ij} = (\nabla q)_i \Delta \mathbf{x}_{ij}$, $q_i^{\max} = \max(q_j)$ and $q_i^{\min} = \min(q_j)$.

6.6 Test problems

In the following, we show four test problems to assess the performance and correctness of our AMR implementation. In particular, we will study the impact of mesh smoothing and the choice of slope limiter in various test cases.

6.6.1 Shock tube

The shock tube tests consists of constant left and right initial states, separated by a diaphragm at $x = 0.3$ in a 1D box. The left state is given by $\rho_L = 1$, $v_L = 0.75$ and $P_L = 1$. The right state is given by $\rho_R = 0.125$, $v_L = 0$ and $P_L = 0.1$. For the test we use an adiabatic index of $\gamma = 1.4$. The simulation is evolved until $t = 0.2$. A static mesh with 512 cells in the x -direction is used to resolve the box of size 1.

Figure 6.3 shows the profiles of the density ρ , velocity v , pressure P and specific internal energy u . From left to right, a rarefaction wave, a contact discontinuity and a

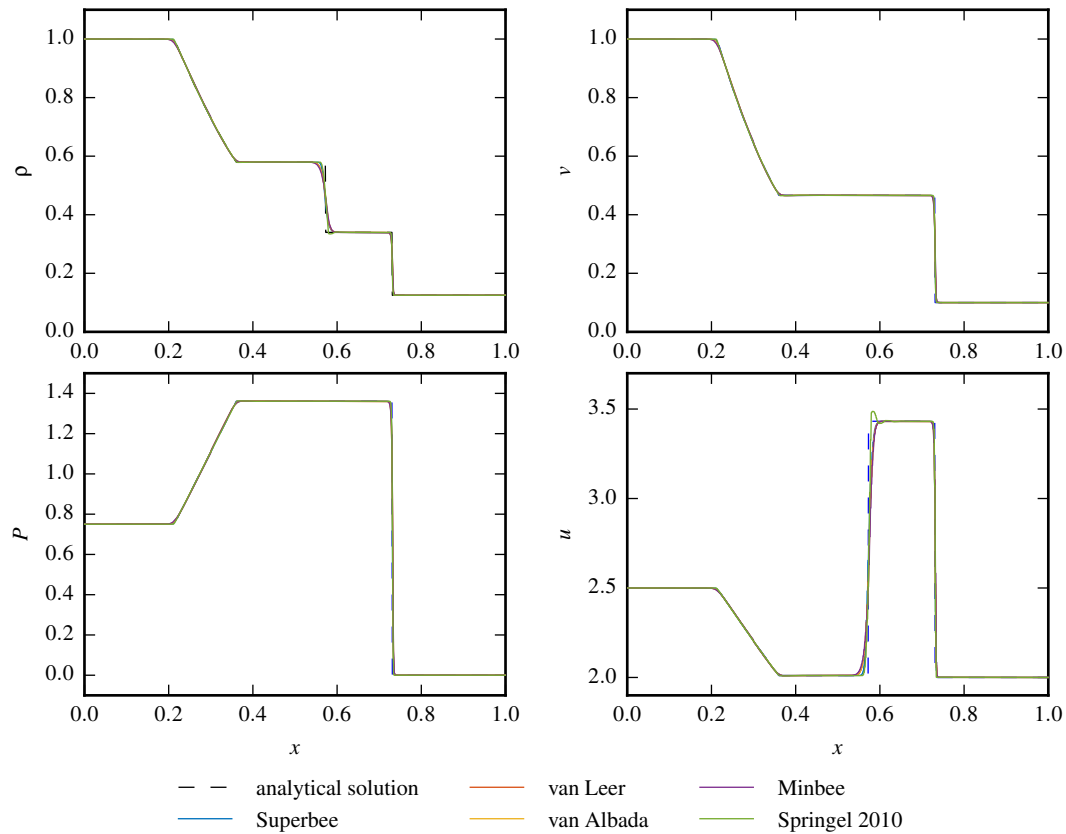


Figure 6.3: Solution of the shock wave test at $t = 0.2$. From left to right, a rarefaction fan, a contact discontinuity and a shock wave is visible. All tested slope limiters are more or less indistinguishable from each other. The limiter of Springel [2010] is a bit less restrictive, but shows slight oscillations, especially visible in the internal energy u at the contact discontinuity.

shock wave are visible. All tested slope limiter produce results almost indistinguishable from each other. The shock wave is sharply resolved in all cases, but also a little bit smeared out compared with the analytical solution. Also, the rarefaction fan is well resolved in all cases. The most difficult wave is the contact discontinuity. In all cases the wave is smeared out more than the shock wave, but still well resolved. The limiter proposed in Springel [2010] produces a sharper result in the density ρ , however still slightly smearing the contact wave. This comes at a price of slight oscillations, which are especially visible in the lower panel that shows the internal energy u .

6.6.2 Kelvin-Helmholtz instability

The Kelvin-Helmholtz instability test involves a contact discontinuity subject to a shearing flow. In a two dimensional periodic box of size 1 we set up a middle layer, ranging from $0.25 < y < 0.75$, with a density of $\rho = 2$ and a surrounding region

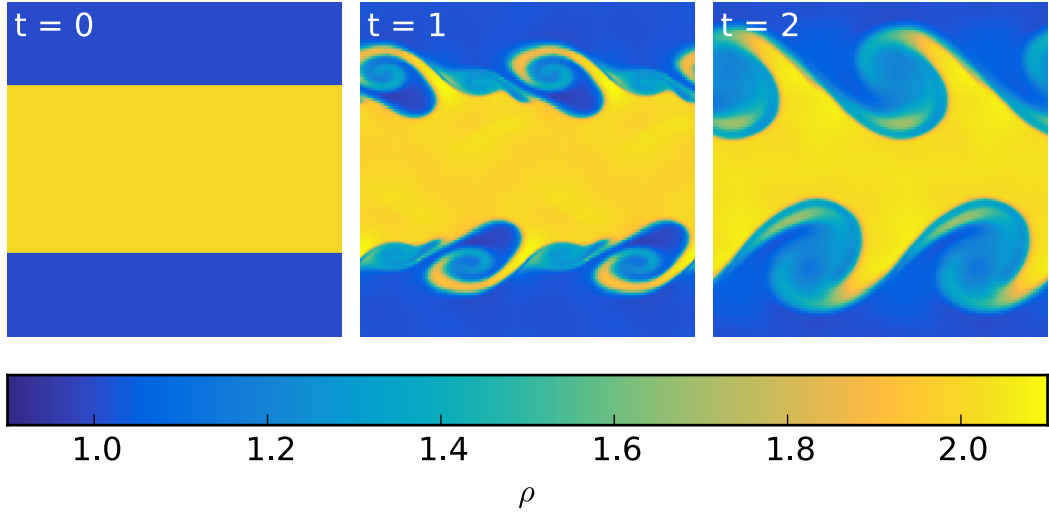


Figure 6.4: The figure shows the Kelvin-Helmholtz instability at $t = 0$, at $t = 1$ and at $t = 2$. The run uses AMR and mesh smoothing is applied twice. The initial conditions are seeded with an initial velocity perturbation to trigger the fluid instability. Over time billows start to form and grow.

with $\rho = 1$. The pressure is constant throughout the box with $P = 2.5$ and $\gamma = 5/3$. The middle layer moves with $v_x = 0.5$ to the right, whereas the outer region moves with the same speed to the left. Initially, we start with a constant mass resolution corresponding to a resolution of $\Delta x = 1/128$ in the outer layer and $\Delta x = 1/256$ in the middle layer. The simulation is followed up to $t = 2$. The AMR mesh is refined to keep the mass within a cell roughly constant. We compare runs with AMR and mesh smoothing, AMR without mesh smoothing, and a static grid without AMR, against each other.

In Figure 6.4, we show the initial conditions and snapshots at $t = 1$ and $t = 2$ for a run using AMR and mesh smoothing. The initial instability seeds small billows, which grow over time. The impact of resolving the high density region in the middle with four times as many cells as the outer regions can be assessed in Figure 6.5. All panels show the output at the final time $t = 2$. The left most panel is identical to the final result shown in Figure 6.4. The middle panel applies AMR, but no mesh smoothing. The rightmost panel shows a run on a Cartesian mesh without AMR and resolves the complete box with the highest resolution used in the run with AMR, i.e. with 256×256 cells in total. The Cartesian mesh run shows the most detailed billows. Especially the low density regions of the vortices show more detailed structure than in the AMR runs, which is due to the higher resolution available in these regions in the Cartesian mesh run and due to the fall back to first order convergence at level jumps. However, the overall structure is mostly unaffected by using AMR. Also, the differences between using mesh smoothing and not using mesh smoothing are rather minor for this test. The AMR level map at the final time is shown in Figure 6.6. The high resolution region follows the high density region of the billows.

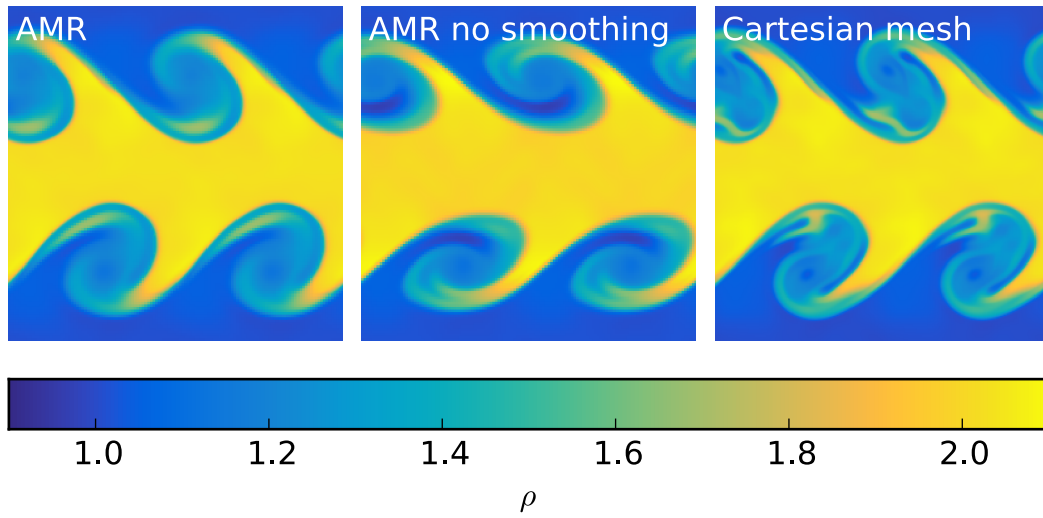


Figure 6.5: The figure compares the results obtained at $t = 2$ in a run with mesh smoothing applied twice, a run with AMR and no mesh smoothing and a Cartesian mesh without using AMR at a resolution of 256×256 cells.

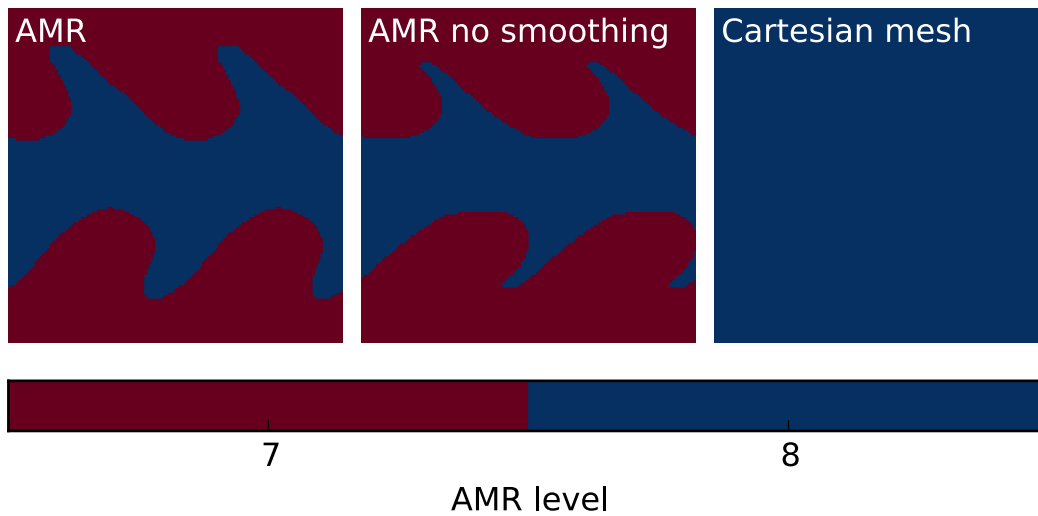


Figure 6.6: The figure shows a map of the final AMR level at $t = 2$. The run in the left panel applies mesh smoothing twice, while the middle panel shows a run without any mesh smoothing. The right panel shows the corresponding level of the Cartesian run without AMR.

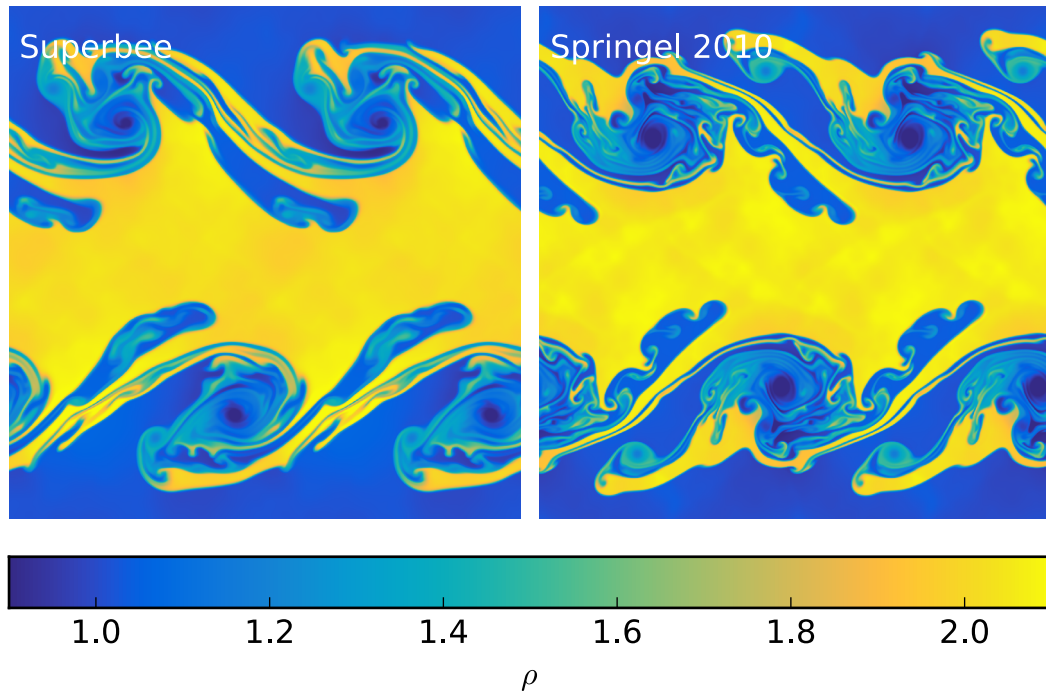


Figure 6.7: A high resolution version of the Kelvin-Helmholtz instability on a 1024×1024 static grid without AMR. Both panels show the density at $t = 2$. The run shown in the left panel is using a Superbee slope limiter, while the right panel shows a run with the limiter proposed in Springel [2010].

To assess the difference induced by the choice of slope limiters, we compare a Superbee like limiter with the limiter discussed in Springel [2010]. In Figure 6.7 we show the final output at $t = 2$ for a run with 1024×1024 cells. The overall shape is similar for both slope limiters. The Superbee limiter in the left panel smooths out the solution slightly more. Especially secondary Kelvin Helmholtz instabilities in the “finger” like structures following the billows are more suppressed by the Superbee limiter. The limiter of Springel [2010] also allows for a richer structure in the vortices of the primary billows.

6.6.3 Sedov-Taylor blast wave

The Sedov-Taylor blast wave test simulates an explosion due to a large energy injection in a single point. Initially we start from a Cartesian mesh with 128^2 cells. A total energy of $E = 1$ is injected over the four central cells. The background density is $\rho = 1$ at a pressure of $P = 10^{-4}$, and we use an adiabatic index of $\gamma = 5/3$.

Due to the energy injection, an outgoing blast wave develops. Figure 6.8 shows the density of the simulation at nine instances in time. Initially the region behind the blast wave has a diamond like shape. This is an artifact due to the rectangular mesh: Information can only flow directly along coordinate axis. A flow in a diagonal direction

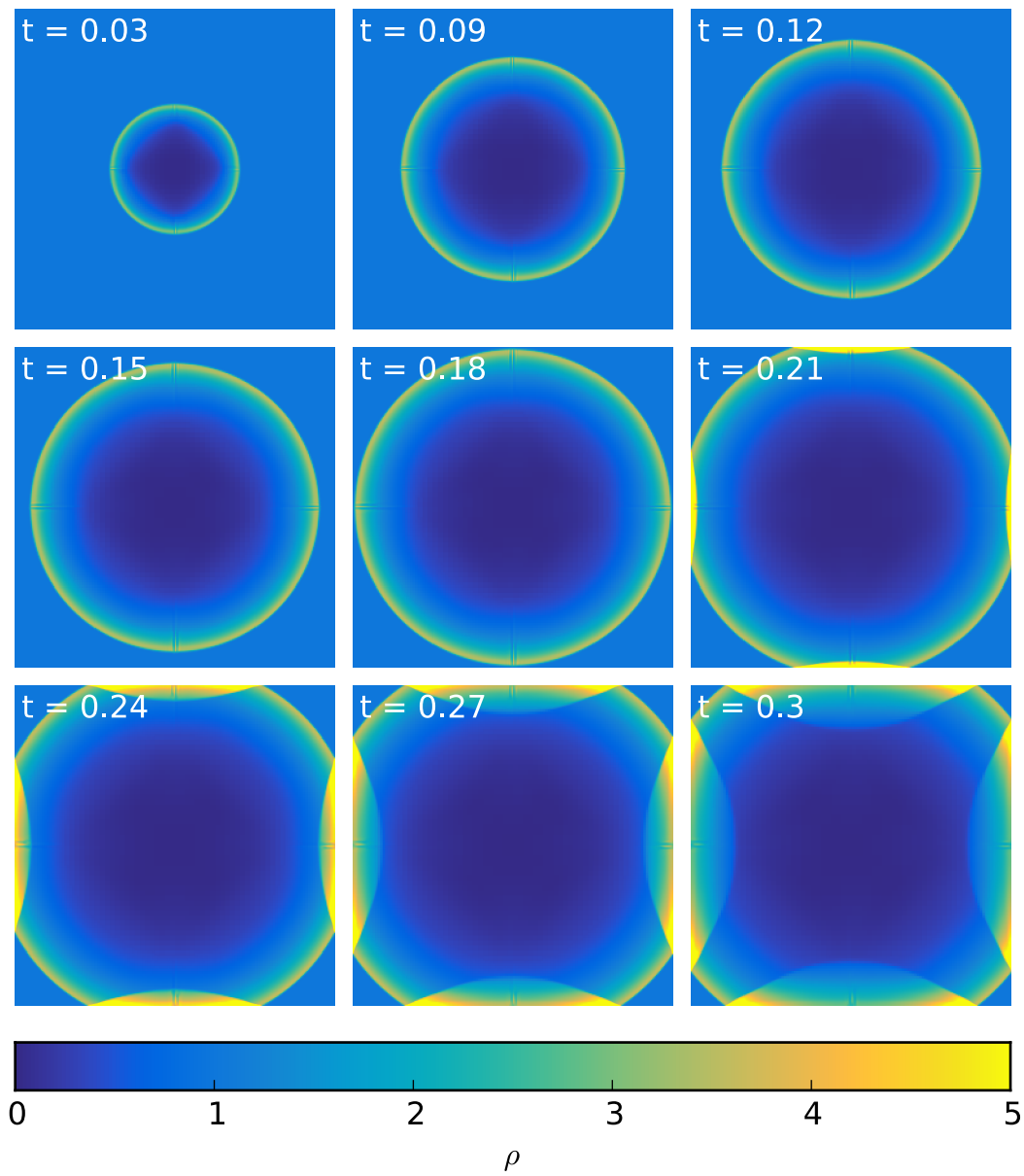


Figure 6.8: The time evolution of a 2D Sedov-Taylor blast wave. Initially the shape of the blast wave is non spherical due to artifacts introduced by the AMR mesh allowing fluxes only along the coordinate axis. However, rather quickly a round outgoing blast wave is established. At late times the blast wave interacts with itself, due to the periodic boundaries.

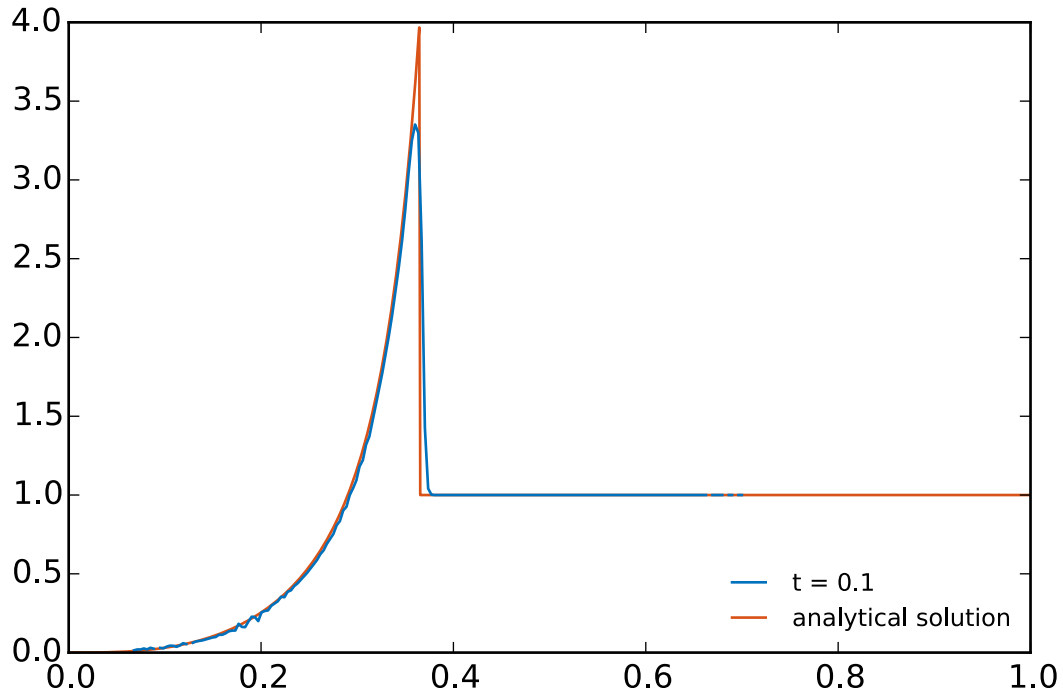


Figure 6.9: A radial profile through the Sedov Taylor blast wave at $t = 0.1$. The green line shows the analytical solution while the blue line is the output of our simulation at $t = 0.1$. The position of the shock wave agrees well with the analytical expectation. However, the maximum density reached in the simulation is lower than the analytical expectation.

takes two steps, as two interfaces are involved. This effect is most pronounced behind the blast wave, due to the low density and thus lower resolution. At around $t = 0.21$, the blast wave interacts with itself, due to the periodic boundaries. This leads to a further density enhancement directly at the boundary by two interacting shock waves.

Figure 6.9 shows a radial density profile of the simulation at $t = 0.1$. For comparison we show the analytically expected solution of the setup. The position of the blast wave is well matched. However, the peak density reached in the blast wave is lower. The maximum density reached is about $\rho = 3.3$ compared to the expected value of $\rho = 4$. The blast wave is a bit more extended as well. This problem can be resolved by using higher resolution.

6.6.4 Rayleigh-Taylor instability

The setup consists of a fluid with density $\rho = 2$ in the upper half of the box atop of a fluid with $\rho = 1$ in the lower half. We choose a simulation domain of size $L_x = 0.5$ and $L_y = 2$, with periodic boundary conditions in the x -direction and reflective

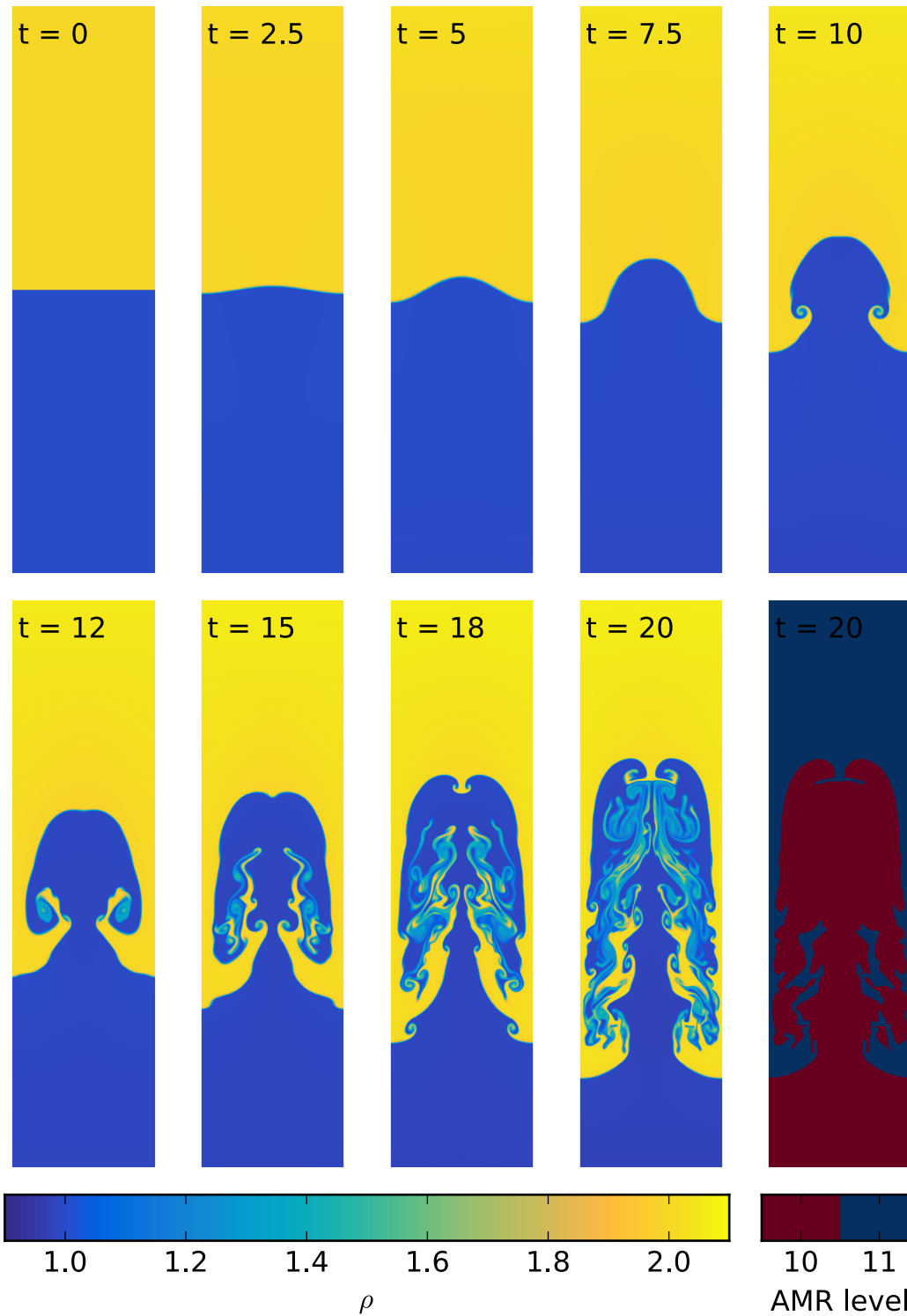


Figure 6.10: Time evolution of the Rayleigh-Taylor instability over time. The panels show the evolution of the density from $t = 0$ up to $t = 20$. The rightmost panel in the bottom row shows a map of the refinement levels at $t = 20$.

boundary conditions in the y -direction. An external gravitational field pointing downwards with $g = -0.1$ is imposed. The pressure is chosen to balance gravity by

$$P(y) = P_0 + g(y - 0.75)\rho, \quad (6.20)$$

where $P_0 = 2.5$ and an adiabatic index of $\gamma = 1.4$ is assumed. The hydrostatic equilibrium is slightly disturbed by adding a small velocity perturbation in the y -direction:

$$v_y(x, y) = w_0 [1 - \cos(4\pi x)] [1 - \cos(4\pi y/3)], \quad (6.21)$$

with $w_0 = 0.0025$. The resolution of the box is 256×1024 cells.

The initially small perturbation in the y -component of the velocity starts to lift some of the fluid upwards resulting in the time evolution shown in Figure 6.10. Due to the lower pressure higher up in the box, the fluid element continues to rise further, until a fluid instability starts to form. At the interface between the denser and lighter fluid vortices form and material eventually falls back. The rightmost panel in the lower row of Figure 6.10 shows the AMR refinement map at the final time $t = 20$. This panel nicely shows the adaptivity of the AMR mesh to the fluid density.

6.7 Summary

We have described and tested an extension of the moving-mesh code AREPO with a classic tree-based AMR module based on Cartesian grids. Our extension makes only the minimum amount of changes in AREPO required such that the AMR mesh can be used as an alternative to the moving-mesh in applications of the code. This allows for detailed comparisons of the performance of the moving-mesh technique relative to that of classic AMR using the same base code, thereby eliminating other sources of spurious differences that can otherwise creep in when completely independent codes are compared. Furthermore, the AMR mesh can now be used in applications where a moving-mesh offers no significant advantages. Its relative simplicity compared with an unstructured Voronoi mesh makes it also suitable as a development platform for new numerical schemes, such as the DG approach which we discuss in the next chapter.

7

Discontinuous Galerkin Hydrodynamics

7.1 Introduction

Discontinuous Galerkin methods were first introduced in Reed and Hill [1973] and later extended to non-linear problems [Cockburn et al., 1989, 1990; Cockburn and Shu, 1989, 1991, 1998]. First, they have been applied in engineering problems [see e.g. Cockburn et al., 2011; Gallego-Valencia et al., 2014], but very recently also to astrophysical problems [Mocz et al., 2014; Zanotti et al., 2015]. In this chapter we outline the equations and main ideas behind DG and introduce our implementation for the AMR module of AREPO.

In principle, finite volume schemes can be extended to high order methods. Most implementations use a simple linear data reconstruction resulting in a second order scheme. The next higher order method uses a parabolic data reconstruction, as implemented in piecewise parabolic schemes [Colella and Woodward, 1984]. While a linear reconstruction needs only the direct neighbours of each cell, a further layer is needed for a parabolic reconstruction. Thus, with the increase of the order of a scheme, the required stencil will grow as well. Especially in a parallelized code, this affects the scalability, as the ghost region around the local domain has to grow as well for a deeper stencil, resulting in a larger data exchange among different MPI processes and higher memory need.

In contrast, DG methods only need information about their direct neighbours, independent of the order of the scheme. Furthermore, the computational workload is not only spent on computing fluxes between cells, but has an internal contribution from each cell as well. The latter part is much easier to parallelize in a hybrid parallelization code. Additionally, DG provides a framework to derive discretized equations up to an arbitrary convergence order. These features make DG methods a compelling approach for future exa-scale machines. Building higher order methods

with a classical finite volume approach is a rather difficult task in comparison, which might explain why only second and third order finite volume methods are used in practice.

In the following we will first describe how the solution is described using a set of basis functions. Then, we explain how initial conditions can be derived and how they are evolved forward in time. Finally, we consider a DG extension to AMR meshes and discuss suitable slope limiters.

7.2 Field representation using basis functions

Instead of describing the solution with averaged values \mathbf{q} within each cell, in DG the solution is represented by polynomials of degree k . This polynomial representation is continuous inside a cell, but discontinuous across cells, hence the name discontinuous Galerkin method. Inside a cell K , the state is described by a function $\mathbf{q}^K(\mathbf{x}, t)$. This function is only defined on the volume of cell K . In the following, we will write \mathbf{q}^K as the polynomial representation of the state inside cell K . The polynomials of degree k form a vector space, and the state \mathbf{q}^K within a cell can be represented using weights \mathbf{w}_l^K , where l denotes the component of the weights vector. Each \mathbf{w}_l contains an entry for each of the five conserved hydrodynamic quantities. Using a set of suitable orthogonal basis functions $\phi_l^K(\mathbf{x})$ the state in a cell can be expressed as

$$\mathbf{q}^K(\mathbf{x}, t) = \sum_{l=1}^{N(k)} \mathbf{w}_l^K(t) \phi_l^K(\mathbf{x}). \quad (7.1)$$

Note how the time and space dependence on the right hand side is split up into two functions. This will provide the key ingredient for discretizing the continuous partial differential equations into a set of coupled ordinary differential equations.

The vector space of all polynomials up to degree k has the dimension $N(k)$. The l -th component of the vector can be obtained through a projection of the state \mathbf{q} onto the l -th basis function:

$$\mathbf{w}_l^K(t) = \frac{1}{|K|} \int_K \mathbf{q}(\mathbf{x}, t) \phi_l^K(\mathbf{x}) dV, \quad (7.2)$$

with $|K|$ being the volume of cell K and $\mathbf{w}_l^K = (w_{\rho,l}, \mathbf{w}_{p,l}, w_{e,l})$ being the l -th component of the weight vector of the density, momentum density and total energy density. The integrals can be either solved analytically or numerically using Gauss quadrature rules. By $w_{i,l}$ we refer to a single component of the l -th weight vector, i.e. $w_{0,0}$ and $w_{0,1}$ are the zeroth and first weight of the density, which correspond to the mean density and a quantity proportional to the gradient inside a cell, respectively.

7.2.1 Basis functions

We use a tensor product of Legendre polynomials as basis functions ϕ_l^K . To more easily accommodate an AMR mesh with variable cell sizes, the cells are rescaled such

that they span a coordinate system extending from -1 to 1 . The transformation is given by

$$\boldsymbol{\xi} = \frac{2}{\Delta x^K} (\mathbf{x} - \mathbf{x}^K), \quad (7.3)$$

with \mathbf{x}^K being the centre of cell K .

The full set of basis functions can be written as

$$\{\phi_l(\boldsymbol{\xi})\}_{l=1}^{N(k)} = \left\{ \tilde{P}_u(\xi_1) \tilde{P}_v(\xi_2) \tilde{P}_w(\xi_3) \mid u, v, w \in \mathbb{N}_0 \wedge u + v + w \leq k \right\}, \quad (7.4)$$

where \tilde{P}_u are scaled Legendre polynomials of degree u . The sum of the degrees of the individual basis functions has to be equal or smaller than the degree k of the DG scheme. Thus, the vector space of all polynomials up to degree k has the dimensionality

$$N(k) = \sum_{u=0}^k \sum_{v=0}^{k-u} \sum_{w=0}^{k-u-v} 1 = \frac{1}{6}(k+1)(k+2)(k+3). \quad (7.5)$$

Legendre polynomials

The Legendre polynomials are solutions to the Legendre equation with integer number n :

$$\frac{d}{d\xi} \left[(1 - \xi^2) \frac{d}{d\xi} P_n(\xi) \right] + n(n+1)P_n(\xi) = 0, \quad n \in \mathbb{N}_0. \quad (7.6)$$

The solutions $P_n(\xi)$ are polynomials of degree up to n . The first six polynomials are:

$$P_0(\xi) = 1 \quad (7.7)$$

$$P_1(\xi) = \xi \quad (7.8)$$

$$P_2(\xi) = \frac{1}{2}(3\xi^2 - 1) \quad (7.9)$$

$$P_3(\xi) = \frac{1}{2}(5\xi^3 - 3\xi) \quad (7.10)$$

$$P_4(\xi) = \frac{1}{8}(35\xi^4 - 30\xi^2 + 3) \quad (7.11)$$

$$P_5(\xi) = \frac{1}{8}(63\xi^5 - 70\xi^3 + 15\xi) \quad (7.12)$$

and can be obtained through the recursion relation

$$(n+1)P_{n+1}(\xi) = (2n+1)\xi P_n(\xi) - nP_{n-1}(\xi). \quad (7.13)$$

The scaling is chosen as

$$\tilde{P}(\xi)_l = \sqrt{2l+1}P(\xi)_l. \quad (7.14)$$

This results in the following orthogonality relation:

$$\int_{-1}^1 \tilde{P}_i(\xi) \tilde{P}_j(\xi) d\xi = \begin{cases} 0 & \text{if } i \neq j \\ 2 & \text{if } i = j. \end{cases} \quad (7.15)$$

7.3 Initial conditions

To obtain the initial conditions, we have to find weight vectors \mathbf{w}_l^K at $t = 0$ corresponding to the initial conditions $\mathbf{q}(\mathbf{x}, 0)$. The polynomial representation of a scalar quantity described by the weight vector is

$$q_i^K(\mathbf{x}, 0) = \sum_{l=1}^{N(k)} w_{i,l}^K(0) \phi_l^K(\mathbf{x}). \quad (7.16)$$

The difference between the prescribed actual initial condition and the polynomial representation should be minimal, which can be achieved by varying the weight vectors \mathbf{w}_l^K in each cell for each hydrodynamical component i individually:

$$\min_{\{w_{i,l}^K(0)\}_l} \int_K q_i^K(\mathbf{x}, 0) - q_i(\mathbf{x}, 0) dV, \quad (7.17)$$

Thus, the l -th component of the initial weights \mathbf{w}_l^K is given by

$$w_l^K(0) = \frac{1}{|K|} \int_K \mathbf{q}(\mathbf{x}, 0) \phi_l^K(\mathbf{x}) dV. \quad (7.18)$$

Transformed into the ξ coordinate system, the equation becomes

$$w_l^K(0) = \frac{1}{8} \int_{[-1,1]^3} \mathbf{q}(\boldsymbol{\xi}, 0) \phi_l(\boldsymbol{\xi}) d\boldsymbol{\xi}. \quad (7.19)$$

In principal, the integral can be computed analytically for known analytical initial conditions. Alternatively, it can be computed numerically using a Gauss quadrature rule:

$$w_l^K(0) = \frac{1}{8} \sum_{q=1}^{(k+1)^3} \mathbf{q}(\mathbf{x}_q, 0) \phi_l(\boldsymbol{\xi}_q) \omega_q, \quad (7.20)$$

using $(k+1)^3$ sampling points \mathbf{x}_q and corresponding quadrature weights ω_q . Note that for polynomial initial conditions of up to degree k the Gauss quadrature rule is exact.

7.4 Time evolution equations

The solution is discretized using time dependent weight vectors $\mathbf{w}_l^K(t)$. The time evolution equations for these weights can be derived from the Euler equation,

$$\frac{\partial \mathbf{q}}{\partial t} + \sum_{\alpha=1}^3 \frac{\partial \mathbf{F}_\alpha(\mathbf{q})}{\partial x_\alpha} = 0. \quad (7.21)$$

To obtain an evolution equation for the l -th weight, the Euler equation is multiplied from the right with ϕ_l and integrated over the the volume of cell K ,

$$\frac{d}{dt} \int_K \mathbf{q}^K \phi_l^K dV - \sum_{\alpha=1}^3 \int_K \frac{\partial \mathbf{F}_\alpha(\mathbf{q})}{\partial x_\alpha} \phi_l^K dV = 0. \quad (7.22)$$

Integrating the second term by parts leads to a volume integral over the interior of the cell and a surface integral with surface normal vector \mathbf{n} :

$$\frac{d}{dt} \int_K \mathbf{q}^K \phi_l^K dV - \sum_{\alpha=1}^3 \int_K \mathbf{F}_\alpha \frac{\partial \phi_l^K}{\partial x_\alpha} dV + \sum_{\alpha=1}^3 \int_{\partial K} \mathbf{F}_\alpha \phi_l^K n_\alpha dA = 0. \quad (7.23)$$

We will now discuss the three terms in turn, starting with the first one. Inserting the definition of \mathbf{q}^K and using the orthogonality relation of the basis functions simplifies this term to the time derivative of the l -th weight:

$$\frac{d}{dt} \int_K \mathbf{q}^K \phi_l^K dV = |K| \frac{d\mathbf{w}_l^K}{dt}. \quad (7.24)$$

We transform the next term into the ξ -coordinate system. The term involves a volume integral, which is solved using a Gauss quadrature rule:

$$\begin{aligned} & \sum_{\alpha=1}^3 \int_K \mathbf{F}_\alpha(\mathbf{q}^K(\mathbf{x}, t)) \frac{\partial \phi_l^K(\mathbf{x})}{\partial x_\alpha} dV \\ &= \frac{(\Delta x^K)^2}{4} \sum_{\alpha=1}^3 \int_{[-1,1]^3} \mathbf{F}_\alpha(\mathbf{q}^K(\boldsymbol{\xi}, t)) \frac{\partial \phi_l(\boldsymbol{\xi})}{\partial \xi_\alpha} d\boldsymbol{\xi} \\ &= \frac{(\Delta x^K)^2}{4} \sum_{\alpha=1}^3 \sum_{q=1}^{(k+1)^3} \mathbf{F}_\alpha(\mathbf{q}^K(\boldsymbol{\xi}_q, t)) \left. \frac{\partial \phi_l}{\partial \xi_\alpha} \right|_{\boldsymbol{\xi}_q} \omega_q. \end{aligned} \quad (7.25)$$

The flux vector \mathbf{F}_α can be easily evaluated at the $(k+1)^3$ quadrature points $\boldsymbol{\xi}_q$ using the polynomial representation $\mathbf{q}^K(\boldsymbol{\xi}_q, t)$. An analytical expression can be obtained for the derivatives of the basis functions.

Finally, the last term is a surface integral over the cell boundary. Again, we transform the equation into the ξ -coordinate system and apply a Gauss quadrature rule to compute the integral:

$$\begin{aligned} & \sum_{\alpha=1}^3 \int_{\partial K} \mathbf{F}_\alpha \phi_l^K(\mathbf{x}) n_\alpha dA \\ &= \frac{(\Delta x^K)^2}{4} \int_{\partial[-1,1]^3} \mathcal{F}(\mathbf{q}_L^K(\boldsymbol{\xi}, t), \mathbf{q}_R^K(\boldsymbol{\xi}, t)) \phi_l(\boldsymbol{\xi}) n_\alpha dA' \\ &= \frac{(\Delta x^K)^2}{4} \sum_{a \in \partial[-1,1]^3} \sum_{q=1}^{(k+1)^2} \mathcal{F}(\mathbf{q}_L^K(\boldsymbol{\xi}_{a,q}, t), \mathbf{q}_R^K(\boldsymbol{\xi}_{a,q}, t)) \phi_l(\boldsymbol{\xi}_q) \omega_{a,q}. \end{aligned} \quad (7.26)$$

Each of the interface elements a is sampled using $(k + 1)^2$ quadrature points $\xi_{a,q}$. The numerical flux \mathcal{F} between the discontinuous states at both sides of the interface is computed using an exact or approximative HLLC Riemann solver. Note that only this term couples the individual cells with each other.

Equations (7.25) and (7.26) can be combined into a function $\mathbf{R}_l^K(\mathbf{w}_1, \dots, \mathbf{w}_{N(k)})$. Combining this with Equation (7.24) gives the following system of coupled ordinary differential equations solved for the weight vectors \mathbf{w}_l^K :

$$\frac{d\mathbf{w}_l^K}{dt} + \mathbf{R}_l^K(\mathbf{w}_1, \dots, \mathbf{w}_{N(k)}) = 0. \quad (7.27)$$

7.4.1 Time integration

Equation (7.27) is solved using a strong stability preserving (SSP) Runge-Kutta integrator [Gottlieb et al., 2001]. We define $\mathbf{y} = (\mathbf{w}_1, \dots, \mathbf{w}_{N(k)})$ and thus we have to solve

$$\frac{d\mathbf{y}}{dt} + R(\mathbf{y}) = 0. \quad (7.28)$$

A third order SSP Runge-Kutta scheme is given by

$$\mathbf{y}^{(0)} = \mathbf{y}^n \quad (7.29)$$

$$\mathbf{y}^{(1)} = \mathbf{y}^{(0)} - \Delta t^n R(\mathbf{y}^{(0)}) \quad (7.30)$$

$$\mathbf{y}^{(2)} = \frac{3}{4}\mathbf{y}^{(0)} + \frac{1}{4}\left(\mathbf{y}^{(1)} - \Delta t^n R(\mathbf{y}^{(1)})\right) \quad (7.31)$$

$$\mathbf{y}^{(3)} = \frac{1}{3}\mathbf{y}^{(0)} + \frac{2}{3}\left(\mathbf{y}^{(2)} - \Delta t^n R(\mathbf{y}^{(2)})\right) \quad (7.32)$$

$$\mathbf{y}^{n+1} = \mathbf{y}^{(3)}. \quad (7.33)$$

with initial value \mathbf{y}^n , final value \mathbf{y}^{n+1} , intermediate states $\mathbf{y}^{(0)}, \mathbf{y}^{(1)}, \mathbf{y}^{(2)}$, and time step size Δt^n .

7.4.2 Time-step calculation

The time step has to fulfill the following Courant criterium [Cockburn and Shu, 1989]:

$$\Delta t^K = \frac{C}{2k+1} \left(\frac{|v_1^K| + c^K}{\Delta x_1^K} + \frac{|v_2^K| + c^K}{\Delta x_2^K} + \frac{|v_3^K| + c^K}{\Delta x_3^K} \right)^{-1}, \quad (7.34)$$

with Courant factor C and sound speed c^K . The minimum over all cells is determined and taken as the global maximum allowed time step. Note the $(2k+1)^{-1}$ dependence of the time step, which leads to a reduction of the timestep for high order schemes.

7.4.3 External force fields

The coupling of an external force field to the Euler equations can be straightforwardly implemented in DG. The Euler equations become

$$\frac{\partial \mathbf{q}}{\partial t} + \sum_{\alpha=1}^3 \frac{\partial \mathbf{F}_\alpha(\mathbf{q})}{\partial x_\alpha} = \mathbf{s}, \quad (7.35)$$

with a source term

$$\mathbf{s} = \begin{pmatrix} 0 \\ \rho \mathbf{g} \\ \rho \mathbf{v} \cdot \mathbf{g} \end{pmatrix}. \quad (7.36)$$

Multiplication with the basis functions $\phi_l^K(\mathbf{x})$ and integration over the cell volume gives the corresponding source terms for the weights \mathbf{w}_l^K :

$$\begin{aligned} \mathbf{s}_l^K &= \int_K \mathbf{s}(\mathbf{x}, t) \phi_l^K(\mathbf{x}) \, dV \\ &= \frac{|K|}{8} \int_{[-1,1]^3} \mathbf{s}(\boldsymbol{\xi}, t) \phi_l(\boldsymbol{\xi}) \, d\boldsymbol{\xi} \\ &= \frac{|K|}{8} \sum_{q=1}^{(k+1)^3} \mathbf{s}(\boldsymbol{\xi}_q, t) \phi_l(\boldsymbol{\xi}_q) \omega_q. \end{aligned} \quad (7.37)$$

7.5 DG with adaptive mesh refinement

The extension of DG to an AMR mesh requires a mapping of the weights \mathbf{w}_l^K to corresponding weights $\mathbf{w}_l^{A \dots H}$ of smaller sub cells if a cell is refined. A corresponding mapping is required for derefining a cell, i.e. for merging these weights into a single cell. We note that finite volume methods with AMR fall back to first order accuracy at a level jump. This problem is not present in DG methods, making them an interesting method to be coupled with AMR.

7.5.1 Refinement

In the case of refining a cell, the weights of a sub cell A are given by minimizing the following term for each quantity i separately:

$$\min_{\{w_{i,l}^A\}_l} \int_A (q_i^K - q_i^A)^2 \, dV. \quad (7.38)$$

This again is achieved by computing the following projection integral over the space of sub cell A

$$w_{i,l}^A = \frac{1}{|A|} \int_A q_i^K \phi_l^A \, dV. \quad (7.39)$$

For q_i^K we insert the polynomial representation and obtain

$$w_{i,l}^A = \sum_{j=1}^{N(k)} w_{i,j}^K \frac{1}{|A|} \int_A \phi_l^A \phi_j^K dV. \quad (7.40)$$

The remaining integrals can be precomputed and form a projection matrix

$$(\mathbf{P}_A)_{l,j} = \frac{1}{|A|} \int_A \phi_l^A \phi_j^K dV. \quad (7.41)$$

In scaled ξ -coordinates, the matrix is given by

$$(\mathbf{P}_A)_{l,j} = \frac{1}{8} \iiint_{[-1,1]^3} \phi_l \left(\frac{\xi_1 - 1}{2}, \frac{\xi_2 - 1}{2}, \frac{\xi_3 - 1}{2} \right) \phi_j(\xi_1, \xi_2, \xi_3) d\xi. \quad (7.42)$$

For each sub cell A, \dots, H a corresponding projection matrix is defined.

In the following, we will define the vector $\hat{\mathbf{w}}_i = (w_{i,0}, \dots, w_{i,N(k)})$ for the weights of a single hydrodynamical quantity i . Using this notation the projection can be written in the compact form:

$$\hat{\mathbf{w}}_i^A = \mathbf{P}_A \hat{\mathbf{w}}_i^K. \quad (7.43)$$

No information is lost by refining a cell. The degrees of freedom of the sub cells are sufficient to represent the polynomial of the original cell K .

7.5.2 Derefinement

In case of derefining the sub cells A, \dots, H into a single cell K , a similar term has to be minimized as in the case of refinement:

$$\min_{\{w_{i,j}^K\}_j} \left(\int_A (q_i^K - q_i^A)^2 dV + \int_B (q_i^K - q_i^B)^2 dV + \dots \right) \quad (7.44)$$

This is fulfilled by choosing the weights of the coarse cell as

$$w_{i,j}^K = \frac{1}{|K|} \left(\int_A q_i^A \phi_j^K dV + \int_B q_i^B \phi_j^K dV + \dots \right). \quad (7.45)$$

In this expression, the polynomial representation can be inserted again

$$w_{i,j}^K = \frac{1}{|K|} \left(\int_A \sum_{l=1}^{N(k)} w_{i,l}^A \phi_l^A \phi_j^K dV + \int_B \sum_{l=1}^{N(k)} w_{i,l}^B \phi_l^B \phi_j^K dV + \dots \right),$$

which can be written in a more compact form using $\hat{\mathbf{w}}_i$ and the transposed projection matrices \mathbf{P}^\top :

$$\hat{\mathbf{w}}_i^K = \frac{1}{8} \left(\mathbf{P}_A^\top \hat{\mathbf{w}}_i^A + \mathbf{P}_B^\top \hat{\mathbf{w}}_i^B + \dots \right). \quad (7.46)$$

7.5.3 Refinement criterion

The usual AMR refinement criteria such as keeping the mass in a cell constant within a given factor can be applied to DG as well. A more interesting and computationally challenging refinement criterion is to refine steep gradients. The refinement criterion has to be implemented in a way which avoids runaway refinement of a resolved gradient. We refine a cell K if

$$\max(w_{2,0}^K, w_{3,0}^K, w_{4,0}^K) > \alpha \cdot w_t. \quad (7.47)$$

Here, $w_{2,0}^K$, $w_{3,0}^K$, and $w_{4,0}^K$ are the changes in density over a cell divided by $\sqrt{3}$. The target slope is set by the parameter w_t and the factor α controls the gradual refinement, introduced to avoid oscillation between a refined and derefined state.

The corresponding refinement criterium for a node L of the AMR tree is

$$\max(w_{2,0}^L, w_{3,0}^L, w_{4,0}^L) > \frac{1}{\alpha} \cdot w_t. \quad (7.48)$$

If this criterium is met, node L is kept and the cells below that node are not derefined into a single cell. Otherwise the cells are derefined.

7.6 Slope limiting

As for finite volume methods, the polynomial representation within a cell can lead to over- or undershooting at cell boundaries. This happens especially in the case of higher order schemes. To prevent growing oscillations, a slope limiter is applied. This slope limiter diminishes or erases the weights corresponding to the higher order polynomials. The art of a good slope limiter is to be only active when needed. If the limiting is done at unnecessary places, the advantages of a higher order scheme are lost. However, if the limiter is not restrictive enough, spurious oscillations are not sufficiently damped.

7.6.1 Component-wise limiter

This simple limiter limits each hydrodynamical quantity i separately. The linear change over a cell in each direction ($w_{\{2,3,4\},i}^K$) is compared against gradient estimates based on the mean values in the cell K and its neighbouring cells $W_K, E_K, N_K, S_K, T_K, B_K$.

$$\tilde{w}_{2,i}^K = \min\text{mod}(w_{2,i}^K, \frac{\beta}{\sqrt{3}}(w_{1,i}^K - w_{1,i}^{W_K}), \frac{\beta}{\sqrt{3}}(w_{1,i}^{E_K} - w_{1,i}^K)) \quad (7.49)$$

$$\tilde{w}_{3,i}^K = \min\text{mod}(w_{3,i}^K, \frac{\beta}{\sqrt{3}}(w_{1,i}^K - w_{1,i}^{S_K}), \frac{\beta}{\sqrt{3}}(w_{1,i}^{N_K} - w_{1,i}^K)) \quad (7.50)$$

$$\tilde{w}_{4,i}^K = \min\text{mod}(w_{4,i}^K, \frac{\beta}{\sqrt{3}}(w_{1,i}^K - w_{1,i}^{B_K}), \frac{\beta}{\sqrt{3}}(w_{1,i}^{T_K} - w_{1,i}^K)). \quad (7.51)$$

The minmod function is defined as

$$\text{minmod}(a, b, c) = \begin{cases} s \min(|a|, |b|, |c|) & s = \text{sign}(a) = \text{sign}(b) = \text{sign}(c) \\ 0 & \text{otherwise.} \end{cases} \quad (7.52)$$

If the weights $\tilde{w}_{\{2,3,4\},i}^K$ are equal to $w_{\{2,3,4\},i}^K$, the state of cell K is left unchanged, otherwise all the weights associated with the linear polynomials are set to $\tilde{w}_{\{2,3,4\},i}^K$ and all higher moments are set to zero. In this case, the state within a cell is given by

$$q_i^K(\mathbf{x}, t) = w_{1,i}^K + \tilde{w}_{2,i}^K \Phi_2^K + \tilde{w}_{3,i}^K \Phi_3^K + \tilde{w}_{4,i}^K \Phi_4^K. \quad (7.53)$$

The parameter β is chosen in the range of $[0.5, 1]$, where the choice of $\beta = 0.5$ corresponds to a TVD scheme. If a larger value is chosen, the scheme is less restrictive, but more prone to spurious oscillations.

In the case of AMR, direct neighbour cells on the same level may not be available in all 6 directions. In this case, virtual cells at the same level are constructed using the projection operators defined for refining or derefining cells.

Alternatively the limiting can be done in characteristic variables, where the slopes $w_{\{2,3,4\},i}^K$ and mean values $w_{1,i}$ are transformed into characteristic variables using the flux tensor $\mathbf{F}(\mathbf{q})$ of the mean cell value \mathbf{q} . To further reduce the limiting to only discontinuities, a total variation bounded (TVB) limiter can be obtained by replacing the minmod function with

$$\text{minmodB}(a, b, c) = \begin{cases} a & \text{if } |a| \leq M(\Delta x^K)^2 \\ \text{minmod}(a, b, c) & \text{otherwise,} \end{cases} \quad (7.54)$$

with a parameter M [Cockburn and Shu, 1998]. This modification further improves the convergence properties of the scheme.

7.6.2 Positivity limiter

At all times, the density ρ , pressure P and energy e should remain positive throughout the entire computational domain. However, due to higher moments this might be violated in some parts of the solution. This will turn into a problem for the DG solver, if the positivity property is violated at a quadrature point inside the cell or an interface. To avoid this problem, a so-called positivity limiter is used [Zhang and Shu, 2010]. This limiter strictly guarantees positivity only on a set of discrete points within a cell, but if they are spaced densely enough, the solution can be expected to remain positive everywhere. To guarantee positivity, a strong stability preserving Runge-Kutta scheme and positivity preserving Riemann solver is needed in addition.

The set of points where positivity is enforced has to include the cell interfaces, because fluxes are computed there. A possible choice of integration points, which include the integration edges, are the Gauss-Lobatto-Legendre (GLL) points. In the following, we will be using tensorial products of GLL and Gauss points, where one

coordinate is chosen from the set of GLL points and the remaining two are taken from the set of Gauss points:

$$S_x = \{(\hat{\xi}_r, \xi_s, \xi_t) : 1 \leq r \leq m, 1 \leq s \leq k+1, 1 \leq t \leq k+1\} \quad (7.55)$$

$$S_y = \{(\xi_r, \hat{\xi}_s, \xi_t) : 1 \leq r \leq k+1, 1 \leq s \leq m, 1 \leq t \leq k+1\}$$

$$S_z = \{(\xi_r, \xi_s, \hat{\xi}_t) : 1 \leq r \leq k+1, 1 \leq s \leq k+1, 1 \leq t \leq m\} \quad (7.56)$$

The full set of integration points is $S = S_x \cup S_y \cup S_z$, which includes all points where fluxes are evaluated in the integration step.

First, the minimum density at all points in the set S is computed:

$$\rho_{\min}^K = \min_{\boldsymbol{\xi} \in S} \rho^K(\boldsymbol{\xi}). \quad (7.57)$$

We define a reduction factor θ_1^K as

$$\theta_1^K = \min \left\{ \left| \frac{\bar{\rho}^K - \epsilon}{\bar{\rho}^K - \rho_{\min}^K} \right|, 1 \right\}, \quad (7.58)$$

with the mean density in the cell $\bar{\rho}^K$ (the 0-th density weight) and the minimum target density ϵ . All high order weights of the density are reduced by this factor

$$w_{j,1}^K \leftarrow \theta_1^K w_{j,1}^K, \quad j = 2, \dots, N(k). \quad (7.59)$$

To guarantee a positive pressure, a similar approach is taken:

$$\theta_2^K = \min_{\boldsymbol{\xi} \in S} \tau^K(\boldsymbol{\xi}), \quad (7.60)$$

with

$$\tau^K(\boldsymbol{\xi}) = \begin{cases} 1 & \text{if } P^K(\boldsymbol{\xi}) \geq \epsilon \\ \tau_* & \text{such that } P(\mathbf{q}^K(\boldsymbol{\xi}) + \tau_*(\mathbf{q}^K(\boldsymbol{\xi}) - \bar{\mathbf{q}}^K)) = \epsilon. \end{cases} \quad (7.61)$$

The equation for τ can not be solved analytically and has to be solved numerically. The equation is solved using a Newton-Raphson method. Now, the higher order weights of all quantities are reduced by θ_2

$$w_{j,i}^K \leftarrow \theta_2^K w_{j,i}^K, \quad j = 2, \dots, N(k), \quad i = 1, \dots, 5. \quad (7.62)$$

Additionally the timestep has to be modified slightly to

$$\Delta t^K = C \min \left(\frac{1}{2k+1}, \frac{\hat{w}_1}{2} \right) \left(\frac{|v_1^K| + c^K}{\Delta x_1^K} + \frac{|v_2^K| + c^K}{\Delta x_2^K} + \frac{|v_3^K| + c^K}{\Delta x_3^K} \right)^{-1}, \quad (7.63)$$

with the first GLL weight \hat{w}_1 . For a second order DG scheme the weights are $\hat{w}_1 = 1$ and $\hat{w}_1 = 1/3$ for a third and fourth order method.

7.7 Discussion

We summarized the ideas and equations behind a discontinuous Galerkin hydrodynamics implementation on top of an AMR mesh. Detailed results of test problems of our implementation can be found in Schaal et al. [2015]. In the following, we will summarize the main advantages and characteristics of a DG method:

- In addition to flux computations on the interface between neighbouring cells, internal fluxes are computed. The ratio of internal to interface flux computations rises with increasing order. These computations are easier to map to novel massive parallel compute architectures.
- The computation to memory access and computation to communication ratios are more favourable compared with traditional finite volume methods.
- The stencils involve only direct neighbours, even for higher order methods.
- DG provides a framework to derive higher order methods. It is in principle clear how to derive a numerical scheme of arbitrary order.

These advantages make DG methods an interesting approach for discretizing the Euler equations. However, at shocks, the standard method falls back to first order accuracy. If the problem at hand is dominated by shocks and discontinuities, this might be a major drawback. Otherwise, for smooth flow problems, DG shows clear advantages. In the following chapter we will focus on simulating subsonic turbulence with our DG implementation, which is an application involving relatively smooth flows.

8

Subsonic Turbulence Simulations using Discontinuous Galerkin Hydrodynamics

8.1 Introduction

Supersonic turbulence in the interstellar medium may well play a key role for regulating star formation [Klessen et al., 2000; Mac Low and Klessen, 2004]. Cosmological structure formation is believed to be another area where supersonic turbulence plays an important role, for example providing additional pressure in support for clusters of galaxies [Schuecker et al., 2004]. Also, subsonic turbulence is thought to be ubiquitously present in the intracluster medium and in part in the intergalactic medium as well.

The representation of the sub-cell solution using polynomials in DG is especially effective if smooth problems are considered. In such a case, the discontinuities between adjacent cells are minimal and the representation within a cell is very accurate. This makes subsonic turbulence simulations a very interesting first application of our new DG implementation.

As shown in Bauer and Springel [2012], subsonic turbulence can pose a hard problem for some of the simulation methods used in computational astrophysics. Standard SPH in particular struggles to reproduce results as accurate as finite volume codes, and a far higher computational effort would be required to obtain an equally large inertial range as obtained with a finite volume method. However, we should point out that many improvements on standard SPH have been proposed in recent years [see e.g. Abel, 2011; Heß and Springel, 2010; Hopkins, 2013, 2014; Price, 2008; Read and Hayfield, 2012; Read et al., 2010; Wadsley et al., 2008], which may also have helped to improve the performance of SPH in simulations of turbulence.

In this chapter, we aim to examine how well our newly developed DG methods fair in simulating turbulent flows. In particular, we want to see whether an improvement in accuracy and computational efficiency compared with standard second-order finite volume methods is realized.

8.2 Simulational setup

We shall consider an effectively isothermal gas in which we drive subsonic turbulence through a forcing on large scales. The imposed isothermality prevents the buildup of internal energy and pressure through the turbulent cascade over time. Technically, we simulate an ideal gas but reset slight deviations from isothermality back to the imposed temperature level after every timestep, allowing us to directly measure the dissipated internal energy.

We consider a 3D simulational domain of size $L = 1$. In the following, we will compare runs with a finite volume scheme and runs using our new DG hydro solver on a fixed Cartesian mesh. In the case of DG simulations we vary the resolution as well as the convergence order of the code. A summary of all of our runs is given in Table 8.1.

Note that we always state the convergence order, i.e. $\mathcal{O} = k + 1$ instead of k for our DG runs. At a fixed convergence order of 3, we vary the resolution from 32^3 up to 256^3 , and at a fixed resolution of 128^3 we change the convergence order from 1 up to 4. This allows us to asses the impact of both parameters against each other. The number of basis functions is $N(0) = 1$ for a first order method, $N(1) = 4$ for a second order method, $N(2) = 10$ for a third order, and $N(3) = 20$ for a fourth order method. In Table 8.1 we also state the approximate number of degrees of freedom per dimension to better compare the impact of increasing the order versus increasing the resolution level.

8.2.1 Turbulent driving

We use the same driving method as in Bauer and Springel [2012], which is based on Federrath et al. [2008, 2009]; Federrath et al. [2010]; Schmidt et al. [2006] and Price and Federrath [2010]. We generate a turbulent acceleration field in Fourier space containing power in a small range of modes with $k_{min} = 6.27$ and $k_{max} = 12.57$. The amplitude of the modes is described by a paraboloid centred around $(k_{min} + k_{max})/2$. The phases are drawn from an Ornstein–Uhlenbeck (OU) process. This random process is given by

$$\boldsymbol{\theta}_t = f \boldsymbol{\theta}_{t-\Delta t} + \sigma \sqrt{(1-f^2)} \mathbf{z}_n, \quad (8.1)$$

with random variable \mathbf{z}_n and decay factor f , given by $f = \exp(-\Delta t/t_s)$, with correlation length t_s . The phases are updated after a time interval of Δt . The variance of the process is set by σ . The expected mean value of the sequence is zero, $\langle \boldsymbol{\theta}_t \rangle = 0$, and the correlations between random numbers over time are

Overview over our turbulence simulations				
Label	Numerical method	Conv. order \mathcal{O}	Resolution	(d.o.f./cell) ^{1/3}
FV_X_1	finite volume	1	32 ³ ... 512 ³	1
FV_X_2	finite volume	2	32 ³ ... 512 ³	1
DG_X_1	discontinuous Galerkin	1	128 ³	1
DG_X_2	discontinuous Galerkin	2	128 ³	1.59
DG_X_3	discontinuous Galerkin	3	32 ³ ... 256 ³	2.15
DG_X_4	discontinuous Galerkin	4	128 ³	2.71

Table 8.1: Summary of the turbulence simulations discussed in this chapter. The X in the name is a placeholder for the resolution level. As a reference solution we consider ordinary finite volume simulations with up to 512³ resolution elements. In case of DG, we vary the resolution from 32³ up to 256³ for the third order code, as well as the convergence order from 1 up to 4 at a resolution of 128³ cells. To better asses the impact of a higher order method, we state the number of degrees of freedom per cell per dimension. The number of degrees of freedom per cell are 1, 4, 10 and 20 (from 1 order up to 4 order) in the case of DG.

$\langle \boldsymbol{\theta}_t \boldsymbol{\theta}_{t+\Delta t} \rangle = \sigma^2 f$. This guarantees a smooth, but frequent change of the turbulent driving field.

We want a purely solenoidal driving field, because we are interested in smooth subsonic turbulence in this study. A compressive part would only excite sound waves, which would eventually steepen to shocks if the driving is strong enough. These compressive modes are filtered out through a Helmholtz decomposition in Fourier space:

$$\hat{\mathbf{a}}(\mathbf{k})_i = \left(\delta_{ij} - \frac{k_i k_j}{|\mathbf{k}|^2} \right) \hat{\mathbf{a}}_0(\mathbf{k})_j. \quad (8.2)$$

The acceleration field is incorporated as an external source term in the DG equations. The formalism is similar to adding an external gravitational field. We have to compute the following DG integrals for \mathbf{a}_l^K :

$$\begin{aligned} \mathbf{a}_l^K(t) &= \int_K \mathbf{a}(\mathbf{x}, t) \phi_l^K(\mathbf{x}) dV \\ &= \frac{|K|}{8} \int_{[-1,1]^3} \mathbf{a}(\boldsymbol{\xi}, t) \phi_l(\boldsymbol{\xi}) d\boldsymbol{\xi} \\ &= \frac{|K|}{8} \sum_{q=1}^{(k+1)^3} \mathbf{a}(\boldsymbol{\xi}_q, t) \phi_l(\boldsymbol{\xi}_q) \omega_q, \end{aligned} \quad (8.3)$$

thus we have to evaluate the driving field for $(k+1)^3$ inner quadrature points $\boldsymbol{\xi}$ for each Runge-Kutta stage. An additional evaluation at the cell centre is required to compute the allowed time step size. The evaluation is done with a discrete Fourier sum over the few non-zero modes of the driving field. If the update frequency of the driving field is smaller than the typical timestep size, storing the acceleration field

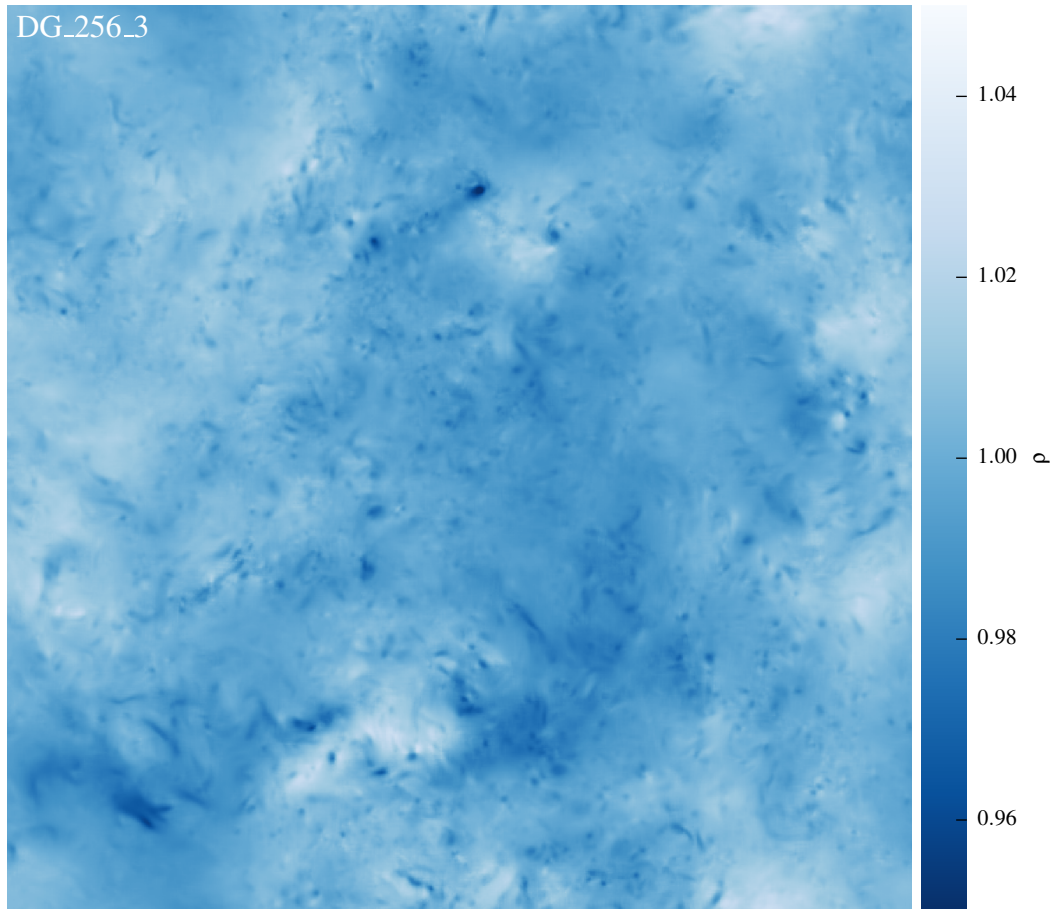


Figure 8.1: A thin slice through the middle of our best resolved DG simulation at third order showing the density field. The field uses the sub-cell information given by the high order DG weights. Every cell is sub-sampled four times.

for each inner quadrature point can speed up the computations. In case of the finite volume runs, we add the driving field through two half step kick operators at the beginning and end of a time step, like for ordinary gravity.

The overall amplitude of the acceleration field is rescaled such that a given Mach number is reached. Our target Mach number is $\mathcal{M} \sim 0.2$. The decay time scale is chosen as half the eddy turnover time scale, $t_s = \frac{1}{2} \frac{L}{\mathcal{M}c} = 2.5$ in our case. The acceleration field is updated 10 times per decay time scale, $\Delta t = 0.1t_s = 0.25$.

8.2.2 Dissipation measurement

We use an adiabatic index of $\gamma = 1.01$ instead of the isothermal index $\gamma = 1$. The slight deviation from $\gamma = 1$ allows us to measure the dissipated energy while the

dynamics of the fluid is essentially isothermal. After each timestep, the expected specific internal energy is computed as

$$\epsilon = \frac{c^2}{\gamma - 1} \frac{\rho^{\gamma-1}}{\rho_0^{\gamma-1}}, \quad (8.4)$$

with sound speed c and reference density $\rho_0 = 1$. This specific internal energy is enforced at all quadrature points within a cell. Thus, the weights associated with the total energy density using the kinetic momentum and density field have to be adjusted:

$$\begin{aligned} w_{e,l}^K(t) &= \int_K \left(\frac{1}{2} \frac{\mathbf{p}(\mathbf{x}, t)^2}{\rho(\mathbf{x}, t)} + \rho(\mathbf{x}, t) \epsilon(\mathbf{x}, t) \right) \phi_l^K(\mathbf{x}) \, dV \\ &= \frac{|K|}{8} \int_{[-1,1]^3} \left(\frac{1}{2} \frac{\mathbf{p}(\boldsymbol{\xi}, t)^2}{\rho(\boldsymbol{\xi}, t)} + \rho(\boldsymbol{\xi}, t) \epsilon(\boldsymbol{\xi}, t) \right) \phi_l(\boldsymbol{\xi}) \, d\boldsymbol{\xi} \\ &= \frac{|K|}{8} \sum_{q=1}^{(k+1)^3} \left(\frac{1}{2} \frac{\mathbf{p}(\boldsymbol{\xi}_q, t)^2}{\rho(\boldsymbol{\xi}_q, t)} + \rho(\boldsymbol{\xi}_q, t) \epsilon(\boldsymbol{\xi}_q, t) \right) \phi_l(\boldsymbol{\xi}_q) \omega_q. \end{aligned} \quad (8.5)$$

Afterwards, the average internal energy density in the cell can be recomputed as

$$\rho \epsilon = w_{e,0}^K - \frac{1}{2} \frac{\mathbf{w}_{p,0}^K{}^2}{w_{\rho,0}^K}. \quad (8.6)$$

The dissipated energy is given by the difference between the average internal energy before and after adjusting the weights of the total energy density. Afterwards the positivity limiter is applied to guarantee non-negative values in our DG simulations.

8.2.3 Power spectrum measurement

The power spectrum of a scalar or vector field $w(\mathbf{x})$ is proportional to the Fourier transformed of the two point correlation function:

$$C_w(\mathbf{l}) = \langle w(\mathbf{x} + \mathbf{l}) w(\mathbf{x}) \rangle_{\mathbf{x}}. \quad (8.7)$$

Thus

$$E_w(\mathbf{k}) = (2\pi)^{3/2} \mathcal{F}(C_w(\mathbf{l})) = \int_V C_w(\mathbf{l}) \exp(-i\mathbf{k}\mathbf{l}) \, d^3\mathbf{l} \quad (8.8)$$

$$= |\hat{w}(\mathbf{k})|^2, \quad (8.9)$$

where \hat{w} is the Fourier transform of w ¹. Here, we are only interested in the 1D power spectrum, thus we average $E_w(\mathbf{k})$ over spherical shells:

$$E_w(k) = 4\pi k^2 \langle E_w(\mathbf{k}) \rangle, \quad (8.10)$$

¹We are using the convention of normalizing the Fourier transform symmetrically with $(2\pi)^{-3/2}$.

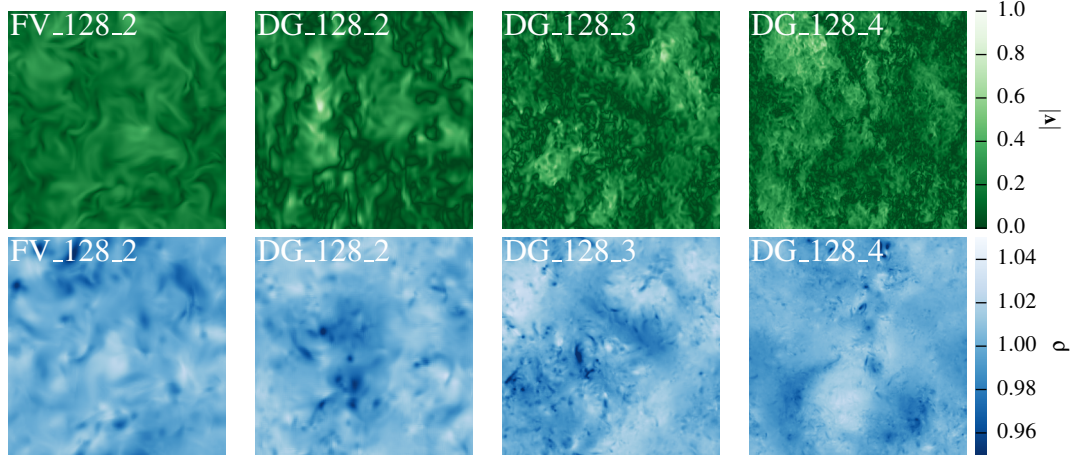


Figure 8.2: Thin slices through the density and velocity field at $t = 30$. We compare the finite volume simulations against DG simulations of order 2 up to 4. Already 2nd order DG shows features which are finer than in the 2nd order finite volume run. The higher moments available in 3rd and 4th order DG allows a representation of finer features without increasing the spatial resolution. The thin lines of zero velocity are much more pronounced in case of DG than in the finite volume case.

where $k = |\mathbf{k}|$. The overall normalization of the Fourier transformation is chosen such that the integral over the power spectrum is equivalent to the total energy:

$$\sigma^2 = \int w(x) d\mathbf{x} = \int E_w(k) dk = \frac{1}{(2\pi)^3 N^3} \sum_{i,j,k=0}^{N-1} |\hat{w}_{ijk}|^2, \quad (8.11)$$

with \hat{w}_{ijk} being the discrete Fourier transformation of the discretized continuous field w .

Usually we show $kE(k)$ instead of $E(k)$ directly in log-log plots. This means a horizontal line in a log-log plot represents equal energy per decade and makes interpreting the area under a curve easier.

8.3 Results

In Figure 8.2 we show a first visual overview of our simulation results at a resolution of 128^3 cells. The panels show the state at the final output time $t = 30$ for the magnitude of the velocity and the density in a thin slice through the middle of the box. Each cell is subsampled four times for this plot using the full sub-cell information present for each DG or finite volume cell. In the case of the finite volume scheme, we used the estimated gradients in sub-sampling the cells.

The finite volume and DG results are similar at second order accuracy. However, already the second order DG run visually shows more small scale structure than the finite volume run. By increasing the order of accuracy and therefore allowing for more degrees of freedom within a cell, DG is able to represent considerably more

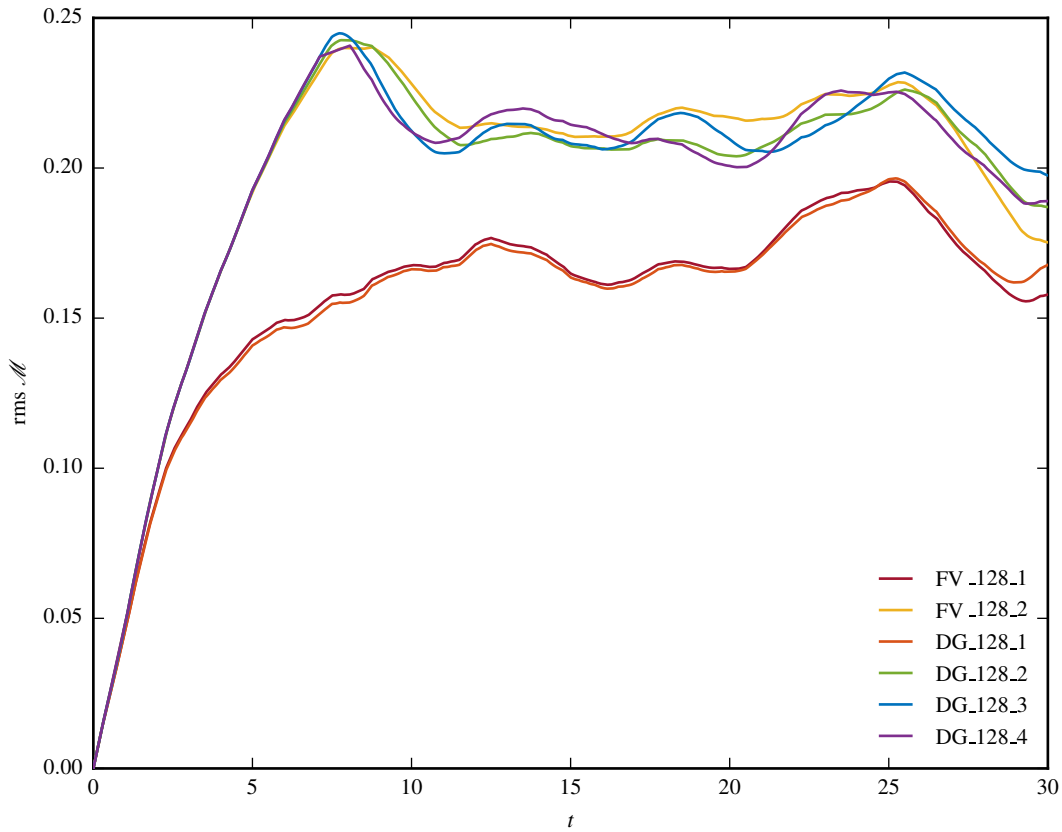


Figure 8.3: Time evolution of the root mean square Mach number \mathcal{M} . The runs with a higher than first order convergence order agree well with each other and manage to establish a Mach number of about $\mathcal{M} \sim 0.2$ at $t = 12$ after an initial phase. However, the first order finite volume and DG runs do not manage to reach the same Mach number and fall substantially short of achieving a comparable kinetic energy throughout the entire run time.

structure at the same number of cells. Interestingly, the velocity field has regions of (almost) zero velocity. These thin stripes can be well represented in DG. The finite volume run shows the same features, but they are not as pronounced. Additionally, Figure 8.1 shows a thin density slice for our highest resolution DG run DG_256_3. The high resolution and third order accuracy allows for more small scale details than in any other of our simulations.

8.3.1 Mach number evolution

All of our runs with a convergence order larger or equal to second order reach an average Mach number of $\mathcal{M} \sim 0.21$ after $t = 12$. The detailed history of the Mach number varies a bit from run to run. The differences between the different DG runs and finite volume runs are however insignificant. The same holds true for the other runs not shown in Figure 8.3. Interestingly, both, the first order finite volume and

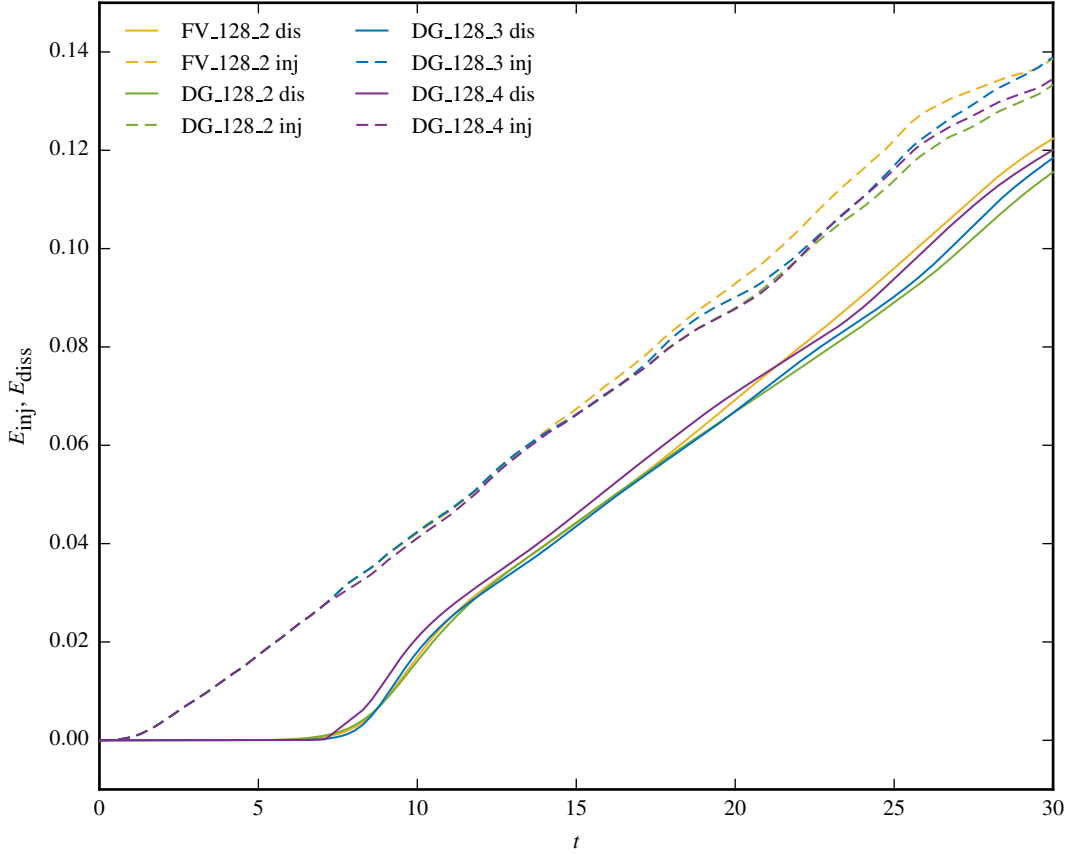


Figure 8.4: The dashed lines show the injected energy, while the solid lines give the dissipated energy over time. Dissipation becomes only relevant after an initial start-up phase. Thereafter, a quasi-stationary state establishes.

DG runs fall substantially behind and can only reach a steady state Mach number of about $\mathcal{M} \sim 0.17$. The low numerical accuracy leads to a too high numerical dissipation rate in this case, preventing a fully established turbulent cascade. A similar problem was found in Bauer and Springel [2012] for simulations with standard SPH. Besides problematic convergence properties of SPH, the high artificial viscosity and noisy character of standard SPH were identified as the main reasons for its problems in properly following subsonic turbulence. These problem could be alleviated significantly by using a time dependent artificial viscosity parameterization, but the noise inherent in SPH's gradient estimates still limited the accuracy of the results.

8.3.2 Injected and dissipated energy

The globally injected and dissipated energy in our turbulence simulations is shown in Figure 8.4 over time. The rate of energy injection through the driving forces stays almost constant over time. At around $t = 12$, the variation starts to increase slightly.

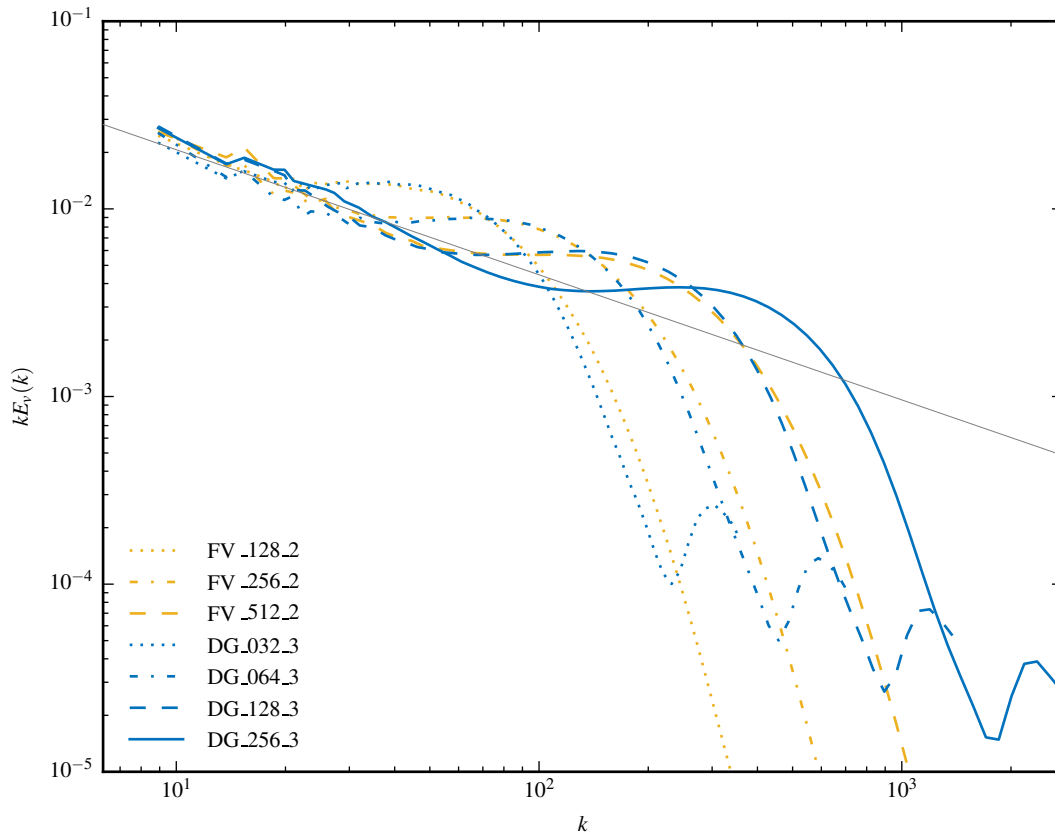


Figure 8.5: Comparison of the velocity power spectra of our second order finite volume runs against our third order DG runs. Interestingly, the spectra of the DG runs match with the ones obtained from the finite volume runs at a quarter of the resolution. Thus, in total, DG obtains similar results using only about half as many degrees of freedom per dimension as finite volume schemes.

At this point the variations between individual runs start to grow as well. Initially, the dissipation is negligible, but at around $t = 8$ dissipation suddenly kicks in at a high rate, but then quickly transitions to a lower level at around $t = 12$ which is then stable until the end of our runs, indicating that a quasi-stationary state has been reached. The difference between both curves – the kinetic energy – remains rather constant after $t = 12$. Thus, in the following we only use outputs after $t = 12$ for our analysis.

8.3.3 Velocity power spectra

In Figures 8.5 and 8.6 we show velocity power spectra of our runs. First, we focus on a resolution study of our third order DG and second order finite volume runs in Figure 8.5. In case of the finite volume runs, we show the power spectra up to the Nyquist frequency $k_n = 2\pi N/2L$, with N being the number of cells per dimension. For our DG runs we show the full power spectrum instead, obtained from the grid used in

the Fourier transformation up to $k_g = 2\pi 4N/2L = 4k_n$. The finite volume runs have a second peak not shown here at modes above k_n , induced by noise resulting from the discontinuities across cell boundaries. The third and higher order DG methods show a still declining power spectrum at k_n and only at even higher modes close to k_g start to show a noise induced rise. This is due to the available sub-cell information encoded in the DG weights.

All runs show an inertial range at scales smaller than the driving range on large scales. The inertial range is followed by a numerical dissipation bottleneck. This bottleneck is similar to the experimentally observed physical bottleneck effect. The energy flowing down to smaller scales can not be dissipated fast enough at the resolution scale and piles up there before it is eventually transformed to heat. The bottleneck feature moves to ever smaller scales as the numerical resolution is increased. Especially our highest resolution DG run *DG_256_3* shows a rather large inertial range. However, the slope of the inertial range is slightly steeper than the expected $k^{-5/3}$ Kolmogorov scaling. We think a Mach number of $\mathcal{M} \sim 0.21$ and the associated density fluctuations are maybe already too high for a purely Kolmogorov-like turbulence cascade, which is only expected for incompressible gas.

Interestingly, the power spectra of our finite volume runs match those of our third order DG simulations, except that the finite volume scheme requires four times higher spatial resolution per dimension. Considering the 10 degrees of freedom per cell for third order DG, the effective number of degrees of freedom is still lower by a factor of 6.4 in the case of DG, which corresponds to a factor of 1.86 per dimension. This underlines the power of higher order numerical methods, especially if comparatively smooth problems such as subsonic turbulence are studied.

In Figure 8.6 we compare the impact of the numerical convergence order on the power spectrum of our DG runs. As a comparison we include a second order finite volume run as well. All runs have a numerical resolution of 128^3 . Already the second order DG method shows a bit more extended inertial range than the second order finite volume run. But the second order DG method already uses four degrees of freedom per cell. Increasing the convergence order alone improves the inertial range considerably. The change in going from second to third order is a bit larger than the change from third to fourth order.

8.3.4 Density PDFs

In Figure 8.7 we show the probability density function (PDF) of the density field for some of our runs. The PDF is averaged from $t = 12$ up to $t = 30$ and sub-sampled 4^3 times for each cell. We take the estimated density gradients into account for the finite volume runs. The finite volume run shows the smallest range of realized density values at the sampling points. Slightly more sampling points pile up at the extreme density values. This is due to the slope limited gradients used here, preventing more extreme density values. The DG runs show a more extended range of density values, with the range increasing with convergence order, because the higher order polynomial representations allow for a more detailed structure with more extrema

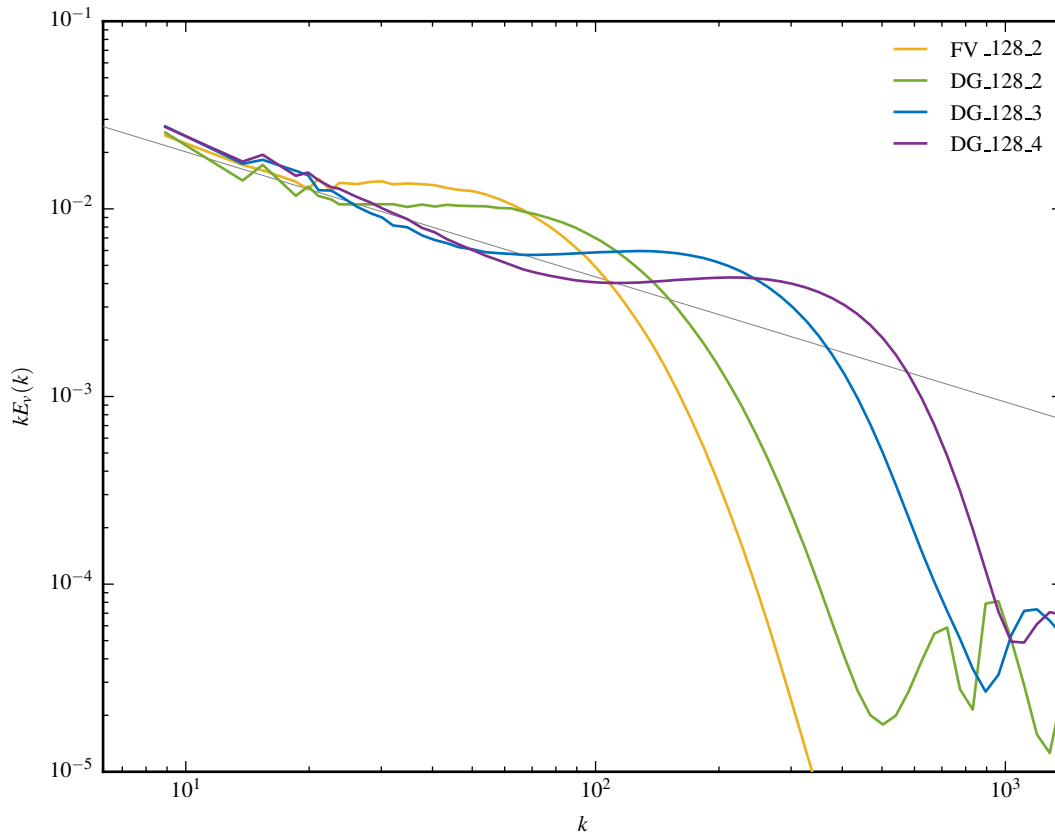


Figure 8.6: Velocity power spectrum for our DG runs at different convergence order at a resolution of 128^3 cells. Already second order DG shows a large inertial range and a dissipation bottleneck at small scales.

within a cell. If only the mean values within the cells are considered, the PDFs are all rather similar to each other and not so different from the finite volume run shown.

8.4 Discussion

In Section 8.3.3, we already found that the DG results are as good as finite volume results but need only a bit more than half as many degrees of freedom. Finite volume methods have formally only one degree of freedom per cell, however, the gradients still need to be stored for every cell, which further increases their memory requirements and computational work load.

But on the other hand, DG has to solve $(k + 1)^2$ Riemann problems per interface instead of just one and requires $(k + 1)^3$ cell internal flux evaluations per cell. The later are cheaper than solving Riemann problems on the interfaces, as the flux can be directly evaluated. Furthermore, we use an approximate Riemann solver in our DG runs instead of the exact solver used in the finite volume runs. This is justified,

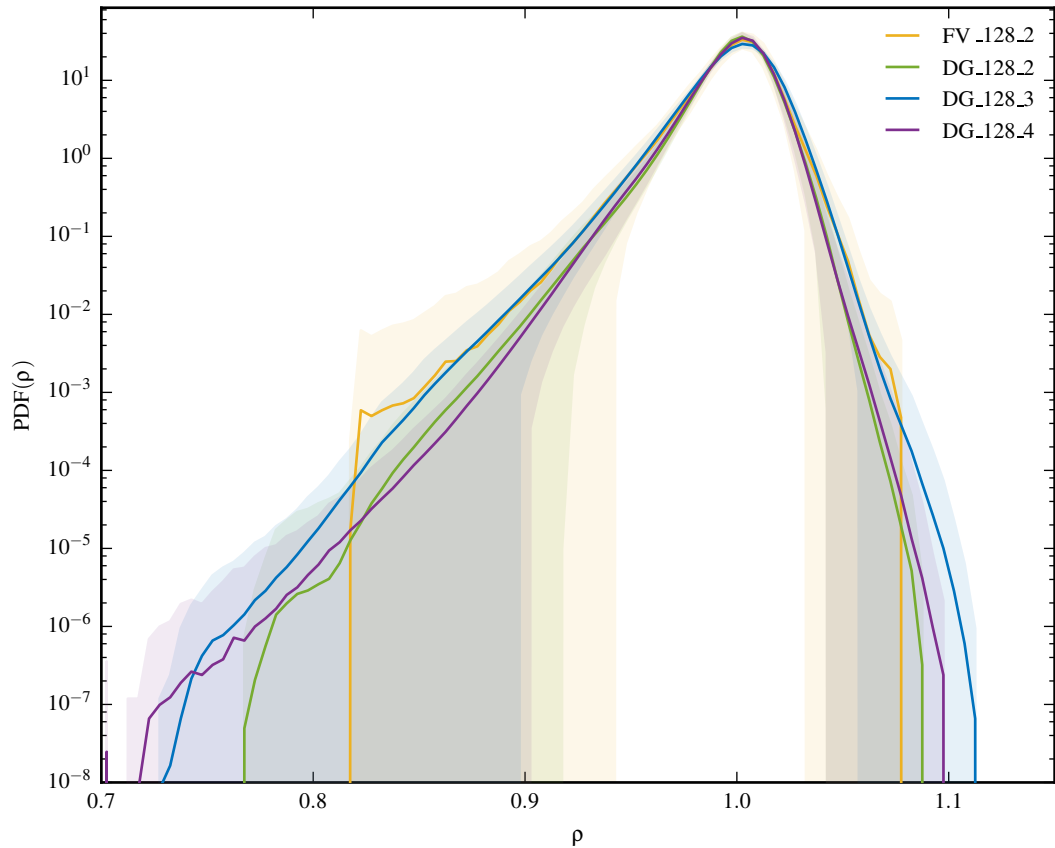


Figure 8.7: The density PDF for our runs at a resolution of 128^3 cells. The PDF is obtained by subsampling each cell 4^3 times. In the finite volume case, we take the estimated density gradients into account. For DG, we use the full polynomial information present in each cell. The shaded area represents the standard deviation over time. Interestingly, finite volume schemes show a sharp drop off at the low and high density ends which is absent in this form in the DG calculations.

as DG generally leads to a smaller jump at the interface than in finite volume, due to the better representation of the state within a cell.

The ultimate question for comparing numerical methods, is the computational efficiency, i.e. what is the best numerical accuracy which can be obtained for a given invested total runtime. A fair comparison involving the run time is complicated. The runs used in this study were performed on different machines and the number of CPUs used had to be altered, as the memory requirement change by several orders of magnitude between our smallest and largest run. The comparison is even further complicated by the fact that both implementations of our hydro solver are optimized to different levels, which can distort simple comparisons of the run times. Nevertheless, a straightforward comparison of the total CPU time used can give a rough estimate of the efficiency of our DG method compared to a corresponding finite volume scheme.

Both the finite volume method at second order accuracy and the DG scheme at third order accuracy show very good weak scaling when increasing the resolution for the range of resolutions studied here. If we compare the run time for roughly equal power spectra, we find that the DG_032_3 run is about 1.14 times faster than the corresponding FV_128_2 run. This factor increases if we increase the resolutions: The DG_064_3 is already 1.34 times faster than the FV_256_2 run. The DG_128_3 run is 1.53 times faster than the FV_512_2 run, which comes close to the factor 1.86 more degrees of freedom needed in the finite volume run to achieve the same accuracy. Thus, DG does not only need less degrees of freedom to obtain the same accuracy but also considerably less run time. This combination makes DG a very interesting method for solving the Euler equations and reinforces its potential as an attractive approach for future exa-scale application codes in astrophysics.

Part IV

Conclusion

9

Conclusion and Outlook

9.1 Conclusion

9.1.1 Radiative transfer and reionization

We presented a novel radiative transfer implementation using GPUs. The correctness of the results obtained with both of our advection implementations – a cone-based advection method and a moment-based approach using an M1 closure – was demonstrated. Our implementation passed the standard reionization radiative transfer tests outlined in Iliev et al. [2006a]. The differences in accuracy between our cone-based and moment-based advection methods were not found to be significant in problems relevant for reionization. Thus, we used the moment-based method for our largest production runs, because of its lower computational and memory requirements. Using GPUs we could considerably speed up the radiative transfer computations.

We note that an accurate determination of the speed up achieved with GPUs compared to a traditional CPU code is very difficult. A CPU-only version should in principle use the full chip and all available hardware acceleration features, such as vectorization, to allow for a fair comparison. To obtain a rough estimate, we replaced all CUDA kernel invocations with OpenMP augmented loops, yielding a multithreaded CPU version. All further optimizations were left to the compiler. This still gives only a rough estimate, as more effort went into optimizing the GPU version. In doing this, we obtained a speedup of about 4 compared to an OpenMP optimized version of our code.

Our radiative transfer implementation was used to study hydrogen reionization in the Illustris universe in post processing. The AGN population rises too late to cause hydrogen reionization, therefore we only considered stellar sources of UV photons originating from stars in our analysis. In contrast, for helium, the harder spectra

of AGNs would contribute considerably towards full helium reionization at a later epoch. Another source of UV radiation not considered in our study are so-called Population-III stars. An important choice had to be made for the parametrization of the fraction of photons escaping from galaxies and being able to reionize the IGM. We considered two models for this quite uncertain factor – a globally constant escape fraction, and a global, but time-variable escape fraction as suggested in the literature. Using the time dependent escape fraction we could reproduce numerous key observables of cosmic reionization.

We were able to show that it is plausible that the stellar populations forming in the Illustris Universe alone cause hydrogen reionization. In particular, our results reproduce the ionization history inferred from Ly- α data. Also, the UV background is reproduced well in our variable escape fraction model, though it appears slightly overproduced at the end. This could be mitigated by further fine-tuning of the used parameters, which was not attempted as part of this work. We found an optical depth towards the last scattering surface of $\tau = 0.065$, which is in very good agreement with the latest Planck data. Interestingly, the duration of reionization depends on the escape fraction model used; the transition from an 80% neutral to a 20% neutral IGM took between 190 Myr and 340 Myr in our simulations. The size distribution of small bubbles stays constant for a long time, meaning that small bubbles are created roughly at the same rate at which they grow into larger ones. The distribution of ionization fractions shows a peak, which moves to smaller scales as reionization progresses. After reionization is completed, the peak is at a neutral fraction of about 5×10^{-5} .

9.1.2 Discontinuous Galerkin hydrodynamics

A promising, comparatively young approach to solve the Euler equations are so-called discontinuous Galerkin methods. Currently, their use in astrophysics is still in its infancy, but this may well change in light of rising demands for accuracy and computational efficiency. Formulating a discontinuous Galerkin solver for a moving Voronoi mesh is still an area of open research and presently an unsolved problem. Thus, we decided to implement the DG method using a structured AMR mesh. This is facilitated by an AMR module we developed for the AREPO code, which provides an alternative mesh usable instead of a Voronoi mesh in this code. This also allows more direct comparisons of results obtained with the moving-mesh hydro solver against traditional AMR techniques. It also provides an environment to implement novel numerical methods without the need to develop auxiliary code infrastructure (such as I/O, time-stepping, search trees, etc.) from scratch.

We have given a brief overview over the concepts and equations behind DG, and tested the method on a number of simple problems. A more extensive compilation of results obtained with our implementation for the most common astrophysical test problems can be found in Schaal et al. [2015]. We then used our new DG solver to simulate subsonic turbulence as a first scientific application. Here, the advantages of DG became clearly visible. As expected, the higher order methods yield a larger

inertial range for subsonic turbulent cascades at a lower number of degrees of freedom than corresponding finite volume schemes. Also, the total runtime is considerable shorter with DG than with a conventional finite volume method. Naturally, the smooth nature of subsonic turbulence is favourable for DG in this problem, so these advantages are not necessarily equally large in other applications. If the simulation is dominated by shocks, both methods might be more similar and the advantages of DG could be reduced substantially.

9.2 Outlook

A future extension of our radiative transfer code could be the inclusion of helium reionization. This would require the advection of three independent radiation fields instead of just one, due to the two ionization edges of helium. Additionally, simulations of a larger box including a representative population of rare AGNs should be run until $z \sim 3$. This would still be computationally feasible using today's supercomputers.

An interesting and demanding future development could be the dynamic coupling of the radiative transfer solver with the cosmological simulation model. Ideally, the radiative transfer solver would be running on the GPUs, while the other computations are handled by the CPUs. To be efficient, both computations have to run at the same time and overlap, requiring moderate adjustments to our present code.

Cosmological simulations of structure formation have evolved significantly since the first generations of dark matter only simulations. Nowadays, baryonic physics is included as well, and numerous approximate treatments of galaxy formation physics are incorporated. Recently, simulations have started to include magneto-hydrodynamics on a regular basis. In future simulations, radiation hydrodynamics and other advanced ingredients such as cosmic ray physics will be included as well. Thus, there is a great need for efficient, yet sufficiently accurate methods for treating radiative transfer that can be dynamically coupled to hydrodynamics.

A good radiative transfer scheme must resolve the angular dependence of the distribution of radiation intensity. This becomes clear by considering the conflicting results of Davis et al. [2014]; Krumholz and Thompson [2012]; Rosdahl et al. [2015] for a radiation pressure driven outflow problem. The M1 method lies between the flux limited diffusion method and the more accurate VET approach, but it still does not reproduce the VET results in this problem. Assuming the latter are indeed correct, this implies that more angular information has to be retained in a radiative transfer scheme for more reliable results. Thus, an adaption of our cone-based method to radiation hydrodynamics including radiation pressure and thermal coupling would be another interesting future development, allowing us to independently check the reported VET results for the outflow problem. Other developments along this line of thought are the TRAPHIC [Pawlik and Schaye, 2008] and the SIMPLEX2 [Paardekooper et al., 2010] algorithms, and it would be interesting as well to compare them in more detail to our methodology.

The DG implementation on an AMR mesh within AREPO we introduced here might as well provide the basis of a powerful radiative transfer solver. For example, Guermond et al. [2014] introduced an equilibrium discontinuous Galerkin radiative transfer solver, discretizing the radiation field into N angular directions. Adapting their approach to a time-dependent cosmological radiative transfer problem might be very promising. Ultimately, a DG-like discretization using a moving Voronoi mesh is also highly desirable, provided this is mathematically tractable in an efficient way. The inclusion of high-order self-gravity and galaxy formation physics source terms in DG are other obvious future developments. The coming years will show whether DG can challenge and partially replace finite volume methods as a viable and practical method to simulate cosmological structure formation using exascale supercomputer.

Appendix

Bibliography

- T. Abel. rpSPH: a novel smoothed particle hydrodynamics algorithm. *MNRAS*, 413: 271–285, 2011.
- T. Abel and B. D. Wandelt. Adaptive ray tracing for radiative transfer around point sources. *MNRAS*, 330:L53–L56, 2002.
- T. Abel, M. L. Norman, and P. Madau. Photon-conserving Radiative Transfer around Point Sources in Multidimensional Numerical Cosmology. *ApJ*, 523:66–71, 1999.
- O. Agertz, A. V. Kravtsov, S. N. Leitner, and N. Y. Gnedin. Toward a Complete Accounting of Energy and Momentum from Stellar Feedback in Galaxy Formation Simulations. *ApJ*, 770:25, 2013.
- K. Ahn and P. R. Shapiro. Does radiative feedback by the first stars promote or prevent second generation star formation? *MNRAS*, 375:881–908, 2007.
- K. Ahn, I. T. Iliev, P. R. Shapiro, G. Mellema, J. Koda, and Y. Mao. Detecting the Rise and Fall of the First Stars by Their Impact on Cosmic Reionization. *ApJ*, 756:L16, 2012.
- S. S. Ali, S. Bharadwaj, and B. Pandey. What will anisotropies in the clustering pattern in redshifted 21-cm maps tell us? *MNRAS*, 363:251–258, 2005.
- G. Altay, R. A. C. Croft, and I. Pelupessy. SPHRAY: a smoothed particle hydrodynamics ray tracer for radiative transfer. *MNRAS*, 386:1931–1946, 2008.
- M. A. Alvarez and T. Abel. Quasar HII regions during cosmic reionization. *MNRAS*, 380:L30–L34, 2007.
- M. A. Alvarez, V. Bromm, and P. R. Shapiro. The H II Region of the First Star. *ApJ*, 639:621–632, 2006.
- D. Aubert and R. Teyssier. A radiative transfer scheme for cosmological reionization based on a local Eddington tensor. *MNRAS*, 387:295–307, 2008.
- D. Aubert and R. Teyssier. Reionization Simulations Powered by Graphics Processing Units. I. On the Structure of the Ultraviolet Radiation Field. *ApJ*, 724:244–266, 2010.

Bibliography

- S. Baek, P. Di Matteo, B. Semelin, F. Combes, and Y. Revaz. The simulated 21 cm signal during the epoch of reionization: full modeling of the Ly- α pumping. *A&A*, 495:389–405, 2009.
- R. Barkana and A. Loeb. In the beginning: the first sources of light and the reionization of the universe. *Phys. Rep.*, 349:125–238, 2001.
- R. Barkana and A. Loeb. Gamma-Ray Bursts versus Quasars: Ly α Signatures of Reionization versus Cosmological Infall. *ApJ*, 601:64–77, 2004.
- N. Battaglia, H. Trac, R. Cen, and A. Loeb. Reionization on Large Scales. I. A Parametric Model Constructed from Radiation-hydrodynamic Simulations. *ApJ*, 776:81, 2013.
- A. Bauer and V. Springel. Subsonic turbulence in smoothed particle hydrodynamics and moving-mesh simulations. *MNRAS*, 423:2558–2578, 2012.
- A. Bauer, V. Springel, M. Vogelsberger, S. Genel, P. Torrey, D. Sijacki, D. Nelson, and L. Hernquist. Hydrogen Reionization in the Illustris Universe. *ArXiv e-prints*, 2015.
- R. H. Becker, X. Fan, R. L. White, M. A. Strauss, V. K. Narayanan, R. H. Lupton, J. E. Gunn, J. Annis, N. A. Bahcall, J. Brinkmann, A. J. Connolly, I. Csabai, P. C. Czarapata, M. Doi, T. M. Heckman, G. S. Hennessy, Ž. Ivezić, G. R. Knapp, D. Q. Lamb, T. A. McKay, J. A. Munn, T. Nash, R. Nichol, J. R. Pier, G. T. Richards, D. P. Schneider, C. Stoughton, A. S. Szalay, A. R. Thakar, and D. G. York. Evidence for Reionization at $z \sim 6$: Detection of a Gunn-Peterson Trough in a $z=6.28$ Quasar. *AJ*, 122:2850–2857, 2001.
- C. L. Bennett, D. Larson, J. L. Weiland, N. Jarosik, G. Hinshaw, N. Odegard, K. M. Smith, R. S. Hill, B. Gold, M. Halpern, E. Komatsu, M. R. Nolte, L. Page, D. N. Spergel, E. Wollack, J. Dunkley, A. Kogut, M. Limon, S. S. Meyer, G. S. Tucker, and E. L. Wright. Nine-year Wilkinson Microwave Anisotropy Probe (WMAP) Observations: Final Maps and Results. *ApJS*, 208:20, 2013.
- S. Bird, M. Haehnelt, M. Neeleman, S. Genel, M. Vogelsberger, and L. Hernquist. Reproducing the kinematics of damped Lyman α systems. *MNRAS*, 447:1834–1846, 2015.
- R. J. Bouwens, G. D. Illingworth, P. A. Oesch, I. Labbé, M. Trenti, P. van Dokkum, M. Franx, M. Stiavelli, C. M. Carollo, D. Magee, and V. Gonzalez. Ultraviolet Luminosity Functions from 132 $z \sim 7$ and $z \sim 8$ Lyman-break Galaxies in the Ultra-deep HUDF09 and Wide-area Early Release Science WFC3/IR Observations. *ApJ*, 737:90, 2011.
- G. L. Bryan, M. L. Norman, B. W. O’Shea, T. Abel, J. H. Wise, M. J. Turk, D. R. Reynolds, and D. C. Collins. ENZO: An Adaptive Mesh Refinement Code for Astrophysics. *ApJS*, 211:19, 2014.

- S. Cantalupo and C. Porciani. RADAMESH: cosmological radiative transfer for Adaptive Mesh Refinement simulations. *MNRAS*, 411:1678–1694, 2011.
- C. L. Carilli, S. Furlanetto, F. Briggs, M. Jarvis, S. Rawlings, and H. Falcke. Probing the dark ages with the Square Kilometer Array. *New A Rev.*, 48:1029–1038, 2004.
- J. Caruana, A. J. Bunker, S. M. Wilkins, E. R. Stanway, S. Lorenzoni, M. J. Jarvis, and H. Ebert. Spectroscopy of $z \sim 7$ candidate galaxies: using Lyman α to constrain the neutral fraction of hydrogen in the high-redshift universe. *MNRAS*, 443:2831–2842, 2014.
- R. Cen. A Fast, Accurate, and Robust Algorithm for Transferring Radiation in Three-dimensional Space. *ApJS*, 141:211–227, 2002.
- J. Chardin, D. Aubert, and P. Ocvirk. A study of simulated reionization histories with merger trees of HII regions. *A&A*, 548:A9, 2012.
- J. Chardin, D. Aubert, and P. Ocvirk. Local reionization histories with a merger tree of the HII regions. *A&A*, 568:A52, 2014.
- B. Ciardi, A. Ferrara, S. Marri, and G. Raimondo. Cosmological reionization around the first stars: Monte Carlo radiative transfer. *MNRAS*, 324:381–388, 2001.
- B. Ciardi, A. Ferrara, and S. D. M. White. Early reionization by the first galaxies. *MNRAS*, 344:L7–L11, 2003.
- B. Cockburn, S.-Y. Lin, and C.-W. Shu. TVB Runge Kutta Local Projection Discontinuous Galerkin Finite Element Method for Conservation Laws III: One-Dimensional Systems. *Journal of Computational Physics*, 84:90–113, 1989.
- B. Cockburn, S. Hou, and C.-W. Shu. The Runge-Kutta local projection discontinuous Galerkin finite element method for conservation laws. IV. The multidimensional case. *Mathematics of Computation*, 54:545–581, 1990.
- B. Cockburn, G. Karniadakis, and C. Shu. *Discontinuous Galerkin Methods: Theory, Computation and Applications*. Lecture Notes in Computational Science and Engineering. Springer Berlin Heidelberg, 2011. ISBN 9783642640988.
- B. Cockburn and C.-W. Shu. Tvb runge-kutta local projection discontinuous galerkin finite element method for conservation laws. ii. general framework. *Mathematics of Computation*, 52(186):411–435, 1989.
- B. Cockburn and C.-W. Shu. The runge-kutta local projection P^1 -discontinuous-galerkin finite element method for scalar conservation laws. *RAIRO-Modélisation mathématique et analyse numérique*, 25(3):337–361, 1991.
- B. Cockburn and C.-W. Shu. The Runge-Kutta Discontinuous Galerkin Method for Conservation Laws V. Multidimensional Systems. *Journal of Computational Physics*, 141:199–224, 1998.

Bibliography

- P. Colella and P. R. Woodward. The Piecewise Parabolic Method (PPM) for Gas-Dynamical Simulations. *Journal of Computational Physics*, 54:174–201, 1984.
- R. A. C. Croft and G. Altay. Radiation-induced large-scale structure during the reionization epoch: the autocorrelation function. *MNRAS*, 388:1501–1520, 2008.
- S. W. Davis, J. M. Stone, and Y.-F. Jiang. A Radiation Transfer Solver for Athena Using Short Characteristics. *ApJS*, 199:9, 2012.
- S. W. Davis, Y.-F. Jiang, J. M. Stone, and N. Murray. Radiation Feedback in ULIRGs: Are Photons Movers and Shakers? *ApJ*, 796:107, 2014.
- J. S. Dillon, A. Liu, C. L. Williams, J. N. Hewitt, M. Tegmark, E. H. Morgan, A. M. Levine, M. F. Morales, S. J. Tingay, G. Bernardi, J. D. Bowman, F. H. Briggs, R. C. Cappallo, D. Emrich, D. A. Mitchell, D. Oberoi, T. Prabu, R. Wayth, and R. L. Webster. Overcoming real-world obstacles in 21 cm power spectrum estimation: A method demonstration and results from early Murchison Widefield Array data. *Phys. Rev. D*, 89(2):023002, 2014.
- S. G. Djorgovski, S. Castro, D. Stern, and A. A. Mahabal. On the Threshold of the Reionization Epoch. *ApJ*, 560:L5–L8, 2001.
- C. P. Dullemond. RADMC: A 2-D Continuum Radiative Transfer Tool. Astrophysics Source Code Library, record ascl:1108.016, 2011.
- C. P. Dullemond. RADMC-3D: A multi-purpose radiative transfer tool. Astrophysics Source Code Library, record ascl:1202.015, 2012.
- R. S. Ellis, R. J. McLure, J. S. Dunlop, B. E. Robertson, Y. Ono, M. A. Schenker, A. Koekemoer, R. A. A. Bowler, M. Ouchi, A. B. Rogers, E. Curtis-Lake, E. Schneider, S. Charlot, D. P. Stark, S. R. Furlanetto, and M. Cirasuolo. The Abundance of Star-forming Galaxies in the Redshift Range 8.5-12: New Results from the 2012 Hubble Ultra Deep Field Campaign. *ApJ*, 763:L7, 2013.
- R. Falgout, J. Jones, and U. Yang. The design and implementation of hypre, a library of parallel high performance preconditioners. In A. Bruaset and A. Tveito, editors, *Numerical Solution of Partial Differential Equations on Parallel Computers*, volume 51 of *Lecture Notes in Computational Science and Engineering*, pages 267–294. Springer Berlin Heidelberg, 2006. ISBN 978-3-540-29076-6.
- X. Fan, M. A. Strauss, D. P. Schneider, J. E. Gunn, R. H. Lupton, R. H. Becker, M. Davis, J. A. Newman, G. T. Richards, R. L. White, J. E. Anderson, Jr., J. Annis, N. A. Bahcall, R. J. Brunner, I. Csabai, G. S. Hennessy, R. B. Hindsley, M. Fukugita, P. Z. Kunszt, Ž. Ivezić, G. R. Knapp, T. A. McKay, J. A. Munn, J. R. Pier, A. S. Szalay, and D. G. York. High-Redshift Quasars Found in Sloan Digital Sky Survey Commissioning Data. IV. Luminosity Function from the Fall Equatorial Stripe Sample. *AJ*, 121:54–65, 2001.

- X. Fan, V. K. Narayanan, M. A. Strauss, R. L. White, R. H. Becker, L. Pentericci, and H.-W. Rix. Evolution of the Ionizing Background and the Epoch of Reionization from the Spectra of $z \sim 6$ Quasars. *AJ*, 123:1247–1257, 2002.
- X. Fan, C. L. Carilli, and B. Keating. Observational Constraints on Cosmic Reionization. *ARA&A*, 44:415–462, 2006a.
- X. Fan, M. A. Strauss, R. H. Becker, R. L. White, J. E. Gunn, G. R. Knapp, G. T. Richards, D. P. Schneider, J. Brinkmann, and M. Fukugita. Constraining the Evolution of the Ionizing Background and the Epoch of Reionization with $z \sim 6$ Quasars. II. A Sample of 19 Quasars. *AJ*, 132:117–136, 2006b.
- X. Fan, M. A. Strauss, R. H. Becker, R. L. White, J. E. Gunn, G. R. Knapp, G. T. Richards, D. P. Schneider, J. Brinkmann, and M. Fukugita. Constraining the Evolution of the Ionizing Background and the Epoch of Reionization with $z \sim 6$ Quasars. II. A Sample of 19 Quasars. *AJ*, 132:117–136, 2006c.
- C.-A. Faucher-Giguère, A. Lidz, L. Hernquist, and M. Zaldarriaga. A Flat Photoionization Rate at $2 \leq z \leq 4.2$: Evidence for a Stellar-Dominated UV Background and against a Decline of Cosmic Star Formation beyond $z \sim 3$. *ApJ*, 682:L9–L12, 2008a.
- C.-A. Faucher-Giguère, A. Lidz, L. Hernquist, and M. Zaldarriaga. Evolution of the Intergalactic Opacity: Implications for the Ionizing Background, Cosmic Star Formation, and Quasar Activity. *ApJ*, 688:85–107, 2008b.
- C.-A. Faucher-Giguère, A. Lidz, M. Zaldarriaga, and L. Hernquist. A New Calculation of the Ionizing Background Spectrum and the Effects of He II Reionization. *ApJ*, 703:1416–1443, 2009.
- C. Federrath, R. S. Klessen, and W. Schmidt. The Density Probability Distribution in Compressible Isothermal Turbulence: Solenoidal versus Compressive Forcing. *ApJ*, 688:L79–L82, 2008.
- C. Federrath, R. S. Klessen, and W. Schmidt. The Fractal Density Structure in Supersonic Isothermal Turbulence: Solenoidal Versus Compressive Energy Injection. *ApJ*, 692:364–374, 2009.
- C. Federrath, J. Roman-Duval, R. S. Klessen, W. Schmidt, and M.-M. Mac Low. Comparing the statistics of interstellar turbulence in simulations and observations. *A&A*, 512:A81, 2010.
- S. L. Finkelstein, R. E. Ryan, Jr., C. Papovich, M. Dickinson, M. Song, R. Somerville, H. C. Ferguson, B. Salmon, M. Giavalisco, A. M. Koekemoer, M. L. N. Ashby, P. Behroozi, M. Castellano, J. S. Dunlop, S. M. Faber, G. G. Fazio, A. Fontana, N. A. Grogin, N. Hathi, J. Jaacks, D. D. Kocevski, R. Livermore, R. J. McLure, E. Merlin, B. Mobasher, J. A. Newman, M. Rafelski, V. Tilvi, and S. P. Willner.

- The Evolution of the Galaxy Rest-Frame Ultraviolet Luminosity Function Over the First Two Billion Years. *ArXiv e-prints*, 2014.
- K. Finlator, F. Özel, and R. Davé. A new moment method for continuum radiative transfer in cosmological re-ionization. *MNRAS*, 393:1090–1106, 2009.
- K. Finlator, S. P. Oh, F. Özel, and R. Davé. Gas clumping in self-consistent reionization models. *MNRAS*, 427:2464–2479, 2012.
- B. Fryxell, K. Olson, P. Ricker, F. X. Timmes, M. Zingale, D. Q. Lamb, P. MacNeice, R. Rosner, J. W. Truran, and H. Tufo. FLASH: An Adaptive Mesh Hydrodynamics Code for Modeling Astrophysical Thermonuclear Flashes. *ApJS*, 131:273–334, 2000.
- S. R. Furlanetto, M. Zaldarriaga, and L. Hernquist. The Growth of H II Regions During Reionization. *ApJ*, 613:1–15, 2004.
- S. R. Furlanetto, S. P. Oh, and F. H. Briggs. Cosmology at low frequencies: The 21 cm transition and the high-redshift Universe. *Phys. Rep.*, 433:181–301, 2006.
- J. P. Gallego-Valencia, J. Löbber, S. Müthing, P. Bastian, C. Klingenberg, and Y. Xia. Implementing a discontinuous galerkin method for the compressible, inviscid euler equations in the dune framework. *PAMM*, 14(1):953–954, 2014.
- S. Genel, M. Vogelsberger, V. Springel, D. Sijacki, D. Nelson, G. Snyder, V. Rodriguez-Gomez, P. Torrey, and L. Hernquist. Introducing the Illustris project: the evolution of galaxy populations across cosmic time. *MNRAS*, 445:175–200, 2014.
- R. A. Gingold and J. J. Monaghan. Smoothed particle hydrodynamics - Theory and application to non-spherical stars. *MNRAS*, 181:375–389, 1977.
- N. Y. Gnedin. Cosmological Reionization by Stellar Sources. *ApJ*, 535:530–554, 2000.
- N. Y. Gnedin. Cosmic Reionization on Computers. I. Design and Calibration of Simulations. *ApJ*, 793:29, 2014.
- N. Y. Gnedin and T. Abel. Multi-dimensional cosmological radiative transfer with a Variable Eddington Tensor formalism. *New A*, 6:437–455, 2001.
- N. Y. Gnedin and A. A. Kaurov. Cosmic Reionization on Computers. II. Reionization History and Its Back-reaction on Early Galaxies. *ApJ*, 793:30, 2014.
- N. Y. Gnedin and P. A. Shaver. Redshifted 21 Centimeter Emission from the Pre-Reionization Era. I. Mean Signal and Linear Fluctuations. *ApJ*, 608:611–621, 2004.
- K. M. Górski, E. Hivon, A. J. Banday, B. D. Wandelt, F. K. Hansen, M. Reinecke, and M. Bartelmann. HEALPix: A Framework for High-Resolution Discretization and Fast Analysis of Data Distributed on the Sphere. *ApJ*, 622:759–771, 2005.

- S. Gottlieb, C.-W. Shu, and E. Tadmor. Strong stability-preserving high-order time discretization methods. *SIAM review*, 43(1):89–112, 2001.
- T. H. Greif. Multifrequency radiation hydrodynamics simulations of H₂ line emission in primordial, star-forming clouds. *MNRAS*, 444:1566–1583, 2014.
- M. Gritschneider, T. Naab, A. Burkert, S. Walch, F. Heitsch, and M. Wetzstein. iVINE - Ionization in the parallel TREE/SPH code VINE: first results on the observed age-spread around O-stars. *MNRAS*, 393:21–31, 2009.
- M. Grossi and V. Springel. The impact of early dark energy on non-linear structure formation. *MNRAS*, 394:1559–1574, 2009.
- J.-L. Guermond, G. Kanschat, and J. Ragusa. Discontinuous galerkin for the radiative transport equation. In X. Feng, O. Karakashian, and Y. Xing, editors, *Recent Developments in Discontinuous Galerkin Finite Element Methods for Partial Differential Equations*, volume 157 of *The IMA Volumes in Mathematics and its Applications*, pages 181–193. Springer International Publishing, 2014. ISBN 978-3-319-01817-1.
- J. E. Gunn and B. A. Peterson. On the Density of Neutral Hydrogen in Intergalactic Space. *ApJ*, 142:1633–1641, 1965.
- F. Haardt and P. Madau. Radiative Transfer in a Clumpy Universe. IV. New Synthesis Models of the Cosmic UV/X-Ray Background. *ApJ*, 746:125, 2012.
- K. Hasegawa and M. Umemura. START: smoothed particle hydrodynamics with tree-based accelerated radiative transfer. *MNRAS*, 407:2632–2644, 2010.
- L. Hernquist and V. Springel. An analytical model for the history of cosmic star formation. *MNRAS*, 341:1253–1267, 2003.
- S. Heß and V. Springel. Particle hydrodynamics with tessellation techniques. *MNRAS*, 406:2289–2311, 2010.
- G. Hinshaw, D. Larson, E. Komatsu, D. N. Spergel, C. L. Bennett, J. Dunkley, M. R.olta, M. Halpern, R. S. Hill, N. Odegard, L. Page, K. M. Smith, J. L. Weiland, B. Gold, N. Jarosik, A. Kogut, M. Limon, S. S. Meyer, G. S. Tucker, E. Wollack, and E. L. Wright. Nine-year wilkinson microwave anisotropy probe (wmap) observations: Cosmological parameter results. *The Astrophysical Journal Supplement Series*, 208(2):19, 2013.
- R. W. Hockney and J. W. Eastwood. *Computer Simulation Using Particles*. McGraw-Hill, 1981.
- P. F. Hopkins. A general class of Lagrangian smoothed particle hydrodynamics methods and implications for fluid mixing problems. *MNRAS*, 428:2840–2856, 2013.

Bibliography

- P. F. Hopkins. GIZMO: A New Class of Accurate, Mesh-Free Hydrodynamic Simulation Methods. *ArXiv e-prints*, 1409.7395, 2014.
- P. F. Hopkins, G. T. Richards, and L. Hernquist. An Observational Determination of the Bolometric Quasar Luminosity Function. *ApJ*, 654:731–753, 2007.
- P. F. Hopkins, E. Quataert, and N. Murray. Stellar feedback in galaxies and the origin of galaxy-scale winds. *MNRAS*, 421:3522–3537, 2012.
- W. Hu. Reionization Revisited: Secondary Cosmic Microwave Background Anisotropies and Polarization. *ApJ*, 529:12–25, 2000.
- L. Hui and N. Y. Gnedin. Equation of state of the photoionized intergalactic medium. *MNRAS*, 292:27, 1997.
- I. Iliev, M. Santos, A. Mesinger, S. Majumdar, and G. Mellema. Epoch of Reionization modelling and simulations for SKA. *Advancing Astrophysics with the Square Kilometre Array (AASKA14)*, art. 7, 2015.
- I. T. Iliev, E. Scannapieco, and P. R. Shapiro. The Impact of Small-Scale Structure on Cosmological Ionization Fronts and Reionization. *ApJ*, 624:491–504, 2005.
- I. T. Iliev, B. Ciardi, M. A. Alvarez, A. Maselli, A. Ferrara, N. Y. Gnedin, G. Mellema, T. Nakamoto, M. L. Norman, A. O. Razoumov, E.-J. Rijkhorst, J. Ritzerveld, P. R. Shapiro, H. Susa, M. Umemura, and D. J. Whalen. Cosmological radiative transfer codes comparison project - I. The static density field tests. *MNRAS*, 371:1057–1086, 2006a.
- I. T. Iliev, G. Mellema, U.-L. Pen, H. Merz, P. R. Shapiro, and M. A. Alvarez. Simulating cosmic reionization at large scales - I. The geometry of reionization. *MNRAS*, 369:1625–1638, 2006b.
- I. T. Iliev, G. Mellema, K. Ahn, P. R. Shapiro, Y. Mao, and U.-L. Pen. Simulating cosmic reionization: how large a volume is large enough? *MNRAS*, 439:725–743, 2014.
- A. Jeon-Daniel, B. Ciardi, and L. Graziani. Clumping factors of H II, He II and He III. *MNRAS*, 443:2722–2732, 2014.
- M. Kaplinghat, M. Chu, Z. Haiman, G. P. Holder, L. Knox, and C. Skordis. Probing the Reionization History of the Universe using the Cosmic Microwave Background Polarization. *ApJ*, 583:24–32, 2003.
- N. Kashikawa, K. Shimasaku, Y. Matsuda, E. Egami, L. Jiang, T. Nagao, M. Ouchi, M. A. Malkan, T. Hattori, K. Ota, Y. Taniguchi, S. Okamura, C. Ly, M. Iye, H. Furusawa, Y. Shioya, T. Shibuya, Y. Ishizaki, and J. Toshikawa. Completing the Census of Ly α Emitters at the Reionization Epoch. *ApJ*, 734:119, 2011.

- B. Keating, P. Timbie, A. Polnarev, and J. Steinberger. Large Angular Scale Polarization of the Cosmic Microwave Background Radiation and the Feasibility of Its Detection. *ApJ*, 495:580–596, 1998.
- R. S. Klessen, F. Heitsch, and M.-M. Mac Low. Gravitational Collapse in Turbulent Molecular Clouds. I. Gasdynamical Turbulence. *ApJ*, 535:887–906, 2000.
- K. Kohler, N. Y. Gnedin, and A. J. S. Hamilton. Large-Scale Simulations of Reionization. *ApJ*, 657:15–29, 2007.
- K. Korista, J. Baldwin, G. Ferland, and D. Verner. An Atlas of Computed Equivalent Widths of Quasar Broad Emission Lines. *ApJS*, 108:401–415, 1997.
- A. V. Kravtsov, A. A. Klypin, and A. M. Khokhlov. Adaptive Refinement Tree: A New High-Resolution N-Body Code for Cosmological Simulations. *ApJS*, 111:73–94, 1997.
- M. R. Krumholz and T. A. Thompson. Direct Numerical Simulation of Radiation Pressure-driven Turbulence and Winds in Star Clusters and Galactic Disks. *ApJ*, 760:155, 2012.
- M. R. Krumholz, R. I. Klein, C. F. McKee, and J. Bolstad. Equations and Algorithms for Mixed-frame Flux-limited Diffusion Radiation Hydrodynamics. *ApJ*, 667:626–643, 2007.
- M. Kuhlen and C.-A. Faucher-Giguère. Concordance models of reionization: implications for faint galaxies and escape fraction evolution. *MNRAS*, 423:862–876, 2012.
- P. Kunasz and L. H. Auer. Short characteristic integration of radiative transfer problems - Formal solution in two-dimensional slabs. *J. Quant. Spec. Radiat. Transf.*, 39:67–79, 1988.
- C. Leitherer, D. Schaerer, J. D. Goldader, R. M. G. Delgado, C. Robert, D. F. Kune, D. F. de Mello, D. Devost, and T. M. Heckman. Starburst99: Synthesis models for galaxies with active star formation. *The Astrophysical Journal Supplement Series*, 123(1):3, 1999.
- C. D. Levermore and G. C. Pomraning. A flux-limited diffusion theory. *ApJ*, 248:321–334, 1981.
- A. Lidz, L. Hui, M. Zaldarriaga, and R. Scoccimarro. How Neutral Is the Intergalactic Medium at $z \sim 6$? *ApJ*, 579:491–499, 2002.
- A. Loeb and R. Barkana. The Reionization of the Universe by the First Stars and Quasars. *ARA&A*, 39:19–66, 2001.
- A. Loeb and G. B. Rybicki. Scattered Ly α Radiation around Sources before Cosmological Reionization. *ApJ*, 524:527–535, 1999.

Bibliography

- L. B. Lucy. A numerical approach to the testing of the fission hypothesis. *AJ*, 82: 1013–1024, 1977.
- M.-M. Mac Low and R. S. Klessen. Control of star formation by supersonic turbulence. *Reviews of Modern Physics*, 76:125–194, 2004.
- P. Madau, F. Haardt, and M. J. Rees. Radiative Transfer in a Clumpy Universe. III. The Nature of Cosmological Ionizing Sources. *ApJ*, 514:648–659, 1999.
- A. Maselli, A. Ferrara, and B. Ciardi. CRASH: a radiative transfer scheme. *MNRAS*, 345:379–394, 2003.
- P. McDonald and J. Miralda-Escudé. The Ly α Forest Flux Distribution at $Z \sim 5.2$ and the Evolution of the Ionizing Background. *ApJ*, 549:L11–L14, 2001.
- P. McDonald, J. Miralda-Escudé, M. Rauch, W. L. W. Sargent, T. A. Barlow, R. Cen, and J. P. Ostriker. The Observed Probability Distribution Function, Power Spectrum, and Correlation Function of the Transmitted Flux in the Ly α Forest. *ApJ*, 543:1–23, 2000.
- M. McQuinn, L. Hernquist, M. Zaldarriaga, and S. Dutta. Studying reionization with Ly α emitters. *MNRAS*, 381:75–96, 2007a.
- M. McQuinn, A. Lidz, O. Zahn, S. Dutta, L. Hernquist, and M. Zaldarriaga. The morphology of HII regions during reionization. *MNRAS*, 377:1043–1063, 2007b.
- M. McQuinn, A. Lidz, O. Zahn, S. Dutta, L. Hernquist, and M. Zaldarriaga. The morphology of HII regions during reionization. *MNRAS*, 377:1043–1063, 2007c.
- M. McQuinn, A. Lidz, M. Zaldarriaga, L. Hernquist, P. F. Hopkins, S. Dutta, and C.-A. Faucher-Giguère. He II Reionization and its Effect on the Intergalactic Medium. *ApJ*, 694:842–866, 2009.
- G. Mellema, A. C. Raga, J. Canto, P. Lundqvist, B. Balick, W. Steffen, and A. Noriega-Crespo. Photo-evaporation of clumps in planetary nebulae. *A&A*, 331:335–346, 1998.
- G. Mellema, I. T. Iliev, M. A. Alvarez, and P. R. Shapiro. C²-ray: A new method for photon-conserving transport of ionizing radiation. *New A*, 11:374–395, 2006a.
- G. Mellema, I. T. Iliev, U.-L. Pen, and P. R. Shapiro. Simulating cosmic reionization at large scales - II. The 21-cm emission features and statistical signals. *MNRAS*, 372:679–692, 2006b.
- A. Mesinger and S. Furlanetto. Efficient Simulations of Early Structure Formation and Reionization. *ApJ*, 669:663–675, 2007.
- A. Mesinger, S. Furlanetto, and R. Cen. 21CMFAST: a fast, seminumerical simulation of the high-redshift 21-cm signal. *MNRAS*, 411:955–972, 2011.

- A. Mignone, C. Zanni, P. Tzeferacos, B. van Straalen, P. Colella, and G. Bodo. The PLUTO Code for Adaptive Mesh Computations in Astrophysical Fluid Dynamics. *ApJS*, 198:7, 2012.
- D. Mihalas and B. W. Mihalas. *Foundations of radiation hydrodynamics*. Oxford University Press, 1984.
- J. Miralda-Escudé, M. Haehnelt, and M. J. Rees. Reionization of the Inhomogeneous Universe. *ApJ*, 530:1–16, 2000.
- P. Mocz, M. Vogelsberger, D. Sijacki, R. Pakmor, and L. Hernquist. A discontinuous Galerkin method for solving the fluid and magnetohydrodynamic equations in astrophysical simulations. *MNRAS*, 437:397–414, 2014.
- R. Mondal, S. Bharadwaj, S. Majumdar, A. Bera, and A. Acharyya. The effect of non-Gaussianity on error predictions for the Epoch of Reionization (EoR) 21-cm power spectrum. *MNRAS*, 449:L41–L45, 2015.
- M. F. Morales and J. S. B. Wyithe. Reionization and Cosmology with 21-cm Fluctuations. *ARA&A*, 48:127–171, 2010.
- N. Murray, E. Quataert, and T. A. Thompson. The Disruption of Giant Molecular Clouds by Radiation Pressure & the Efficiency of Star Formation in Galaxies. *ApJ*, 709:191–209, 2010.
- T. Nakamoto, M. Umemura, and H. Susa. The effects of radiative transfer on the reionization of an inhomogeneous universe. *MNRAS*, 321:593–604, 2001.
- S. Nayakshin, S.-H. Cha, and A. Hobbs. Dynamic Monte Carlo radiation transfer in SPH: radiation pressure force implementation. *MNRAS*, 397:1314–1325, 2009.
- M. L. Norman, D. R. Reynolds, G. C. So, and R. P. Harkness. Direct Numerical Simulation of Reionization in Large Cosmological Volumes I: Numerical Methods and Tests. *ArXiv e-prints*, 2013.
- P. A. Oesch, R. J. Bouwens, G. D. Illingworth, I. Labbé, R. Smit, M. Franx, P. G. van Dokkum, I. Momcheva, M. L. N. Ashby, G. G. Fazio, J.-S. Huang, S. P. Willner, V. Gonzalez, D. Magee, M. Trenti, G. B. Brammer, R. E. Skelton, and L. R. Spitler. The Most Luminous $z \sim 9-10$ Galaxy Candidates Yet Found: The Luminosity Function, Cosmic Star-formation Rate, and the First Mass Density Estimate at 500 Myr. *ApJ*, 786:108, 2014.
- M. Ouchi, K. Shimasaku, H. Furusawa, T. Saito, M. Yoshida, M. Akiyama, Y. Ono, T. Yamada, K. Ota, N. Kashikawa, M. Iye, T. Kodama, S. Okamura, C. Simpson, and M. Yoshida. Statistics of 207 Ly α Emitters at a Redshift Near 7: Constraints on Reionization and Galaxy Formation Models. *ApJ*, 723:869–894, 2010.
- J.-P. Paardekooper, C. J. H. Kruip, and V. Icke. SimpleX2: radiative transfer on an unstructured, dynamic grid. *A&A*, 515:A79, 2010.

Bibliography

- J.-P. Paardekooper, S. Khochfar, and C. Dalla Vecchia. The First Billion Years project: proto-galaxies reionizing the Universe. *MNRAS*, 429:L94–L98, 2013.
- A. R. Parsons, A. Liu, J. E. Aguirre, Z. S. Ali, R. F. Bradley, C. L. Carilli, D. R. DeBoer, M. R. Dexter, N. E. Gugliucci, D. C. Jacobs, P. Klima, D. H. E. MacMahon, J. R. Manley, D. F. Moore, J. C. Pober, I. I. Stefan, and W. P. Walbrugh. New Limits on 21 cm Epoch of Reionization from PAPER-32 Consistent with an X-Ray Heated Intergalactic Medium at $z = 7.7$. *ApJ*, 788:106, 2014.
- A. H. Pawlik and J. Schaye. TRAPHIC - radiative transfer for smoothed particle hydrodynamics simulations. *MNRAS*, 389:651–677, 2008.
- A. H. Pawlik, J. Schaye, and E. van Scherpenzeel. Keeping the Universe ionized: photoheating and the clumping factor of the high-redshift intergalactic medium. *MNRAS*, 394:1812–1824, 2009.
- A. H. Pawlik, J. Schaye, and C. Dalla Vecchia. Spatially adaptive radiation-hydrodynamical simulations of galaxy formation during cosmological reionization. *ArXiv e-prints*, 2015.
- L. Pentericci, A. Fontana, E. Vanzella, M. Castellano, A. Grazian, M. Dijkstra, K. Boutsia, S. Cristiani, M. Dickinson, E. Giallongo, M. Giavalisco, R. Maiolino, A. Moorwood, D. Paris, and P. Santini. Spectroscopic Confirmation of $z \sim 7$ Lyman Break Galaxies: Probing the Earliest Galaxies and the Epoch of Reionization. *ApJ*, 743:132, 2011.
- M. Petkova and V. Springel. An implementation of radiative transfer in the cosmological simulation code GADGET. *MNRAS*, 396:1383–1403, 2009.
- M. Petkova and V. Springel. A novel approach for accurate radiative transfer in cosmological hydrodynamic simulations. *MNRAS*, 415:3731–3749, 2011a.
- M. Petkova and V. Springel. Simulations of galaxy formation with radiative transfer: hydrogen reionization and radiative feedback. *MNRAS*, 412:935–946, 2011b.
- A. Pillepich, M. Vogelsberger, A. Deason, V. Rodriguez-Gomez, S. Genel, D. Nelson, P. Torrey, L. V. Sales, F. Marinacci, V. Springel, D. Sijacki, and L. Hernquist. Halo mass and assembly history exposed in the faint outskirts: the stellar and dark matter haloes of Illustris galaxies. *MNRAS*, 444:237–249, 2014.
- Planck Collaboration, P. A. R. Ade, N. Aghanim, C. Armitage-Caplan, M. Arnaud, M. Ashdown, F. Atrio-Barandela, J. Aumont, C. Baccigalupi, A. J. Banday, and et al. Planck 2013 results. XVI. Cosmological parameters. *A&A*, 571:A16, 2014.
- Planck Collaboration, R. Adam, P. A. R. Ade, N. Aghanim, Y. Akrami, M. I. R. Alves, M. Arnaud, F. Arroja, J. Aumont, C. Baccigalupi, and et al. Planck 2015 results. I. Overview of products and scientific results. *ArXiv e-prints*, 2015a.

- Planck Collaboration, P. A. R. Ade, N. Aghanim, M. Arnaud, M. Ashdown, J. Aumont, C. Baccigalupi, A. J. Banday, R. B. Barreiro, J. G. Bartlett, and et al. Planck 2015 results. XIII. Cosmological parameters. *ArXiv e-prints*, 2015b.
- D. J. Price. Modelling discontinuities and Kelvin Helmholtz instabilities in SPH. *Journal of Computational Physics*, 227:10040–10057, 2008.
- D. J. Price and C. Federrath. A comparison between grid and particle methods on the statistics of driven, supersonic, isothermal turbulence. *MNRAS*, 406:1659–1674, 2010.
- A. Rahmati, A. H. Pawlik, M. Raičević, and J. Schaye. On the evolution of the H I column density distribution in cosmological simulations. *MNRAS*, 430:2427–2445, 2013.
- A. O. Razoumov and C. Y. Cardall. Fully threaded transport engine: new method for multi-scale radiative transfer. *MNRAS*, 362:1413–1417, 2005.
- A. O. Razoumov, M. L. Norman, T. Abel, and D. Scott. Cosmological Hydrogen Reionization with Three-dimensional Radiative Transfer. *ApJ*, 572:695–704, 2002.
- J. I. Read and T. Hayfield. SPHS: smoothed particle hydrodynamics with a higher order dissipation switch. *MNRAS*, 422:3037–3055, 2012.
- J. I. Read, T. Hayfield, and O. Agertz. Resolving mixing in smoothed particle hydrodynamics. *MNRAS*, 405:1513–1530, 2010.
- W. H. Reed and T. Hill. Triangularmesh methodsfor the neutrontransportequation. *Los Alamos Report LA-UR-73-479*, 1973.
- M. J. Rees. ‘First light’ in the universe: what ended the ‘dark age’? *Phys. Rep.*, 333:203–214, 2000.
- B. E. Robertson, R. S. Ellis, S. R. Furlanetto, and J. S. Dunlop. Cosmic Reionization and Early Star-Forming Galaxies: A Joint Analysis of New Constraints from Planck and Hubble Space Telescope. *ArXiv e-prints*, 2015.
- V. Rodriguez-Gomez, S. Genel, M. Vogelsberger, D. Sijacki, A. Pillepich, L. V. Sales, P. Torrey, G. Snyder, D. Nelson, V. Springel, C.-P. Ma, and L. Hernquist. The merger rate of galaxies in the Illustris Simulation: a comparison with observations and semi-empirical models. *ArXiv e-prints*, 2015.
- J. Rosdahl, J. Blaizot, D. Aubert, T. Stranex, and R. Teyssier. RAMSES-RT: radiation hydrodynamics in the cosmological context. *MNRAS*, 436:2188–2231, 2013.
- J. Rosdahl, J. Schaye, R. Teyssier, and O. Agertz. Galaxies that Shine: radiation-hydrodynamical simulations of disk galaxies. *ArXiv e-prints*, 2015.

Bibliography

- G. B. Rybicki and A. Loeb. Polarization of the Ly α Halos around Sources before Cosmological Reionization. *ApJ*, 520:L79–L81, 1999.
- L. V. Sales, F. Marinacci, V. Springel, and M. Petkova. Stellar feedback by radiation pressure and photoionization. *MNRAS*, 439:2990–3006, 2014.
- L. V. Sales, M. Vogelsberger, S. Genel, P. Torrey, D. Nelson, V. Rodriguez-Gomez, W. Wang, A. Pillepich, D. Sijacki, V. Springel, and L. Hernquist. The colours of satellite galaxies in the Illustris simulation. *MNRAS*, 447:L6–L10, 2015.
- C. Scannapieco, M. Wadepuhl, O. H. Parry, J. F. Navarro, A. Jenkins, V. Springel, R. Teyssier, E. Carlson, H. M. P. Couchman, R. A. Crain, C. Dalla Vecchia, C. S. Frenk, C. Kobayashi, P. Monaco, G. Murante, T. Okamoto, T. Quinn, J. Schaye, G. S. Stinson, T. Theuns, J. Wadsley, S. D. M. White, and R. Woods. The Aquila comparison project: the effects of feedback and numerical methods on simulations of galaxy formation. *MNRAS*, 423:1726–1749, 2012.
- K. Schaal, A. Bauer, P. Chandrashekar, R. Pakmor, C. Klingenberg, and V. Springel. Astrophysical hydrodynamics with a high-order discontinuous Galerkin scheme and adaptive mesh refinement. *ArXiv e-prints*, 2015.
- J. Schaye, T. Theuns, M. Rauch, G. Efstathiou, and W. L. W. Sargent. The thermal history of the intergalactic medium*. *MNRAS*, 318:817–826, 2000.
- J. Schaye, R. A. Crain, R. G. Bower, M. Furlong, M. Schaller, T. Theuns, C. Dalla Vecchia, C. S. Frenk, I. G. McCarthy, J. C. Helly, A. Jenkins, Y. M. Rosas-Guevara, S. D. M. White, M. Baes, C. M. Booth, P. Camps, J. F. Navarro, Y. Qu, A. Rahmati, T. Sawala, P. A. Thomas, and J. Trayford. The EAGLE project: simulating the evolution and assembly of galaxies and their environments. *MNRAS*, 446:521–554, 2015.
- W. Schmidt, W. Hillebrandt, and J. C. Niemeyer. Numerical dissipation and the bottleneck effect in simulations of compressible isotropic turbulence. *Computers & Fluids*, 35(4):353 – 371, 2006.
- P. Schuecker, A. Finoguenov, F. Miniati, H. Böhringer, and U. G. Briel. Probing turbulence in the Coma galaxy cluster. *A&A*, 426:387–397, 2004.
- B. Semelin and I. Iliev. The physics of Reionization: processes relevant for SKA observations. *Advancing Astrophysics with the Square Kilometre Array (AASKA14)*, art. 13, 2015.
- B. Semelin, F. Combes, and S. Baek. Lyman-alpha radiative transfer during the epoch of reionization: contribution to 21-cm signal fluctuations. *A&A*, 474:365–374, 2007.
- D. Semenov, T. Henning, C. Helling, M. Ilgner, and E. Sedlmayr. Rosseland and Planck mean opacities for protoplanetary discs. *A&A*, 410:611–621, 2003.

- T. R. Seshadri and K. Subramanian. Vishniac-type contribution to the polarization of the CMBR? *Phys. Rev. D*, 58(6):063002, 1998.
- P. R. Shapiro, I. T. Iliev, and A. C. Raga. Photoevaporation of cosmological minihaloes during reionization. *MNRAS*, 348:753–782, 2004.
- D. Sijacki, M. Vogelsberger, S. Genel, V. Springel, P. Torrey, G. Snyder, D. Nelson, and L. Hernquist. The Illustris simulation: Evolving population of black holes across cosmic time. *ArXiv e-prints*, 2014.
- G. So, M. L. Norman, D. Reynolds, and R. Harkness. Direct Numerical Simulation of Reionization in Large Cosmological Volumes II: Clumping Factor Evolution and the Photon Budget for Reionization. In *American Astronomical Society Meeting Abstracts #221*, volume 221 of *American Astronomical Society Meeting Abstracts*, page 432.04, 2013.
- G. C. So, M. L. Norman, D. R. Reynolds, and J. H. Wise. Fully Coupled Simulation of Cosmic Reionization. II. Recombinations, Clumping Factors, and the Photon Budget for Reionization. *ApJ*, 789:149, 2014.
- A. Sokasian, T. Abel, and L. E. Hernquist. Simulating reionization in numerical cosmology. *New A*, 6:359–379, 2001.
- V. Springel. E pur si muove: Galilean-invariant cosmological hydrodynamical simulations on a moving mesh. *MNRAS*, 401:791–851, 2010.
- V. Springel and L. Hernquist. The history of star formation in a Λ cold dark matter universe. *MNRAS*, 339:312–334, 2003.
- V. Springel, S. D. M. White, G. Tormen, and G. Kauffmann. Populating a cluster of galaxies - I. Results at $z=0$. *MNRAS*, 328:726–750, 2001.
- V. Springel, J. Wang, M. Vogelsberger, A. Ludlow, A. Jenkins, A. Helmi, J. F. Navarro, C. S. Frenk, and S. D. M. White. The Aquarius Project: the subhaloes of galactic haloes. *MNRAS*, 391:1685–1711, 2008.
- G. S. Stinson, C. Brook, A. V. Macciò, J. Wadsley, T. R. Quinn, and H. M. P. Couchman. Making Galaxies In a Cosmological Context: the need for early stellar feedback. *MNRAS*, 428:129–140, 2013.
- B. Su and G. L. Olson. Benchmark results for the non-equilibrium Marshak diffusion problem. *J. Quant. Spec. Radiat. Transf.*, 56:337–351, 1996.
- H. Susa. Smoothed Particle Hydrodynamics Coupled with Radiation Transfer. *PASJ*, 58:445–460, 2006.
- R. Teyssier. Cosmological hydrodynamics with adaptive mesh refinement. A new high resolution code called RAMSES. *A&A*, 385:337–364, 2002.

Bibliography

- P. Torrey, M. Vogelsberger, S. Genel, D. Sijacki, V. Springel, and L. Hernquist. A model for cosmological simulations of galaxy formation physics: multi-epoch validation. *MNRAS*, 438:1985–2004, 2014.
- P. Torrey, G. F. Snyder, M. Vogelsberger, C. C. Hayward, S. Genel, D. Sijacki, V. Springel, L. Hernquist, D. Nelson, M. Kriek, A. Pillepich, L. V. Sales, and C. K. McBride. Synthetic galaxy images and spectra from the Illustris simulation. *MNRAS*, 447:2753–2771, 2015.
- P. Tozzi, P. Madau, A. Meiksin, and M. J. Rees. Radio Signatures of H I at High Redshift: Mapping the End of the “Dark Ages”. *ApJ*, 528:597–606, 2000.
- H. Trac and R. Cen. Radiative Transfer Simulations of Cosmic Reionization. I. Methodology and Initial Results. *ApJ*, 671:1–13, 2007.
- H. Trac, R. Cen, and A. Loeb. Imprint of Inhomogeneous Hydrogen Reionization on the Temperature Distribution of the Intergalactic Medium. *ApJ*, 689:L81–L84, 2008.
- H. Y. Trac and N. Y. Gnedin. Computer Simulations of Cosmic Reionization. *Advanced Science Letters*, 4:228–243, 2011.
- M. Vogelsberger, S. Genel, D. Sijacki, P. Torrey, V. Springel, and L. Hernquist. A model for cosmological simulations of galaxy formation physics. *MNRAS*, 436:3031–3067, 2013.
- M. Vogelsberger, S. Genel, V. Springel, P. Torrey, D. Sijacki, D. Xu, G. Snyder, S. Bird, D. Nelson, and L. Hernquist. Properties of galaxies reproduced by a hydrodynamic simulation. *Nature*, 509:177–182, 2014a.
- M. Vogelsberger, S. Genel, V. Springel, P. Torrey, D. Sijacki, D. Xu, G. Snyder, D. Nelson, and L. Hernquist. Introducing the Illustris Project: simulating the coevolution of dark and visible matter in the Universe. *MNRAS*, 444:1518–1547, 2014b.
- J. W. Wadsley, G. Veeravalli, and H. M. P. Couchman. On the treatment of entropy mixing in numerical cosmology. *MNRAS*, 387:427–438, 2008.
- F. Walter, F. Bertoldi, C. Carilli, P. Cox, K. Y. Lo, R. Neri, X. Fan, A. Omont, M. A. Strauss, and K. M. Menten. Molecular gas in the host galaxy of a quasar at redshift $z = 6.42$. *Nature*, 424:406–408, 2003.
- D. H. Weinberg, J. Miralda-Escudé, L. Hernquist, and N. Katz. A Lower Bound on the Cosmic Baryon Density. *ApJ*, 490:564–570, 1997.
- S. Wellons, P. Torrey, C.-P. Ma, V. Rodriguez-Gomez, M. Vogelsberger, M. Kriek, P. van Dokkum, E. Nelson, S. Genel, A. Pillepich, V. Springel, D. Sijacki, G. Snyder, D. Nelson, L. Sales, and L. Hernquist. The Formation of Massive, Compact Galaxies at $z=2$ in the Illustris Simulation. *ArXiv e-prints*, 2014.

- C. Wetterich. Phenomenological parameterization of quintessence. *Physics Letters B*, 594:17–22, 2004.
- D. Whalen and M. L. Norman. A Multistep Algorithm for the Radiation Hydrodynamical Transport of Cosmological Ionization Fronts and Ionized Flows. *ApJS*, 162:281–303, 2006.
- R. L. White, R. H. Becker, X. Fan, and M. A. Strauss. Probing the Ionization State of the Universe at $z > 6$. *AJ*, 126:1–14, 2003.
- J. H. Wise, V. G. Demchenko, M. T. Halicek, M. L. Norman, M. J. Turk, T. Abel, and B. D. Smith. The birth of a galaxy - III. Propelling reionization with the faintest galaxies. *MNRAS*, 442:2560–2579, 2014.
- J. S. B. Wyithe and A. Loeb. A characteristic size of ~ 10 Mpc for the ionized bubbles at the end of cosmic reionization. *Nature*, 432:194–196, 2004.
- J. S. B. Wyithe and A. Loeb. Undetected Sources Allow Transmission of the Ly α Line from Galaxies Prior to Reionization. *ApJ*, 625:1–5, 2005.
- N. Yoshida, A. Sokasian, L. Hernquist, and V. Springel. Early Structure Formation and Reionization in a Warm Dark Matter Cosmology. *ApJ*, 591:L1–L4, 2003a.
- N. Yoshida, A. Sokasian, L. Hernquist, and V. Springel. Early Structure Formation and Reionization in a Cosmological Model with a Running Primordial Power Spectrum. *ApJ*, 598:73–85, 2003b.
- O. Zahn, A. Lidz, M. McQuinn, S. Dutta, L. Hernquist, M. Zaldarriaga, and S. R. Furlanetto. Simulations and Analytic Calculations of Bubble Growth during Hydrogen Reionization. *ApJ*, 654:12–26, 2007.
- O. Zahn, A. Mesinger, M. McQuinn, H. Trac, R. Cen, and L. E. Hernquist. Comparison of reionization models: radiative transfer simulations and approximate, seminumeric models. *MNRAS*, 414:727–738, 2011.
- M. Zaldarriaga. Polarization of the microwave background in reionized models. *Phys. Rev. D*, 55:1822–1829, 1997.
- O. Zanotti, F. Fambri, and M. Dumbser. Solving the relativistic magnetohydrodynamics equations with ADER discontinuous Galerkin methods, a posteriori subcell limiting and adaptive mesh refinement. *ArXiv e-prints*, 2015.
- S. Zaroubi. The Epoch of Reionization. In T. Wiklind, B. Mobasher, and V. Bromm, editors, *Astrophysics and Space Science Library*, volume 396 of *Astrophysics and Space Science Library*, page 45, 2013.
- X. Zhang and C.-W. Shu. On positivity-preserving high order discontinuous Galerkin schemes for compressible Euler equations on rectangular meshes. *Journal of Computational Physics*, 229:8918–8934, 2010.

Acknowledgments

I am very grateful to many people for their support during my PhD and while writing this thesis.

In particular, I would like to express my sincere thanks to Prof. Volker Springel for accepting me as a PhD student and proposing a topic. I appreciated many helpful discussions and encouragements. He always took time for support and patient explanations. I can not imagine a better supervisor. Thank you!

I would also like to thank Prof. Cornelis Dullemond who kindly agreed to referee this thesis.

Furthermore, I would like to thank my colleagues in the TAP group at HITS who helped me with countless explanations and advises. I would like to thank my office-mates Christian Arnold, Rüdiger Pakmor, Christoph Pfrommer, Ewald Puchwein, Kevin Schaal and Rainer Weinberger for all the discussions (not only about physics) and for the brilliant working atmosphere. Here, all the administrative and support people at HITS should be mentioned for their work. I would like to thank Ralf Westermann and his team for preparing such a great lunch for us during the last five years. Especially I would like to thank Klaus Tschira for his support to HITS. Without him, this institute would never have been possible.

I would like to express my gratitude towards my family and my beloved parents. I thank them for their aid, support and continuous encouragements during my whole life. But especially, I would like to thank Jana for her encouragement and support during writing this thesis – and even more important to me – for all the time spend together and her love.